Université libre de Bruxelles
Sciences de la Terre et de l'Environnement
Géochimie et Minéralogie Appliquée

Imaging measurements of volcanic SO2 using space and ground based sensors.

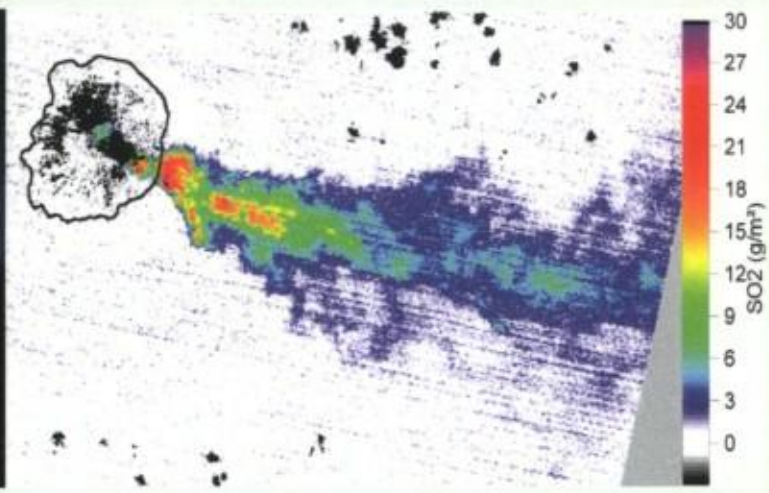

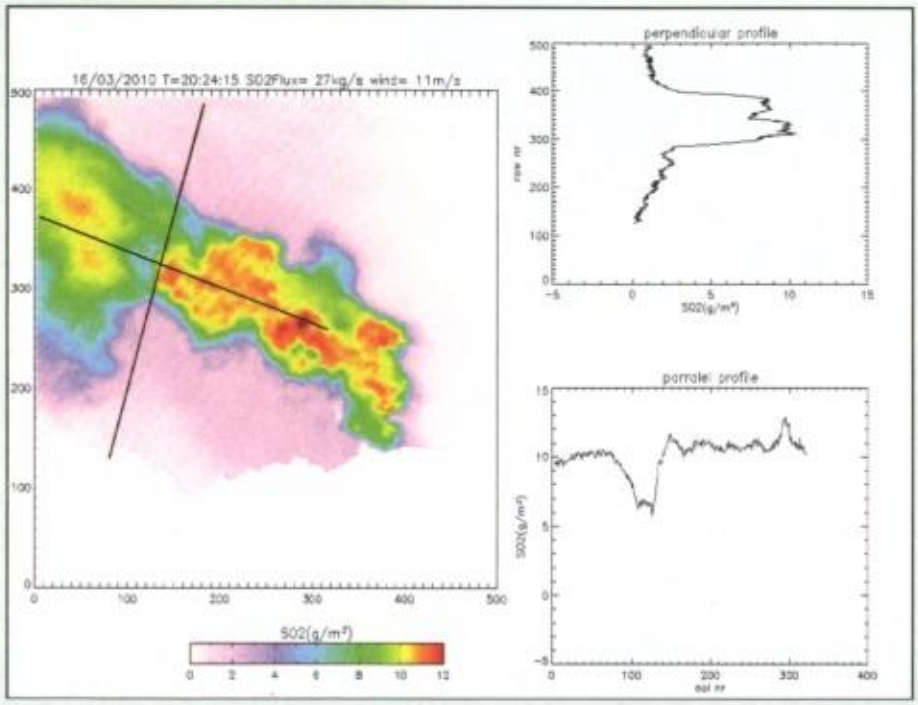

Thesis submitted for obtaining
the degree of « Docteur en Sciences »

Robin Campion

June 2011

Université Libre de Bruxelles

Département des Science de la Terre et de l'Environnement
Laboratoire de Géochimie et Minéralogie Appliquée

Imaging measurements of volcanic SO_2 using space and ground based sensors.

Thesis submitted by **Robin Campion**
for obtaining the degree of « Docteur en Sciences »

Advisor: Alain Bernard
Co-advisor: Pierre-François Coheur

June 2011

Dédié à François le Guern,
Pionnier de l'étude des gaz volcaniques.
Un Grand volcanologue, d'une gentillesse et d'une modestie exceptionnelle, qui m'avait dit un jour « Les bons volcanologues meurent dans leur lit »

Abstract

Sulfur dioxide (SO_2) is a gas typical of high temperature magmatic degassing, being its third most abundant constituent after water vapor and carbon dioxide. SO_2 flux measurements are used to characterized and monitor volcanic degassing. This thesis presents advanced methods for measuring the SO_2 emitted in the troposphere by passive degassing volcanoes. These methods are based on the absorption of infrared (IR) and ultraviolet (UV) light by SO_2 molecules. They make use of the data acquired by satellite borne sensors (ASTER, OMI and MODIS), and collected in the field using a UV camera equipped with filters

ASTER is a multispectral sensor observing the Earth in the thermal IR with a 90 m ground resolution. The developed retrieval algorithm works with band ratios (B10+B12)/2B11 and B14/B11, to avoid spectral interference from other variables than SO_2. With this algorithm, the impact of interferers such as atmospheric water vapor, sulfate aerosols and ground emissivity is minimal, as demonstrated by radiative transfer simulations by applying of the algorithm to real ASTER images and by comparing the results with ground based data. ASTER is a kind of unifying thread for this thesis because its high ground resolution fills the gap existing between highly localized ground based SO_2 measurements and the global coverage of other satellites with coarser pixels such as OMI and MODIS.

OMI is an imaging spectrometer operating in the UV, with a daily global coverage, a high sensitivity to SO_2 and a ground resolution of 13x24km. The OMI-ASTER comparison shows that the SO_2 columns measured on OMI pixels are two orders of magnitude smaller than those of ASTER, because of the huge difference in the pixel size of the two satellites. The flux measurements however are generally in good agreement. The analysis of a large number of images shows that ASTER is better for cloud free scenes while OMI has an optimal signal to noise ratio when the plume is lying above a low cloud cover. A practical detection limit for SO_2 flux measurements in tropospheric plumes has also been established: 5kg/s.

The comparison between ASTER measurements of SO_2 column amounts with those of MODIS (a multispectral IR imager with 1km ground resolution) shed light on systematic errors in MODIS measurements. These errors were quantified and their origins were separated and identified. This work demonstrates the limitations of MODIS for SO_2 measurements.

A UV camera equipped with filters has also been developed to achieve 2D SO_2 from the ground at a high spatial and temporal resolution. The potential provided by this new type of instruments has been demonstrated during a field campaign on Turrialba Volcano (Costa Rica). The integration of measurements obtained using the camera, ASTER and OMI revealed a high and sustained SO_2 flux, which can be explained only by the degassing of a recently intruded magma body. The slow decrease of SO_2 flux since January 2010 suggests a progressive exhaustion of the volatile content of the magma.

Finally, we applied the band ratio algorithm to a series of ASTER images of the recent eruption of Eyjafjallajökull in April-May 2010. The SO_2 measurements provide interesting insights into the complex eruptive dynamics and into the control of hydromagmatic interactions on eruptive gas release into the atmosphere.

Résumé

Le dioxyde de soufre (SO_2) est un gaz typique du dégazage magmatique de haute température, dont il est le troisième composant le plus abondant derrière H_2O et CO_2. Le flux de SO_2 est un excellent paramètre pour caractériser le dégazage volcanique et surveiller son évolution dans le temps. Cette thèse présente de nouvelles méthodes de mesures des flux de SO_2 émis par l'activité volcanique. Ces méthodes se basent sur l'absorption de la molécule de SO_2 dans l'infrarouge (IR) et l'ultraviolet (UV). Elles utilisent les données prises par des senseurs embarqués sur des satellites (ASTER, OMI et MODIS) ou opérés depuis le sol (caméra UV munie de filtres).

Le senseur ASTER opère dans l'IR thermique avec une résolution spatiale de 90 m par pixel. L'algorithme de mesure développé pour ce satellite n'est sensible qu'à la concentration en SO_2 et pratiquement pas aux paramètres interférents qui posaient problèmes aux méthodes existantes : la vapeur d'eau atmosphérique, les aérosols de sulfate dans le panache et l'émissivité de la surface sous-jacente. ASTER est un peu le fil conducteur de cette thèse, car sa haute résolution spatiale lui permet de faire le lien entre des mesures au sol et les mesures faites par d'autres satellites comme OMI et MODIS.

Le satellite OMI est un spectromètre imageant qui opère dans l'UV, avec une couverture globale journalière, une haute sensitivité au SO_2 et une résolution spatiale de 13x24km. La comparaison OMI-ASTER montre que les colonnes mesurées sur les pixels d'OMI sont de deux ordres de grandeur inférieurs à celles d'ASTER, à cause de la différence de résolution spatiale entre les deux satellites. Les mesures de flux, par contre, montrent une très bonne concordance. L'analyse d'un grand nombre d'images a permis d'établir qu'ASTER est meilleur pour des scènes sans nuages tandis qu'OMI est meilleur quand une couverture nuageuse présente sous le panache augmente son rapport signal sur bruit. Une limite de détection pratique a aussi été établie pour les flux de SO_2 dans les panaches volcaniques dans la basse troposphère : 5kg/s.

La comparaison des mesures d'ASTER avec celle de MODIS a permis de démontrer les limites de MODIS pour la mesure du SO_2. Des erreurs systématiques sur les mesures de MODIS on été mises en évidence et quantifiées. Ces erreurs sont dues aux interférents spectraux que sont la vapeur d'eau atmosphérique et les aérosols sulfatés. L'émissivité est aussi un important facteur d'erreur pour MODIS.

Une caméra UV équipée d'un système de filtres a également été développée pour mesurer le SO_2 en 2D, à haute résolution spatiale et temporelle. Le potentiel offert par ce nouveau type d'instrument a été démontré lors d'une campagne de mesures sur le volcan Turrialba (Costa Rica). La combinaison de mesures de SO_2 réalisée avec la caméra, ASTER et OMI a permis de mettre en évidence des flux très élevés (30-50kg/s) qui ne peuvent s'expliquer que par une intrusion récente de magma juvénile en cours de dégazage.

Enfin, les mesures de SO_2 ont réalisées à partir des images ASTER pendant l'éruption du volcan Eyjafjallajökull en avril-mai 2010. Ces mesures fournissent des informations intéressantes sur les dynamismes éruptifs qui se sont succédé et sur le contrôle des émissions de SO_2 dans l'atmosphère par les interactions magma-eau.

Remerciements

La thèse est écrite ! Une page se tourne, la fin d'une aventure de quatre ans et demi. De belles années, définitivement ! Je voudrais remercier toutes les personnes qui m'ont aidé dans l'accomplissement de cette thèse.

Tout d'abord, je remercie mon promoteur Alain Bernard et mon co-promoteur Pierre-François Coheur, pour leur soutien, leur confiance accordée durant toute cette année, et pour la liberté qu'ils m'ont laissée, de choisir les axes de recherches qui ont conduit à la rédaction de cette thèse.

J'ai pu tout au long de cette thèse bénéficier de l'aide extrêmement précieuse de plusieurs personnes de l'Institut d'Aéronomie Spatiale de Belgique, et je voudrais les remercier du fond du cœur : Christian Hermans pour la confection des cellules de calibration, Gaia Pinardi pour m'avoir fourni les images OMI et les vents ECMWF, Caroline Fayt, Alexis Merlot et Michel Van Roozendael pour le prêt d'un DOAS lors des campagnes de terrain et leurs explications sur « comment ça marche ».

Toute ma reconnaissance va également à Daniel Hurtmans et Lieven Clarisse du Service de Chimie Quantique et Photophysique, pour leur aide dans le domaine des transferts radiatifs.

Je remercie chaleureusement Pierre Quicqueré et Benjamin Morin pour leur soutien lors des campagnes de terrains, et pour m'avoir fait passer du statut de doctorant anonyme à celui d'antihéros de la cinématographie volcanique.

Je remercie Thomas Lecocq pour son amitié et son aide dans le traitement des données sismiques, et Benjamin Barbier, pour les 3 ans passés ensemble dans le bureau le plus désordonné du DSTE (ok c'était surtout mon désordre). A propos du DSTE je regretterai certainement l'atmosphère conviviale qui régnait entre les « djeunes ». Merci à vous tous Gaëlle, Marjorie, Aurélien, Marguerite, Céline, Julien, Vinciane, Fréderic, Claire, Julie, Ivan, Franck et Jérôme.

Je remercie ma Maman pour ses bons petits plats, mon Papa et puis Nathalie, mon amour, pour son soutien au moment où j'en avais le plus besoin.

Enfin, tout comme il l'avait fait voilà quatre ans pour mon mémoire, mon Frère a relu mes premiers jets avec attention et patience. Je lui en suis éternellement reconnaissant.

Introduction : Volcanic gases

Volcanic activity is certainly one of the most fascinating natural phenomena, and poses a direct risk to the lives and belongings of more than 500 millions human beings (e.g. Tilling and Lipman, 1993). Volcanism emits two kinds of materials: solid products and gases. Solid material (though initially molten), can emplace as massive rock units known as lava, or be fragmented and dispersed by the eruption processes, forming pyroclastic deposits. If intensive research has been dedicated to volcanic rocks for more than two centuries, relatively little interest was paid to volcanic gases until the late 1950s. The primary reasons for this were the lack of reliable and adapted sampling techniques, and the difficulty or the danger of approaching high temperature gas sources. However, volcanic gases are an important object of research for three main reasons:

1°) They are the driving force of eruptions

2°) They are messengers of the magma.

3°) They influence the chemistry of the Earth Atmosphere and its Climate

These reasons will be detailed in this chapter, but first, we will begin with a short review of the data about the gas contents in the magmas.

1.1 Origin and abundance of volcanic gases

The Earth mantle contains a small but significant amount of volatiles, a term that defines compounds that are under gaseous state at surface pressure and temperature, and that includes water, carbon, sulphur, halogens and noble gases. In particular, sulphur in the mantle is associated with iron, copper, nickel and platinum group elements as an independent high pressure and temperature solid phase known as monosulphide solid solution (Bishop et al., 1975). Isotopic signatures of volcanic gases (He, C, H, O) and their variations over different geodynamical contexts allow insights in the origin of volatiles in the mantle (e.g. Allard et al. 1983). Part of them has been trapped since the accretion of the Earth, while the other part is derived from the hydrated and carbonated oceanic crust and sediments that dive in the subduction zones (e.g. Fischer and Marty, 2005, Churikova et al. 2007). This recycling mechanism of volatiles explains why subduction zone magmas are generally richer in volatiles than oceanic ridge magmas. The relative abundances of volatiles in the mantle, although not known precisely, must thus be highly heterogeneous. During the partial melting of the mantle that leads to magma generation, volatiles partition heavily into the melt phase.

In subduction zones, volatiles released by the dehydration of the subducted slab are even responsible for magma generation, by lowering the solidus of the overlying mantle wedge.

The initial (i.e. pre-eruptive) content of volatile dissolved in the magma can be measured by microprobe analysis of the melt inclusions trapped inside phenocrysts that formed in the magma chamber (e.g. Metrich and Clochiatti, 1996; Spiliaerts et al., 2006). Only early formed minerals (i.e. highest Mg# olivines or highest An. plagioclases) have to be considered to avoid volatile depletion associated to early magma degassing. However numerous evidences from experimental petrology (e.g. Scaillet and Pichavent, 2003) and mass calculation budgets of degassing (e.g. Wallace, 2001) indicate that part of the volatiles in the magma are present as a separated fluid phase coexisting with the silicate melt in the magma chamber, and possibly even in the upper mantle (e.g. Allard, 2010). This fluid phase could amount to 1weight % of the total magma in subduction zones volcanoes and is significantly enriched in carbon and sulphur compared to the composition of volatiles dissolved in the silicate melt (Scaillet and Pichavent, 2003).

The volatile content of the magma increases with its differentiation because the first minerals that form by fractional crystallization (olivine, plagioclase and pyroxene) are anhydrous. Only in the latest phases of differentiation will oversaturation of H_2O and S lead to the formation of hydrated (amphiboles, micas) and S bearing minerals (Sulphides, anhydrite).

When reaching saturation, volatile elements exsolve from the magma and escape into the atmosphere as gaseous compounds. Direct sampling of magmatic gases (Le Guern et al., 1979, review in Symonds et al., 1994) shows that

- H is present very predominantly as H_2O, with minor amounts of H_2. Water vapor is the most abundant volcanic gas.
- CO_2 is the predominant carbon compound and CO being present only in small amounts in high temperature gases.
- SO_2 is generally the predominant sulphur compound although, depending on the oxidation state of the magma and its water content, up to 50% of the sulphur in magmatic gases can be present as H_2S.
- Halogen compounds are present as HCl, HF and HBr.

The solubility of all volatile species in the magma decreases with decreasing pressure. Temperature, magma composition, and, for sulphur, the oxygen fugacity of the magma also have an influence. The solubility also varies significantly from species to species.

Experimental petrology (e.g. Burnham, 1975, Wallace and Carmichael, 1992, Caroll and Webster, 1994, Moretti et al., 2003) has allowed quantification of the solubility of the main volatile species as a function of pressure for different magma types. The general trend resulting from all these studies is the following hierarchy in volatile solubility, which appears to be valid whatever the magma type:

$$S_{CO2} < S_{SO2} < S_{H2O} < S_{HCl} < S_{HF}$$

The consequences of this are that gases do not exsolve from the magma at the same depth and at the same time during magma ascent. Furthermore, the equilibrium composition of the volatile phase coexisting with the magma varies with the depth at which the equilibrium between dissolved volatiles of gas is considered. These facts are essential to interpret field measurement of volcanic gases in term of eruption dynamics (see part 1.3)

1.2 Role in eruptions

Gases are the driving force of volcanic eruptions (e.g. Tazieff and Sabroux, 1983). The gas content of the magma is the most crucial parameter controlling the eruption explosivity and hence its dangerousness. The progressive exsolution of volatiles from the melt forms bubbles, which decrease the bulk density of the magma and provide it the excess of buoyancy needed to eventually reach the surface. The bubbles grow and expand until they exceed the surface tension of the magma, which causes fragmentation of the silicate melt and propels the fragments (named pyroclasts) into the atmosphere. Intensive research over the last thirty years has led to the development of numerous analogical and mathematical models of magma degassing and explosivity (e.g., Jaupart et Vergniolles 1988, Slezin, 2003, review by Sparks, 2003). The "linear" exsolution-expansion model describes well the violent onset of basaltic and silicic eruptions, which are characterized by continuous jets of mixed pyroclasts and gases. These are known as lava fountains for fluid basaltic lavas or plinian columns for viscous differentiated magma, although there is no fixed boundary between them. In the detail however, other models are needed to describe the often cyclic behaviour of long lasting eruptive activity, which displays markedly different behaviours depending on magma viscosity.

Figure 1.1: Several expressions of explosive volcanic manifestations.
Top: basaltic explosive activity. In 2001, the South-East crater of Mt Etna was producing paroxysmal episodes with a regular 2 days periodicity. Lava fountains (a) were jetting from the crater to a height of ~400m. These were occasionally interrupted by explosions of hectometric lava bubbles (b). Cyclic paroxysmal activity is typical of Mt Etna and has been demonstrated by Allard et al. (2005) to result from the destabilisation of a foam of gas segregated at depth from the magma. During the 3-4h long paroxysms, flow regime alternated between dispersed pyroclasts and gas jets and gas slug explosions. Between two paroxysms complete rest predominated.
Bottom: (c) Vulcanian explosion (here in Krakatau, June 2009) occurs when gas pressure under a lava plug exceeds the plug resistance, causing its destruction. Parts of the plug are ejected away as ballistics. Deeper parts of the plug continue to degas during their trajectory (ash and gas trails of some fragments). (d) At the lava dome of Santiaguito, Guatemala, the overpressure is released in a quieter way through annular gas and ash venting around the plug, which forms a dome-coulee slowly creeping away from the summit.

1.2.1 Basaltic magmas

For low viscosity basaltic magmas, bubbles are able to grow and migrate upwards faster than the magma flow in the conduit. Bubble rise velocity is proportional to the square of their size, so large bubbles can catch up smaller bubbles during their ascent and absorb them, becoming even larger and rising even faster. The slug of gas formed in this way takes a hydrodynamic shape and can occupy the whole width of the conduit. This model allows explaining the typical strombolian activity, consisting of discrete explosions separated by quiet intervals. An alternative model (Jaupart and Vergniolles, 1988) is that bubbles accumulate under the roof of the magmatic chamber, forming a foam. This foam will periodically collapse and engage in the upper conduit, producing slugs of gas (strombolian activity, fig. 1.1b) or massive flow of mixed gas and lava fragments (episodic lava fountain, fig. 1.1a).

1.2.2 Silicic magmas

The high viscosity of silicic magmas hampers the bubbles to grow more than a few millimetres (bubble nucleation is favoured over their growth), and hampers them to rise in the magma column. Therefore, gain of volume related to vesiculation of the magma produces an important overpressure in the magma chamber. Another key effect of volatile exsolution is to promote magma crystallisation and increase dramatically its viscosity. Complete degassing of the magma in the superficial portion of the conduit will thus lead to the formation of a plug of near-solid lava. Pressure from deeper degassing builds up under the plug until exceeding its resistance. Depending on the abundance of gas and the rheology and permeability of the plug, overpressure release can occur as a violent explosion that completely destroy the plug (Iguchi et al., 2008), or as increased extrusion rate and pressurised gas and ash venting from zones of lower resistance and higher permeability (Young et al., 2003). In this last case the plug can further grow into a lava dome. Lava domes do exhibit some permeability thanks to their vesicular texture, which allows some deeper degassing (Edmonds et al., 2003b). Permeable zones in a lava dome concentrate where vesicles are elongated and can interconnect: in internal shear zones, and at the interface between the dome and the conduit walls (Bluth and Rose, 2004).

All these models (and a fortiori these few lines) are still far from the incredible complexity and diversity displayed by volcanic activity, which make each volcano and even

each eruption unique. Forecasting the dynamics of an upcoming eruption remains the biggest challenge of modern volcanology. Because of their key role in eruption processes, monitoring the composition and fluxes of volcanic gas appears as one of the most promising tool to succeed in this challenge.

1.3 Messengers of the magma

Volcanic gases have an intrinsically higher mobility than the magma from which they derive. Therefore, they carry information from the magma that are extremely valuable for early warning of an upcoming eruption, for understanding the magma dynamics, or even for assessing its content in volatiles. Two types of situations must be distinguished when interpreting gas measurements, whether the gas is emitted directly by the magma into the atmosphere, or not.

1.3.1 Direct magmatic degassing

Direct magmatic degassing predominates at volcanoes that are already erupting or have magma at the surface or very close to it. The high thermal emissions associated to this kind of activity allow the gases to rise buoyantly in the atmosphere as a distinct plume, which makes a good target for spectroscopic remote sensing techniques (see section 1.5). The gas transfer from the magma to the atmosphere is direct, limiting the loss of components to a few negligible processes such as high temperature mineral depositions (Le Guern and Bernard, 1983) and condensation of a liquid aerosol phase (Mather et al., 2004). So the composition of the plume reflects the gas mixture emitted by the magma (Horrocks et al., 2003) and can be interpreted to unravel its degassing dynamics. The essential concept that is needed for the interpretation is the differential solubility of volatiles in the magma (see paragraph 1.1). We can illustrate this with three examples, taken from the literature, of different magmatic processes that were revealed using measurements of the molar ratios of volcanic gases:

- Measurements of the volcanic gases emitted by cyclic lava fountains at Etna using open path FTIR spectrometry (Allard et al. 2004) revealed that CO_2/SO_2, SO_2/HCl and SO_2/HF ratios were significantly higher than their values in primitive melt inclusions. This was interpreted as evidence that a gas phase, enriched in insoluble compounds,

was exsolving from the magma at depth and accumulating as a foam prior to the fountaining episode. The rapid ascent of the foam prevented reequilibration of the gas composition with the magma and preserved its deep signature. Repose periods between fountain episodes were characterized by gas compositions enriched in HCl and HF over CO_2 and SO_2.

- A similar pattern was found at Stromboli where the gases released by strombolian explosions display much higher $CO_2/SO_2$and SO_2/HCl ratios than passive degassing between two explosions (Burton et al., 2007). Melt inclusion studies and modelling have even allowed evaluating the equilibrium depth corresponding to the measured gas compositions. These are 1.5 km for Etna and 2.5 km for Stromboli, which is much deeper than the source region inferred from seismological investigations.

- Still in Etna, systematic monitoring of the molar ratios CO_2/SO_2 and SO_2/HCl in the passive degassing plume emitted by the central craters, allow detecting recharges of the shallow magma reservoir by new volatiles-rich magma batches, and its progressive exhaustion in volatiles through passive degassing (Aiuppa et al., 2007). Residual degassing dominated by halogen compounds (HCl and HF), is observed at flank vents producing lava flows. (Burton et al., 2003)

- At Soufrière Hills volcano, an andesitic lava dome that has been erupting since 1995, alternating dome growth and repose intervals, Significant difference in gas composition is observed between dome growth phase (SO_2/HCl<1) and repose interval (SO_2/HCl >2.5). Interpretation of these data (Edmonds et al., 2001) is that HCl and HF degas only at very shallow level, when lava is emitted at the surface (dome building). The flux of these elements can be used as a proxy for dome growth rate. Conversely, SO_2 exsolves at deeper level but its release into the atmosphere is controlled by the permeability of the lava dome.

If coupled with melt inclusion studies (e.g. Spiliaert 2006), measurements of magmatic gas compositions can thus provide extremely valuable insights, and even quantitative constraints, into the dynamics of magma degassing at erupting volcanoes. Measurements of *fluxes* of gases are a good proxy for the long term magma flux beneath a volcano and help to put constraints on the magnitude of the degassing processes. A major discovery resulting from

gas flux measurements is that, nearly systematically, the amount of actually erupted magma is several times smaller than what would be necessary to produce these gas fluxes. Various explanations have been proposed to account for this, which are:

- The emplacement of unerupted degassed magma under the form of dykes, which contribute to endogenous growth of the volcano (Francis et al., 1993)
- The existence of convection cells where lighter undegassed magma rises to the surface, degasses and sinks back to the magma chamber where it finally crystallized as cumulates. (Kazahaya et al. 1994, Allard, 1997)
- The deep exsolution of a volatile phase and its migration towards the top of the magma chamber. (Wallace, 2001)

The common point of all of these hypotheses is that most of the magma involved in volcanic activity remains under the Earth surface, and that eruptions represent only the "tip of the iceberg" of magmatic processes.

1.3.2 Blurring the message: Hydrothermal systems

The gases exsolved from the magma residing under a dormant volcano will encounter hydrothermal systems on their path between the magma chamber and the surface. Hydrothermal systems are hot convecting aquifers that nearly always overtop magmatic bodies. Their surface expressions include hot springs, boiling mud pools, crater lakes, fumaroles, and diffuse degassing areas. Magmatic gases encountering hydrothermal systems undergo aqueous dissolution reactions that will trap the most soluble species and deeply modify their overall composition (Giggenbach, 1980, Symonds et al. 2001).

Halogens are the most soluble compounds and are readily dissolved following the reactions:

$$HCl(g) \rightarrow H^+(aq) + Cl^-(aq) \qquad (1.1)$$

And $$HF(g) \rightarrow H^+(aq) + F^-(aq). \qquad (1.2)$$

Sulphur dioxide is also quite soluble (although less than HCl and HF). Its reaction with water, called disproportionation, involves changes in redox state of the sulphur and can be written as (Kusakabe et al., 2000)

$$4SO_2(g) + 4H_2O \rightarrow 3HSO_4^-(aq) + 3H^+(aq) + H_2S(aq). \qquad (1.3)$$

All these reaction produce H^+ ions, which generates a significant acidity in hydrothermal systems associated to degassing magmatic bodies. This acidity is responsible

for extensive alteration of the host rocks and generates new minerals (clay minerals, sulfates, sulphides and fluorides).

CO_2 and magmatic H_2S also dissolve in hydrothermal systems as $H_2CO_3(aq)$ and $H_2S(aq)$, but, due to their lower solubility, they will escape in the gas phase that is often formed by ebullition of the fluid at the apex of the convection cell. These two gases can thus pass through hydrothermal systems and reach the surface. Together with water vapor they dominate the composition of low temperature fumaroles.

When new magma intrudes under a hydrothermal system it starts releasing gases at depth. These gases, thanks to their higher mobility, will interact with the hydrothermal system and reach the surface well before the magma itself. This will trigger a whole range of changes that can be interpreted as precursory signs of an upcoming eruption. An increase in carbon dioxide emission will generally be the earliest of these signs. Thanks to its low solubility in the magma, it exsolves very early in the magma ascent, and thanks to its low solubility in water it can pass through the hydrothermal system without being significantly absorbed. The possible effects of this include increase of CO_2 content in fumaroles, diffuse CO_2 flux and CO_2 bubbling within crater lakes. These latest two phenomena were observed 3 months before a dome building eruption in Kelud volcano in November 2007. These precursory signs of the eruption preceded the other geophysical signals such as seismicity and deformation. Increase in H_2S emissions can also constitute an early warning sign of increased magmatic SO_2 input and disproportionation (Symonds et al., 2001). The main advantage of H_2S is that it is easily detected even at very low concentration thanks to its typical rotten egg smell. However, precipitation of sulphide minerals and native sulphur and oxidation into sulfate are efficient sinks for this gas and can mask its increase.

Only later, if the heat of the rising magma creates a dry pathway within the hydrothermal system, or if the input of gases exceeds its scrubbing capacity will SO_2, HCl and HF be released as gas species through the fumaroles. The occurrence of these compounds in the gas emissions of a previously resting volcano must thus be considered as an alarming sign of magma proximity. For example, the SO_2 fluxes at Mt Pinatubo increased steadily from 0 (before the unrest begins) to 10000 Tons/day in June 1991, a few days before the beginning of magmatic activity (Daag et al. 1996).

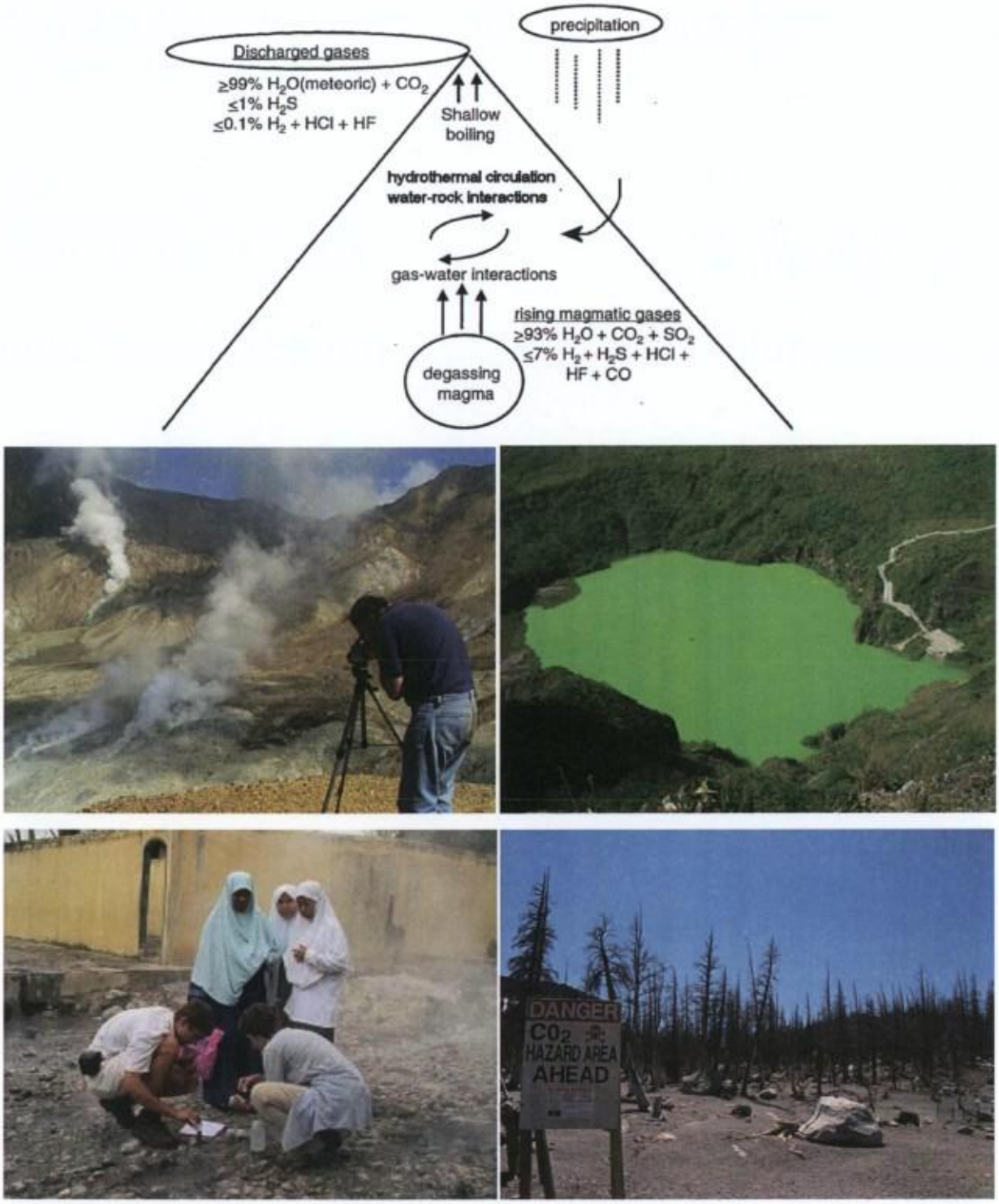

Figure 1.2: Hydrothermal systems and their surface manifestations.(a) Very schematic representation of a hydrothermal system and its scrubbing effect on magmatic gases (modified after Symonds, 2001). (b) Fumarolic field (T=50-250°C) in the crater of Papandayan volcano (Indonesia). (c) The crater lake of Kelud (Indonesia) was fed by neutral chloride-sulfate-bicarbonate hot springs from two superposed hydrothermal system. (d) Hot springs on the flank of Mt Sorikmarapi (Indonesia) are sulfate rich steam condensate from the hydrothermal system of the volcano. (e) CO_2 is released by the shallow boiling of hydrothermal system of Long Valley Caldera (California, USA) and reaches the surface in high diffuse flux areas.

1.4 Impact on the atmosphere and environment

A last fascinating aspect of volcanic gases is their impact on the chemistry of the Earth atmosphere, on its climate and on its environment. The initial atmosphere of our planet was formed by the degassing of the volatiles trapped in the magma ocean that was occupying the Earth surface. It must thus have a composition similar to present day's volcanic gases. The cooling of the Earth, and the development of life led to the changes that formed the present days atmosphere: water vapor condensed, forming the oceans, HCl dissolved in water and reacted with rocks forming salt, SO_2 was converted into sulfate, later on CO_2 formed carbonated rocks, and was consumed by photosynthesis to produce organic matter and the gaseous oxygen that we now breath.

1.4.1 Effect on the climate

The effect of volcanic emissions on the Earth climate is limited to eruptions that are strong enough to inject sulphur dioxide in the stratosphere. Within a few months, SO_2 is oxidized by the OH radical via the reaction chain (Eatough et al., 1994):

$$OH+SO_2+M \rightarrow HOSO_2+M$$

$$HOSO_2+O_2 \rightarrow SO_3+HO_2$$

$$SO_3+2H_2O \rightarrow H_2SO_4+H_2O \quad (1.4)$$

and forms an aerosol of very fine (micron size) sulphuric acid droplets. The presence of this aerosol in the stratosphere increases the backscattering of solar radiation towards space. The transmitted fraction of direct solar radiation reaching the surface can thus be significantly reduced (see fig. 1.3). The consequences of this are multiple (Robock, 2000).

- A net cooling in the troposphere, because less solar energy is available. This effect is well known since Benjamin Franklin's observation of cool winter following the 1783 Laki eruption.
- A net heating in the stratosphere, because part of the solar radiation is absorbed by the aerosol and converted into heat. Models (Robock, 2000) and measurements (Randel et al. 1995) show that stratospheric heating is actually more important than tropospheric cooling

- Changes in the global atmospheric circulations resulting from a lower temperature contrast between the troposphere and lower stratosphere. This leads to uneven repartition in the cooling of the low atmosphere. Figure 1.4 shows that, even if the global effect of Mt Pinatubo eruption was an average decrease of 0.6°C in the surface temperature, some region underwent a warmer than average winter due to this circulation anomaly.

The impact of volcanic eruptions on climate is rather short lived because stratospheric aerosols have only a 2-3 years residence time.

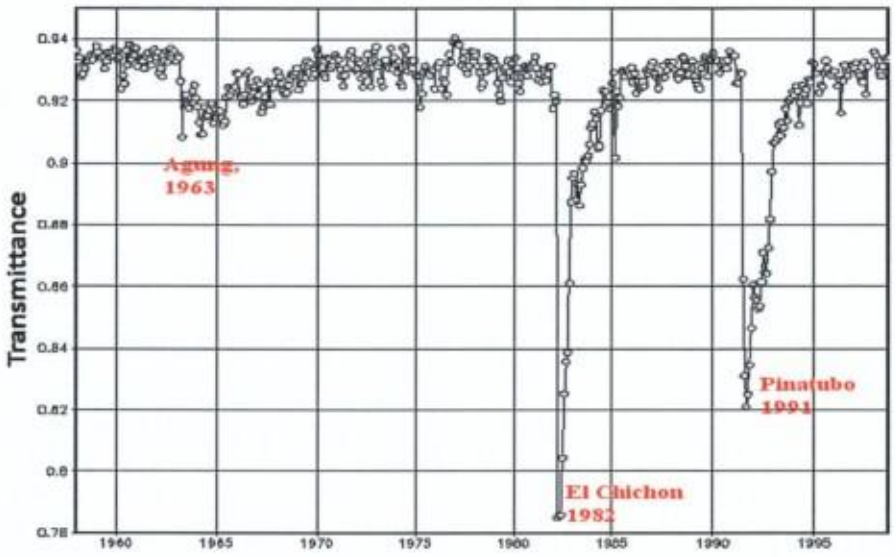

Figure1.3 : LIDAR measurements of stratospheric transmittance recorded in Hawaii between 1960 and 1999 show significant decreases due to aerosols injected by major eruptions (after Robock ,2000)

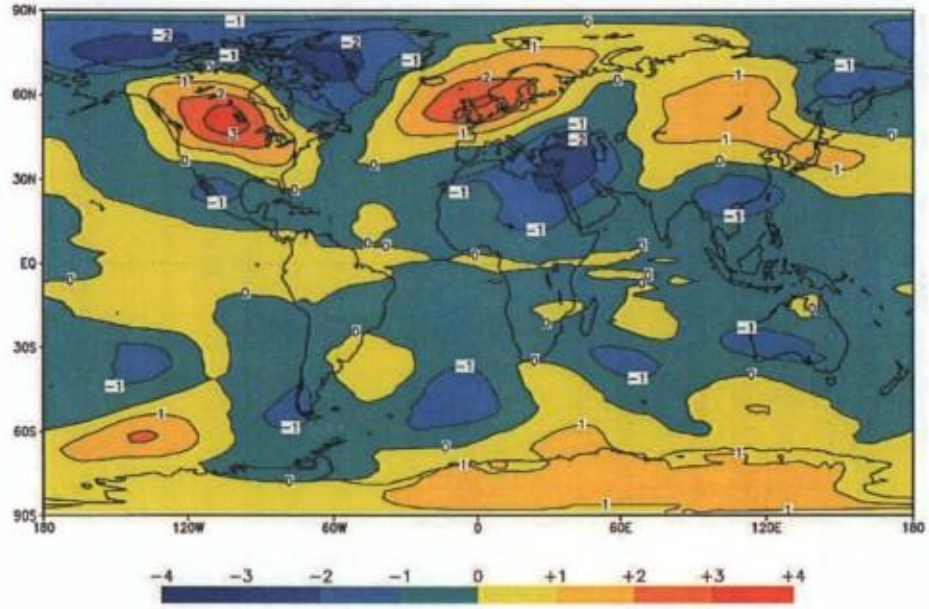

Figure1.4 : Surface temperature anomalies measured during the winter following the eruption of Mt Pinatubo in June 1991 (after Robock , 2000).

1.4.2 Role in Ozone destruction

The role of volcanic gases in ozone destruction was discovered after the Chichon and Pinatubo eruption in 1982 and 1991, which caused a ~5% decrease in global stratospheric ozone (e.g. Brasseur and Granier, 1992, Randel et al., 1995, review by Solomon, 1999). Stratospheric ozone (O_3) is a vital component of the Earth atmosphere because it blocks harmful ultraviolet (UV) from the Sun. Its presence in the stratosphere is the result of a dynamic equilibrium that takes place in the stratosphere, involving dioxygen, atomic oxygen and shortwave UV. This equilibrium is known as the Chapman cycle and described by the following four reactions:

$$O_2 + h\nu \rightarrow O^{\cdot} + O^{\cdot} \quad (1.5)$$

$$O_2 + O^{\cdot} \rightarrow O_3 \quad (1.6)$$

$$O_3 + h\nu \rightarrow O_2 + O^{\cdot} \quad (1.7)$$

$$O_3 + O^{\cdot} \rightarrow O_2 + O_2 \quad (1.8)$$

On the other hand, stratospheric ozone is destroyed by several catalytic reactions cycles of the type (Solomon, 1998):

$$O_3 + X \rightarrow XO + O_2 \quad (1.9)$$

$$O^{\cdot} + XO \rightarrow O_2 + X \quad (1.10)$$

So that stratospheric ozone concentration follows a dynamic equilibrium. In these reactions, X is a catalysing molecule, which can be nitrogen oxide (NO), hydrogen oxides (H, OH, and HO_2) or halogens atoms (Cl and Br). Volcanic eruptions that are strong enough to inject volcanic gases in the stratosphere have both a direct and an indirect impact on ozone destruction.

The direct impact results from the injection of halogenated species by eruptive columns. Although it has been believed for long that most halogenated species in eruptive columns were washed out by condensation of water and precipitation, in situ measurements (Rose et al., 2006) and satellite retrievals (Theys et al., 2009) have recently documented significant abundance of respectively HCl and BrO in the young stratospheric volcanic plumes of two medium size eruptions.

The indirect impact comes from the stratospheric aerosol of sulphuric acid formed by major eruptions (see par. 1.4.1). Atomic chlorine is formed in the stratosphere by the photodissociation of $Cl_2$and HClO molecules. However, most of the chlorine in the stratosphere is present as gaseous HCl and $ClONO_2$, which are the "reservoir" species for stratospheric chlorine. The reactions converting HCl and $ClONO_2$ into Cl_2 are heterogeneous

phase reactions that need a particulate catalyst. With the notable exception of polar stratospheric clouds, particulate matter is rare in the stratosphere, so it is usually the limiting factor for these reactions. This explains why the famous "ozone hole" affects mainly the high latitude stratosphere. Brasseur and Granier (1992) have shown that H_2SO_4 from volcanic aerosols can play this catalyst role in Cl_2 formation, leading to more ubiquitous ozone destruction than just above Polar Regions.

1.4.3 Acidic rain and VOG

Acidic compounds (SO_2, HCl, HF, H_2S) present in volcanic gases are not chemically stable in the atmosphere. They are removed by condensation and deposition processes, affecting vegetation, soils, infrastructures and Man (see review by Delmelle, 2003).

In dry conditions, these gases condensate slowly, forming acidic aerosol. The efficiency of the condensation processes is highly variable, depending on atmospheric humidity and on the considered gas species. The term *vog* was forged to describe the harmful mixture of acidic volcanic gases and aerosol. Vog is removed from the atmosphere by dry deposition (Delmelle et al. 2001), which is a rather inefficient process. Vog can thus be transported over long distances. It is suspected (Grattan et al., 2003) that massive vog emissions from the Laki eruption (Iceland, 1783) caused a peak in mortality in Europe due to a dramatic and long lasting volcanic pollution event.

In wet conditions, precipitations will efficiently wash out acidic gases and aerosols under the form of acidic rain. Wet deposition processes are so efficient that acidic rains are usually limited to a few tenth of km around the volcano (e.g. Rowe, 1995), but produce more concentrated effects. Chemical burning of the vegetation, corrosion of infrastructure and drinking water contamination have been reported at strongly degassing volcanoes such as Nyiragongo, Ambrym, Poas, Kilauea or Turrialba.

Figure 1.5: Impact of volcanic emissions from Turrialba volcano (Costa Rica) on the environment. The metal sheets covering the stable to the right were extensively corroded by acidic gases and aerosols, while the forest that used to cover the volcano (in the background) is now completely dead. The beginning of the current unrest in Turrialba (further investigated in chapter 6) dates from 2006.

1.5 Measurement methods

1.5.1 Direct Sampling

From the eve of volcanology until the mid 70s, direct sampling was the only available way to study volcanic gases. Sampling methods used vacuum filled bottles sometimes containing a desiccating agent to block further reactions of the volcanic gases with water. These reactions, together with others involving sulphur compounds, result from the thermodynamic reequilibration as the gas mixture cools. They have for long constituted an obstacle to interpretation of volcanic gases, until they could be completely understood and modelled (e.g. Gerlach, 1982). An approach developed to overcome that problem was in situ analysis with a portable gas chromatograph operating at a temperature high enough to avoid thermodynamic reequilibration to occur (LeGuern et al., 1982). This approach however was not pursued due to the logistic challenges that it poses of bringing sensible, fragile and relatively heavy instruments in the very mouth of an active volcano. A standard sampling method (Giggenbach 1975) has emerged over the years, which make use of vacuum filled

bottles containing 100ml of NaOH solution. Acidic gases (SO_2, CO_2, HCl, HF, H_2S) and water vapor dissolve into the basic solution while incondensable species (N_2, O_2, H_2, He, Ar) fill the vacuum space of the bottle.

Thermodynamic modelling is then used to recalculate the proportion of S bearing species in the high temperature gas mixture. Direct sampling gives unique and very complete information on the composition of volcanic and fumarolic gases, but is a technically difficult operation and implies working in harsh and/or hazardous environment. Furthermore, sample contamination with atmospheric air happens easily and severely complicates interpretation of the results. Two additional shortcomings of direct sampling may restrain its interest for the study of a phenomenon so dynamic as a volcano:

1. The time delay between sample collection in an often remote location and its complete analysis in an adequate laboratory
2. The scarce sampling frequency, which is often too low to fully apprehend rapid dynamic fluctuations of the "real composition" (e.g. Tazieff, 1970)

1.5.2 Remote sensing

Remote sensing methods have been developed since the mid seventies to reduce personal risk for scientists investigating volcanic gases. They are based on absorption of light by gaseous molecules in the diluted and cooled plumes emitted by volcanoes in the atmosphere. By their very nature, remote sensing methods can not measure volume concentrations, but only measure path-integrated concentrations. This makes the comparison difficult with direct sampling methods for validation sake, and explains why published studies about validation of remote sensing measurements are so rare. Path-integrated concentration is also termed column amount and abbreviated CA throughout this thesis. It is a physical quantity whose units are expressed in ppm.m, molecule/cm^2, or g/m^2.

A notable limitation on working with diluted plumes is that only major species and species with low concentration in the atmosphere can be reliably measured, otherwise the "volcanic" signal is small compared to the atmospheric background. This is unfortunately the case for CO_2 and H_2O, the two most abundant compounds of volcanic gases.

A last limitation of remote sensing method is that require modelling of the radiative transfer in the atmosphere and in the plume (see chapter 2) and a model never fully reproduce reality. The following pages contain a brief overview of the most widely used remote sensing techniques operated from the ground: COSPEC, DOAS and FTIR.

1.5.2.1 COSPEC

Invented around 1970 (Moffat and Millàn, 1971), the COSPEC is a correlation spectrometer. It measures irradiance ratios at pairs of wavelength coinciding with peaks and troughs of the absorption spectrum of SO_2. The measurement of SO_2 column amount in the plume is achieved through the comparison with measurements of calibration cells containing known amount of SO_2. In the details, the opto-mechanical system of the COSPEC is rather complex, because the wavelength selection is achieved through the use of a rotating disk with several opening slits see details in Millàn(2008). The data output of COSPEC is a measurement of the column amount (CA) SO_2 (in ppm.m or g/m^2) in the line of sight of the instrument. Sulphur dioxide flux can be calculated with COSPEC using two different strategies (Stoiber et al. 1983). Unfortunately the light intensity measured at the different spectral bands of the COSPEC is not output so that the instrument works a bit as a "black box".

By traversing perpendicularly to the volcanic plume with the COSPEC pointing upwards vertically a profile of SO_2 CA in the plume is obtained (figure 1.6b). The SO_2 flux can then be calculated by integrating this CA profile over the traverse and multiplying by the wind speed. Alternatively to the traverse method, scanning in a vertical plane from a fixed position can also be performed, to obtain a profile of the SO_2 CA as a function scan angle. However, calculating SO_2 flux from scanning position requires a geometrical conversion of angular SO_2 CA measurements into measurements as a function of length, which can introduce a significant error due to inaccurate knowledge of the plume geometry (Williams-Jones et al., 2008).

COSPEC was during 25 years the only available tool to quantify gas emissions in the atmosphere by volcanoes, and became a paradigm of SO_2 flux measurements. It was used all over the world and contributed significantly to the management of volcanic crisis (e.g. in Pinatubo, Daag et al., 1996). However a COSPEC is a bulky and costly device, is not manufactured anymore and has potential sources of error due to light scattering issues (see chapter 2 for more details).

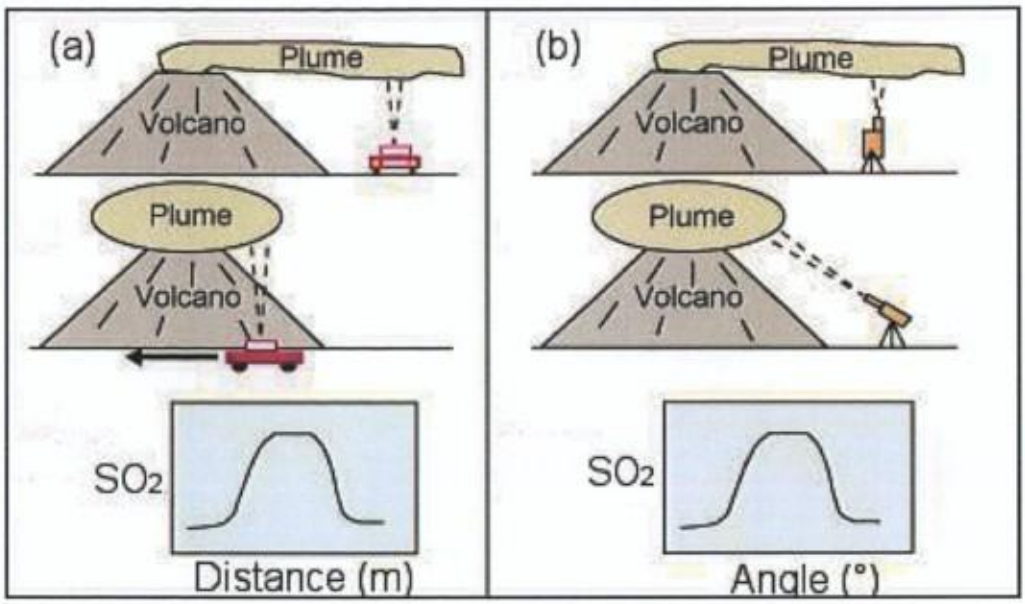

Figure 1.6: Scheme showing the two operation mode for COSPEC measurements: (a) traverse measurements, (b) scanning measurements. Top: view parallel to the plume direction, mid: view perpendicular to the plume, down resulting measurement profiles. (Modified after http://volcano.oregonstate.edu/book/export/html/151)

1.5.2.2 DOAS

The DOAS technique (Differential Optical Absorption Spectrometry) was applied to the volcano in the beginning of the nineties (Edner et al., 1994), but was greatly popularized among volcanologists thanks to the development of compact and relatively cheap UV spectrometers that can be operated by a laptop through an USB interface. (Galle et al., 2002). The design of such a spectrometer (called mini-DOAS in the literature) is illustrated in figure 1.7. The incoming light is collected by a telescope and transferred to the spectrometer through an optical fiber (to increase versatility and ease of use). Inside the spectrometer, the light is collimated using 2 mirrors on the diffracting grating, which separate the different wavelength and reflects them on a linear CCD array. Each element of the CCD array records the light intensity for a narrow wavelength interval, digitizes this value and sends it to the USB port. The total signal that is output to the computer by the whole CCD array constitutes a discrete spectrum of the incoming radiation.

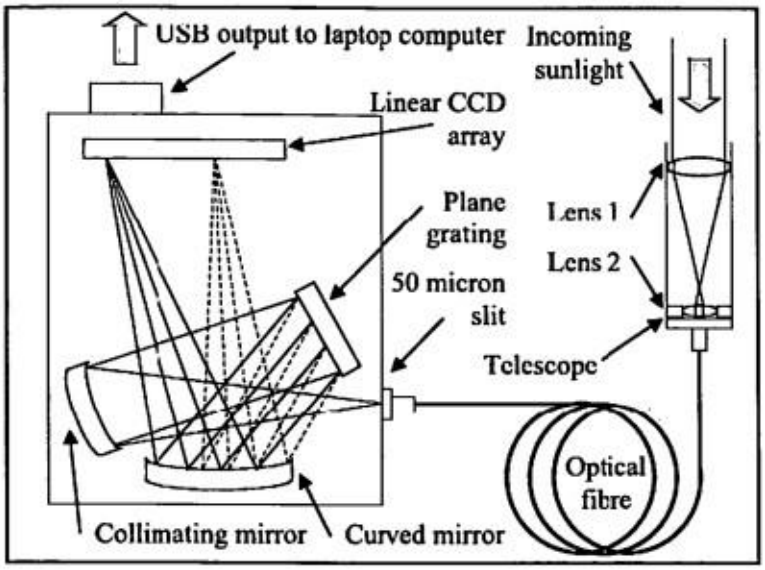

Figure 1.7: Schematic drawing of internal the architecture of a mini-DOAS (after Galle et al., 2002)

The operating mode of the mini-DOAS is basically the same as for the COSPEC, but the output of each measurement is a full spectrum of the incoming UV radiation and not just an SO_2 column. The UV spectrum is then processed using the DOAS technique (detailed in the next chapter) for retrieving the SO_2 column. The advantages of the mini-DOAS over COSPEC are multiple and include:

- Several practical features, such as compactness, lightness, low cost, low power consumption, and directly digitized output
- The possibility to retrieve other volcanic gases than just SO_2, such as BrO (Bobrowski et al., 2003) and ClO (Lee et al. 2005)
- The potential to assess the quality of the measurement by examining the residual obtained after the DOAS processing (see section 4 of chapter 2) and to correct for radiative transfer effects.

These advantages have made of the mini-DOAS the most used instruments for measuring SO_2 emissions from volcano, in replacement of their COSPEC ancestors. The next step of the generalisation of the DOAS technique for volcano monitoring has been the installation of networks of automatic scanning mini-DOAS's on the foot of active volcanoes. This step started in the around the mid 2000s (Edmonds et al., 2003a) and more than 20 volcanoes worldwide are now equipped with such a network, under the impulse of the NOVAC project (Galle et al. 2010). The instruments of these networks scan the sky every few minutes during day light and provide continuous, near real time, high frequency estimations of the SO_2 flux emitted by the equipped volcanoes.

1.5.2.3 FTIR spectrometry

In the mid 1990s (Mori et Notsu, 1997, Francis et al., 1998, Love et al., 1998), another spectrometric technique was adapted to the study of volcanic gases: open-path Fourier Transform Infrared spectrometry. This is a high spectral resolution technique that relies on interferometry between a beam reflected by a moving mirror and a beam reflected by a fix mirror. A beam splitter separates the incoming light toward the two mirrors, and redirect the two reflected (and out of phase) beams towards the detector. The signal recorded is an interferogram, i.e. a measure of the light intensity as a function of the mirror position. Then a Fast Fourier Transform algorithm is applied to convert this interferogram into a high resolution spectrum. On a volcano, FTIR spectrometers can be operated in two different modes.

- In the first mode, known as the absorption mode, the volcanic gases lie between the spectrometer and a heat source, which can be lava (flowing or ejected in a fountain), a heated crater wall, or the sun. The volcanic gases, which are colder than the radiation source, produce an absorption spectrum.
- In the emission mode, the plume is viewed against a colder background, usually a cloudless sky, and thus a thermal emission feature is recorded by the instrument.

The former technique may be difficult to implement in the field but provides measurements over a wide wavelength domain, while the last one is more versatile and easy to implement, but allows measurement only on a restricted wavelength interval (8-15µm due to signal-to-noise and atmospheric transmittance restrictions), and can therefore measure less species. The spectra are processed using a line-by-line radiative transfer model to retrieve column amounts of absorbing gases in the line of sight of the instruments.

FTIR spectroscopy allows to measure many volcanic gases thanks to their absorption/emission spectrum, including SO_2, HCl, HF,SiF_4, CO, COS, H_2O and CO_2 (Notsu and Mori, 2010). The latest two species are difficult to measure accurately because they are already abundant in the Earth atmosphere. The relevant information arising from FTIR measurements is more the concentration ratio between the different volcanic gases than their column amounts (which is mostly a result of plume dilution). FTIR measurements of concentration ratios between the volcanic gases have allowed major breakthrough in our understanding of volcano dynamics and in volcano monitoring, as discussed in section 1.3.2.

1.5.3 The satellite era

In 1982, scientists studying the ozone layer using images of the TOMS (total ozone mapping spectrometer) noticed a tremendously high amount of ozone above Mexico coinciding with the eruption of El Chichòn volcano. They rapidly discovered that it was not actually ozone, but an artefact due to the absorption of UV light by the massive SO_2 amount released by the eruption (Krueger, 1983), which they estimated at 3.3 10^6 T, but was later recalculated a 7.5 10^6 T (Krueger et al., 1995). Satellite remote sensing of volcanic gas emissions was born. Compared to ground based methods, satellites provide a more complete view of large scale volcanic plumes and are the only tools allowing a quantification of the material (gas, ash and aerosols) injected into the atmosphere by large eruptions. Many satellites have taken the succession of the TOMS, which was able to detect only massive SO_2 emissions due to non-optimal band position and coarse pixel size. The key features of SO_2 sensitive satellites are summarized in Table 1.1.

The principles of satellite remote sensing techniques are broadly similar to ground based techniques, relying on the absorption of light (whether UV or IR) by the gas molecules in the volcanic plume. Modelling of the radiative transfer in the atmosphere is thus required to obtain column amounts from radiance measurements. Sulphur dioxide has been the primary target for space based remote sensing because it has a low concentration in the atmosphere background and strong absorption features both in the UV and in the IR. In the recent years, satellites with improved spectral resolution and/or extended spectral coverage have been able to detect other gases, such as BrO (using OMI, GOME and SCIAMACHY, e.g. Theys et al., 2010) and H_2S (using IASI, Clarisse et al., submitted). However, at the present state of sensor technology, only massive emissions of these compounds can be detected, typically during large scale eruptions. An important notion for satellite remote sensing is that of detection limit. It depends on the absorption coefficient of the target gas and of spectral interferers at the wavelength observed by the satellite, on the detector noise, and on the altitude of the plume. Also important is the pixel size, as the signal of a volcanic plume of a sub-pixel dimension will be "diluted" over the whole pixel. However, because of constraints in the amount of incoming light, an increase in ground resolution (i.e. smaller pixel size) is necessarily gained at the expenses of either S/N ratio, or spectral resolution, or swath width.

Acronym	Instrument	Pixel size at Nadir (km)	Operation period	Comments and reference publication
Ultraviolet sensors				
TOMS	Total Ozone Mapping Spectrometer	62x62, 50x50, 25x25	1978-2004	Successive versions of the TOMS, having improving resolution, have flown over several satellites with various (Krueger et al., 2000)
GOME/ GOME-2	Global Ozone Monitoring Experiment	320 x 40 80 x 40	1996-2003 2006-	UV imaging spectrometer, 1st version onboard ERS-2, second version on board METOP
SCIAMACHY	SCanning Imaging Absorption spectroMeter for Atmospheric CartograpHY	15 x 26	2002-	UV- VNIR imaging spectrometer, on board ENVISAT, discontinuous coverage (Afe et al., 2004)
OMI	Ozone Monitoring Instrument	13 x 24	2004-	UV imaging spectrometer, onboard Aura, Global Coverage (Carn et al., 2008)
Infrared sensors				
HIRS	High Resolution Infrared Sounder	20x20	1978-	Many successive instruments. Multispectral infrared imager for atmospheric sounding, only sensitive to high level SO_2 (Prata et al., 2003)
MODIS	MODerate resolution Imaging Spectroradiometer	1 x 1	1999- (Terra) 2002- (Aqua)	2 multispectral sensors onboard Terra and Aqua, global coverage (Watson et al, 2004)
ASTER	Advanced Spaceborne Thermal Emission and Reflexion radiometer	0.09 x 0.09	1999-	Multispectral Sensor, with stereoscopic view in the VNIR. Programmable acquisition (Pieri et Abrams, 2004).
SEVIRI	Spinning Enhanced Visible and Infrared Image	3 x 3	2006-	Multispectral Sensor on board geostationary satellite MSG, centered on Europe and Africa, 1 image every 15 minutes (Prata and Kerkman, 2007).
AIRS	Advanced Infrared Sounder	13.5 (*)	2002-	High spectral resolution IR imaging spectrometer onboard Aqua, only sensitive to high altitude SO_2 (Prata and Bernardo, 2007)
IASI	Infrared Atmospheric Sounding Interferometer	12.5 (*)	2006-	Fourier Transform Spectrometer onboard METOP, with daily global coverage (Clarisse et al, 2008)

Table 1.1: Current space based sensors able to measure SO_2. Pixel size increase as the viewing angle diverges from Nadir.(*) For AIRS and IASI, the value refers to the diameter of circular footprint of the pixel.

1.5.4 Scope of this thesis.

The scope of this thesis is to develop methods for measuring volcanic SO_2 emissions using satellites. Emissions produced by passive degassing are the main focus of this thesis, because they are the most relevant for volcano monitoring and early detection of volcanic unrest. Unlike eruptions, passive degassing usually produces small scale and low altitude plumes. This makes their detection and quantification difficult by satellite remote sensing. Therefore, only satellites observing the Earth in the "atmospheric windows" and at high ground resolution were used for this thesis. These are ASTER, MODIS and OMI.

The next chapter introduces the theory of radiative transfer in the atmosphere, which is the basis of remote sensing of SO_2. Chapter three describes the methodology developed for retrieving and mapping SO_2 using the images of ASTER. This sensor has the highest ground resolution (90x90m) of all the SO_2-sensitive satellites. This makes it particularly well suited for quantifying SO_2 fluxes in small-scale passive degassing plumes. ASTER is somewhat the unifying thread of this thesis, because its high resolution fills the gap between highly localized ground based SO_2 measurements and the global coverage of the other satellites with coarser pixels.

Chapter four deals with the comparison between SO_2 flux measurements between ASTER and OMI. OMI, which operates in the UV, has become a paradigm of space based SO_2 measurements thanks to its relatively high resolution (13x24km) and its global coverage.

In chapter five we present an algorithm for estimating SO_2 using the image of MODIS. Taking advantage of the simultaneity between the image of MODIS-Terra and ASTER, we compared MODIS SO_2 retrievals with ASTER retrievals resampled to MODIS resolution. This comparison sheds light on the limitations of MODIS for accurate SO_2 retrievals and the reasons of these limitations.

In order to validate ASTER SO_2 measurements with ground based data, a UV-camera equipped with filters was developed to acquire two dimensional measurements of SO_2 in volcanic plumes. This technology is still in full development (e.g. Mori and Burton, 2006, Kern et al., 2010b, Kantzas et al., 2010) and looks very promising for the future of volcanic gas emissions. Chapter six presents the technical and methodological aspects of this instrument, while chapter seven describes the results obtained on Turrialba volcano (Costa Rica) by integrating the satellite SO_2 measurements using ASTER and OMI with the ground based measurements obtained with the UV-camera. These results provide clear insights into the internal processes involved in the recent unrest of that volcano.

Finally the ASTER algorithm has been applied to study a still-hot topic in the volcanic headlines: the eruption of Eyjafjallajökull, which had an unprecedented impact on airline traffic in Europe. Once again, ASTER measurements of SO_2 fluxes emitted by this eruption provide interesting information on its dynamics.

Chapter 2 :
Radiative transfer

Quantitative remote measurements of volcanic gases are based on their spectral properties and how they affect the radiative transfer through the atmosphere. These concepts are presented in this chapter, with an emphasis on the applications used in this thesis. Among the numerous books available on that topic, this synthesis is based on: *An Introduction to Atmospheric Physics* by D.G. Andrews, *An Introduction to Atmospheric Radiation. (2nd edition)* by K.N. Liou, and *Differential Optical Absorption Spectroscopy - Principles and Applications* by Ulrich Platt.

The first part presents the physical quantities and the general processes involved in the radiative transfer. The second and third parts of this chapter are dedicated to the specific cases of thermal infrared (TIR) and ultra violet (UV) radiative transfer.

2.1 Physical processes and quantities

Radiative transfer describes the transport of energy through electromagnetic waves. It's one of the three existing ways of energy transfer (the others being convection and conduction), and the only way that does not require a material medium.

Electromagnetic radiations propagate as waves, characterized by their wavelength λ and their amplitude A. The wavelength of the radiation is related to its energy E by :

$$\lambda = \frac{hc}{E} \qquad (2.1)$$

Where h is Planck's constant ($h=6.626\ 10^{-34}$J.s, and c is the speed of light ($c=2.9979\ 10^{8}$ ms^{-1}). Electromagnetic radiations are classified and named according to their wavelength range, as shown in figure 2.1. Each of these types of radiation has different properties in the way it interacts with matter. Wavenumber (υ), a quantity that is often used in infrared spectroscopy, represent the number of peaks exhibited by the wave in a 1 cm distance. It is expressed in cm^{-1}, and is related to the wavelength (expressed in μm) by $\upsilon=10000/\lambda$

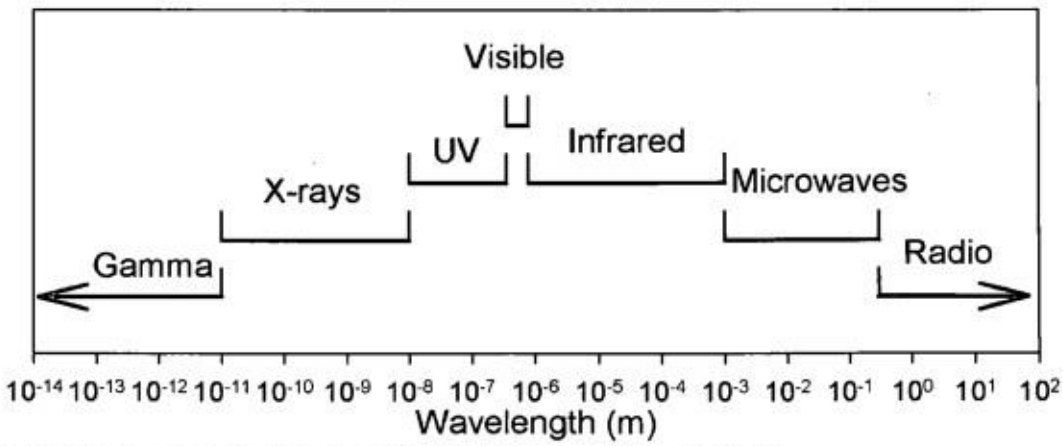

Figure 2.1 :The main wavelength ranges in electromagnetic radiations

2.1.1 Radiance

Radiance (sometimes called spectral intensity) is defined as the flux of energy radiated in a solid angle dω perpendicular to a surface element dl, in a wavelength range dλ.

$$R = \frac{\partial^3 W}{\partial \omega \partial l \partial \lambda} \qquad (2.2)$$

It is thus expressed in units of power per surface per wavelength per steradian ($W.sr^{-1}.m^2.\mu m$, for example). The radiance emitted by body at a temperature T, will follow a spectral distribution described by Planck's law, illustrated in figure 2.2.

$$R = B(\lambda, T) = \varepsilon \frac{2hc^2}{\lambda^5 (\exp((hc/\lambda kT) - 1)} .10^{-6} \qquad (2.3)$$

In this fundamental relation, k, Boltzmann's constant is equal to 1.38065 10^{-23} J/K, and ε is the spectral emissivity, a dimensionless coefficient which can express the efficiency of a surface to emit thermal radiation at a given wavelength. Emissivity is a property of the body's surface that is always ≤ 1 and depends mainly on it composition and roughness. It is an important quantity in remote sensing, used to characterize mineral composition of the Earth surface, vegetal cover, and many other environmentally important quantities.

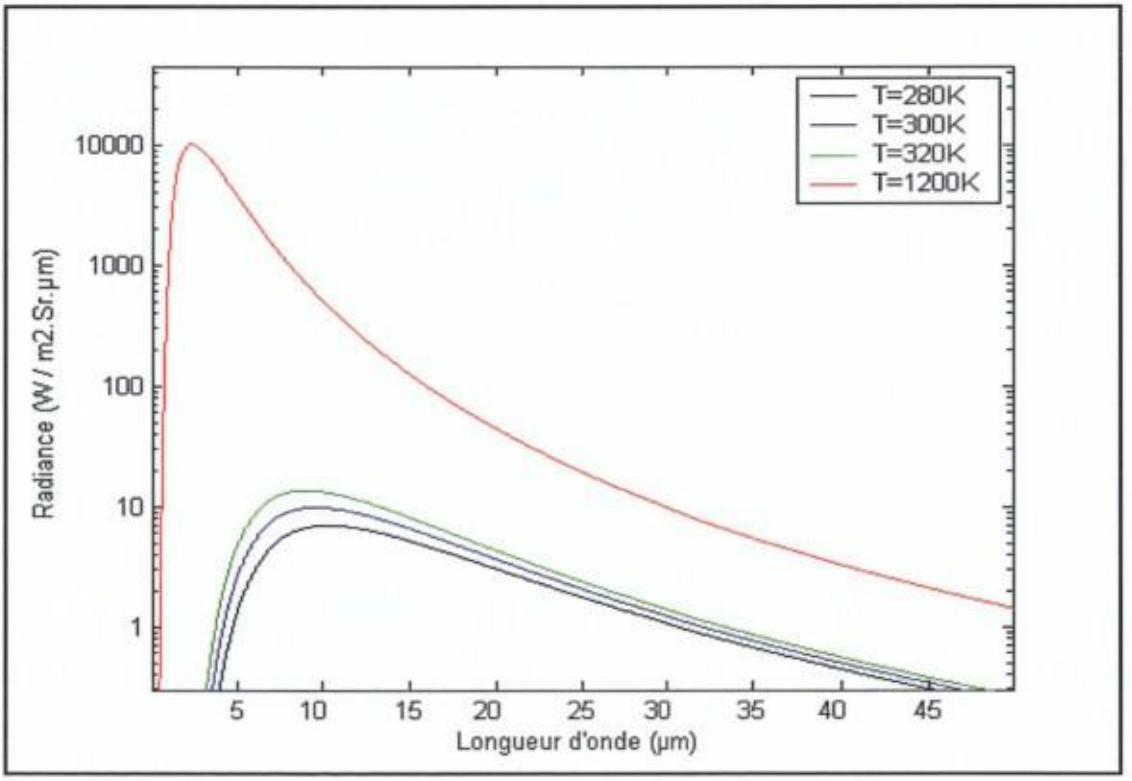

Figure2.2 : Planck's Radiance (semi-logarithmic scale) emitted by 4 black bodies (ε=1) at different temperatures (280, 300, 320 et 1200K)

Interaction with matter affects the propagation of an electromagnetic radiation. Absorption, scattering and emission are the processes that occur. Depending on their relative strength, they will decrease or increase the incident radiance. These interactions are detailed hereafter.

2.1.2 Absorption

Absorption occurs when the energy of the radiation is used by a molecule to undergo a quantum transition to a higher energy level. The return of the molecule to its previous energy level can occur through reemission of a radiation with identical wavelength or through collision with other molecules, energy being converted into heat. The wavelength absorbed by a quantum transition from an energy state E_n to a higher energy state E_{n+1}, is given by equation (2.1).

$$\lambda_a = \frac{hc}{E_{n+1} - E_n} \tag{2.4}$$

Shorter wavelengths therefore yield higher energy transitions. UV absorption lines correspond to shifts of the outer electrons to higher energy orbits, while IR absorption lines reflect transitions between different vibrational and rotational energy levels of atoms in the molecule. As quantum transitions are discrete and depend on the molecular structure, the absorption spectra of molecules will show a pattern that is unique to each substance. Although transitions are discrete, absorption features are not monochromatic rays but narrow lines with a finite width.

Three processes contribute to the broadening of rays into absorption lines. These are, by order of increasing importance:

- Natural broadening has a purely quantic origin and is a direct consequence of the Heisenberg principle.
- Doppler broadening is a consequence of the molecule movements. In a gas, absorbing molecules move with random speeds, following Maxwell-Boltzman's distribution law. The wavelength that a molecule "selects" for producing a transition will thus also have a statistical distribution around its central value λ_a. As the Maxwell-Boltzman's distribution depends on temperature, the Doppler widening of lines increases with the gas temperature.
- Collisionnal broadening is caused by the distortions of energy levels in molecules induced when they collide with other molecules of the gas. Collisionnal broadening depends on the frequency of the collisions and is thus directly proportional to pressure and to the square root of temperature.

The final shape of an absorption line will have a profile described by a Voigt function, whose parameter depends on temperature and pressure. The area under the line is however a constant and a property of the quantum transition associated to line. The parameters (position, intensity, broadening

coefficients, etc...) of absorption lines for 39 atmospheric molecules are compiled in the HITRAN database, resulting from the successive contribution and improvements by hundreds of spectroscopists (Rothman et al., 2008; http://www-cfa.harvard.edu/HITRAN). At short wavelength or for complex molecules however, energy levels are so numerous and close to each other that absorption lines can not be resolved individually and modelling of their absorption is done using empirically measured cross sections.

The loss of radiance $dR(\lambda)$ undergone by a radiation crossing an infinitesimal layer *dl* of absorbing gas *a* is proportional to the gas concentration C_a. This fundamental relation, known as Beer-Lambert-Bouguer's law is expressed by:

$$dR(\lambda) = -k_a(\lambda)C_a R(\lambda)dl \qquad (2.5)$$

Where $k_a(\lambda)$ (expressed in cm^2/molecule) is the absorption cross section of molecule *a*. Integrating this equation over a finite path joining L_0 and L_1 in a medium containing mixture of absorbing gases a_i with respective $k_i(\lambda)$ and C_i we can find :

$$R_{S1}(\lambda) = R_{L0}\exp\left(-\int_{L0}^{L1}\sum_i k_i(\lambda)C_i(l)dl\right) \qquad (2.6)$$

The quantity $-\int_{L0}^{L1}\sum_i k_i(\lambda)C_i(l)dl$, written $\chi(\lambda)$, is called optical thickness. For a homogenous medium (k_i and C_i being constant), optical thickness simplifies into $\sum_i k_i(\lambda)C_i.(L_1-L_0)$. The fraction of transmitted radiance is called transmittance (noted τ) and is equal to $\tau(\lambda)=\exp(-\chi(\lambda))$.

2.1.3 Emission

The atmosphere also emits radiation, which is added to the propagating radiation. Statistical mechanics shows that the emission coefficient of a gas at local thermodynamic equilibrium is equal to its absorption coefficient (this is known as Kirchhoff's law). Therefore the emission associated to a infinitesimal thickness dl follows

$$dR_e(\lambda) = k_a(\lambda)C_a B_\lambda(T)dl \qquad (2.7)$$

Where $B_\lambda(T)$ is Planck's function at the gas temperature T. Because gas in the terrestrial atmosphere have temperature < 500K, their thermal emission radiation has its peak intensity in the thermal infrared and is negligible in the UV and visible wavelengths.

2.1.4 Scattering

Light scattering, another fundamental process of light interaction with matter, is the dispersion of electromagnetic waves by heterogeneities in the propagation medium. The radiance scattered in a direction θ by a particle is given by the general equation

$$R_\lambda(\theta) = R_0 \frac{\omega_\lambda}{4\pi} P_\lambda(\theta) \qquad (2.8)$$

P is the phase function, which describes the angular distribution of the scattered light, and depends on the particle radius and shape. ω, the single scattering albedo of the particle, is defined as the ratio $k_s/(k_s+k_a)$, where k_s and k_a are respectively the scattering and absorption cross section of the particle. The radiation intensity is attenuated in the propagation direction, while it is increased in the other directions. In the atmosphere, heterogeneities range in size from molecules ($\sim 10^{-10}$m) to water droplets (10^{-2}m), which don't scatter light in the same way. Two types of light scattering can be distinguished: Rayleigh scattering and Mie scattering, each of them having distinct physical properties and origin. The size parameter, defined as the ratio of the particle diameter to light wavelength, $u = 2\pi\frac{r}{\lambda}$, determines which of the two type of light scattering do occur.

2.1.4.1 Rayleigh Scattering

Rayleigh scattering occurs when the size parameter is much smaller than one, i.e. when particle size is negligible compared to wavelength, as is the case for gas molecules. In Rayleigh scattering, the oscillating electric field of the electromagnetic radiation produces an oscillating electric dipole, which in turn produces an electromagnetic radiation of the same frequency as the incident one. The radiance scattered by a molecule follows the law

$$R = \frac{R_0}{r^2} p^2 \left(\frac{2\pi}{\lambda}\right)^4 \left(\frac{1+\cos(\theta)}{2}\right) \qquad (2.9)$$

Where R_0 is the radiance of the incident light, θ its propagation direction and λ its wavelength, r is the particle radius and p its polarizability (in m^3). Rayleigh scattering is the process that is responsible for the blue colour of the sky. Oxygen molecules diffuse preferably the shortest wavelengths of the solar spectrum transmitted by the high atmosphere (and filtered for its far UV component). These are the wavelengths corresponding to blue and near UV light. The λ^{-4} dependency of Rayleigh scattering makes it negligible in the Thermal infrared.

2.1.4.2 Mie Scattering

Mie scattering applies when the size parameter of the particles is close or superior to 1. Compared to Rayleigh scattering, wavelength dependence of Mie scattering is lower, but the phase function is strongly anisotropic and much more complex. Its mathematical treatment is complex in details. Mie theory itself is valid only for spherical particles. Light interacting with spherical particles, will undergo both refraction (leading to scattering in the other directions) and absorption (during its path through the particle). The optical thickness (or extinction efficiency) of an aerosol layer with a thickness z containing a number density N of particle with a diameter A is given by

$$\beta_e = AzNk_e$$

k_e is the extinction cross-section of the particles, which is the sum of their scattering cross-section k_s and the absorption cross-section k_a. This parameters is calculated for each wavelength with MALUT (Clarisse et al. 2010), an algorithm that solves the Mie equations numerically, taking the particle radius and the complex refractive index of the aerosol constituent as input parameters. MALUT generates extinction cross sections that can be included as a supplementary absorbing species in the radiative transfer model. The detail of this code is out of the scope of this manuscript.

2.1.4.3 Raman Scattering

This third type of scattering, unlike Rayleigh and Mie scatterings, is inelastic, which means that the wavelength of the scattered light differs from that of the incoming light. This happens because the relaxation of the molecule from its excited state (reached thanks to absorption) leads to a higher or lower energy state than the initial one. This process is typically much less efficient than Rayleigh scattering but produces a smoothing of sharp spectral features, known as the Ring effect, that has to be taken into account in the visible and UV spectrometry.

2.2 General radiative transfer equation

Now that we have reviewed all the possible interactions between radiation and its propagation medium, we can write a general equation of radiative transfer for a radiation propagating upwards through a horizontal layer of atmosphere.

$$\frac{dR_\lambda}{dz} = -R_0\left(\sum_i k_i C_i + \beta_e\right) + \left(\sum_i k_i C_i + \beta_e\right) B_\lambda(T) + \int_0^{2\pi}\int_0^{2\pi} R(\varpi,\phi)\frac{\beta_s}{4\pi}P(\varpi,\phi)\,d\varpi\,d\phi + R_S\tau\frac{\beta_s}{4\pi}\cos(\theta)P(\theta) \qquad (2.10)$$

C_i and k_i are the concentrations and absorption cross sections of the several gas species i. β_e is the extinction coefficient of the aerosol and the sum of β_a and β_s, θ is the solar zenith angle and $P(\omega,\varphi)$ is the phase function of the aerosol particles. The first term of this equation is the fraction of the incoming upwards radiance (R_0) absorbed by the layer, the second term stands for the radiance emitted by the layer. The third term is the radiance produced by multiple scattering inside the layer (the phase function is integrated over a sphere for considering all incoming radiance). The last term represents the sun radiance (R_s) backscattered by the layer. This is a very general equation that can be applied and simplified for the specific geometries and wavelengths of the measurement method.

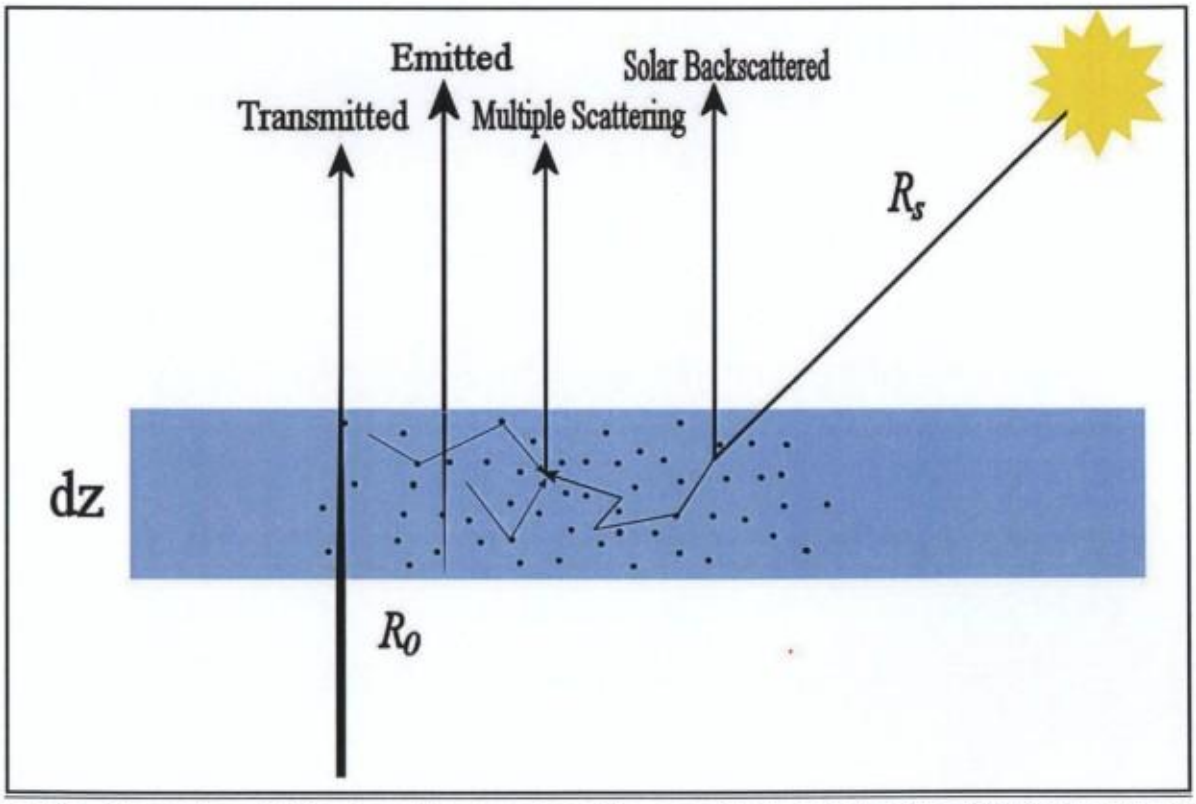

Figure 2.4: General radiative transfer processes for a radiation normal to infinitesimal layer of a plane parallel atmosphere.

2.3 Nadir viewing TIR measurements

This is the configuration of ASTER and MODIS, (and other sensors not exploited in this work such as AIRS and IASI). In this geometry and in the thermal infrared, the dominant source of radiation is thermal emission by the Earth surface and by the atmosphere, while solar backscattered radiance and multiple scattering are negligible. Extinction processes are molecular absorption and aerosol extinction. The latter can be treated as an extinction cross section calculated with Mie theory.

Introducing the optical thickness between height z and the satellite,

$$\chi_\lambda(z) = -\int_z^S \left(\sum_i k_i(\lambda) C_i + \beta_e(\lambda) N\right) dz$$

Equation 2.10 can be simplified as:

$$\frac{dR_\lambda}{d\chi_\lambda(z)} = -R_\lambda + B_\lambda(T_\chi) \qquad (2.11)$$

T_0 being the Earth surface temperature and ε its emissivity, initial condition of equation (2.11) can be constrained as $R_0=\varepsilon B_\lambda(T_0)+(1-\varepsilon)R_d$, which expresses that the radiance at z=0 is equal to the sum of the radiance emitted by the surface plus a contribution of reflected downwelling radiance (R_d). Equation (2.11) can be solved by multiplying it with an integration factor $\exp(-\chi(z))$ and by integrating between the surface (z=0) and the satellite (z=S) along a vertical path where the temperature (T) and optical thickness χ vary with altitude. We obtain thus the following expression of the radiance reaching the sensor

$$R_{s\lambda} = ((1-\varepsilon)R_d + \varepsilon.B_\lambda(T0)).\exp(-\chi_\lambda(0)) + \int_0^S B_\lambda(T(z)).\exp(-\chi_\lambda(z)).\chi_\lambda(z).d\chi_\lambda(z) \qquad (2.12)$$

Then, introducing the transmittance $\tau_\lambda(z)=\exp(-\chi_\lambda(z))$ between altitude z and the satellite, and remembering that $\frac{\partial \tau_\lambda(z)}{\partial z} = -\chi_\lambda(z).\exp(-\chi_\lambda(z))$, we can reformulate (2.12) as

$$R_{s\lambda} = \left((1-\varepsilon)R_d + \varepsilon B_\lambda(T_0)\right)\tau_\lambda(0) + \int_0^S B_\lambda(T(z))\frac{\partial \tau_\lambda(z)}{\partial z} dz \qquad (2.13)$$

The first term of this equation is the fraction of the surface radiance transmitted by the atmosphere (including the volcanic plume), while the second part represents the emissions from every layers of atmosphere (including the plume) attenuated by the atmosphere above them. In the case of the Earth atmosphere, this integral cannot be calculated analytically, because temperature pressure, absorption coefficients and concentrations of absorbing molecules all vary with altitude. Therefore it has to be modelled numerically with radiative transfer algorithms.

In the TIR, sulphur dioxide has two prominent absorption bands:

- The v3 band, located between 7.1 and 7.7 μm, correspond to the symmetrical stretching vibrations of the SO_2 molecule. This band is characterised by lines having high absorption cross sections, but water vapor has also strong absorption lines in that wavelength range, so that the total atmospheric transmittance is very low in that portion of the spectrum. However, as 99% of the total atmospheric water vapor resides below 4km, SO_2 plumes residing higher than 4-5 km are detectable by TIR satellites sing this band.
- The v1 band, located between 8.3 and 9 μm, correspond to the asymmetrical stretching vibrations of the SO_2 molecules. The lines forming that band have lower absorption coefficients than those of the v3 but are located in an "atmospheric window" where the total atmospheric transmittance is high (0.7-0.9), which enables even low altitude plume to be detected. This property is very interesting for measuring plumes produced by passive degassing, which are the main focus of this thesis.

2.3.1 Sulphur dioxide and thermal contrast

Two approximations can be brought to equation (2.13) to help the understanding of the first order error budget on the retrievals of SO_2 using TIR sensors.

1°) Surface emissivity ε is approximated as equal to 1. This is justified as spectral emissivity of water smoothly varies between 0.97 and 0.98 in the considered spectral region.

2°) Atmosphere is considered as transparent except for the SO_2 plume. Under this approximation, the total atmospheric transmittance is thus equal to the plume transmittance. This approximation can be done because the mean atmospheric transmittance around8.5 μm varies between 0.7 and 0.9 (depending on atmospheric humidity).

Applying these simplifications to equation *(2.13)*, it becomes thus

$$R_{s\lambda} = B_\lambda(T_0)\tau_g + B_\lambda(T_g)(1-\tau_g)$$

Where τ_g is the transmittance of the gas plume and T_g is the mean temperature of the plume. Then replacing with the absorptance of the gas plume (A_g =1-τ_g, or the fraction of radiance absorbed by the plume) we obtain the equation

$$R_{s\lambda} = B_\lambda(T_0) + A_g(\lambda)(B_\lambda(T_g) - B_\lambda(T_0)) \qquad (2.14)$$

From this simplified equation, it is obvious that the plume's effect that is perceived by the satellite is proportional to the temperature difference between the plume and the underlying surface. Therefore, as

temperature generally decreases with altitude in the troposphere, lower plumes will be more difficult to detect than higher plumes. Numerical results, obtained with Atmosphit, are shown in figure 2.5 to illustrate the importance of thermal contrasts in SO_2 retrievals. We see that the contribution of the plume to the radiance at sensor depends strongly on the plume temperature, being negative (i.e. net absorption) when the plume is colder than the Earth surface, or positive when it is warmer (in this less frequent case, the plume is then a net emitter). As atmospheric temperature depends on altitude, an incorrect estimation of the plume altitude leads to a systematic error on the SO_2 retrieval, as discussed in more details in chapter 3.

2.3.2 Atmosphit

All the forward simulations of the TIR radiative transfer were made with Atmosphit, an algorithm developed by Daniel Hurtmans, from the Service de Chimie Quantique et Photophysique Atmosphérique of ULB, and downloadable at http://home.scarlet.be/dhurtma/atmosphit.html. Atmosphit is a line-by-line transfer code that treats the atmosphere as a superposition of plane parallel layers containing user defined concentrations of 39 atmospheric molecules. Atmosphit uses the parameters of HITRAN to calculate the transmittance and emission of each layer and then perform the numerical integration on the whole stack of layers. The continuum absorptions of CO_2 and H_2O are handled by a MT_CKD subroutine. The latest version of Atmosphit can incorporate extinction coefficient of aerosol, computed with MALUT, as a supplementary absorber in the layers. Atmosphit can also perform inversion on high resolution radiance spectra to infer the vertical distribution of the absorbing molecules based on the shape of their absorption lines. Atmosphit needs 3 inputs files to work. The FIN file contains the geometrical parameters of the model (viewing angle and sensor's altitude), the source parameters (surface temperature, altitude and emissivity) and the wavelength range of the simulations. The BMD file contains the atmospheric model, consisting of a series of superposed layers with user defined temperature and concentrations of the 39 HITRAN molecules. The HIT file contains portion of the HITRAN database covering the wavelength range of interest. ATMOSPHIT is an accurate program, but line-by-line forward simulation are rather time consuming (about five second per spectra and one hour for generating an ASTER look-up table).

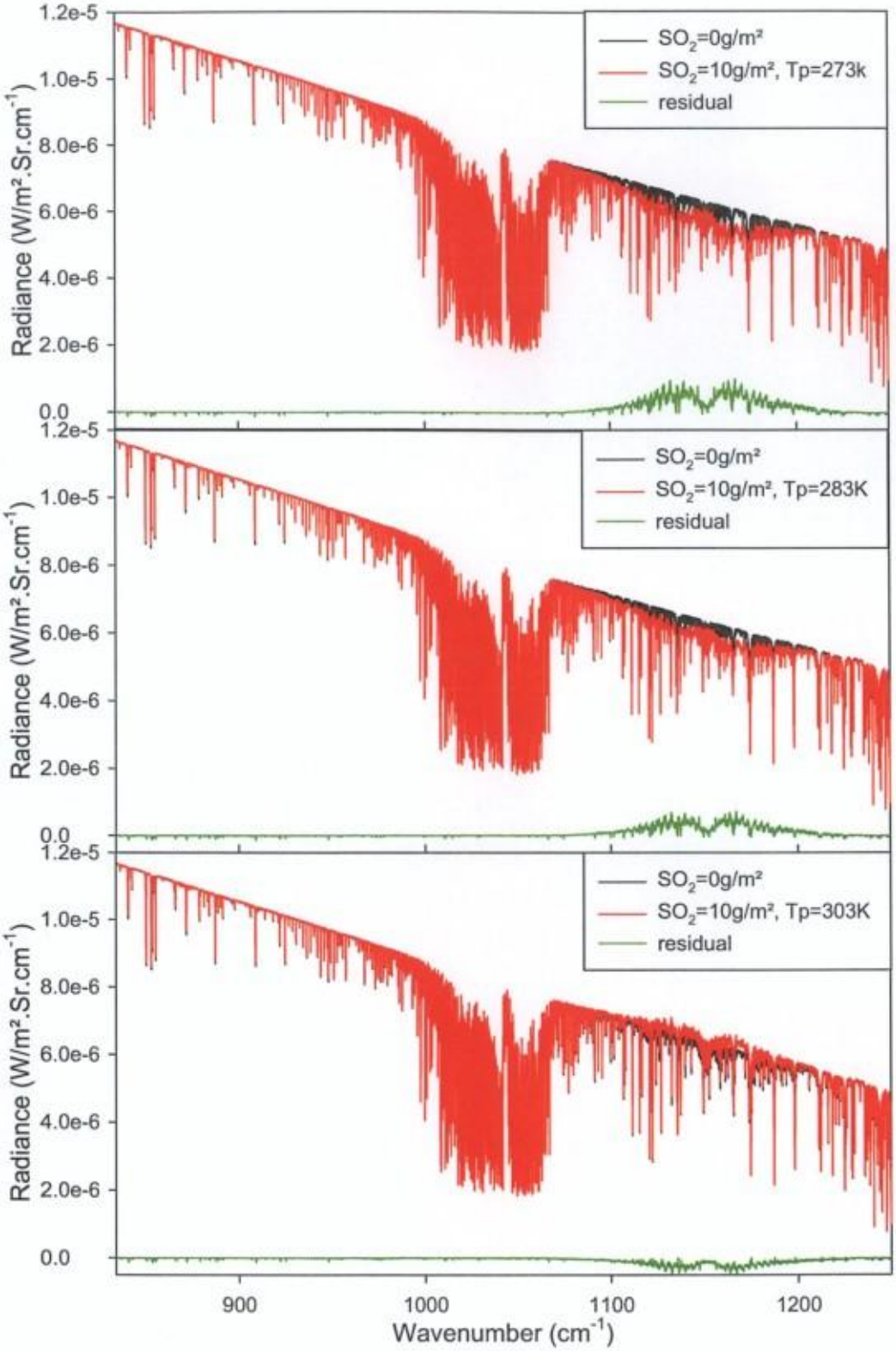

Figure2.5: Simulations of radiance spectra transmitted by an atmosphere (Mid Latitude Summer) containing a plume with 10g/m² of SO_2 at three different temperatures (red curves). The radiance spectrum transmitted by a clean atmosphere is shown in black. Surface temperature is 293K. The radiative effect of the plume is materialized by the green curve, calculated as the difference between the clean atmosphere spectrum and the plume spectrum.

2.4 Ground based UV measurements

In this configuration, used by the SO_2 camera (and by the COSPEC and DOAS techniques), the source of light is the UV component of radiation scattered by the molecules of the upper atmosphere (the « blue sky », see 2.1.3.1). In the UV, neither the Earth surface nor its Atmosphere emits radiation, so all the available radiation comes, indirectly, from the sun. The solar spectrum (figure 2.6) is best approximated by a Planck curve of a ~5500K black body and has thus a significant UV component. Sharp absorption lines conspicuous in the solar spectrum are caused by colder gases in its outer atmosphere and are called Fraunhoffer lines. The shortest wavelengths of solar radiation are absorbed by molecules and ions of the high atmosphere, and by stratospheric ozone, so that only radiation with $\lambda \geq 300$ nm reaches the low atmosphere and Earth surface (see figure 2.6). The volcanic plume, located between the sky (virtual source) and the detector acts as an absorber. Measurements of the radiance of the sky transmitted through a volcanic plume can be idealized by

$$R(\lambda) = R_0(\lambda).\exp(\int_0^l (\beta_S(\lambda,l) + \sum_i k_i(\lambda).c_i(l))dl) \qquad (2.15)$$

In this equation, a generalized form of the Beer-Bouguer-Lambert law that includes scattering extinction, $I_0$is the source radiance (in practical a radiance spectra recorded when the volcanic plume is not in the field of view of the instrument), $\beta_S$is a total scattering coefficient that regroups both Mie scattering on aerosols in-and outside of the plume and Rayleigh scattering. This aerosol extinction has a broadband shape, unlike the SO_2 absorption coefficient, which has strong and sharp features in the UV (see figure 2.7).

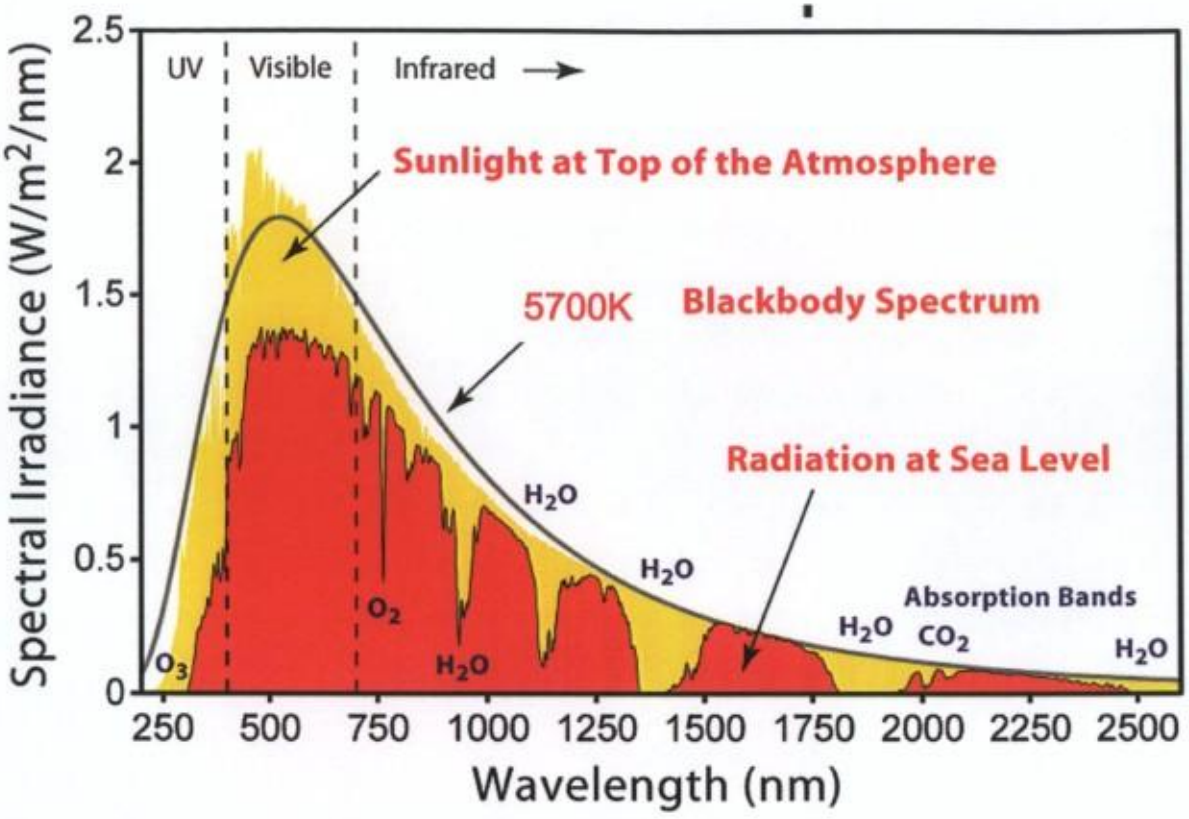

Figure 2.6: Spectrum of direct solar radiation before (yellow surface) and after its passage through the atmosphere (red surface).

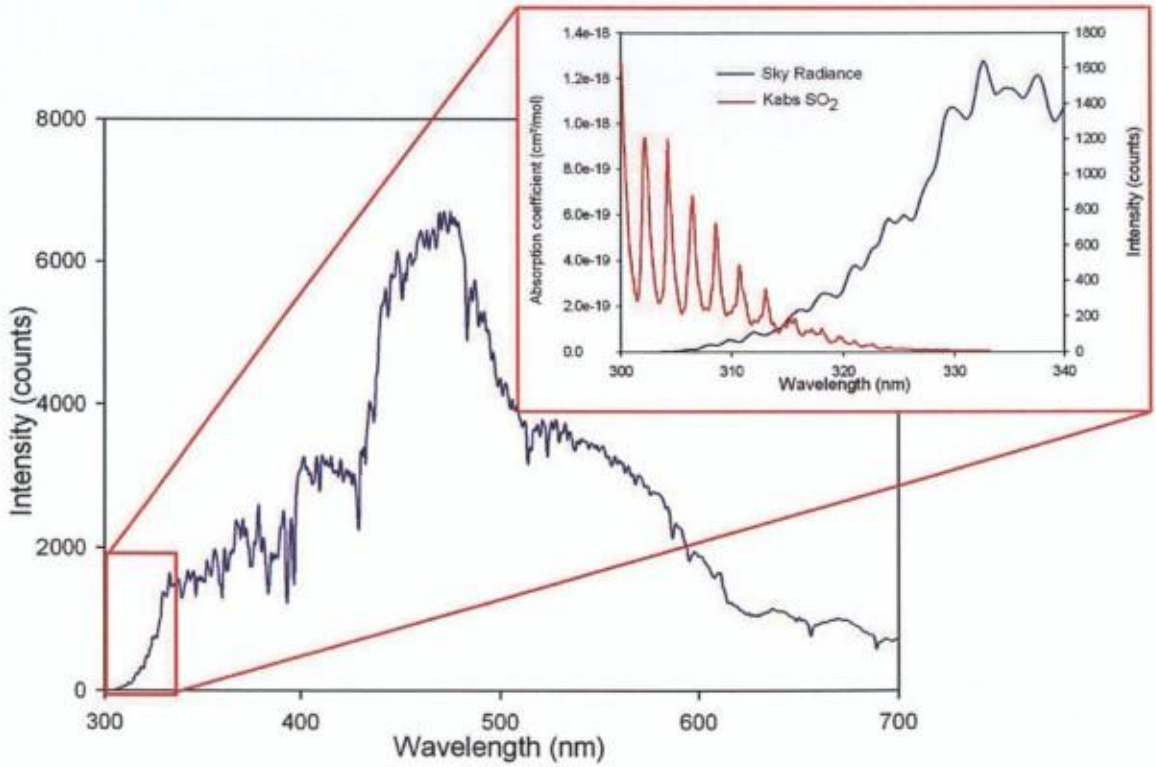

Figure 2.7: Spectrum of the diffuse sky radiation obtained with an Avaspec 2048 spectrometer. The zoomed region shows the spectral absorption bands of SO_2 molecules.

2.4.1 The DOAS technique

In practice, absolute spectroscopy in the atmosphere is made very complicated because the broadband extinction of aerosol is difficult to separate from the effect of instrumental response. Differential Optical Absorption Spectroscopy (in abbreviated DOAS) was therefore developed to overcome this problem. In this technique, the measured radiance spectra is divided by a reference spectra, and extinction is splitted into a broadband component, containing the scattering extinction ε_S as well as the broadband components of the molecular absorption σB_i, and the narrowband component of molecular absorption, σ'_i, (also known as the differential absorption cross section) that has been convolved to the spectrometer response function. Rearranging equation (2.15) with these modifications, and applying a natural logarithm yields

$$\ln\left(\frac{R(\lambda)}{R_0(\lambda)}\right) = \int_0^l \sum_i (\sigma B_i(\lambda).c_i(l) + \varepsilon_S(\lambda,l)).dl + \int_0^l \sum_i (\sigma'_i(\lambda).c_i(l)).dl \qquad (2.16)$$

The first term of the right member of this equation can be approximated by a 3rd or 4rth polynomial, while the second term can be reduced to $\sum_i \sigma'_i(\lambda).\overline{C_i}$, where the quantity $\overline{C_i}$, called slant column amount, is the amount of molecules i that light encounter on its path. Fitting algorithms can numerically find the polynomial coefficients and a set of $\overline{C_i}$ that minimize the least square sum between the left and right member of equation over all the points of the spectrum. DOAS technique has been applied on volcanoes since the late nineties because it is particularly suited for measuring SO_2 (e.g. Galle et al. 2002), but other trace compounds have also been discovered in volcanic plumes, such as BrO (Bobrovski et al., 2006) and ClO (Lee et al., 2005) using this technique. When applying the DOAS technique to measure SO_2 in volcanic plumes, ozone, NO_2 and the Ring effect need to be fitted simultaneously to SO_2 because they absorption features overlap those of SO_2. The Software Q-DOAS, developed at the Belgian Institute for Space Aeronomy (Fayt and Van Roozendael, 2001), was used in this thesis to process UV-spectra.

2.4.2 Air mass factor

The physical quantity retrieved with the DOAS technique is the slant column amount (SCA), but the relevant information from a volcanological point of view is the vertical (or oblique) column amount of SO_2, which equals the SCA only if the optical path of the photons is a straight line that crosses the whole plume. The air mass factor (AMF) defines the ratio between the SCA and the column amount. Although the common practice among the volcanologists using DOAS is considering the AMF equal to 1, Kern (2010a) showed that two processes affect AMF in DOAS measurements of volcanic plumes.

The first process, known as the light dilution effect, is caused by photons being scattered into the spectrometer's field of view without passing into the plume. This effect reduces the average AMF and become increasingly important at large plume-instrument distances. Light dilution is strongly wavelength dependent because of the λ^{-4}relationship of Rayleigh scattering and because the relative contribution of light diluting photons increases at wavelengths where strong SO_2 absorption takes place. Light dilution also depends on SO_2 concentration of the plume, as highly concentrated plumes absorb light so much that the relative contribution of photons that have crossed the plume is small compared to light diluting photons.

The second process, multiple scattering inside the plume, increases the effective pathlength of light insight the plume, and accordingly leads to AMFs bigger than one. Multiple scattering is especially important when the plume contain a high liquid aerosol load, which promote multiple Mie scattering.

When one of these two processes affects SO_2 measurements, the residual of the DOAS fit exhibits a wavelength dependency that mimics the peak and trough features of the absorption coefficient of SO_2, which enable flagging the measurements. Correction of these effects is possible but requires direct modelling of the radiative transfer using Monte Carlo simulations, as demonstrated by (Kern et al., 2010a). However this is a time consuming approach. An alternative solution to cope with light dilution consists in shifting the fit window towards longer wavelengths (Mori et al., 2006) until obtaining a spectrally independent residual.

2.5 Backscattered Ultra Violet (BUV) measurements

Space based UV spectrometry is the measurement technique of OMI (and other sensors not used in this thesis, such as SCIAMACHY or GOME2) and follows the same basic principles as ground based measurements. The solar radiation is backscattered to the space by gas molecules (Rayleigh scattering), by clouds and aerosols (Mie scattering) and by the Earth surface. The Earth surface can be approximated as a lambertian reflector (i.e. whose reflected light has an isotropic distribution).UV reflectivity of the Earth surface does not vary significantly with wavelength and is rather low in the UV (5- 10%, except for sea glint and snow covered surfaces). Because of the increased absorption by ozone and Rayleigh scattering by upper atmosphere molecules, the contribution of surface reflectivity to the overall BUV radiation decreases rapidly at shorter wavelengths. Clouds induce a significant increase in reflectivity and can be approximated as highly effective (although sometimes subpixel) lambertian reflectors. In a cloud free atmosphere, Rayleigh scattering is the dominant backscattering process. The different backscattering processes are illustrated in figure 2.7, while the respective contributions of each layers of the atmosphere to the total backscattered radiance are in figure 2.8. From looking at figure 2.7, we can realize that only a part of the BUV radiation (the one originating from below the plume) effectively crosses the plume. This part will be highly dependent on the plume altitude, the fraction of clouds and their altitude, and the ozone total column and profile. Therefore, the AMF of SO_2 in satellite retrieval is highly dependent on these parameters, which have to be taken into account in the retrieval process. Radiance measurements in the 340-380 nm, where little gaseous absorption takes place, allow an estimation of the reflectivity, which is proportional to the cloud fraction. Retrievals of the O_2-O_2 dimer, a metastable component present in the whole atmosphere at a constant mixing ratio, allow an estimation of the cloud top pressure (and hence altitude). An AMF for SO_2 can be simulated with these measured parameters and an a priori plume altitude, but will be affected by an error arising from inaccuracies over them. More recently Yang et al. (2010) have shown that high resolution spectra from OMI contain enough information to retrieve simultaneously SO_2 column amount *and* plume height. However, the case study they presented, the proximal hyperconcentrated Kasatochi plume, is very specific, and it is not known if their direct fitting algorithm can be applied to more diluted or smaller plumes. Their algorithm seems to be rather time consuming and has not yet been implemented in the OMI standard SO_2 product, which is computed using the Linear Fit algorithm described in chapter 4.

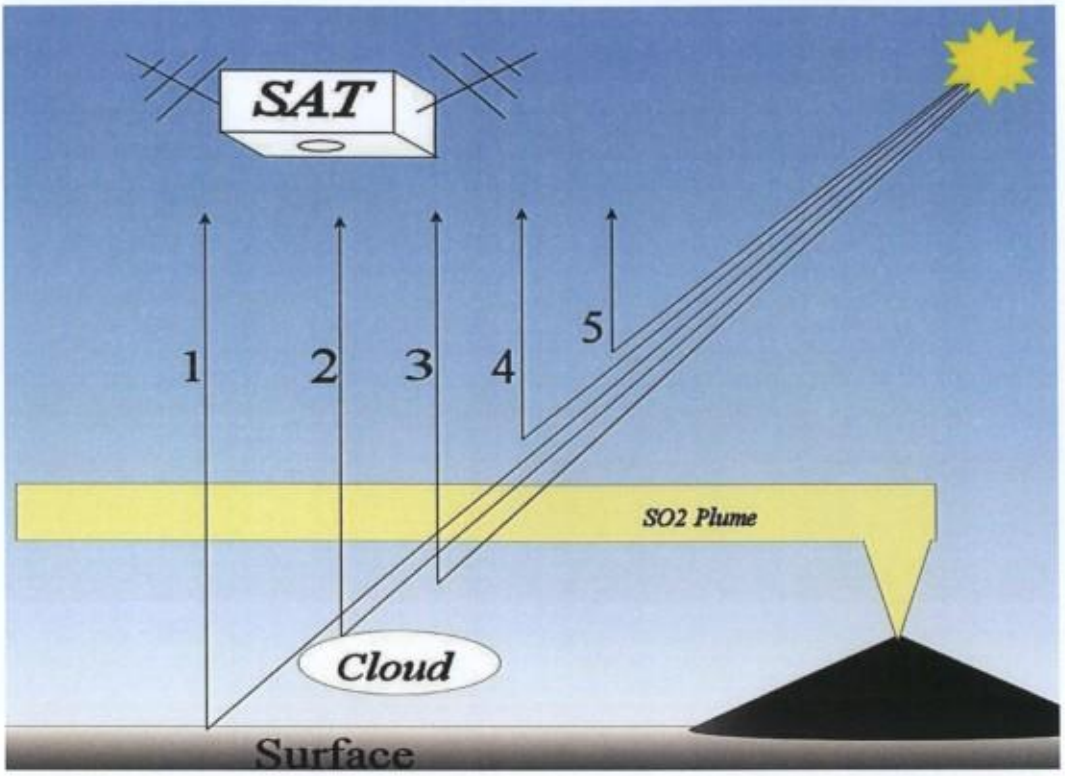

Figure 2.7: The different contributions to the BUV radiance measured at the satellite. 1: surface reflectivity, 2: cloud reflectivity, 3 to 5 backscattering by the low mid and high atmosphere. Multiple scattering has been omitted for clarity. (Horizontal scale not respected)

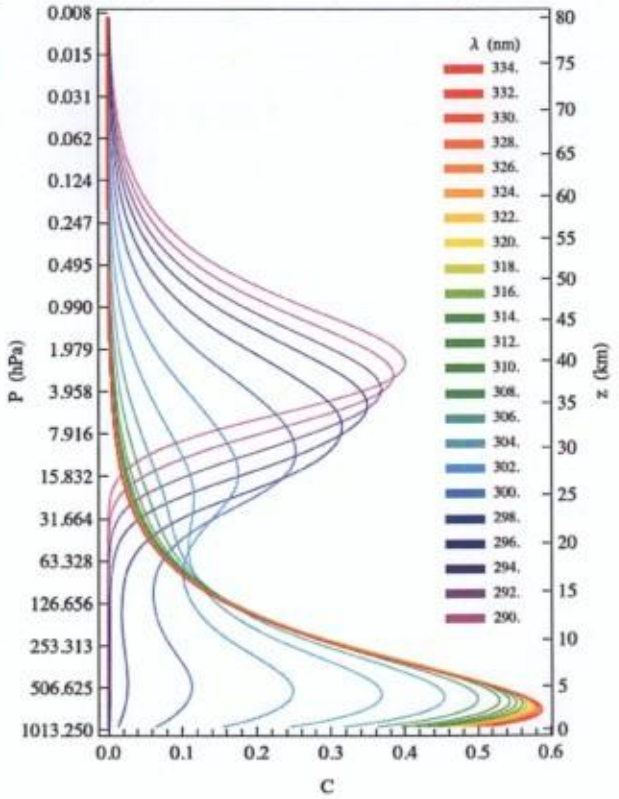

Figure 2.8: Contribution (c) to the BUV radiance by different altitudes of a cloud free atmosphere. Short wavelengths of the BUV spectra come from higher than low wavelength (after Yang et al., 2010) because they are blocked in the high stratosphere by the strong absorption of ozone.

Chapter 3: Measuring volcanic degassing of SO_2 in the lower troposphere with ASTER band ratios.

3.1 Abstract

This chapter, which is an extended version of (Campion et al., 2010), presents a new method for measuring SO_2 with images from the ASTER (Advanced Space-borne Thermal Emission and Reflectance radiometer) orbital sensor. The method consists in adjusting the SO_2 column amount until the ratios of radiance simulated on several ASTER bands match the observations. We present a sensitivity analysis for this method, and two case studies. The sensitivity analysis shows that the selected band ratios depend much less on atmospheric humidity, H_2SO_4 aerosols, surface altitude and emissivity than the raw radiances. Measurements with <25% relative precision are achieved, but only when the thermal contrast between the plume and the underlying surface is higher than 10K. For the case studies we focused on Miyake-jima and Etna, two volcanoes where SO_2 is measured regularly by COSPEC or scanning DOAS. The SO_2 fluxes computed from a series of ten images of Miyake-jima over the period 2000-2002 is in agreement with the long term trend of measurement for this volcano. On Etna, we compared SO_2 column amounts measured by ASTER with those acquired simultaneously by ground-based automated scanning DOAS. The column amounts compare quite well, providing a more rigorous validation of the method. The SO_2 maps retrieved with ASTER can provide quantitative insights into the 2D structure of passive degassing volcanic plumes, their dispersion and their progressive depletion in SO_2.

3.2 1 Introduction

Volcanism is the leading natural source of sulphur dioxide (SO_2) to the atmosphere, with average annual emissions estimated at 10 to 40.10^9Gg/year, according to different authors (Le Guern, 1982; Stoiber et al, 1987; Andres and Kasgnoc, 1997; Graf et al, 1997). These emissions occur through eruptions and passive degassing. The low atmospheric background of SO_2, together with its strong absorption features in the ultra-violet (UV) and infrared (IR), makes this gas a good target for spectrometric measurement from field and space. SO_2 flux measurements have been performed since the 1970s by UV correlation spectrometry (e.g.: Newcomb and Millán, 1970; Stoiber et al., 1983). They have proven to be valuable for our understanding of eruption dynamics and eruption forecasting (see William-Jones et al., 2008, for an extensive review of theory, practice and case studies of SO_2 field measurements on volcanoes). The most commonly used instruments for SO_2 field measurements are now compact UV spectrometers with or without calibration cells (Galle et al, 2002, Elias et al., 2006). However, these sensors can only measure scans or transects of SO_2 column amounts, while volcanic plumes are actually dynamical 3D objects. To expand the investigations on volcanic plumes,

field UV imaging devices have been developed recently (Bobrowski et al, 2006; Mori and Burton, 2007; Bluth et al, 2007, Dalton et al, 2009) and these technologies are currently being rapidly developed as volcano monitoring tools.

Space based sensors are also able to detect and measure volcanic SO_2. They provide a more complete view of large scale volcanic plumes and are the only tools allowing a quantification of the material (gas, ash and aerosols) injected into the atmosphere by large eruptions. Current space-borne sensors sensitive to SO_2 are MODIS, ASTER, AIRS, SEVIRI and IASI operating in the thermal Infrared (TIR), and GOME-2, SCIAMCHY, and OMI in the UV. Thanks to their high sensitivity and daily (or nearly daily) global coverage, OMI (Carn et al, 2008), AIRS (Prata and Bernardo, 2007) and IASI (Clarisse et al. 2008) have already proved very useful for quantifying eruptive emissions of SO_2 as well as tracking SO_2 transport up to several weeks after the eruption. Thanks to its high acquisition frequency (1 image every 15 minutes), the geostationary sensor SEVIRI can also be very useful for near real-time monitoring of volcanoes located in its observation zone. However the low spatial resolution and/or weak sensitivity of these sensors to tropospheric SO_2 complicate the quantification of SO_2 flux in passive degassing plumes.

ASTER was launched in December 1999 on board the EOS Terra satellite on a sun-synchronous orbit (Pieri and Abrams al, 2004). Depending on latitude, the minimal time delay between two images varies between 1 and 7 days, somewhat limiting its use for routine volcano monitoring. The presence of a tight cloud cover at the time of overflight can extend the time delay between two exploitable images. The ASTER sensor is composed of three subsystems (see figure 3.1), operating respectively in the visible-near infrared (ASTER-VNIR), in the shortwave infrared (ASTER-SWIR, down since 2008) and in the thermal infrared (ASTER TIR). This last subsystem has five spectral bands with a 90 meter ground resolution at nadir. The bands are labelled from B10 to B14 with increasing wavelengths and have their centroids located at 8.3, 8.6, 9.1, 10.6 and 11.3 μm (figure 3.2). Following the pioneering works of Realmuto et al. (1994, 1997) for SO_2 retrieval with TIR sensors, ASTER was recognized, prior to launch, as a potential tool for measuring volcanic SO_2 from space (Corradini et al., 2003). Urai (2004) adapted their retrieval scheme to an ASTER image of Miyake-jima volcano (Japan). The method consists in applying a non-linear regression to MODTRAN-simulated radiance in two ASTER spectral bands (band 11 and band 14) for varying SO_2 concentrations. More recently, Pugnaghi et al. (2006) developed several fast retrieval schemes, adapted for Mount Etna, approximating the full radiative transfer calculations with functions of monthly averaged atmospheric parameters. Both studies computed SO_2 fluxes in good agreement with ground based measurements.

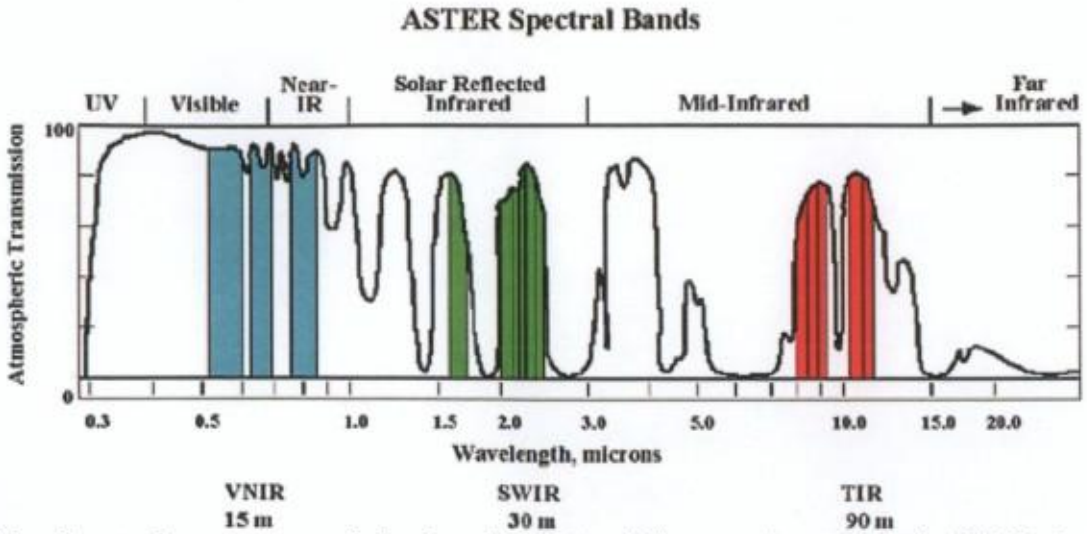

Figure 3.1: Spectral coverage of the bands of the different subsystems of ASTER. Image from http://asterweb.jpl.nasa.gov/characteristics.asp

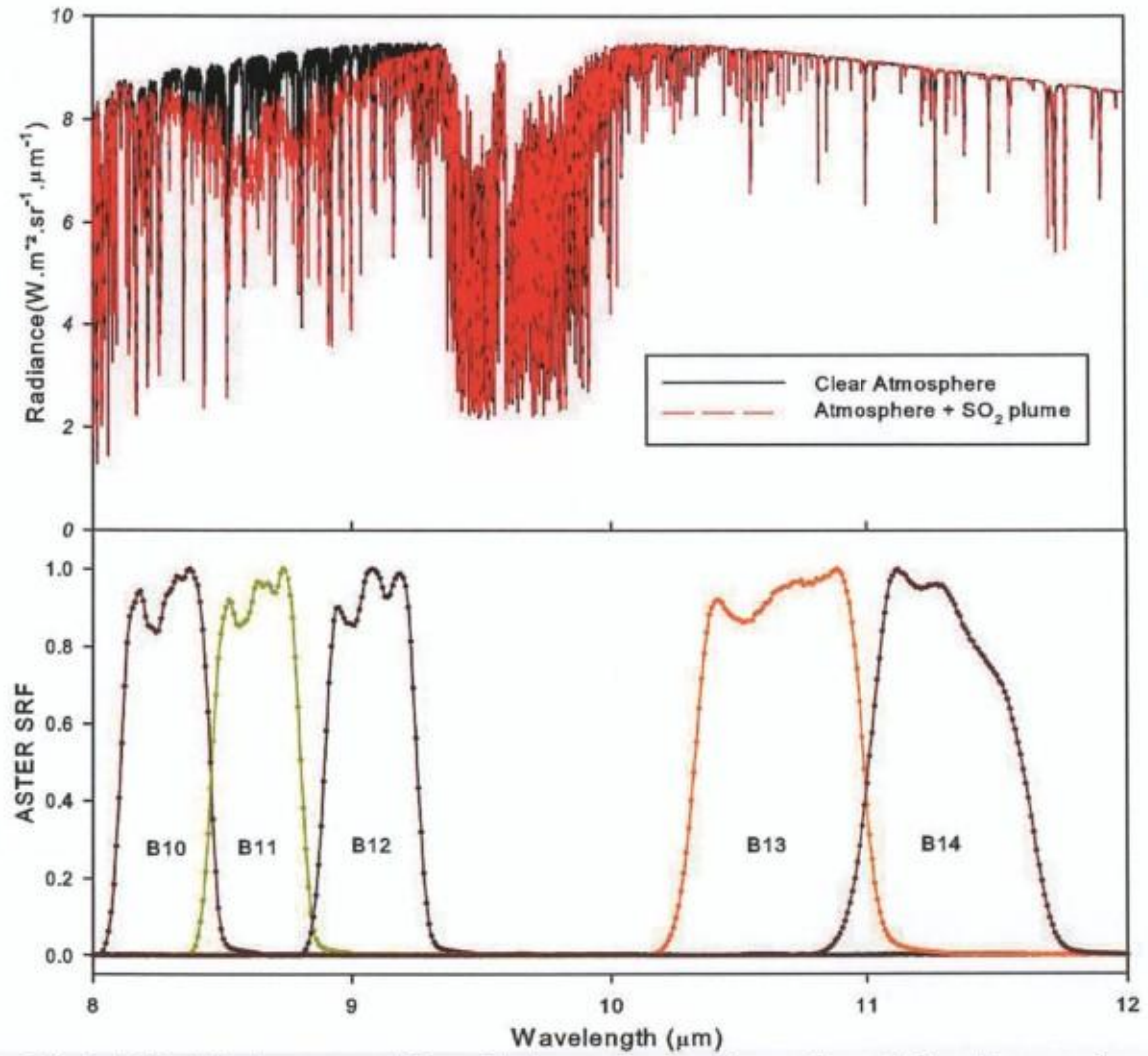

Figure 3.2: (a) Modelled spectra of Top Of Atmosphere radiance for a "clean" atmosphere (black) and for an atmosphere containing 10g/m² of SO_2 at an altitude of 3 km (red dashed). (b) Normalised Spectral Response Function of ASTER TIR bands

However a number of parameters other than SO_2 can affect retrievals that use ASTER radiances. These parameters are plume temperature, atmospheric humidity, surface altitude and surface emissivity. To reduce the effect of the last three parameters, we developed a new method for measuring SO_2, which uses radiative transfer simulation and fitting of ASTER band ratios (B10+B12)/(2B11) and B14/B11. These ratios were selected because of their very low sensitivity to atmospheric humidity, surface altitude and emissivity, which makes the retrievals more robust and straightforward (see section 3).

3.3 Methodology

3.3.1 Radiative transfer simulations

SO_2 molecules in the plume absorb IR radiation emitted by the Earth surface and the lower atmosphere. The ν_1 absorption band of SO_2, extending from 8.1 to 9.5μm, mostly affects ASTER band 11, and, to a less extent, bands 10 and 12 (see figure 3.2 and 3.3). The radiance R_A measured by the sensor is given by the general equation of the TIR radiative transfer in the atmosphere, where wavelength dependence is omitted for sake of clarity

$$R_A = \varepsilon.B(T_0).\tau_0 + \int_0^A B(T_z).\frac{\partial \tau_z}{\partial z} dz + (1-\varepsilon)R_d.\tau_0 \quad (1)$$

B(T)is the blackbody Planck function for temperature T, ε is the surface emissivity, z is the altitude, τ_Z is the transmittance between altitudes z and A, and R_d is the downwelling radiance at the Earth surface. The altitudes of the surface and the sensor are respectively 0 and A. In this equation, the first term represents the Planck radiance that is emitted by the Earth surface at temperature T_0, and partly transmitted by the atmosphere. The second term is the radiance emitted by each layer of the atmosphere, including the plume (the so-called "path radiance"), and the third term is the part of downwelling radiance that is reflected by the surface. In absence of sun glint, this last term becomes negligible in the TIR.

Radiance is simulated with Atmosphit, a line-by-line radiative transfer code developed at the Université Libre de Bruxelles (e.g. Coheur et al, 2005). Atmosphit simulates high-resolution spectra, considering a layered model atmosphere with spectral parameters from the HITRAN database (Rothman et al, 2008) and the MT_CKD (Clough et al., 2005) model for H_2O and CO_2 continua. Fixed parameters for the simulations include the surface altitude and emissivity, and the atmospheric profiles of temperature and concentration of 38 atmospheric molecules. In the spectral region of interest for

ASTER TIR, the molecules that absorb radiation are, in the order of importance, H_2O, O_3, CH_4 and N_2O. The concentration profiles of the latest three molecules are kept fixed and based on standard atmospheric models, because of their weaker absorption and lower variability over short spatial and temporal scale. Temperature and H_2O profiles were defined using radiosonde data from the nearest launching site (available at the RAOB website: http://raob.fsl.noaa.gov/). For the simulations, the volcanic plume is considered as a layer containing given SO_2 column amounts in thermal equilibrium with the atmosphere. Its thickness is assumed to be 400m, but the influence of this parameter on the retrievals was found to be negligible. Surface temperature, plume altitude and SO_2 amount in the plume, are varied incrementally.

3.3.2 Retrieval scheme

The simulated spectra are then integrated over the spectral response functions of ASTER (available at http://www.science.aster.ersdac.or.jp/en/about_aster/sensor/index.html), to get the simulated ASTER radiances on the five bands. The simulations are used to generate five (one per band) 3D matricial look-up-tables containing the radiance values for each SO_2 column amount, ground temperature and plume altitude. A region free of SO_2, representing the variability of temperatures and surface types present under the plume, is selected close to the plume. The pixels of this region are used as a blank to correct slight discrepancies between the simulated and measured radiances. Plume altitude, together with wind speed, is measured on the Visible-Near-Infrared (VNIR) stereoscopic images with the method described by Urai (2004). This method is based on the displacement of distinctive plume features between the nadir and backward looking images, but has some limitations (i.e. wind direction parallel to satellite trajectory and very faint plumes). A cloud detection routine, based on their lower brightness temperature, is applied to exclude them from further analysis.

Surface temperature is measured with bands 13 and 14 with a split window algorithm (Trunk and Bernard, 2008) for sea or, for land, by inverting the radiative transfer with the look-up tables. For each pixel, knowing the measured surface temperature, plume altitude and radiance ratios, the SO_2 column amount is interpolated in the 3D matrix of the simulated radiance ratio. Column amount is first retrieved with (B10+B12)/(2B11). If the result is higher than $15g/m^2$ (very high value, rarely encountered in passive degassing plumes), it is remeasured with B14/B1, to avoid saturation effects (see section 3). Once the SO_2 column amount is measured, over the entire image, traverses are defined automatically as lines of pixels perpendicular to the transport axis. The SO_2 flux is finally computed by integrating the SO_2 column amount over all the pixels of each traverse, and multiplying by the wind speed. The above retrieval scheme is integrated in one program, where the user just defines the

contours of the plume and "background" regions as well as the transport direction of the plume. The program also includes an error estimation routine that is based on SO_2 retrievals with biased altitude, wind speed, and takes into account radiometric noise.

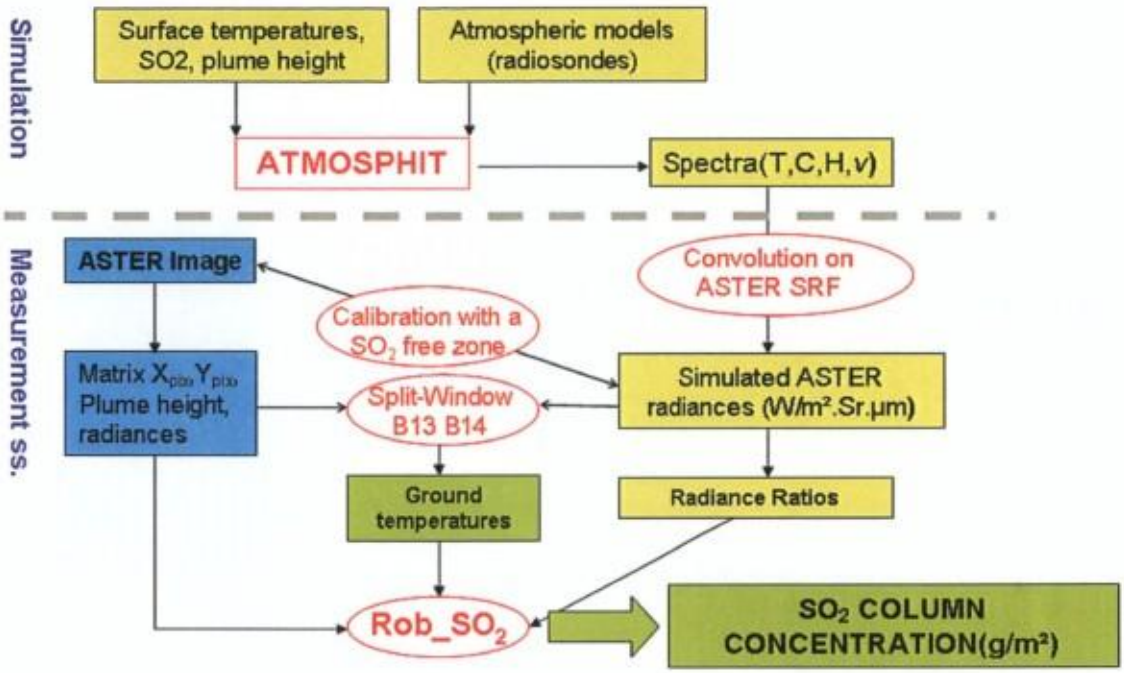

Figure 3.3: Schematic workflow of the SO_2 retrieval algorithm using ASTER. See explanation in the text.

3.4 Sensitivity analysis

In this section we present a sensitivity analysis of radiance ratios in response to SO_2, thermal contrast, atmospheric humidity, surface altitude and emissivity. For comparing the sensitivity of radiance ratios and radiance to each of these parameters, we use the ΔSO_2 equivalent to the bias introduced by varying the parameter.

3.4.1 Sulphur Dioxide

Figure 3.4 shows the simulation of ASTER radiances, (B10+B12)/2B11 and B14/B11 as functions of SO_2 column amount. Absorption of SO_2 causes a slight decrease of B10 and B12 and a sharp decrease of B11, while B13 and B14 are unaffected. Thus, both radiance ratios increase with SO_2 column amount. As SO_2 increases, the sensitivity (B10+B12)/2B11 decreases until complete saturation around ~50 g/m². Such very high values are extremely rare in volcanic plumes. To avoid the negative impact of saturation, retrievals of amounts higher than 15 g/m² are made with the B14/B11 ratio, which presents a higher sensitivity at these high SO_2 burdens.

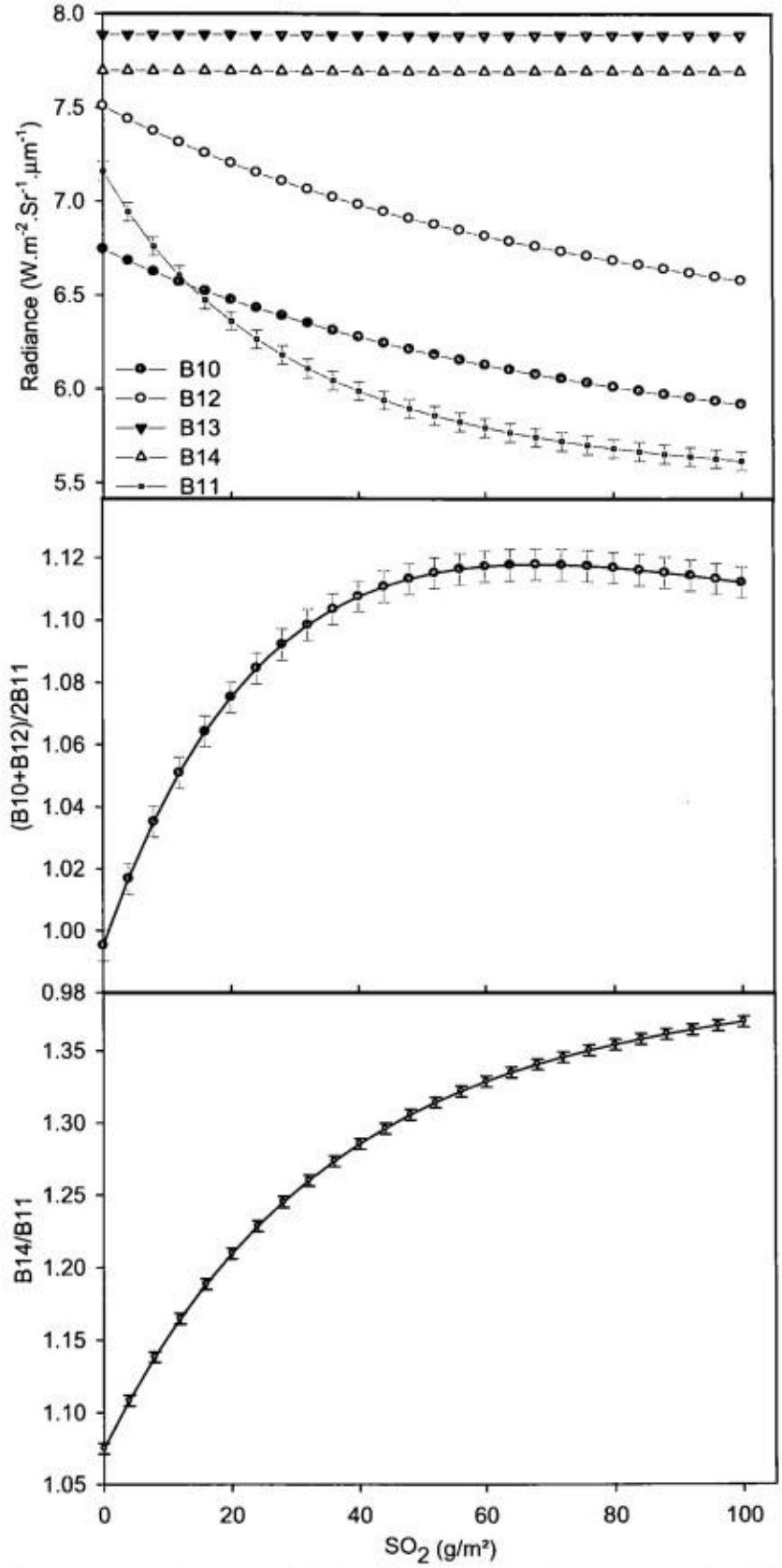

Figure 3.4 : Simulations, as a function of SO_2 concentration (increment=4g/m²), of ASTER radiances, (B10+B12)/2B11 and B14/B11. The simulations reproduce a Miyake-jima case, with surface temperature equal to 289K and plume altitude set to 1100m (T=273K). Error bars represent the typical 1σ observed on homogenous portions of the sea.

3.4.2 Thermal contrast.

Previous studies (Realmuto, 1994, 1997) have demonstrated the importance of thermal contrast between the gas plume and the Earth surface, for both accuracy and precision of the retrievals. The impact of thermal contrast on SO_2 retrievals was already demonstrated theoretically in section 2.3.1 for a simplified case with a surface emissivity of 1 and a transparent atmosphere except for the SO_2 plume. Here, in order to analyse the sensitivity to thermal contrast, we varied surface temperature (figure 3.5) in the simulations while keeping the plume at the same altitude and temperature (3200m and 283K). In this figure, the slope of the curves indicates the sensitivity to SO_2, while the vertical gap between the curves indicates the dependence to temperature. As expected from equation 2, SO_2 is undetectable when the ground has the same temperature as the plume, and sensitivity increases with thermal contrast. Figure 3.5 also shows that, at low column amounts of SO_2, (B10+B12)/2B11 is nearly insensitive to ground temperature. Plume altitude is also critical for thermal contrast as temperature in the troposphere decrease with increasing altitude (except locally in case of thermal inversion). Therefore, error on plume altitude estimation will cause a systematic bias in the SO_2 retrievals. The magnitude of this error decreases when plume altitude (or thermal contrast) increases, as shown in figure 3.6.

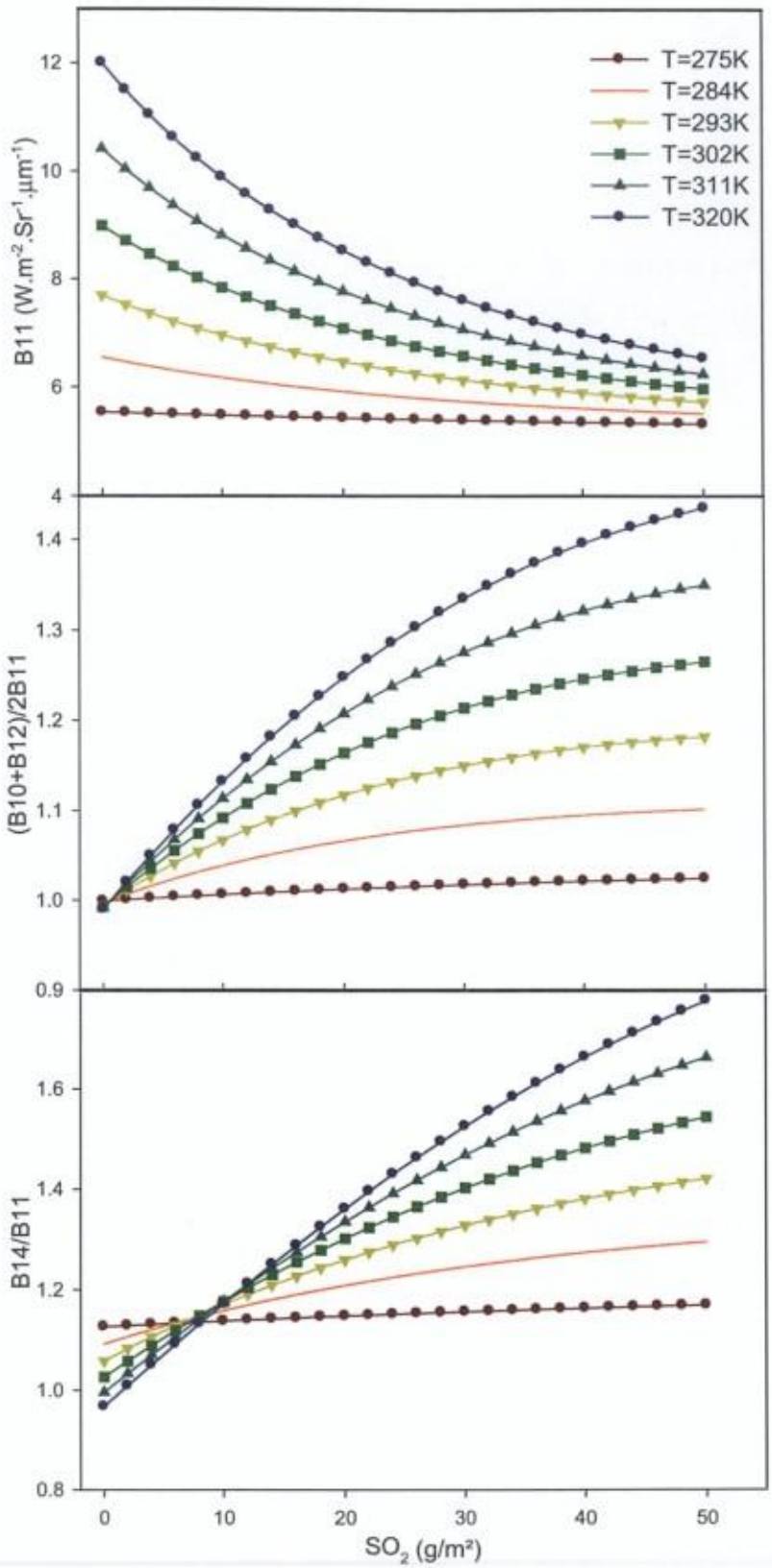

Figure 3.5: Simulations of B11 radiance, (B10+B12)/2B11 and B14/B11 as functions of SO_2 column for several surface temperatures. Plume altitude is 3200m and its temperature is 273K (typical Etna case).

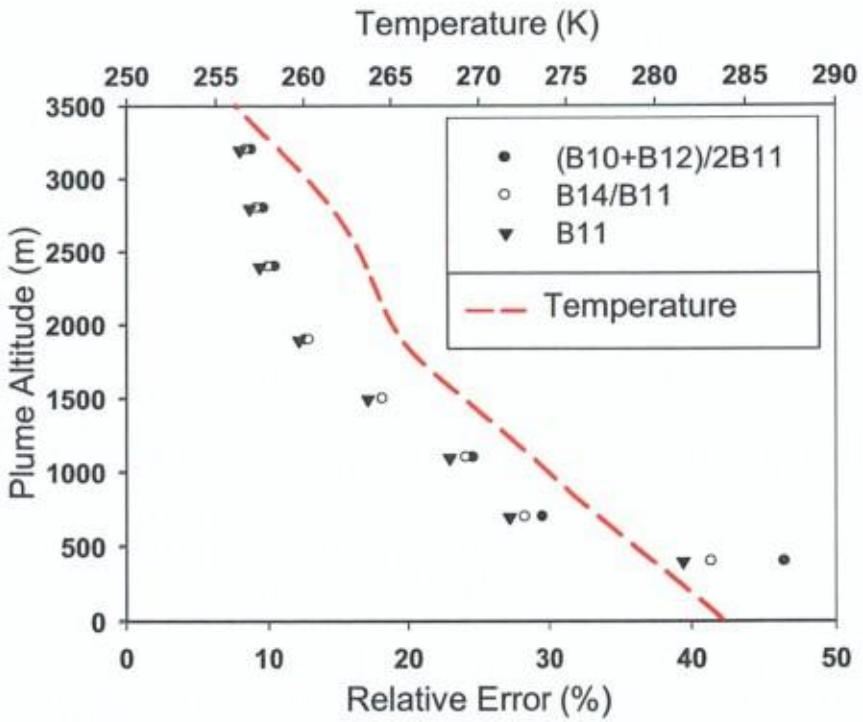

Figure 3.6: Relative retrieval error caused by a 400m bias in plume height estimation. It is shown as a function of plume altitude. The temperature profile used for the simulations (Hachiyo-jima, 1st April 2001) is also shown. Surface temperature is set to 290K.

3.4.3 3.3 Radiometric noise

Radiometric noise affects ASTER images and SO_2 retrievals under the form of cross track lines of pixels above or below the average value. ASTER bands have a NEΔT of about 0.15K, which is better than the 0.3K design requirement (Arai and Tonooka, 2005). At 293K, this translates into a standard deviation of 0.025 $W.sr^{-1}.m^{-2}.\mu m^{-1}$, 0.005 and 0.004 for B11, (B10+B12)/2B11 and B14/B11 respectively. The impact of radiometric noise on the retrievals was evaluated by considering an additive 1σ noise error on radiance and radiance ratios. The result is expressed in terms of an error (called NEΔSO_2) between the perturbed and reference situation as $NE\Delta SO_2 = (SO_2)_{pert}-(SO_2)_{ref}$. It is a random error that varies as a function of thermal contrast between the plume and the ground, as shown in figure 3.7. It increases dramatically when thermal contrast approaches zero. Due to the combination of 3 bands of ASTER, the NEΔSO_2 on retrievals based on (B10+B12)/2B11 is slightly higher with than with raw radiance.

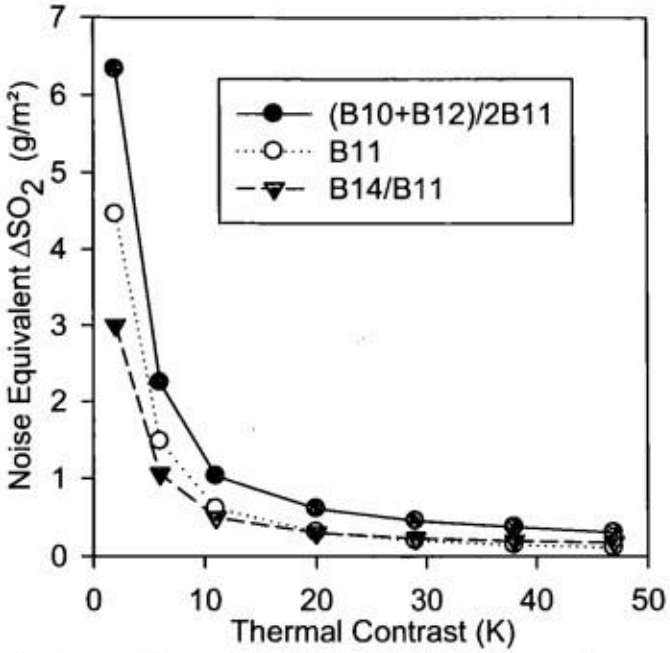

Figure 3.7: Noise Equivalent ΔSO_2 as a function of thermal contrast for retrievals using (B10+B12)/2B11, B11 and B14/B11. Plume altitude is set to 1100m (T=273K).

3.4.4 Atmospheric humidity and surface elevation

Water vapor is the principal and more variable atmospheric gas interfering with SO_2 around 8.5 μm. It is most abundant in the low troposphere, with 95% residing in the lowest 4 km of the atmosphere. Atmospheric humidity varies on a regional scale as a result of topography and atmospheric dynamics. Figure 3.8a shows the simulated effect of water vapor on the raw radiances and on the radiance ratios for a Miyake-jima like atmosphere. Flat slopes indicate that retrievals with radiance ratios are nearly independent on atmospheric humidity. For comparison, in the same conditions, a 40% of atmospheric humidity in the four lowest km induces a systematic ΔSO_2 of about 1g/m² if retrieved with raw radiance.

The total H_2O column amount also strongly decreases with surface altitude, because of the pathlength reduction between the surface and the satellite. Figure 3.8b shows the effect of varying surface altitude on B11 radiance for an Etna-like atmosphere. As for atmospheric humidity, the retrievals with radiance ratios show a remarkable stability, while those with radiance are significantly affected. A 500m elevation difference produces a systematic ΔSO_2 of 1g/m² on raw radiance retrievals. The effect of surface altitude is expected to be stronger in a moist atmosphere.

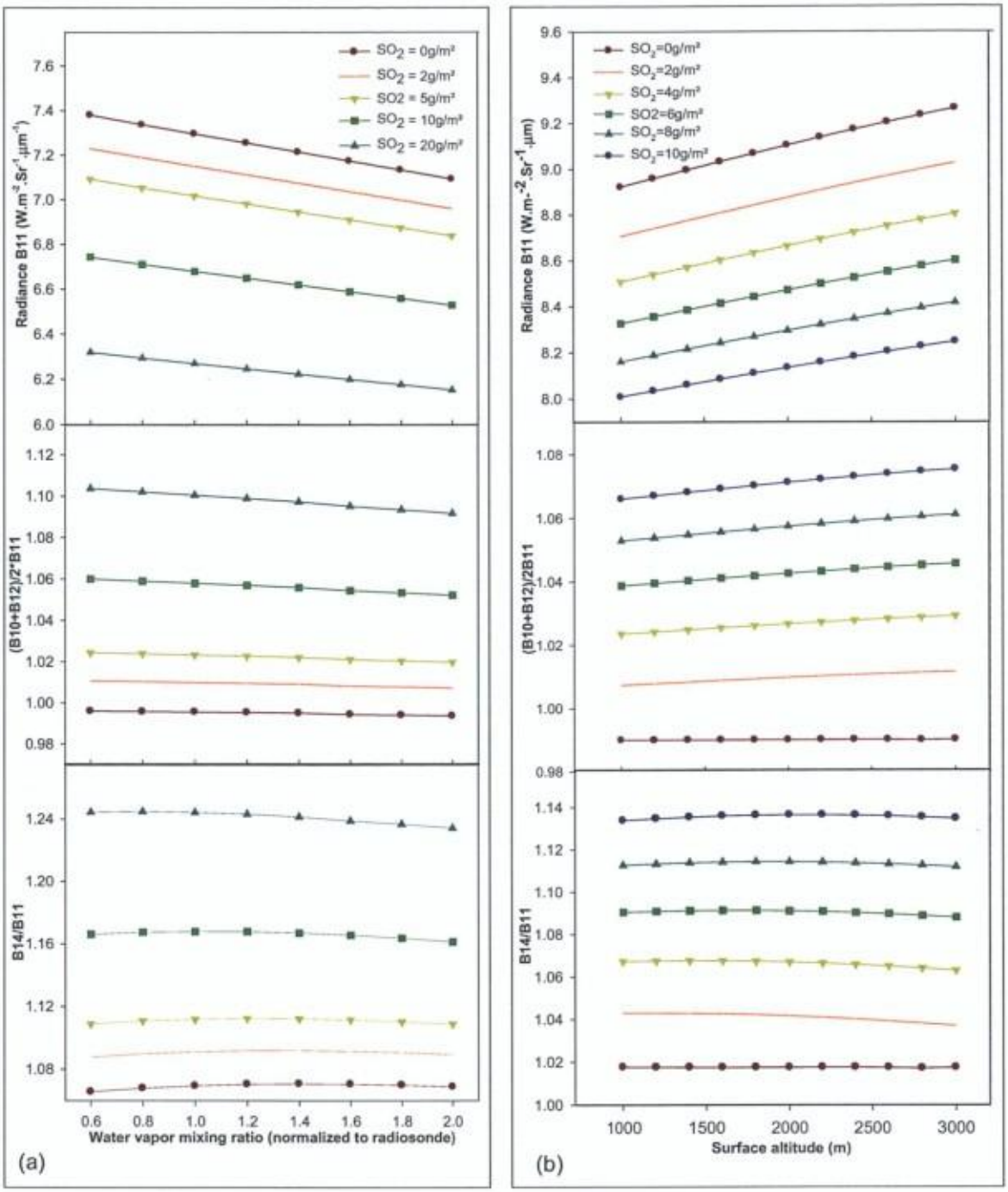

Figure 3.8: Simulation of B11 radiance, (B10+12)/2B11, and B14/B11 for increasing SO_2 concentrations. (a) As a function of atmospheric humidity, varied in the model by multiplying the mixing ratios of H_2O in the lowest 4 km of the reference profile. The reference profile is the one used in the image of April 1st of Miyake-jima. The plume temperature, 273 K, is determined by its altitude (1100m). (b) As a function of surface elevation. Plume altitude is 3200m (T= 281K), and the atmospheric profile is the one used for the image of Etna on 3 August 2001.

3.4.5 Surface emissivity

Temperature Emissivity Separation algorithms do not work properly for surfaces lying under volcanic gas plumes, because their spectral properties differ from the atmosphere. Therefore,*a priori* definition of emissivity is needed before retrieving SO_2, which may bias SO_2 retrievals. The effect of varying emissivity is shown in figure 3.9. Radiance and radiance ratios were simulated with several emissivity spectra: basalt, sea water (references basalt.7f and seawater in the Aster Spectral Library) and grey bodies with emissivity of 0.96, 0.97 and 0.98. The B14/B11 ratio and B11 radiance show a maximal ΔSO_2 of about $2g/m^2$, while (B10+B12)/2B11 is much less sensitive, with an interestingly low $0.5\ g/m^2$.

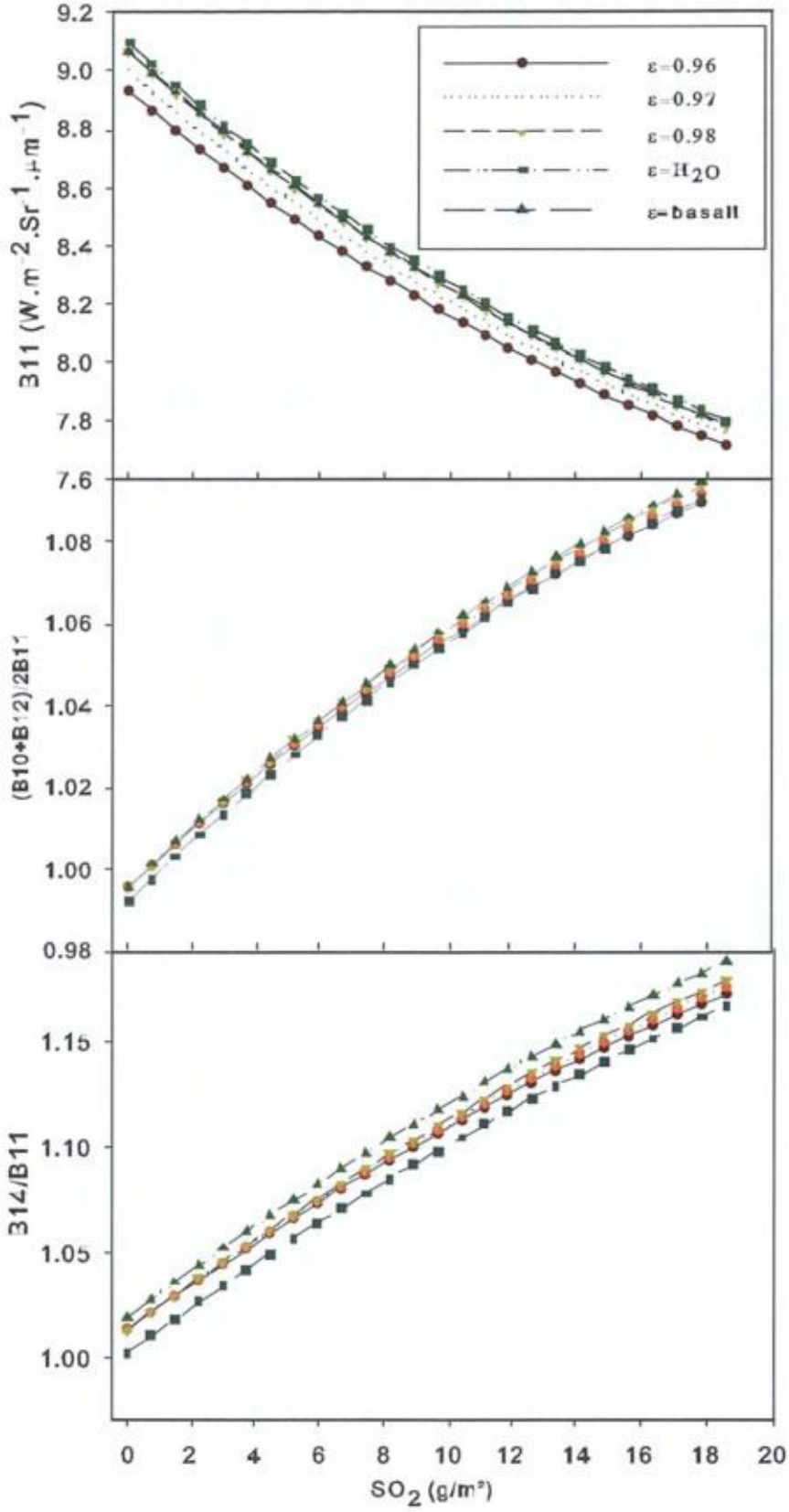

Figure 3.9: Simulations of B11 radiance, (B10+B12)/2B11, and B14/B11 as functions of SO_2 for different surface emissivities: grey bodies with emissivities from 0.96 to 0.98, water and basalt. The parameters of simulations correspond to an Etna-like case, with a surface temperature of 303k and a plume altitude of 3200m (T=281K).

3.4.6 Sulfate aerosols

Aerosols are always present in passive degassing plumes, and direct sampling campaigns (eg: Mather et al. 2004) have shown that sulphuric acid (H_2SO_4) is the dominant component of the particles. Aerosols present in the plume scatter TIR radiation according to the Mie law causing a net extinction of the radiance measured at the sensor. In order to test the effect of aerosol extinction on SO_2 retrievals with ASTER, the extinction coefficient of the aerosol were computed with MALUT (Clarisse et al, 2010) a fast and accurate Mie algorithm. These look-up tables were then used by Atmosphit to simulate the total radiance reaching the sensor in the five spectral bands and in the band ratio used in the algorithm. We considered a 400m thick layer containing varying concentrations of SO_2 and droplets composed of H_2SO_4 (in solution in water at 50% mass ratio), at an altitude of 1500m and a temperature of 275K. The effective radius of the particles is set to 0.5 μm, and the column amount of particles was varied from 0 to 10^8 cm^{-2}, according to the values reported in several studies based on sun photometers (Watson and Oppenheimer, 2001; Mather et al. 2004). Refractive indices of the H_2SO_4-H_2O mixture at 293K were taken from (Palmer et Williams, 1974). The simulated spectra (figure 3.10a) show clearly the broadband extinction of the aerosol. Figure 3.10b shows the effect of aerosol extinction in term of ΔSO_2 for retrievals using raw radiance, and radiance ratios. Sulfate aerosols extinction affects retrievals significantly, but retrievals using (B10+B12)/2B11 are five times less sensitive than radiance, making this ratio particularly interesting.

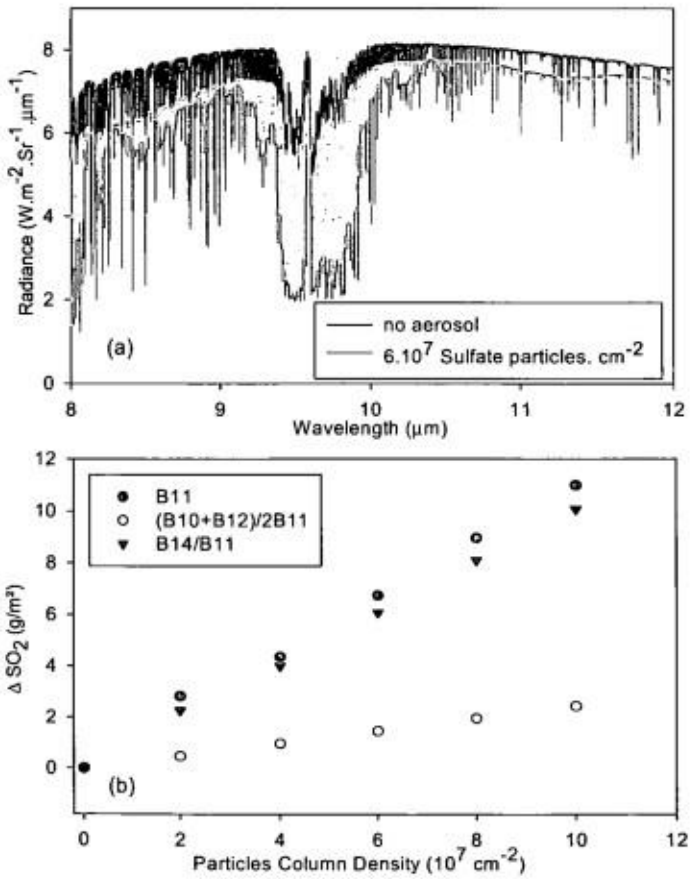

Figure 3.10: (a) Simulated radiance spectra for a Miyake-like atmosphere containing 400m thick layer rich in H_2SO_4 aerosol. The mass fraction of H_2SO_4 in the droplets is 50%. The column density of is 6 10^7 droplet/cm² and their effective radius is 0.5 μm. (b) SO_2 Bias induced by the presence of increasing abundance of H_2SO_4 aerosols.

3.5 Case studies

3.5.1 Miyake-jima

Starting in September 2000, Myake-jima emitted huge amounts of SO_2, passively degassed by a convecting magma body, through a newly formed caldera (Kazahaya et al, 2004). Maximal SO_2 fluxes peaked at >100,000 Tons/day in December 2000, before gradually declining to ~7000 Tons/day at the end of 2002.

An ASTER image (figure 3.11) was acquired during this high degassing period, on 1 April 2001 at 01h44 GMT (11h44 local time). Temperature and humidity profiles come from the radiosonde launched at 00H00 GMT from Hachiyo-jima, an island located 110 km south of the volcano. The map of the SO_2 column amount (figure 3.11b) is obtained by applying the retrieval scheme detailed above to the ASTER L1B image. This map shows a plume extending eastward from the volcano to a distance of 30 km, with the presence of concentrated puffs. An average source flux of 200kg/s (17300 Tons/day) is computed from this image, using a wind speed of 6.5m/s. Flux fluctuations associated to these puffs range to one third of the average value. Progressive dilution of the plume is observed with distance, resulting in homogenization and decreasing column amounts. In Figure 3.11c, the measurements of SO_2 fluxes are plotted versus the plume travel time (calculated as the crater-traverse distance divided by the wind speed). A general decrease of the flux is observed with plume ageing. A similar pattern is present on many images of Miyake-jima that we have analyzed. (See table 1). As the average value of SO_2 retrievals outside of the plume is slightly positive (0.037 g/m²), this decrease is probably not an artefact due to progressive dilution of the plume below detection limit. This decrease could be caused by SO_2 oxidation during plume transport and mixing with the atmosphere. The speed of SO_2 depletion in volcanic plumes is thought to depend strongly on the mechanism involved: slow gas phase oxidation by the OH radicals (McGonigle et al, 2004) or fast aqueous phase oxidation in aerosol droplets (Oppenheimer et al, 1998). An exponential regression applied to the time series of fluxes on 1st April 2001 yields a first order rate constant of about 8.7 10^{-5} s^{-1} , which is in the same order of magnitude as recent measurements in Montserrat by Rodriguez et al, (2008). Alternatively, column amount close to the vents might be overestimated due to sulfate aerosol absorption. Increased visible reflectance in the proximal plume on figure 3.11a supports the presence of high concentrations of liquid, probably H_2SO_4 rich, aerosol.

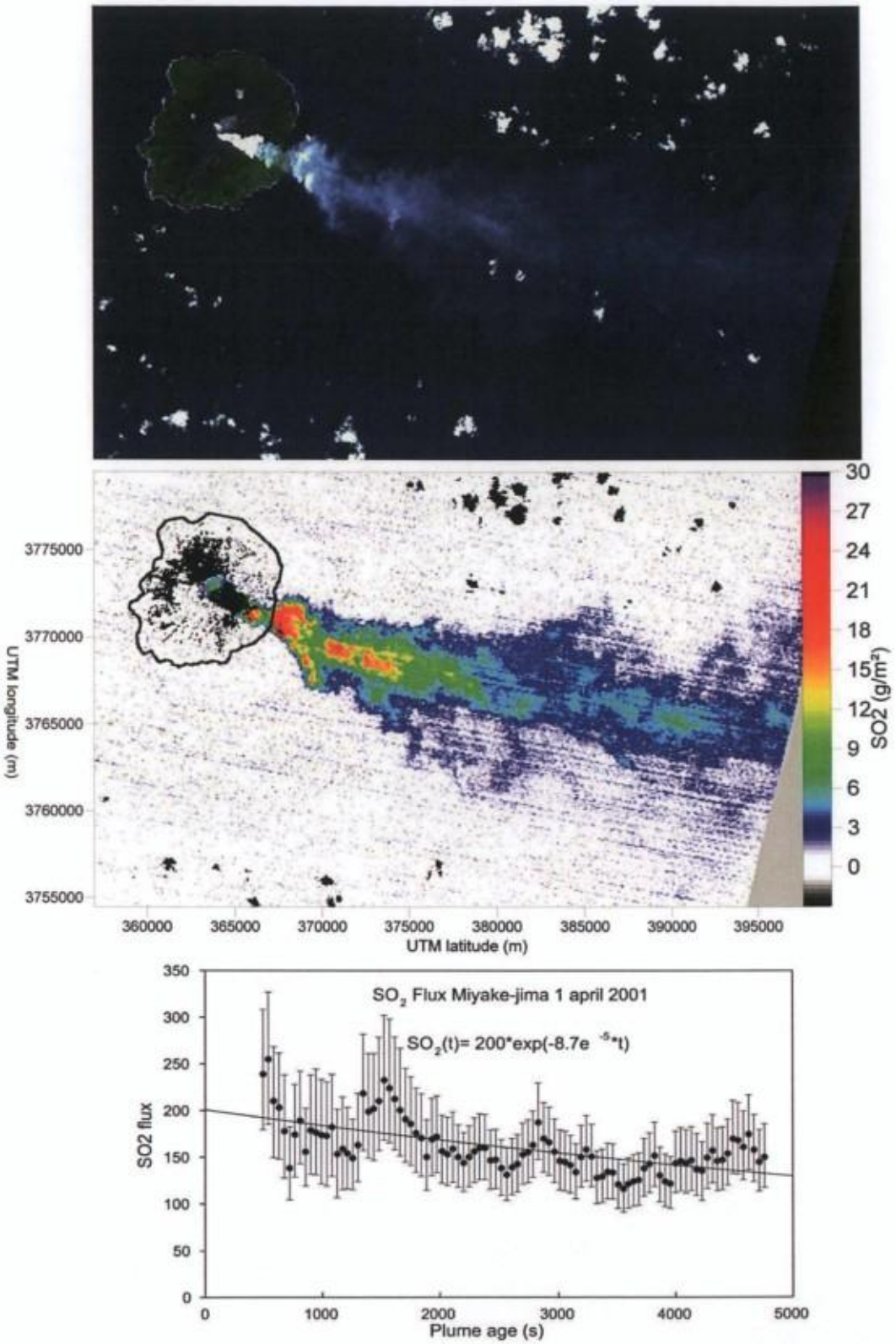

Figure 3.11: (a) ASTER VNIR natural colour image of Miyake-jima on 1st April 2001. (b) SO_2 column amount map produced after application of the algorithm (UTM coordinates, in meters). Cold or cloudy pixels appear as black spots. Horizontal stripping is a consequence of radiometric noise. (c) Evolution of SO_2 flux with plume age. Proximal profiles were removed because of the abundance of opaque clouds.

The image of 15 July (figure 3.12) illustrates a typical case where IR measurements are imprecise and inaccurate. Radiosonde profile shows a weak thermal contrast between the sea (T≈297k) and the warm atmosphere at plume level (293K at 1200 m). Furthermore, southerly wind disperses the plume in a direction sub parallel to the satellite track, making plume height measurements imprecise. Radiometric noise on SO_2 measurement is high (~4g/m²) and relative error due to imprecision in plume height becomes important (40%). Imprecision on the computed flux in this very unfavourable case amounts to (-50% +130%). However, automatic error estimation by the program successfully identifies these unfavourable cases.

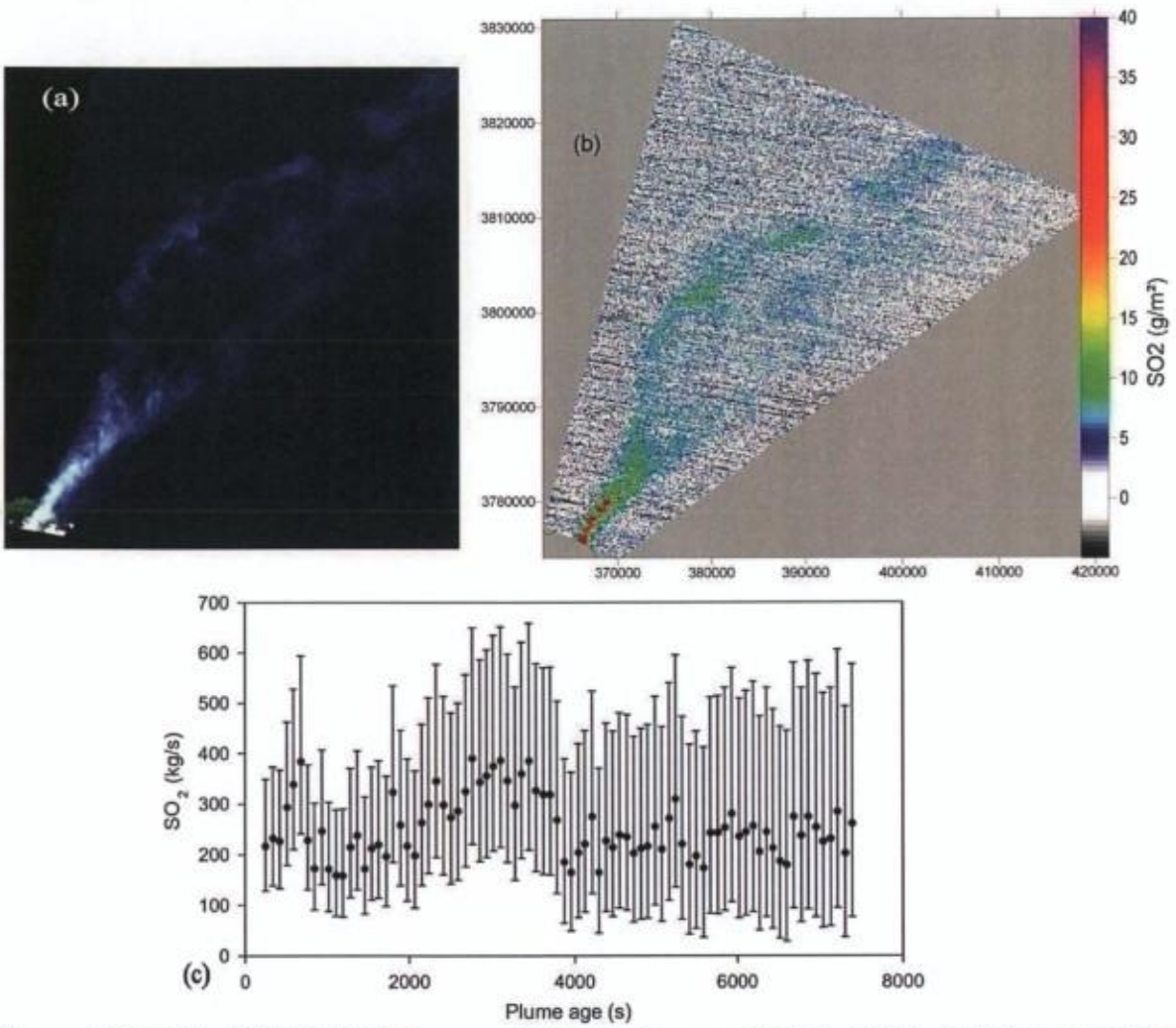

Figure 3.12: (a) ASTER VNIR image of Miyake-jima on 15 July 2001. (b) Corresponding SO_2 map. Due to low thermal contrast between the plume and the sea, NEΔSO_2 is high (~4g/m²) and dominates the image. (c) Time series of flux versus plume age.

A total of eleven ASTER images were analysed for Miyake-jima. The resulting SO_2 fluxes were compared to field measurements that where performed regularly with a COSPEC (Kazahaya et al, 2004). Due to the lack of simultaneity between ASTER and COSPEC, and to the short timescale variability of the field flux measurements series, this does not constitute a strict validation of the method. Despite of this, the retrieved SO_2 fluxes are generally in good agreement with the long term trend of COSPEC measurements, as shown in Table 1 and Figure 3.13.

Date and time Miyake-jima	Source Flux	Max Flux	Min Flux	Estimated Error	Rate Constant	COSPEC or DOAS	Detection Limit (3σ)
2000-11-08, 01:47	34800	57900	25200	+18000/-7000	~ 0*	29600	4.5 g/m²
2001-03-30, 12:58	23800	26400	13600	n.a.	$1.6\ 10^{-4}\ s^{-1}$	*22700*	2.6 g/m²
2001-04-01, 01:44	17300	22000	10000	+4500/-4000	$7.8\ 10^{-5}\ s^{-1}$	*19600*	1.1 g/m²
2001-04-15, 12:58	24200	34000	11000	n.a.	$1.3\ 10^{-4}\ s^{-1}$	*20600*	4.8 g/m²
2001-05-28, 01:37	13700	21300	5500	+3000/-2500	$1.0\ 10^{-4}\ s^{-1}$	25300	2.9 g/m²
2001-07-15, 01:35	16900	27500	7300	+20000/-8000	n.a.*	*15200*	6.6 g/m²
2001-08-23, 01:41	unexploitable due to near-zero thermal contrast						8.7 g/m²
2001-11-27, 01:38	13800	22700	5000	+3900/-2900	$3.2\ 10^{-4}\ s^{-1}$	16700	2.4 g/m²
2002-03-19, 01:35	5800	9900	2800	+1700/-1500	~ 0*	8100	1.9 g/m²
2003-04-07, 01:34	5800	7200	200	+3000/2000	$2.3\ 10^{-4}\ s^{-1}$	5700	3.1 g/m²

Table 1: Summary of ASTER measurements of SO_2 fluxes (in Tons per day). Source fluxes are calculated by applying an exponential regression to the time series of measurements, or by averaging all data when no clear trend can be distinguished. Ground data in italic are an average of the 2 closest measurements. (*) identifies cases where SO_2 depletion is insignificant or masked by plume puffing

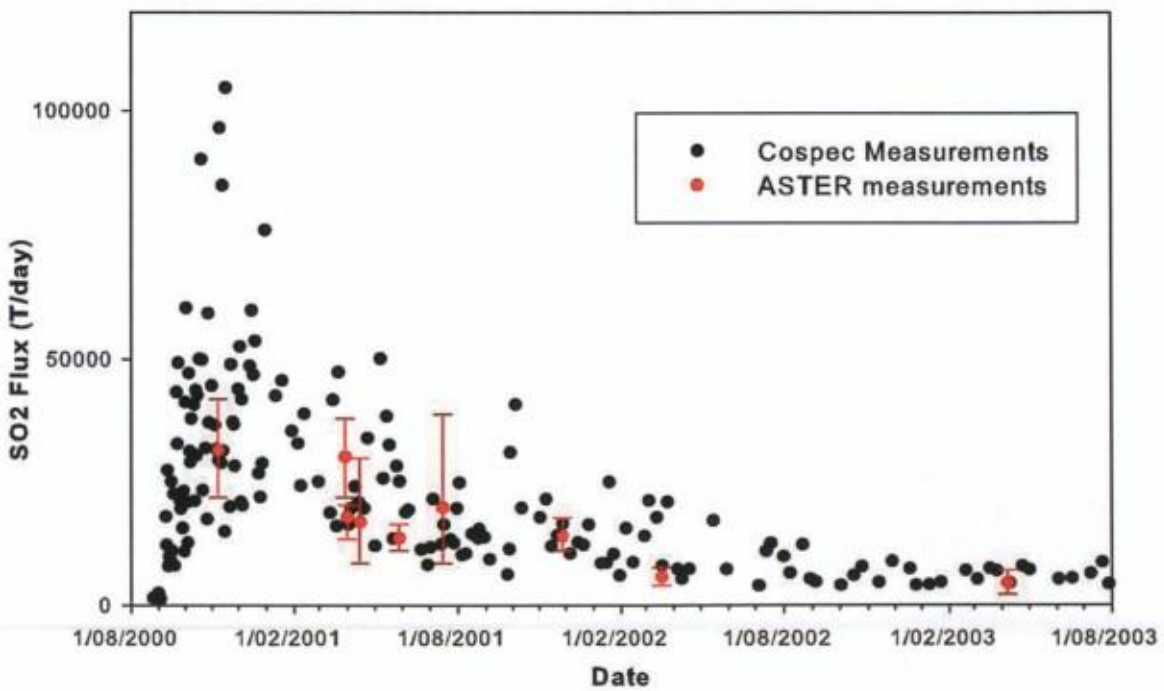

Figure 3.13: ASTER measurements of the SO_2 flux (in Tons per day) from Miyake-jima compared to the evolution of fluxes as measured by helicopter based COSPEC (Kazahaya et al. 2004).

3.5.2 Etna, 3 august 2006

Mt Etna is the highest (3330m) and most active volcano in Europe, with four flank eruptions and several tenths of summit eruptive events since the beginning of this century. Mt. Etna is also a permanent SO_2 emitter, with fluxes varying from 500 to 30000 Tons/days depending on the activity. The flux of SO_2 emitted by Mt Etna is monitored regularly since 1987 using COSPEC (Caltabiano et al, 1994) and permanently by the FLAME network since 2004 (Salerno et al, 2009a, 2009b). The network consists of five fixed scanning DOAS stations located on the Eastern and Northern quadrants of the volcano.

On 3 August 2006, Mt Etna was quiescently degassing between two eruptive episodes at the South-East Summit Crater. The radiosonde profile from Trapani (220 km west of the volcano) indicates a temperature of 281K and a relative humidity of 30% at 3200m, the estimated plume height. The SO_2 map in figure 3.14a shows a homogeneous plume without significant puffs. Radiometric noise, appearing as lines on the SO_2 map is more prominent for "sea" pixels, which have a colder surface temperature and hence a lower thermal contrast with the gas plume. It is interesting to note that no artefacts appear in the map in response to the change in topography (3300m of total height difference between the sea and the summit area of the volcano). This is a convincing evidence that the band ratio algorithm is insensitive to surface elevation, as suggested by theoretical simulations. Patterns in the SO_2 map in relation to emissivity are also extremely limited, which was not the case in retrievals published in (Pugnaghi et al., 2006) where vegetated appeared as positive SO_2 anomalies.

The time series of fluxes (figure 3.14b) show no significant decrease with plume age, indicating that the depletion of SO_2 is much slower than for Miyake-jima, as expected for a plume emitted in the dry free troposphere. The average flux measured by ASTER above the Etna_Milo FLAME station (EMIL) is 47 kg/s which compares rather well with the measurements of the station itself (51 kg/s). The wind speed and plume height used for flux calculations with both methods are respectively 9.5m/s and 3200m.

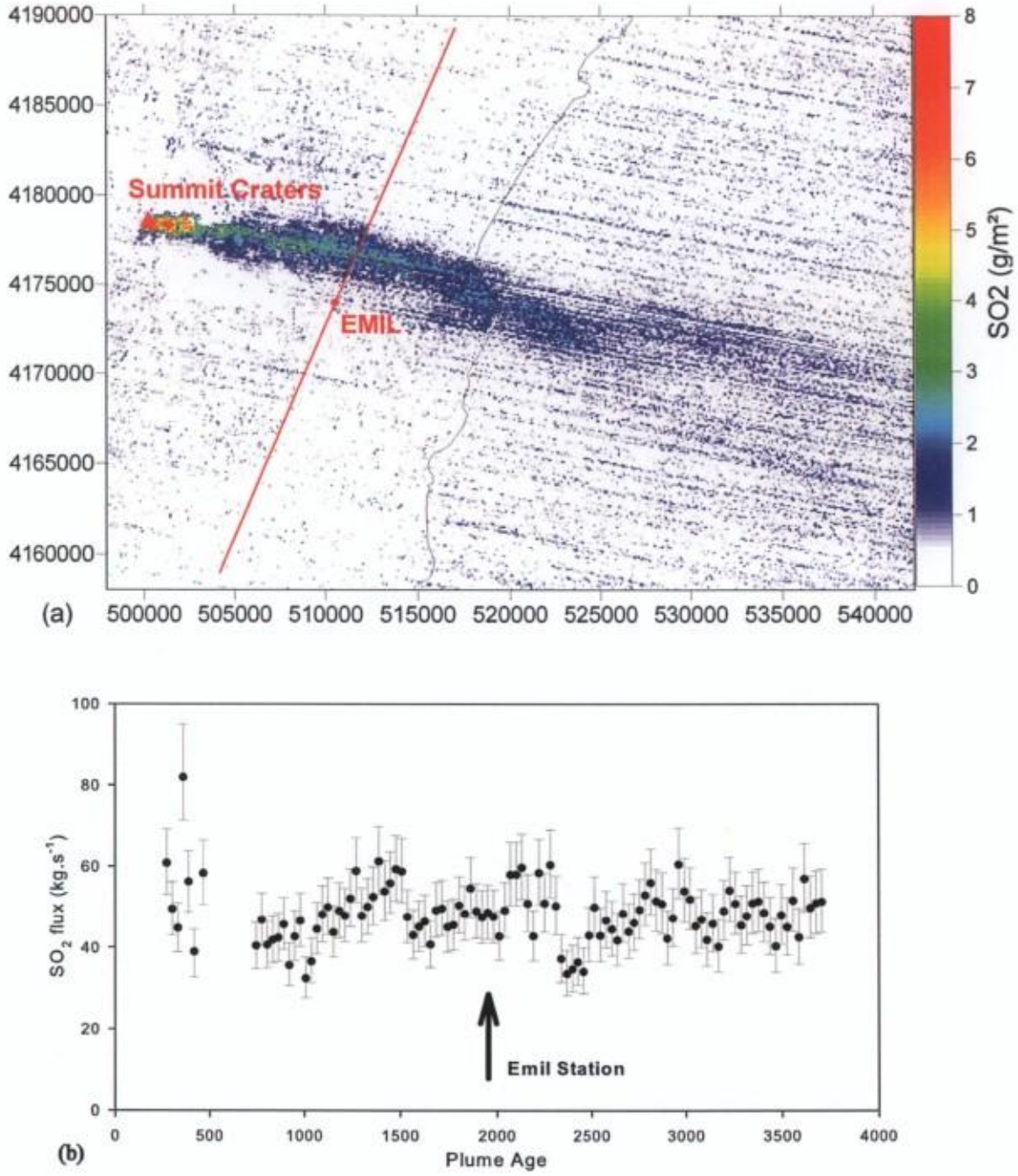

Figure 3.14: Etna, 3 August 2006 (a) SO_2 concentration map showing the location of the summit craters, coastline and the "EMIL" UV scanner station. Noise lines are more prominent above the sea than above the land, due to difference in thermal contrast. (b) Time series of SO_2 fluxes with plume age.

Stable atmospheric conditions and sustained constant degassing allowed the plume to be transported far from the volcano in a coherent way. Thanks to this, the column amounts close to the EMIL station were well above the detection limit of ASTER, allowing a comparison of the two datasets.

For doing this, FLAME measurements were geolocated using the following relations, which assume the plume as a horizontal layer of gas.

$X_i = X_0 + H_p.\sin(\alpha)/\tan(\theta_i)$

$Y_i = Y_0 + H_p\cos(\alpha)/\tan(\theta_i)$

Where X_0 and Y_0 are the UTM coordinates of the station, α is the azimuth of the scanning plan, θ_i is the scan angle and H_p is the plume height. As the plume was optically thin in the VNIR (hampering stereoscopic measurements), this last parameter was determined by fitting the position of the peak SO_2 concentration in the two datasets.

The comparison of FLAME and ASTER measurements of SO_2 column amounts is shown in figure 3.15. ASTER is, as expected, less precise than DOAS with standard deviation of 0.4g/m², but there is no systematic bias between the two measurements method, except for the right "wing" of DOAS measurements, which shows higher value than ASTER.

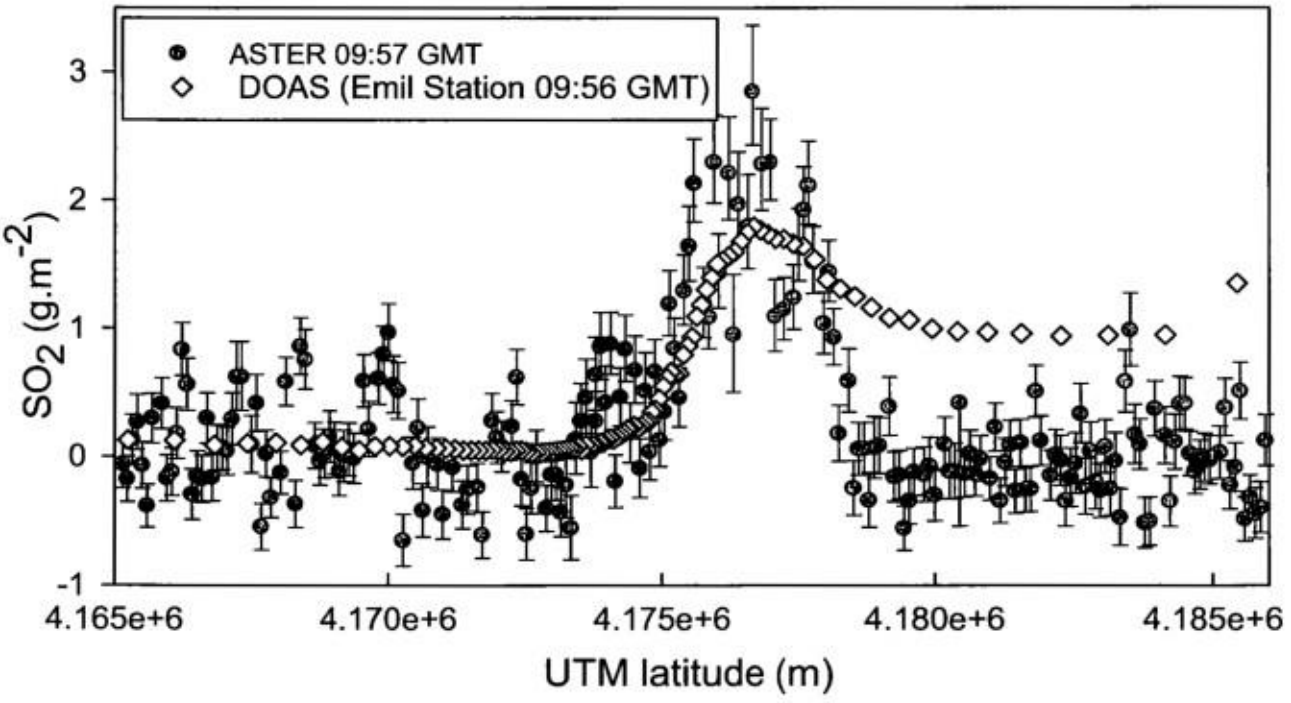

Figure 15: Comparison between measurements of SO_2 column amounts measured by ASTER and EMIL FLAME station in the plume of Etna on 3rd August 2006. (a): Pixel per pixel retrieval (b) Same data filtered with a 9x9 weighted average to reduce noise.

This is probably an artefact of DOAS due to a combination of geolocation inaccuracy and multiple scattering along a path close to the horizon. The effect of geolocation inaccuracy is illustrated schematically in figure 3.16. If the plume thickness is of the same order of magnitude as its width, the two relations used to geolocate the DOAS measurements become increasingly inaccurate at low

scanning angle. The lower portion of the plume appears shifted away compared to its real position, as shown on the figure.

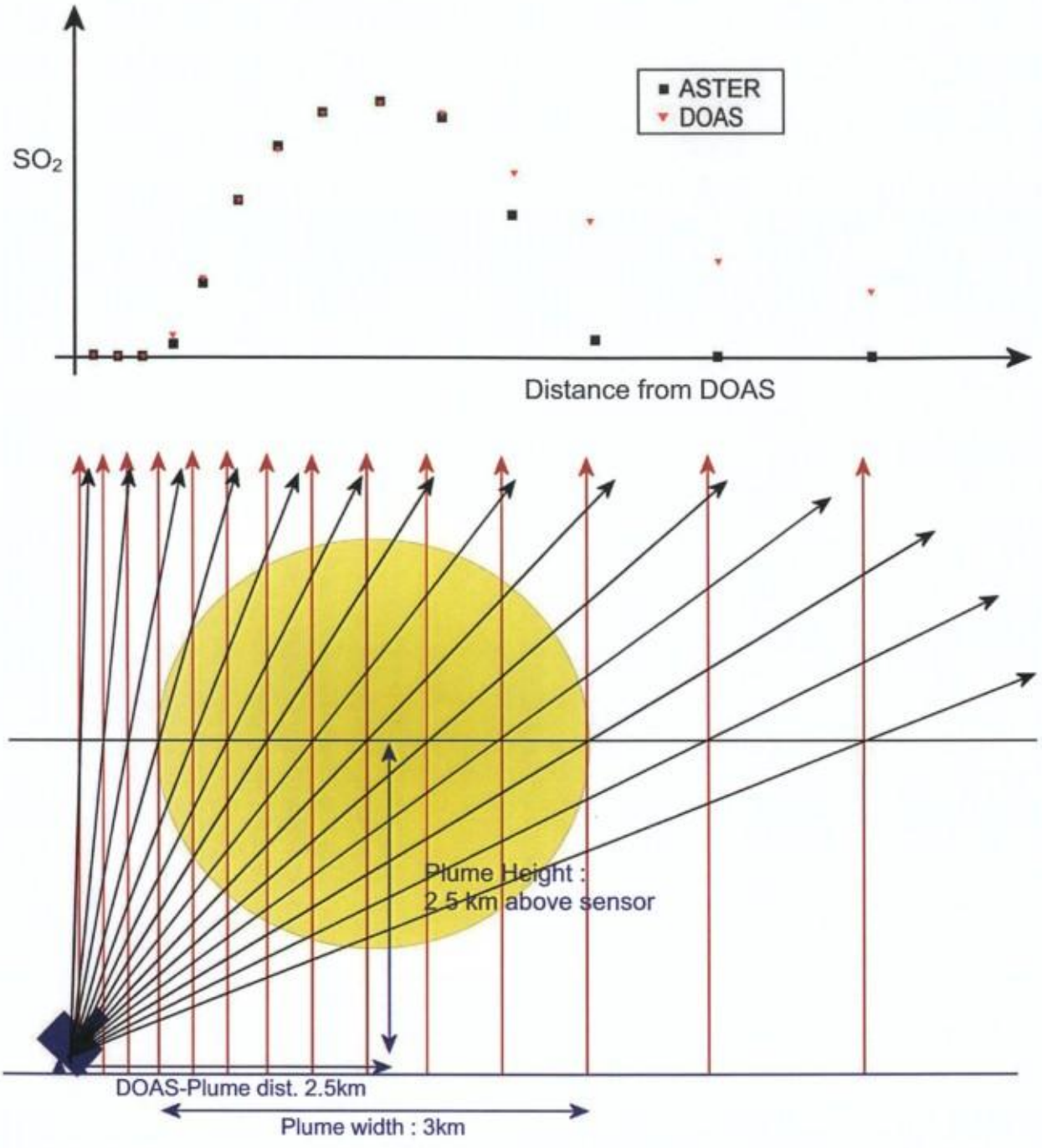

Figure 3.16: Schematic cross section along the scanning plan of the plume (in yellow) of Etna on 3 August 2006. The scheme shows the discrepancy in the geolocation of the DOAS angular measurements (materialized by the black arrows) compared with the nadir viewing geometry of ASTER measurements (vertical red arrows). This discrepancy arises from the use of the plane parallel approximation when the thickness of the plume is similar to its horizontal extension.

3.6 Conclusion

We have developed a new method to retrieve SO_2 fluxes with ASTER TIR multispectral images. This method relies on band ratio simulations and is directly applicable to any cloud free image of a degassing volcano, either island or continental. Theoretical simulations as well as application of the method to real cases demonstrate that the retrievals are straightforward and show no significant dependence on atmospheric humidity, surface altitude and emissivity. The impact of sulfate aerosol on retrievals with (B10+B12)/2B11 is also much reduced compared to retrievals with raw radiance. For these reasons, the band ratio method represents an improvement compared with previous methods relying on raw radiances. Thanks to its high multispectral ground resolution in the TIR, along with its ability to measure the plume's height and transport velocity, ASTER is capable of measuring, with a reasonable accuracy, SO_2 fluxes in small scale passive degassing plumes. Moreover, ASTER is an imaging sensor, and the 2D distribution of the SO_2 in the plumes can provide insights into its dilution and depletion. The long return time of ASTER presently limits its use for monitoring, but the retrieval scheme presented here is applicable to the images of the future Hyperspectral Infrared Imager (HyspIRI, JPL Publication 09-19, 2009). HyspIRI, planned for 2013-2016, will give an image frequency of 1-5 day thanks to its wider swath and continuous acquisition.

ASTER measurements of the SO_2 fluxes on Miyake-jima vary between 40000 and 4000 Tons/day and are in agreement with field measurements. Validation with column amounts measured simultaneously by automated scanning DOAS at Mt Etna was also successful. We emphasize that ASTER measurements achieve good accuracy and precision (25% or better) only when the thermal contrast between the plume and the underlying surface is high enough (>10°C). Hence, for low-altitude island volcanoes, precision and accuracy are increased in the winter, when the thermal inertia of the ocean maintains the surface waters significantly warmer than the atmosphere at the plume altitude. Conversely, over bare volcanic grounds, higher precision is achieved during the summer.

The good agreement between ASTER and COSPEC or DOAS results indicates that SO_2 measurements from ASTER can be used, with a reasonable confidence for long term evaluation of volcanic degassing. This is done in chapter 7 and 8 of this thesis, for two recent case studies of volcanic crises in Turrialba (Ecuador), and Eyjafjallajökull (Iceland).

The total SO_2 burdens measured with ASTER in the plumes of Miyake-jima are also detectable by other sensors such as OMI or MODIS. Cross-comparison of SO_2 retrievals between these sensors is of great interest as the spatial resolution of ASTER images represents the missing link between these sensor and highly local DOAS measurements. Comparison between ASTER and OMI is investigated in chapter 4, while chapter 5 deals with SO_2 retrievals using MODIS and their comparison with simultaneous and resampled ASTER retrievals.

Comparing SO_2 measurements from OMI and ASTER.

4.1 Introduction

Over the past 10 years, our ability to measure SO_2 emissions from volcanoes has been improved significantly thanks to the launch of two satellites.

The first one (chronologically) is ASTER (Pieri and Abrahms, 2002), a multispectral satellite sensor launched in 1999. ASTER observes the Earth in the thermal infrared (TIR) with the unprecedented resolution of 90m. It is flying on board satellite Terra on a sun synchronous orbit. ASTER has five spectral bands in the TIR that are labelled from B10 to B14 and are centered respectively at 8.29, 8.63, 9.07, 10.66 and 11.32 μm. The positions of ASTER's spectral bands are suited for measuring SO_2, and its high resolution allows detection and measurements of small plumes produced by non eruptive volcanic degassing.

The second one is OMI (Levelt et al., 2006), an imaging spectrometer that measures the backscattered ultra violet (BUV) radiance at a spectral resolution of 0.4nm and with a much higher ground resolution, 13 x 24 km at nadir, than its predecessors (TOMS, GOME and SCIAMACHY). OMI is carried by satellite Aura on a sun synchronous orbit that has a 3 hour delay over Terra. OMI's daily global coverage allows a rapid detection and quantification of the global SO_2 output from volcanic eruptions. Furthermore, its ground resolution is fine enough to detect, if not quantify, passive degassing.

A problem common to all remote sensing techniques of SO_2 retrievals is their lack of independent validation. As explained in the introduction of this thesis, it is difficult to validate remote sensing data with in situ measurements because these two groups of techniques do not yield the same physical quantities: path integrated concentrations for the former and volume concentrations for the latter. Rigorous validation is also lacking for satellite measurements because of the practical difficulties of acquiring simultaneous ground based data for objects as localized and dynamic as volcanic gas plumes. This chapter brings results of comparisons of SO_2 flux and column measurements from these two different sensors.

4.2 Retrieval methodologies

4.2.1 ASTER

The SO_2 measurements with ASTER were produced by applying the Band Ratio Algorithm to L1B images (for a full description of the algorithm, see chapter 3 of this thesis or Campion et al., 2010). This algorithm uses the measured values of surface temperature and radiance ratios to interpolate the SO_2 column amount (CA) in look-up tables containing simulated radiance ratios. The line-by-line radiative transfer code Atmosphit is used to compute the forward simulation of the TIR radiative transfer. A priori parameters needed for the simulations are the altitude of SO_2 plume, and the temperature and H_2O profiles in the atmosphere. The former parameter is measured on the stereoscopic VNIR images or assumed as the altitude of the crater. The latter two come from radiosonde data or the ECMWF model.

The main source of error in ASTER measurements of SO_2 CA comes from uncertainty on the thermal contrast between the gas plume and the underlying surface. A reasonably accurate knowledge of the plume altitude is thus necessary. When the thermal contrast is low, the retrievals become more imprecise, due to decreased signal-to-noise ratio, and less accurate. The detection limit of ASTER is also highly dependent on thermal contrast. For plumes presented in this study it varies between 0.3 and 1 10^{18} molec/cm².

The algorithm for ASTER retrievals calculates fluxes by summing the SO_2 CA of each pixels of profiles perpendicular to the user defined plume axis. This sum is then multiplied by the wind speed. The final flux value is calculated as the average of the fluxes measured on each profile.

4.2.2 OMI

The SO_2 measurements used for this work are the operational SO_2 data product, which is available publicly at http://disc.sci.gsfc.nasa.gov/Aura/data-holdings/OMI/omso2_v003.shtml. The product contains four values of SO_2 columns measured with four different a priori distribution profiles of SO_2 (see table 1). It is elaborated by the TOMS/OMI Sulphur Dioxide group, using two different algorithms: the Band Residual Difference Algorithm (Krotkov et al. 2006) for SO_2 residing in the planetary boundary layer and the Linear Fit algorithm (Yang et al, 2007) for any higher plumes.

Product	Representative profile	Center of Mass altitude	Algorithm
PBL_SO2	Boundary Layer	0.9km	BRD
TRL_SO2	Low troposphere	2.5km	LF
TRM_SO2	Middle troposphere	7.5km	LF
UTS_SO2	Tropopause	17km	LF

Table 4.1: The four values of SO_2 CA contained in the OMISO2 operational product, each value is retrieved using an a priori vertical distribution profile defined in column 2 and 3.

As all the plumes analysed for this study resided higher than 2.5 km, only data obtained with the Linear Fit algorithm (Yang et al., 2007) were used. This algorithm uses the TOMRAD radiative transfer model (Bhartia, 2002) for simulating the logarithm of the Sun-normalized BUV radiance measured by the satellite (written N_m). The TOMRAD model N is linearized as

$$N_m = N(\Omega_0, \Xi_0, R_0) + \Delta\Omega \frac{\partial N}{\partial \Omega}\Big|_{\Omega_0} + \Delta\Xi \frac{\partial N}{\partial \Xi}\Big|_{\Xi_0} + \left(\Delta R + \sum_{i=1}^{2} c_i(\lambda - \lambda_0)\right)\frac{\partial N}{\partial R}\Big|_{\Omega_0} + \varepsilon$$

Where Ω is the O_3column amount, Ξ is the SO_2 column amount, and R the Reflectivity. In the initial state for the linearization Ξ_0=0, and R_0 and Ω_0 are respectively the reflectivity and O_3 measured with OMTO3, the operational OMI algorithm for ozone retrieval. λ is the wavelength and λ_0 is the wavelength at which R_0 is retrieved by OMTO3. ε is the total error. The weighting functions of Ozone and SO_2, $\frac{\partial N}{\partial \Omega}$, and $\frac{\partial N}{\partial \Xi}$ are calculated using the finite difference method for several climatology averaged ozone profiles and the four a priori SO_2 profiles, while the reflectivity weighting functions $\frac{\partial N}{\partial R}$ is computed analytically. The linear fit algorithm finds the $\Delta\Xi$, $\Delta\Omega$, ΔR, and coefficients c_i that minimize the error between the modelled and measured values of N at ten discrete wavelengths of the BUV spectrum. The wavelengths, located at 310.80, 311.85, 312.61, 313.20, 314.40, 317.62, 322.42, 331.34, 345.40, and 360.15 nm, are those corresponding to the peaks and troughs of the SO_2 absorption spectrum, plus those used for OMTO3 algorithm. For each image analysed in this study, the final SO_2 CA was linearly interpolated from TRL_SO2 and TRM_SO2 at same altitude as that used for ASTER measurements.

Error on OMI measurements comes from several sources. The four most important sources are (Yang et al, 2009):

- The discrepancy between the assumed and actual altitude of the plume. For low to mid tropospheric plumes in a cloud free atmosphere, a 1km overestimation in the plume altitude yields typically a 20% underestimation of the SO_2 content.
- The subpixel heterogeneities in the SO_2 distribution.

- For high SO_2 CA, the absorption of SO_2 become increasingly non linear. Therefore the $\frac{\partial N}{\partial \Xi}$ weighting function becomes highly dependent on Ξ, inducing a significant underestimation of the actual CA. Yang et al. (2009) investigated this problem with more details, and developed an iterative linear fit algorithm, in which the $\frac{\partial N}{\partial \Xi}$ weighting function is recalculated iteratively until the fit converges. However iterative fit is not implemented in the operational algorithm due to computing time limitations.
- The plume altitude relative to the cloud cover. Plumes located under the cloud cover have their CA severely underestimated. However, OMI allows measurements of the mean cloud top pressure, and pixels having cloud tops higher than, say the TRL altitude, have their TRL_SO2 flagged as unusable in the final product

For this work, an IDL routine was created to compute SO_2 fluxes from OMI images in a semi automatic way. This routine needs as parameters the coordinates of the volcano and the plume altitude, transport speed v and direction θ. The first profile is defined as a portion of the column or row of pixels that contains the volcano summit. Then the routine automatically detects the center of the next profile as the pixel containing the highest CA adjacent to the volcano coordinates. Then the center of the plume is defined in the adjacent profile and so forth. The SO_2 flux through a profile is computed as the sum

$$F = (\sum_i \Xi_i l_i) * \cos\theta * v$$

Where Ξ_i and l_i are the SO_2 CA and length (or width) of the i^{th} pixel of the profile.

4.2.3 What should be compared?

4.2.3.1 Column amounts

Column amount is the direct quantity measured by the two methods. It refers to an amount of gas integrated over a vertical pathway between the surface and the satellite. The units commonly used for column amounts are g/m², molecules/cm², ppm.m and Dobson Units (DU). The latest two are non-SI units inherited from instruments that work with calibration cells. For the sake of standardisation and concision, we chose to use molecules/cm² throughout this article. The conversion factors from one unit to another are given in table 4.2.

From/To	g/m²	molec/cm²	ppm.m	DU
g/m²	1	9.41E+17	3.76E+02	3.50E+01
molec/cm²	1.06E-18	1	3.99E-16	3.72E-17
ppm.m	2.66E-03	2.50E+15	1	9.32
DU	2.86E-02	2.69E+16	1.07E-01	1

Table4.2: Conversion factors for the various units commonly used to measure SO_2 column amounts. Factors are given to convert units at a given line into units at a given column.

The ~2 hours delay between Terra and Aura overpass results in significant motion and dispersion of the plume outside of the 60km frame of the ASTER image. Therefore it is irrelevant to directly compare column amounts from the two sensors, as Thomas et al. (2010) have done for MODIS and OMI.

4.2.3.2 Masses

In the first ever attempt to daily monitor passive degassing from space, Carn et al (2008), reported daily and monthly-averaged SO_2 maps produced non-interactively with the OMI operational algorithm. They demonstrated the potential of that method for automatic identification of the source of the observed plumes. They also demonstrated that the time series of the total SO_2 masses correlated, sometimes even anticipatively, to seismicity and other field observations of the volcano behaviour. The correlation between the OMI-derived SO_2 masses and the DOAS-derived SO_2 was however relatively poor, even if showing some similar trends. They concluded that poorly constrained factors such as wind field, cloud cover and SO_2 lifetime in the atmosphere complicate the relationship between the two datasets.

4.2.3.3 Flux

The SO_2 flux is the information that is the most relevant from a volcanological point of view because it corresponds to the actual rate of magma degassing. Flux is an integrated quantity, so it should not depend on the spatial resolution of the method. Flux is thus clearly the quantity that makes intercomparison of SO_2 measurements the most feasible and relevant. However it should be noted that in some cases reliable flux cannot be derived by any of the two methods even if column amount measurements are accurate. These cases include stagnating plumes due to low/no wind situation, or sheared plumes due to non homogenous wind field. This is more common for plumes emitted at very low altitude, where topography exerts strong control on wind field, than for plumes emitted in the free

troposphere. The wind speed is an essential parameter for calculating SO_2 fluxes, whatever the instrumental technique used for measuring column amounts. It is possible to measure the wind speed, together with its height, using stereoscopic images acquired by ASTER in the visible. However, the method does not work if the plume direction is subparallel to the satellite track or if the plume is optically thin in the visible. In the absence of direct plume height and wind speed data we used the altitude of the emitting vent and the wind speed value of the ECMWF meteorological model. For this intercomparison work, we used the same wind speed and plume altitude values for the three different retrieval methods. This is especially important because these two parameters affect the accuracy of the retrieved flux.

4.3 Case Studies

4.3.1 Etna

Etna (Sicily, Italy), the highest and most active volcano in Europe, is also a powerful permanent emitter of SO_2, with fluxes ranging from 10 to 300 kg/s depending on its activity (passive degassing or effusive-explosive eruption). This volcano is equipped with a permanent array of scanning mini-DOAS (Salerno et al., 2009a) operating since 2006 and comprising a total of 7 stations.

On 3rd August 2006, a steady and sustained gas plume was drifting eastwards from the summit. This plume was measured by ASTER at 09:57, by OMI at 11:55 and by the EMIL station of the network, located in the village of Milo, every 4 minutes between 8:00 and 16:00. Figure 4.1 provides a summary of the comparison between the measurements by the two sensors. Both ASTER and OMI produce a very clear map of the SO_2 in the plume. Due to lower sensitivity and image width, only the proximal part of the plume is seen by ASTER, though at a much higher spatial resolution than OMI. The OMI measurements show a plume extending up to 300km from the volcano. Quantitatively, we observethat the ASTER flux is nearly 40% higher than OMI. Similar discrepancies 20-40% were observed for the four other Etna images analysed (see table 4.3, p.90). ASTER and the scanning DOAS are in excellent agreement with each other, not only for the fluxes, but also for the column amount (see chapter 3 section 5).

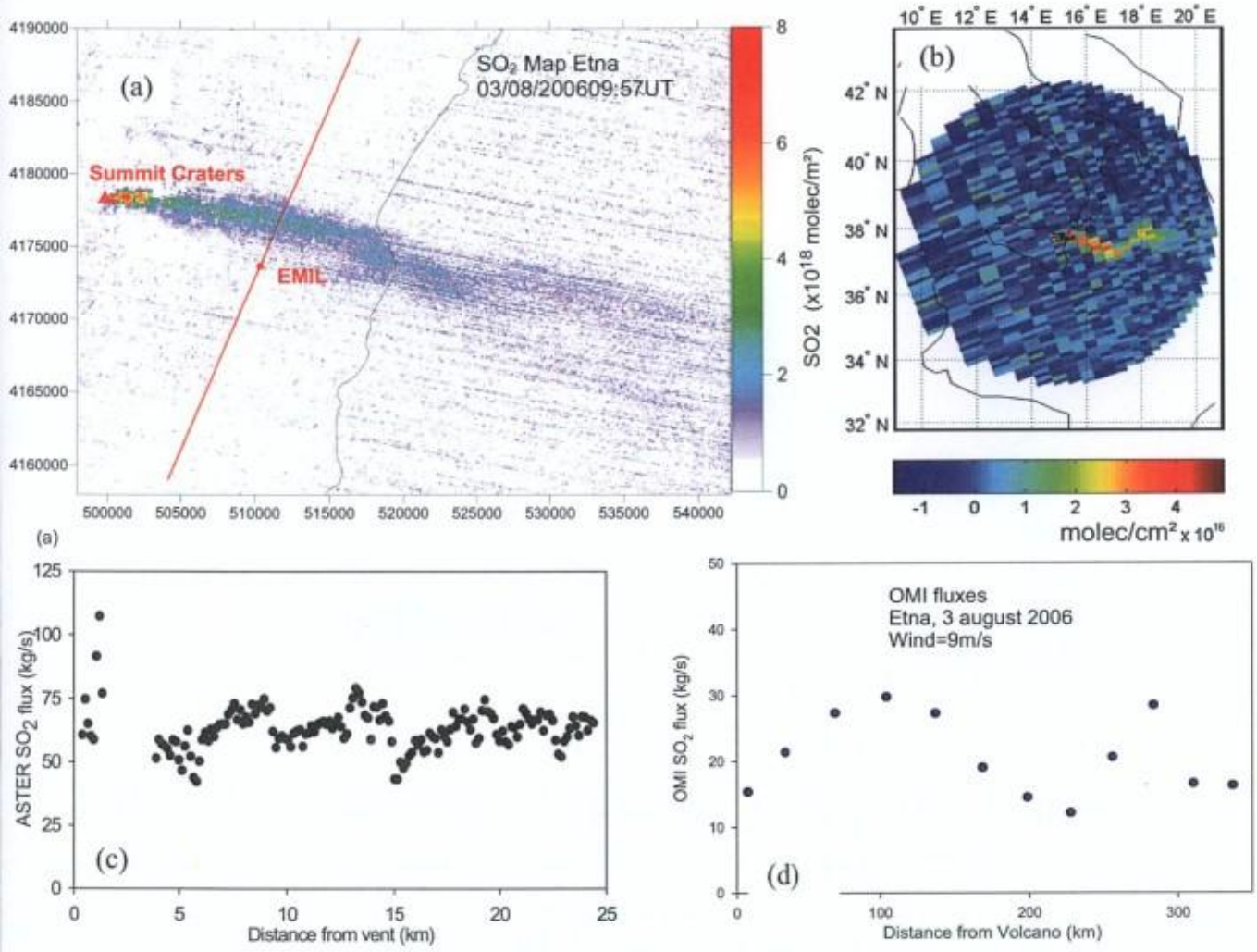

Figure 4.1: (a) ASTER SO_2 map of the passive degassing plume emitted by Mt Etna on 3 August 2006. (b)SO_2 map of the same plume measured by OMI 2 hours later. (c) Flux computed from the ASTER image as a function of distance to the vent. (c) Flux computed from the OMI image as a function of distance.

4.3.2 Nyiragongo

Nyiragongo volcano (1.52°S, 29.25°E, 3470m asl., Democratic Republic of Congo) has been hosting a permanent lava lake since 2002, and for several decades during the 20th century (Tazieff, 1977). The lava lake degasses huge amounts of SO_2, HCl and HF into the atmosphere (Sawyer et al., 2008). On 19 June 2007, ASTER captured the plume of Nyiragongo drifting southwards over the city of Goma (figure 4.2a). OMI captured the same plume 2 hours later (figure 4.2b). SO_2 flux measured by ASTER varies between 30 and 70 kg/s with an average value of 52 kg/s. The flux computed from the OMI image averages to 45 kg/s, with variation between 20 and 60, before slowly decaying. Whether this decay is due SO_2 depletion or dilution below detection limit is unclear. In this case thus, OMI and ASTER are in excellent agreement, because the measurement conditions for both sensors are close to optimal: high thermal contrast for ASTER (15 to 30K) and high amount of UV light for OMI because of the low latitude of the volcano.

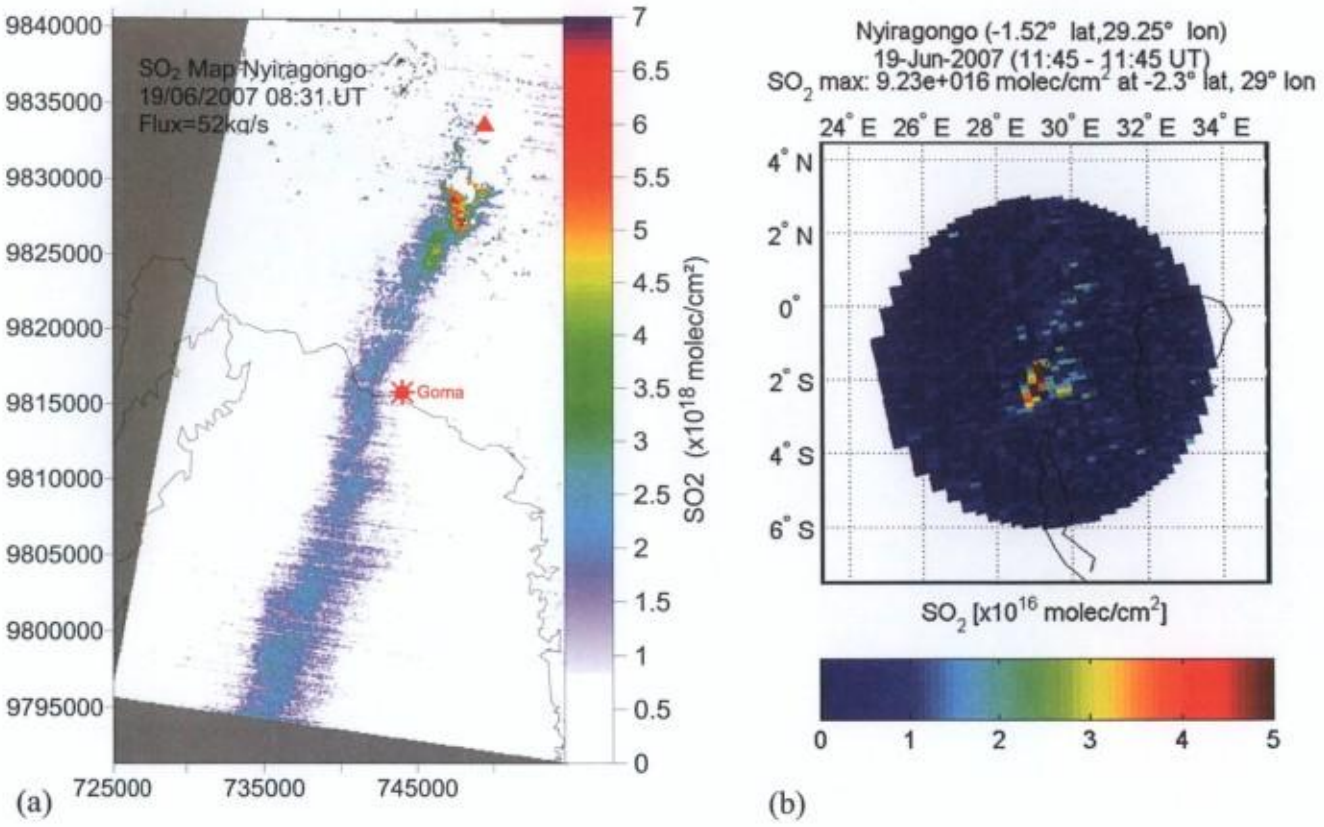

Figure 4.2: (a) ASTER SO_2 map of the passive degassing plume emitted by the lava lake of Nyiragongo on 19th June 2007. (b)SO_2 map of the same plume measured by OMI

4.3.3 Nyamuragira

Nyamuragira (1.408°S, 29.20°E, 3058m asl.), Nyiragongo's neighbour, is also a copious SO_2 emitter, but the SO_2 release occurs only during fissure fed effusive eruptions. Such eruptions affect the volcano every 2-3 years (e.g. Carn et al., 2003). Last eruption of Nyamuragira occurred from January 2 to February 2 2010. ASTER acquired an image of the eruption on the 18th January (Figure 4.3a). A steady plume can be seen on the SO_2 map, drifting westwards. Plume altitude was estimated to be 3500m by Goma Volcano Observatory volcanologist Dieudonné Wafula (pers. comm.). SO_2 fluxes computed from the ASTER image is 170 kg/s. This is considered as a high value, but, according to OMI records for January, the SO_2 emissions were considerably higher at the beginning of the eruption. OMI image, taken two hours later (figure 4.3b), yields a flux of 140 kg/s, which compares well to the ASTER value.

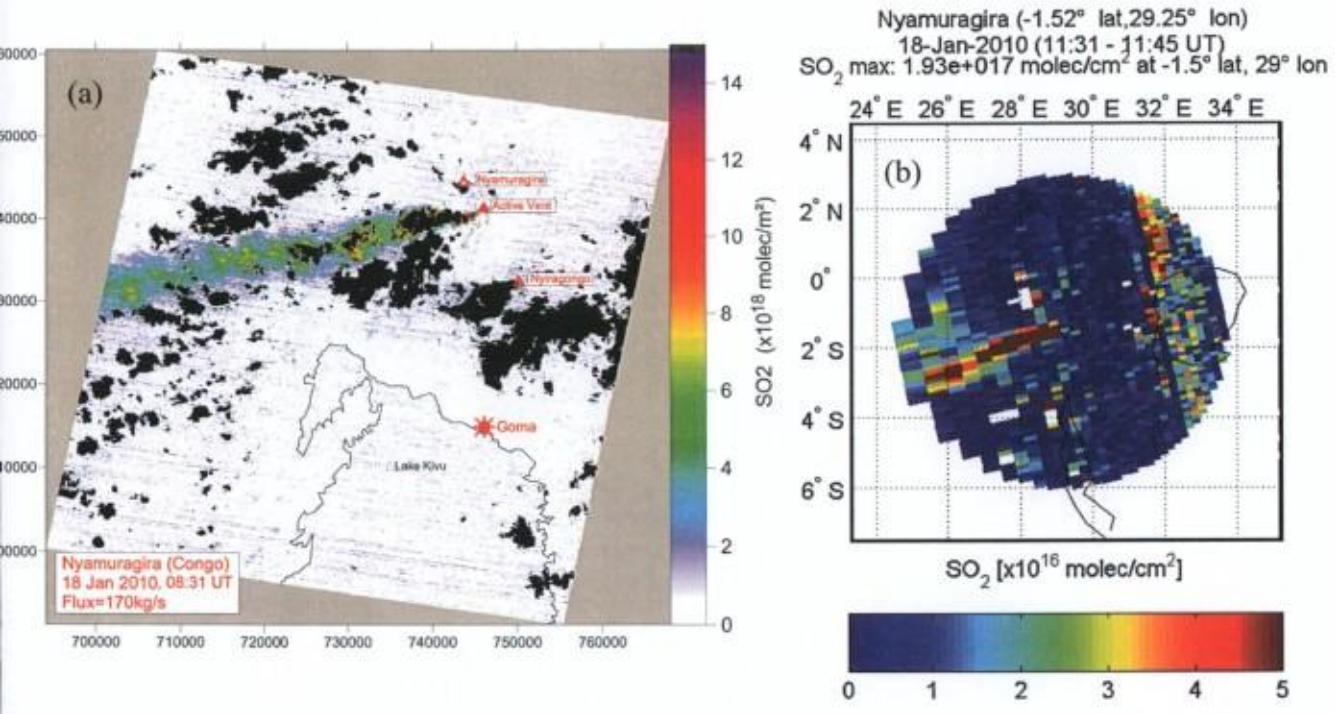

Figure 4.3: (a) ASTER SO_2 map of the plume emitted by the eruption of Nyamuragira on 18th January 2010. (b)SO_2 map of the same plume measured by OMI

4.3.4 Anatahan

Anatahan volcano (16.35°N, 145.67°E,790m asl., Mariana Islands) experienced its first historic eruption in 2003 followed by a long period of episodic eruptive activity. If the initial eruption consisted mostly of powerful explosive phases, the later activity was less explosive and involves strombolian activity, intracalderic lava flows and passive degassing. (BGVN of the Smithsonian Institution, 2003-2009, http://www.volcano.si.edu/world/volcano.cfm?vnum=0804-20=&volpage=var) Satellites retrievals with TOMS and AIRS during the initial explosive phases (Wright et al., 2005), as well as limited ground based measurements (Hilton et al., 2007) point Anatahan as a strong SO_2 emitter. Indeed fluxes measured with ASTER are extremely high, 800kg/s on the 6th February 2005, 400kg/s on the 27th April 2005, and 130kg/s on the 14th June 2005.

On 6th February 2005, the plume was drifting South-Eastward at a speed of 8.5m/s at an altitude of 2000m (measured on the stereoscopic pair of visible image), and can be tracked over the entire image (>60km). Huge column amounts are retrieved in the plume (figure 4.4, and the computed flux, 800kg/s, is the highest ever measured with ASTER. The flux computed from the operational SO_2 product of OMI is significantly lower, reaching "only" 250 kg/s. The possible cause of this is discussed later (p.90)

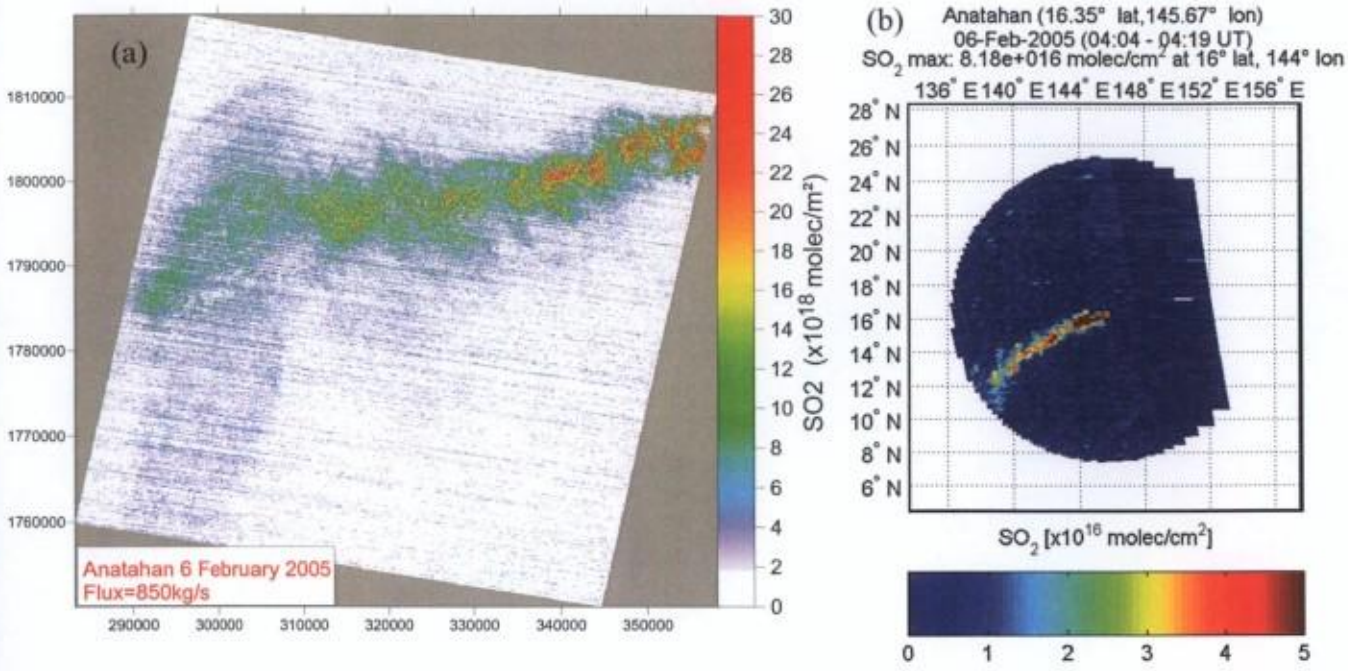

Figure 4.4: (a) ASTER SO_2 map of the passive degassing plume emitted by Anatahan on 6th February 2005. (b)SO_2 map of the same plume measured by OMI

4.3.5 Popocatépetl

Popocatépetl (5426m asl., 19.02°N,98.62°W, Mexico) has been emitting high but variable SO_2 flux since its reawakening in 1994 (Delgado et al., 2001; Delgado, 2008). Even if the fluxes have somewhat decreased since the peak activity in 1997-2002, values up to 50kg/s are still encountered on some days. The plumes are emitted in the high troposphere, several thousand meters above ground level. This makes them easily detectable and reliably measurable by satellites sensors. On 15 December 2007 a medium sized plume was drifting south-eastwards. ASTER image yields an average flux of 24 kg/s (higher values in the proximal parts of the plume might be due to plume stagnation downwind of the volcano). OMI image in figure 4.5b yields a very similar flux (22kg/s), and nicely captures the shift of the plume direction at a distance of ~100km from the volcano (from south-east to east). At Popocatépetl, the SO_2 fluxes show an excellent agreement between the OMI and ASTER on every image that we analyzed. This is likely due to the high altitude of the plume (5500m), which makes retrievals with both instruments more accurate.

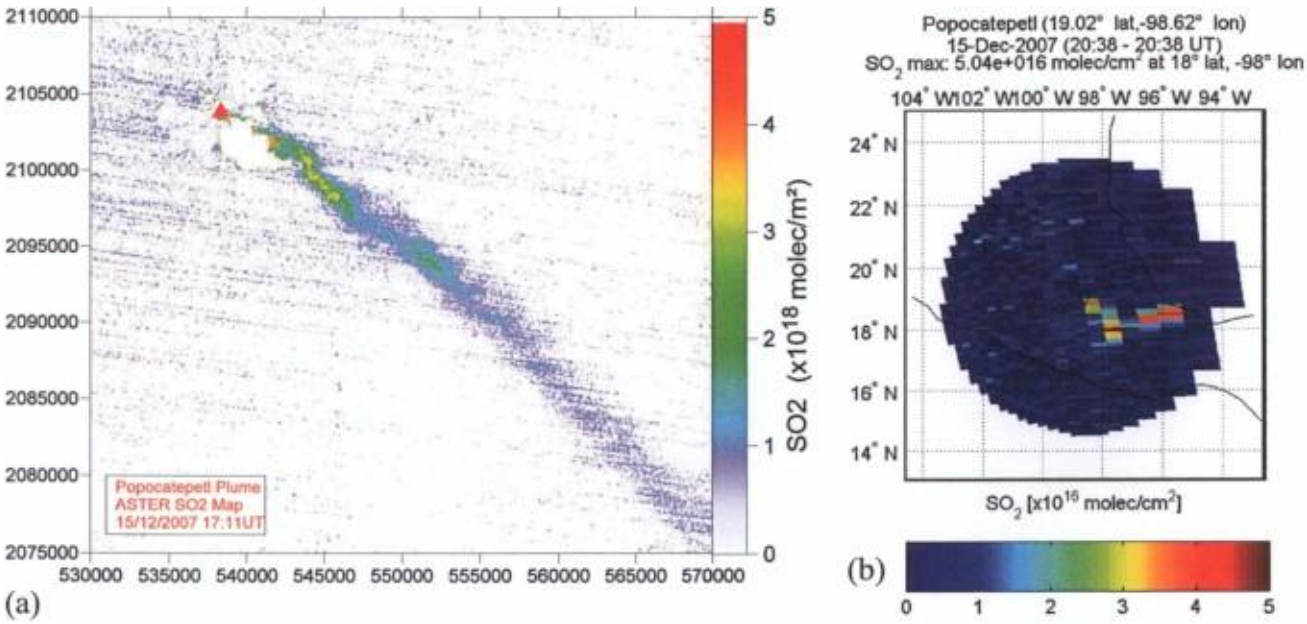

Figure 4.5: (a) ASTER SO_2 map of the passive degassing plume emitted by Popocatépetl on 15th December 2007. (b)SO_2 map of the same plume measured by OMI

4.3.6 Masaya, 9th February 2005

Masaya (11.98°N, 86.16°W,635m asl.) is a low lying shield volcano located in a 10km wide caldera in Nicaragua. It has been a strong and permanent SO_2 emitter since at least the 1970s, with typical flux value ranging between 5 and 20 kg/s (e.g. Stoiber and Williams, 1988, Delmelle et al. 2001). Massaya activity appears to be essentially passive degassing through a glowing vent, without any magma emission at the surface, and only rare and minor phreatic eruptions related to episodic conduit sealing (Duffel et al., 2003).

Due to the low altitude of the volcano and its situation in the subtropical zone, Masaya plume is a difficult target for satellite measurements, while flux of 10 kg/s can be easily detected at higher elevation volcanoes such as Popocatépetl. The case study of Masaya on 9 February 2005 illustrates an example of low altitude plume close to the detection limit of current satellites. The ASTER SO_2 map, although a bit noisy, shows clearly the SO_2 plume, constituted of several puffs. The puffing behaviour of Masaya is a well known characteristic of this volcano and has recently been studied quantitatively by (Branan et al., 2008). The computed flux fluctuates between 5 and 10 kg/s, in the range of the fluxes commonly measured on that volcano in the recent years (e.g. Williams-Jones et al., 2003, Nadeau et al., 2009). The SO_2 map of OMI, on the other hand, does not show any SO_2 plume emanating from Masaya.

The reason of this failure is probably threefold:

- The plume is very low (<1000m asl) and OMI's sensitivity decreases drastically for low altitude plume.
- The plume drifts over a low reflectance surfaces (the rather bold volcanic ground and, at further distance, the Pacific Ocean), which reduces the signal to noise ratio available to OMI.
- The plume dimensions are extremely small (a few hundreds of meters wide times a few km long) compared to OMI's pixel.

4.3.7 Eyjafjallajökull 3rd may 2010

The eruption of Eyjafjallajökull (63.63°N, 19.62°W, 1666m asl., Iceland) was a complex sequence of events (see Sigmundsson et al., 2010 for a review) that started with a mild fissural basaltic eruption on the west flank of the volcano. In a second, much more powerful phase, the eruptive activity migrated in the ice filled central crater of the volcano. This second phase started with violent hydromagmatic explosions and later became of strombolian-vulcanian type when magma became insulated from the melt water. ASTER took many images during all the different phases of the eruption, which are exploited for SO_2 measurements in chapter 8 of this thesis. However, one ASTER image, acquired on 3rd may 2010 turned out to be difficult to analyse, with the resulting SO_2 map (figure 4.7a) being heavily affected by radiometric noise. On the contrary, the OMI SO_2 map from the same day was showing an impressive SO_2 rich plume (4.7b). On this day, the plume was drifting just above a stratocumulus deck, whose temperature is only 5K warmer than the volcanic plume. Therefore, the thermal contrast is very low and the net absorption of the gas plume is drowned in the instrumental noise. On the contrary the cloud deck provides a highly reflective surface that allows an excellent Signal to noise ratio for OMI.

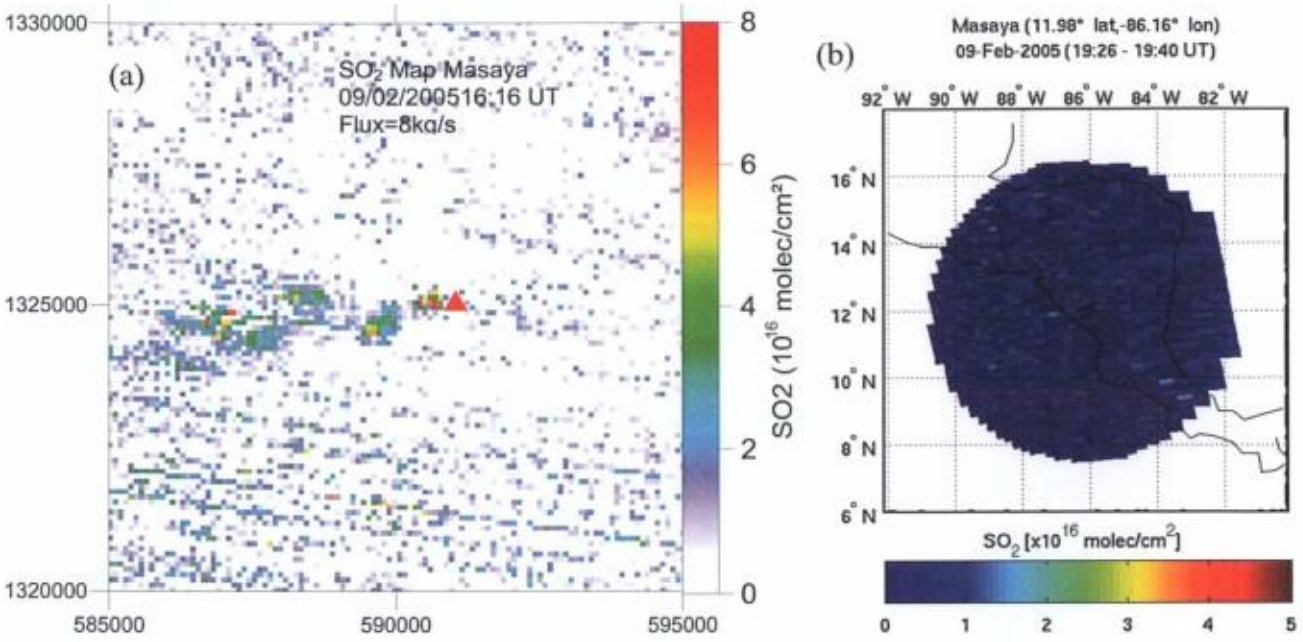

Figure 4.6: (a) ASTER SO_2 map of the small (a few hundred meters wide by a few km long) plume of Masaya on 9th February 2005. (b)SO_2 map of the same plume measured by OMI

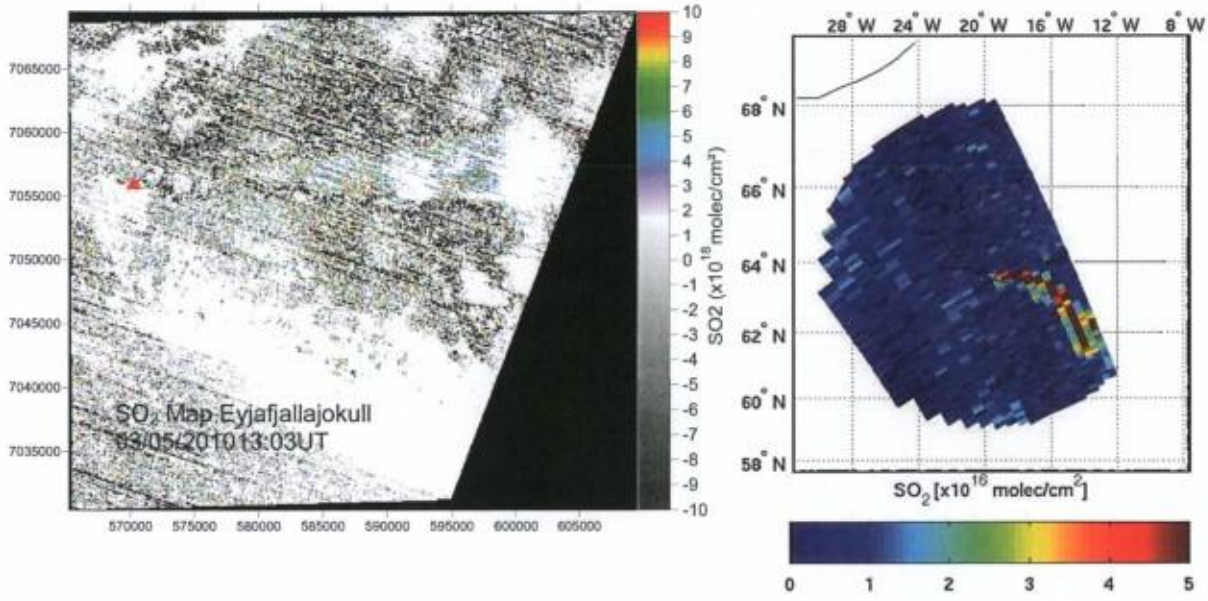

Figure 4.7: (a) ASTER SO_2 map of Eyjafjallajökull plume on 3 May 2010. Radiometric noise dominates the scene due to very low thermal contrast between the underlying cloud deck) and the plume. The plume is barely discernable. (b) The OMI SO_2 map on the same day is showing the massive plume.

4.4 Discussion

4.4.1 SO_2 maps

SO_2 maps from the two sensors show that the dispersion patterns for the plume do not change significantly during the time interval between the two overpasses. SO_2 column amount on individual ASTER pixels maps are systematically higher than on OMI pixels, by two orders of magnitude. This is easily explained by the huge difference in pixel size between the two sensors ($8.1\ 10^3$ m^2 versus 3-5 10^8 m^2). Similarly, Thomas et al., (2009) reported differences by up to 20 times between the MODIS (resolution=$10^6 m^2$) and OMI SO_2 maps. Small scale passive degassing plumes such as those reported in this study are nearly always subpixel to OMI, and the signal is thus "diluted" over the total area of the pixel. ASTER maps resampled to OMI resolution have column amount of the same order of magnitude as the OMI maps. However, since the plume has moved several tens of km between the two overpasses, this resampling is not very meaningful.

4.4.2 SO_2 fluxes

The mean fluxes of all the images analysed so far with both OMI and ASTER are represented on a scatter plot in figure 4.8 and also summarised on table 4.3. When performing a linear regression on the data set (excluding the obvious Anatahan outlier which is discussed separately), the regression line is rather close to 1, and a good correlation coefficient R^2=0.9156 is found. This is a very positive result for the accuracy of both retrieval methods, considering the profoundly different wavelengths and ground resolution of the two sensors. In the details however, ASTER tends to slightly overestimate OMI, as shown by the y-intercept of -4kg/s and the slope of 0.95, slightly inferior to 1.

Volcano	date	ASTER mean flux Kg/s	wind (m/s)	Plume Height (m)	OMI mean flux (kg/s)	Flux DOAS (kg/S)
Etna	3/08/2006	48	9	3200	22	52
	12/08/2006	35	17	3300	21	nd
	30/07/2007	28	10	3300	nd	
	16/09/2007	17	6.5	3300	14	8
	21/06/2008	21	5.6	2600	15	27
Nyiragongo	19/06/2007	52	10	3500	46	
Nyamulagira	18/01/2010	168	8.5	3500	140	
Anatahan	6/02/2005	820	8.5	2000	200	
	27/04/2005	450	2.8	2600	nd	
	14/06/2005	130	6.5	2800	135	
Popo	2/03/2007	17	6	5500	18	nd
	15/12/2007	24	8	5500	22	17
	2/01/2009	14	6	5500	12	15
	26/03/2010	24	13	5500	20	36
Masaya	09/02/2005	8	10	1000	undetected	
Eyjafjallajökull	03/05/2010	unexploitable	15	4000	170	

Table 4.3: Summary of the all the case studies of ASTER-OMI comparisons. Flux value from ground simultaneous based scanning DOAS are indicated if available

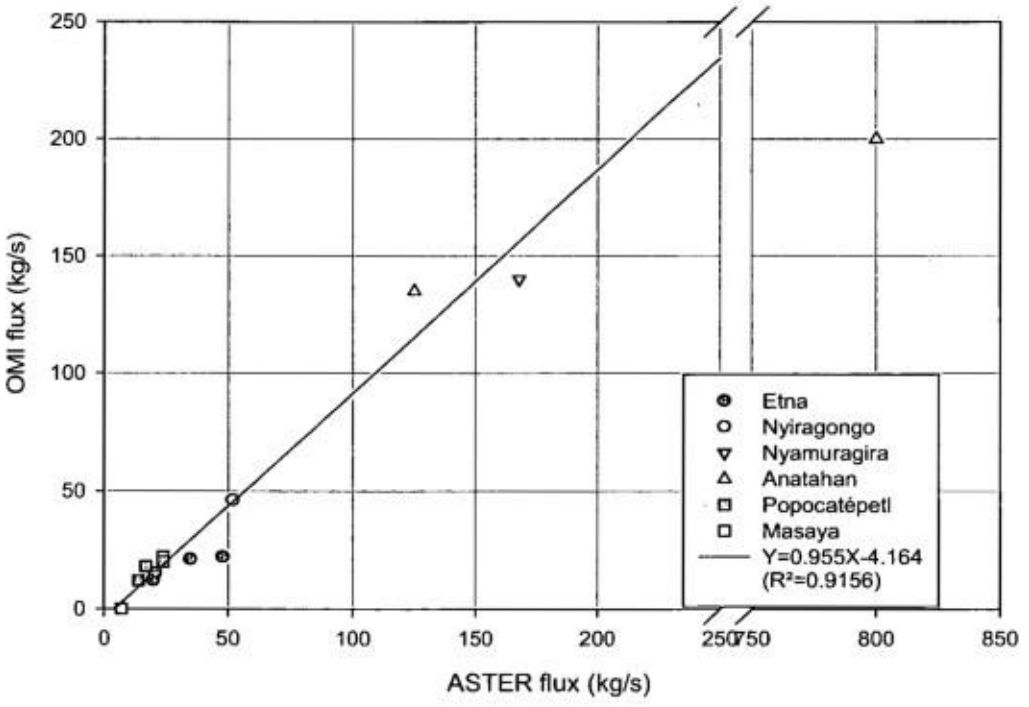

Figure 4.8: OMI fluxes as a function of ASTER fluxes on pair of images acquired on the same day. The regression line was calculated for all the images analyzed in this study except that of Anatahan on 6 February 2005 (see sections 4.3.4 and 4.4.3)

4.4.3 The Anatahan Outlier

A significant discrepancy is observed between ASTER and OMI for the fluxes in the plume emitted by Anatahan on 6 February 2005 (see section 4.3.4 and figure 4.8). The flux computed from ASTER is four times higher than that of OMI, 820kg/s versus 200kg/s. This contrasts with the good agreement observed on all the other cases examined so far. What differs in this plume compared to the others is that the column amounts retrieved by ASTER (if accurate) are extraordinarily high. At such high column amounts, the absorption of UV light by SO_2 is highly non-linear, and such plumes are optically thick in those wavelength. This causes significant underestimation by the linear fit algorithm. The non linearity of absorption is less an issue in the TIR because the absorption coefficient of SO_2 at these wavelengths is two orders of magnitude lower than in the UV. It would be interesting to check if the discrepancy between OMI and ASTER on this specific case would persist after applying the iterative linear fit (see section 4.2.2 and Yang et al., 2009) to the original OMI image.

4.4.4 Detection Limit

We analyzed images from a number of persistently active volcanoes known to emit low SO_2 fluxes, including Stromboli (Italy), Villarica (Chile), Merapi (Indonesia) and Sakura-jima (Japan), with negative results (i.e. no plume identified). Based on literature data on the typical SO_2 flux emitted by these volcanoes and on the results presented in this study, we estimated that the value of 5kg/s should be considered as a lower bound for SO_2 flux measurement using the current space based sensors. Improving this detection limit by future sensors can be achieved mainly in reducing the pixel size, which is the main limiting factor for OMI, and in diminishing the radiometric noise, which is the main limiting factor for ASTER.

4.5 Conclusion and perspectives

This study shows that the images of both ASTER and OMI can be used to measure SO_2 fluxes in small (subpixel in the case of OMI) plumes produced by moderate to strong passive degassing. The two sensors produce generally equal performances and their flux measurements are generally in good agreement with each other. In the detail ASTER will perform better than OMI for low lying plumes, especially if the plume drifts over sun warmed dark volcanic ground, as for the Masaya and Etna case studies. Conversely, OMI will perform better than ASTER for plumes that are drifting above a low cloud cover. Indeed, compared to a cloud clear scene, a cloudy scene provides a better reflectivity but a lower thermal contrast. In those cases, OMI will have a better signal to noise ratio and ASTER a worse one. Therefore, the BUV and TIR infrared sensors are highly complementary for measuring volcanic SO_2. The current abilities of space based sensors to measure the SO_2 flux is currently limited by ground resolution for OMI and imaging frequency for ASTER.

The future BUV sensor TROPOMI, with a pixel size of 10x10km, should allow significant progress in term of detection limit. Similar improvement of sensitivity in the TIR will be provided by the future HyspIRI sensor, which will have the same spectral characteristics as ASTER but a lower detector noise and an even smaller pixel size (60x60m). In addition, HyspIRI will have a much wider (400km) and continuous field of view, which will provide a global coverage in less than 5 days.

Chapter 5: Estimations of SO_2 with MODIS and comparison with ASTER

5.1 Introduction and previous works

MODIS, the MODerate resolution Imaging Spectroradiometer is a sensor that observes the Earth in 36 spectral bands spanning the visible to the thermal infrared (from 0.62 to 14.5μm). One MODIS is flying on Terra spacecraft, providing simultaneous images to ASTER, while the other is on board Aqua, thus acquiring images simultaneously to AIRS and sub-simultaneously to OMI (15minute delay). MODIS is a whiskbroom sensor and provides 2330 km wide images with a nadir resolution 1000m in the thermal infrared. The two MODIS achieve together a daily global coverage (and an even more frequent coverage of high latitude regions). More technical details can be found on the NASA webpage dedicated to MODIS: http://modis.gsfc.nasa.gov

In a very optimistic paper, Watson et al (2004) presented the opportunities offered by MODIS to retrieve several species emitted by volcanic activity: volcanic ash, ice particles, sulfate aerosols and sulphur dioxide. Among MODIS spectral bands, two of them are sensitive to SO_2 absorption in the thermal infrared (cf. figure 5.1).

Band 29 covers the v1 absorption bands of the SO_2 at 8.4 μm. Band 29 is rather similar to ASTER's B11. However it is slightly wider and shifted by ~0.1μm towards shorter wavelengths. This makes MODIS Band 29 a bit more contaminated to H_2O absorption than ASTER's B11. The retrieval scheme of Watson et al. is adapted from Realmuto et al (1994, 1997). They express the radiance reaching the satellite as

$$R_s=(\varepsilon_0 B(T_0) + (1-\varepsilon_0).R_d)\tau_a + R_u \qquad (5.1)$$

This equation is a synthetic writing of equation 2.13, where τ_a is the total atmospheric transmittance, R_d is the downwelling sky radiance reaching the ground and R_u is the total radiance emitted upwards by the different layers of the atmosphere. Watson et al., 2004 use the MODTRAN radiative transfer code to simulate R_d, R_u, and τ_a as functions of SO_2 column amount (CA) for a given temperature and H_2O atmospheric profile. They apply this equation to measure the surface temperature with bands 31 and 32, which are not affected by SO_2. In a second stage the measured surface temperature is reinjected into equation 5.1 and SO_2 is fitted to obtain the least difference between the modelled and measured Band 29 radiance.

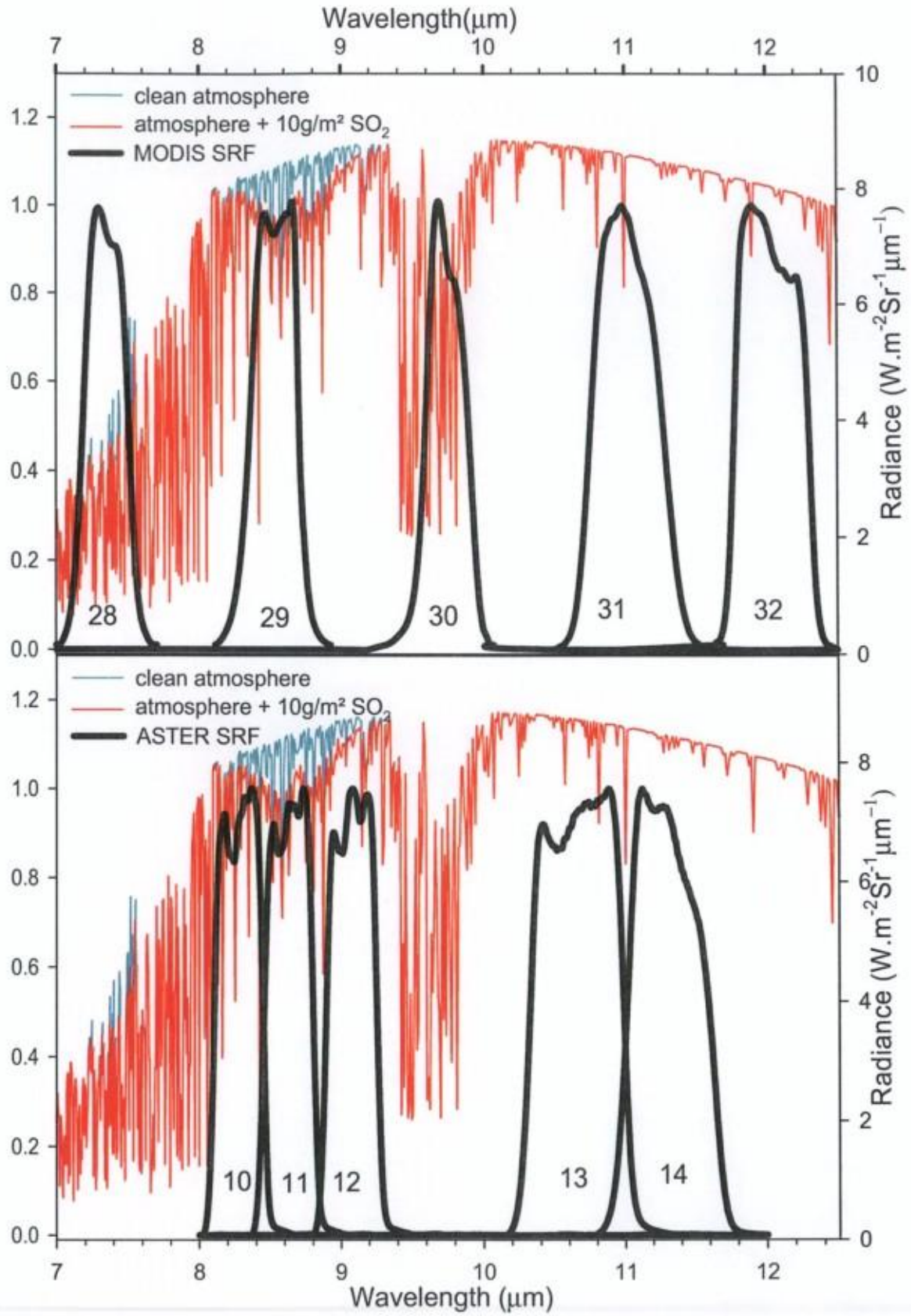

Figure 5.1: Simulated spectra of Top Of Atmosphere radiance for a "clean" atmosphere (blue) and for an atmosphere containing 10g/m² of SO_2 at an altitude of 3 km (red dashed). The spectral response functions (SRF) of MODIS and ASTER are shown in the top and bottom panel.

Band 28 of MODIS, centered at 7.3μm, covers the v3 absorptions bands of SO_2, which are stronger than the v1. However, Band 28 is also affected by the strong absorption bands of H_2O so that the total transmittance of the atmosphere is very low in this region of the IR spectrum. As most of the water vapor resides in the lowest part of the atmosphere, only plumes higher than 5-10 km can be detected by MODIS using Band 28. The algorithms used to retrieve SO_2 at 7.3μm derive from the method of Prata et al, (2003) initially developed for the HIRS (High resolution Infrared Radiation Sounder). The algorithm is based on the difference between the measured radiance and the reconstructed background radiance. The radiance difference, assumed to be caused by SO_2 absorption, is converted as an SO_2 column amount via a simple absorption model that only need the plume altitude as input. The background radiance is linearly interpolated using Band 27 (6.7μm) and Band 31 (11.1μm). As this thesis focuses mostly on passive degassing, which produces low altitude volcanic plumes, retrievals using Band 28 were not developed any further.

Watson et al. (2004) presented convincing examples of SO_2 retrievals with these two techniques in the eruptive plumes of Hekla (Iceland, 2000) and Cleveland (Alaska, 2001). However, three later publications by this same research group reported more mitigated results.

- The MODIS retrievals of SO_2 flux at Popocatépetl presented in (Matiella-Novac et al., 2007) showed significantly lower values (by up to an order of magnitude) than COSPEC measurements.
- Conversely the SO_2 maps retrieved with MODIS in the eruptive plume of Bezymianny (Kearney et al., 2008) shows so high CA values that the authors used an arbitrary maximum threshold to exclude high SO_2 from appearing in their maps. Although not explicitly stated, abundant ash in the plume probably introduced a significant positive bias in the retrieval.
- Thomas et al. (2010) compared SO_2 retrievals from MODIS and two UV sensors: OMI (Ozone Monitoring Instrument) and the late Earth Probe TOMS. In order to compare MODIS and OMI data on a pixel per pixel basis, they developed a nice resampling methodology of the MODIS data to the coarser OMI resolution. Thomas et al. observed that MODIS measurements were generally smaller than OMI at the plume edges and higher at the plume center. While the former observation can be explained by the lower sensitivity of MODIS to SO_2, the latter might have two different causes: Or MODIS overestimates the real SO_2 burdens because of sulfate aerosol interference, or OMI underestimates it because of non-linear light absorption by high SO_2 burdens

(see chapter 4.3). Unfortunately, Thomas et al. did not compare retrievals obtained with the same a priori vertical distribution profile of SO_2 which is crucial for both UV and IR retrieval schemes.

Many problems encountered in MODIS retrievals come from the absorption of other species (hereafter called interferers) overlapping the spectral absorption bands of SO_2. The main interferers are volcanic ash, water vapor and sulfate aerosols. Retrieving all these species together with SO_2 (and necessarily surface temperature) is impossible as the number of unknown (5) exceeds the number of usable bands (i.e. Bands 28, 29, 31 and 32).

In a recent paper, Corradini et al. (2009) proposed a correction procedure to apply to SO_2 retrievals when volcanic ash is present in the plume. This procedure consists of two steps. In the first step, SO_2 and ash are retrieved separately. For ash, the standard brightness temperature difference (Prata et al., 1989, Wen and Rose, 1994) is applied to band 31 and 32 to obtain the effective radius and optical thickness of ash aerosol in the plume. In a second step, look-up tables of Bands 28 and 29 radiances are computed for several values of SO_2 CA, ash optical thickness and effective radius, using MODTRAN and a Mie calculation code. Finally, pixels where both ash and SO_2 were identified in the first step are remeasured using the new look-up tables to obtain the corrected values. Corradini et al. (2009) applied their procedure to images of an eruptive plume emitted by Mt Etna. They demonstrated that ash absorption was inducing a threefold overestimation of the uncorrected retrievals compared to the corrected values. Retrievals with Band 28 were found to need a much lower correction than retrievals that use Band 29. However this procedure implicitly requires assigning a priori values for surface temperature and emissivity. Therefore its applicability is limited to scenes where the volcanic plume is drifting above a homogeneous surface (in practice ocean scenes with no other clouds than the volcanic plume).

Even when ash is absent of the volcanic plume, which is usually the case for plumes produced by passive degassing and effusive eruptions, multi-species retrievals are inherently unstable. This is because the absorption cross sections of both SO_2 and H_2O are one order of magnitude superior in Band 28 than in Band 29. The consequence is that water vapor cannot be completely discriminated from SO_2. The CA of water vapor has a rather high variability over a MODIS view. This variability is caused by the local meteorological conditions and variations in the pathlength between the surface and the sensor (surface altitude and cloud top height).

A last notable interfering species is sulfate aerosol, which is always present in volcanic plumes together with SO_2. Figure 5.2 shows the net radiance loss (extinction) in an atmosphere containing sulfate aerosol. It is a broadband feature with characteristic peaks and troughs, which affects Band 29 significantly.

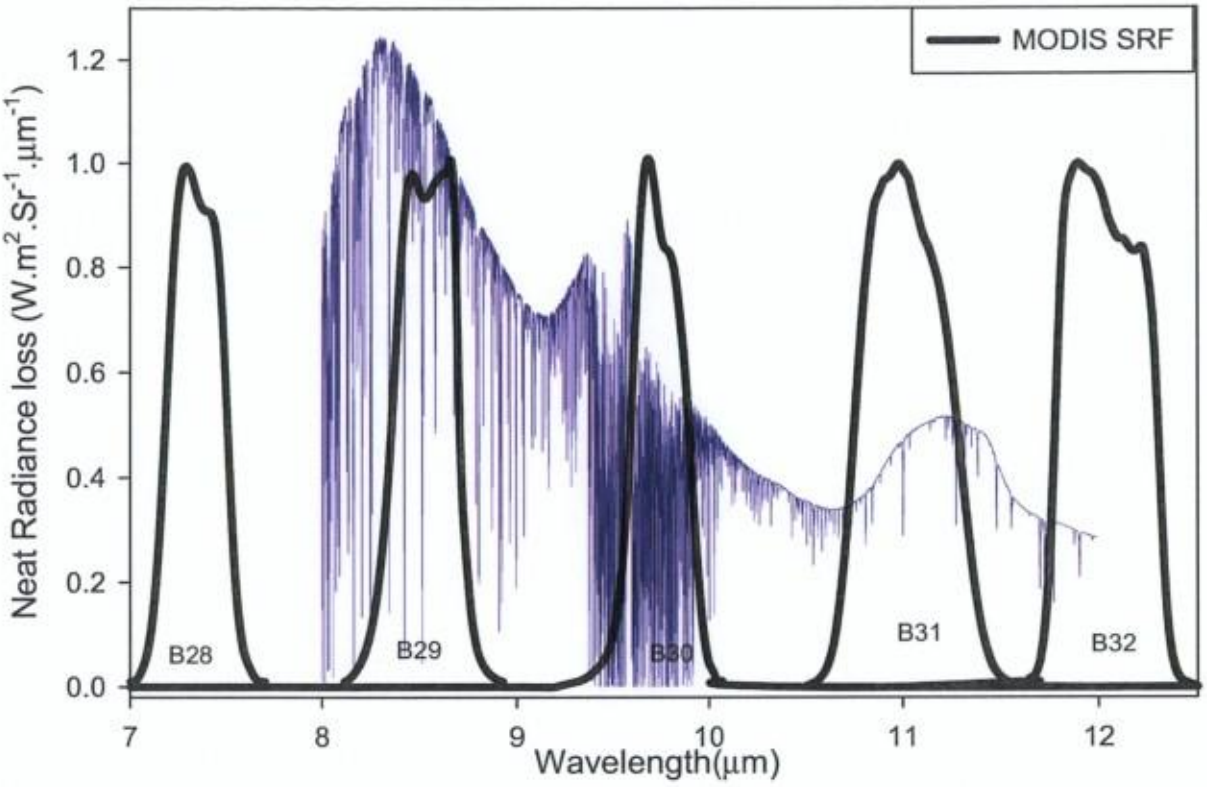

Figure 5.2: Radiance loss over the spectral region of interest for MODIS retrievals. The radiance loss is calculated as the difference between radiance simulated through a clean atmosphere and through an atmosphere containing sulfate aerosol. Aerosol particles have a with a column amount of 6 10^7 cm^{-2} and a radius of 0.5µm. The broad band extinction of sulfate aerosol is clearly visible, overwritten by narrow absorption lines of gas molecules

5.2 Algorithm description

As for ASTER (see chapter 3), the algorithm that was developed for retrieving SO_2 from MODIS images starts with simulations of the Atmospheric radiative transfer with Atmosphit. Simulations treat surface temperatures, SO_2 CA and satellite viewing angle (SVA) as variables, while plume height, surface emissivity, and atmospheric profiles of temperature, water vapor and other atmospheric molecules are entered *a priori* by the user and kept fixed. The radiance spectra simulated at high resolution are then integrated on the spectral response function of bands 28, 29, 31 and 32 of MODIS, which are available on the web site of the

MODIS Characterization and Support Team (http://www.mcst.ssai.biz/mcstweb/index.html). Four (one per band) look-up-table are created, which contain the simulated band radiances as functions of the three variables.

In the second step, the user delimits a region containing the plume, and another region free of SO_2 outside of the plume that will be used as a "blank" to correct the simulated radiances. The choice of the "blank" region is made so as to represent the diversity of the surfaces and atmospheric conditions present in the "plume" region, and may influence the final retrievals of SO_2 CAs in the "plume" region.

In the third step, the surface temperature is measured for each pixel by an inversion algorithm that uses the look-up tables of bands 31 and 32, which are unaffected by SO_2. Then the "blank" file is searched for the pixel(s) whose values of Band 31 and Band 32 are the closest to those measured on the pixel of interest. This operation of finding the "spectrally closest pixel" is aimed at finding the Band 29 background value for the pixel of interest. This background radiance is then used to correct the look-up table of simulated Band 29 radiances.

Finally, the SO_2 CA is interpolated from the SVA and the measured temperature in the corrected Band 29 look up tables.

Unlike ASTER's B11, the band 29 of MODIS is not surrounded by two other bands that allow to work with a band ratio and to correct for the broadband features of the radiance spectrum. The MODIS algorithm developed in this thesis has thus the same unavoidable limitations of interferences with water vapor, aerosols and surface emissivity as the other retrieval algorithms. Furthermore, MODIS retrievals have an additional error source common to all the other infrared sensors: the error on thermal contrast between the plume and the absorbing surface.

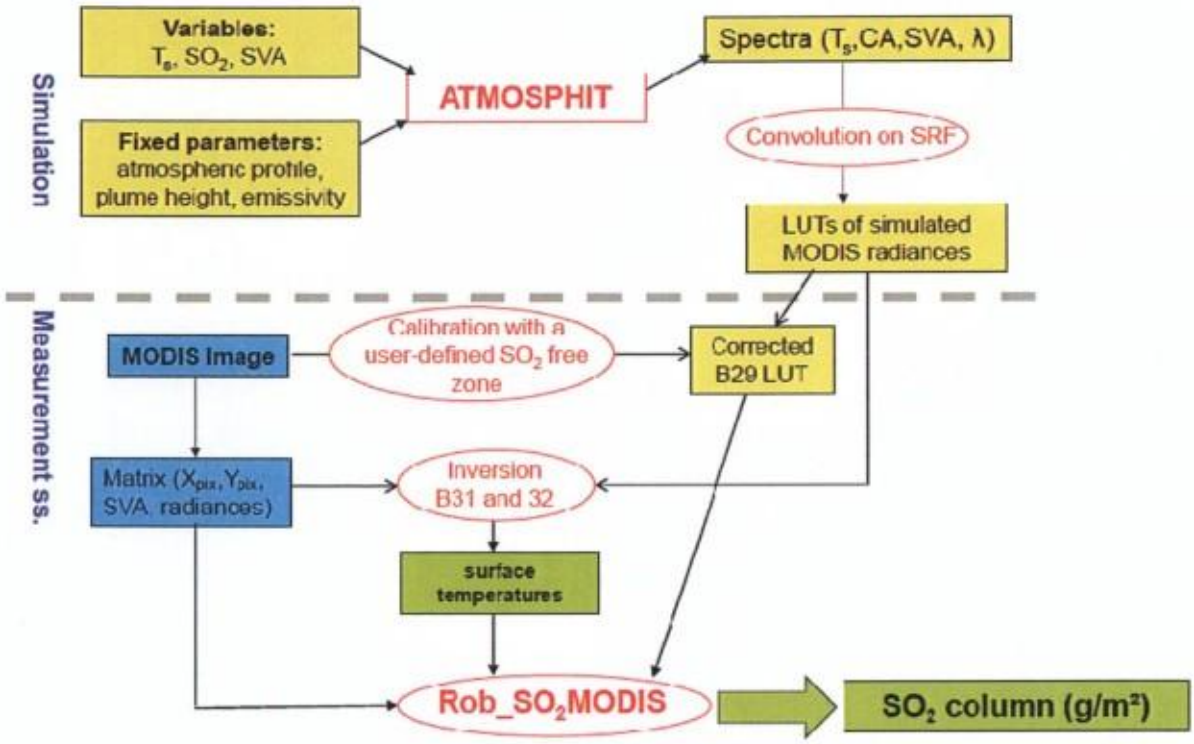

Figure 5.3: Schematic workflow of the MODIS_SO2 algorithm (see details in the text)

5.3 Example of retrievals Hekla, 2000

The eruption Hekla, in February 2000, occurred after a 10 year repose period. As most other eruptions of this volcano, it started with an explosive fissural subplinian phase that lasted a few hours and expelled andesitic tephra up to the low stratosphere (12 km, Lacasse et al., 2004). The activity gradually evolved into a quieter lava effusion fed by the lowest parts of the fissure (Ölafsdottir et al., 2002). Rose et al. (2003) have published a satellite chronology of the SO_2 and aerosol emissions by the initial phase of the eruption. Their data of SO_2 mass in the cloud is used to compare with the results of retrievals with our algorithm for the image acquired on 28th February 2000. On that day, the explosive activity, initiated two days before, had already decreased and the plume was detached from the volcano, stretching between Greenland and Northern Russia. The total SO_2 mass measured in the plume with our MODIS algorithm is 190 kT. This compares well with the value of 160-240 kT reported by (Rose and al., 2003) with their 8.5μm algorithm. The SO_2 map produced with my algorithm is presented in figure 5.4, together with the one of Rose et al. Difference in the shape of the plumes between the two maps results from the different projection systems. In figure 5.4, the column amounts in the map are displayed in Dobson Units for the sake of comparison.

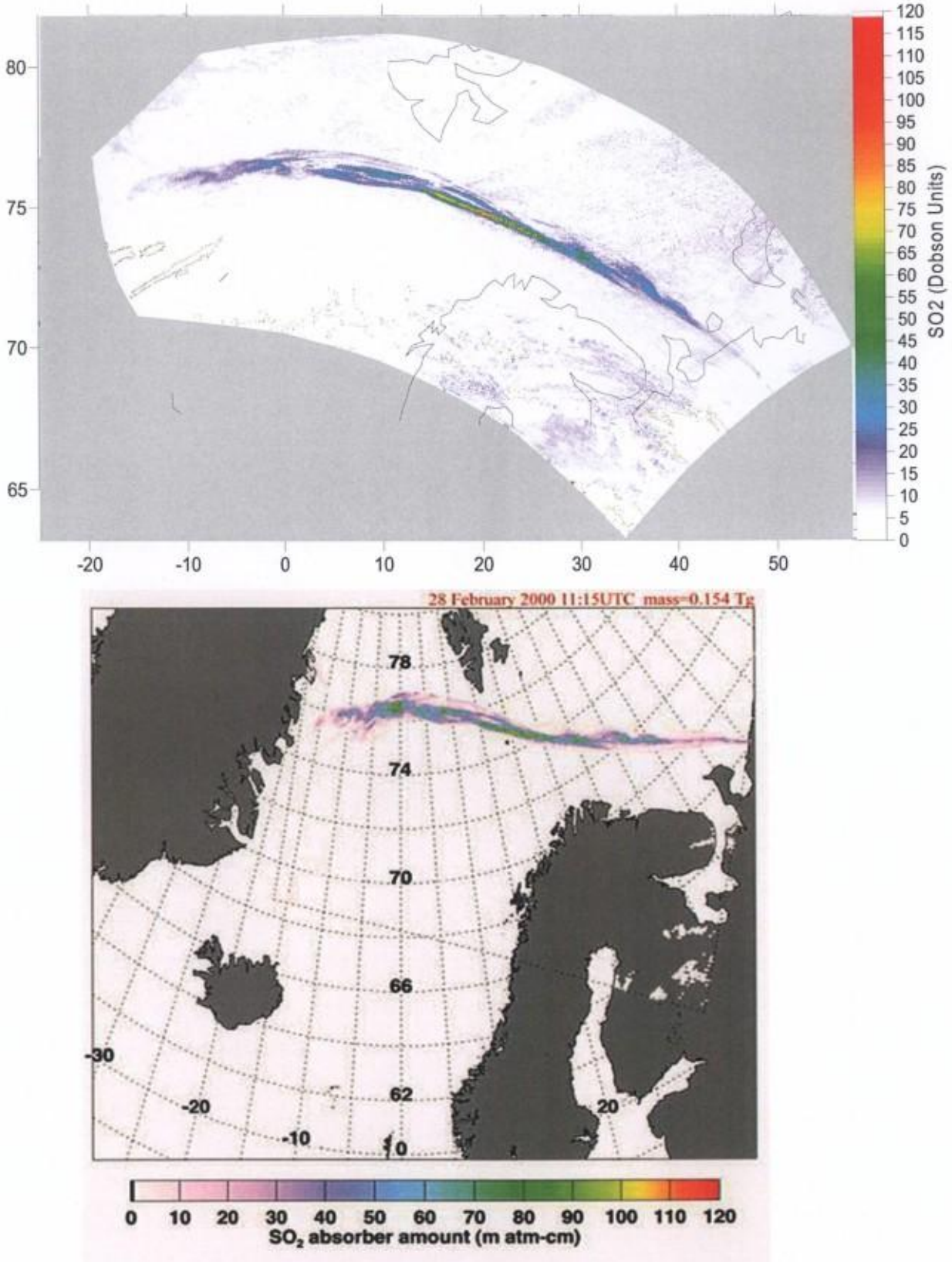

Figure 5.4: (a) SO_2 map of the plume of on 28 February Hekla obtained using my algorithm. (b) SO_2 map from the same day published by Rose et al. 2004. Distortion between the two maps results from different projection system

5.4 Comparison with ASTER

EOS-Terra, the satellite carrying one of the two MODIS, is also carrying ASTER, which therefore acquires images simultaneously to MODIS. ASTER was designed as the "zoom" of the Terra platform, taking narrower, but higher resolution images (60x60km with 90x90m pixels in the TIR). The opportunity to compare simultaneous SO_2 retrievals with MODIS and ASTER had never been exploited, although it allows exploring the effects of the different ground resolution and spectral characteristics on the SO_2 retrievals. Due to its coarser pixel size, MODIS is unable to detect small plumes, so comparison between ASTER and MODIS retrievals requires working on large SO_2 plumes. Ideally the plume also should be ash free, because ash interferes on SO_2 retrievals around 8.5μm (Watson et al., 2004, Corradini et al. 2009). For these two reasons, case studies are restricted to very intense passive degassing or effusive eruption. An important point for making comparisons between the two sensors relevant is to use the same a priori parameters in both retrieval schemes. Here the assumed plume height, atmospheric profiles and surface emissivity are common for both Atmosphit simulations of radiance.

5.4.1 Point spread function

Comparing SO_2 column amounts measured with ASTER and MODIS requires resampling SO_2 retrievals of ASTER to the resolution of MODIS. A problem inherent to resampling is that sensitivity (spatial response) of a physical pixel is not constant over the target surface, and even exceeds its nominal size (Huang et al. 2002), which is 1km square at nadir for MODIS. The point spread function (PSF) describes the sensitivity of the pixel over the target surface. It is a property of the sensor, whose characterisation is made during the pre-flight tests. In the case of MODIS the PSF has not been characterised completely and only its projections on the cross track and along track planes are available. These projections are known respectively as scan-and track-line spread functions and are displayed in figure 5.5. Barnes et al. (1998) reported the characteristics of the scan and track line spread functions of the thirty six bands of MODIS Terra. Based on these data, a synthetic 3D PSF was reconstructed, which that has the shape a piece of Toblerone® chocolate and is stored as a 21x11 matrix.

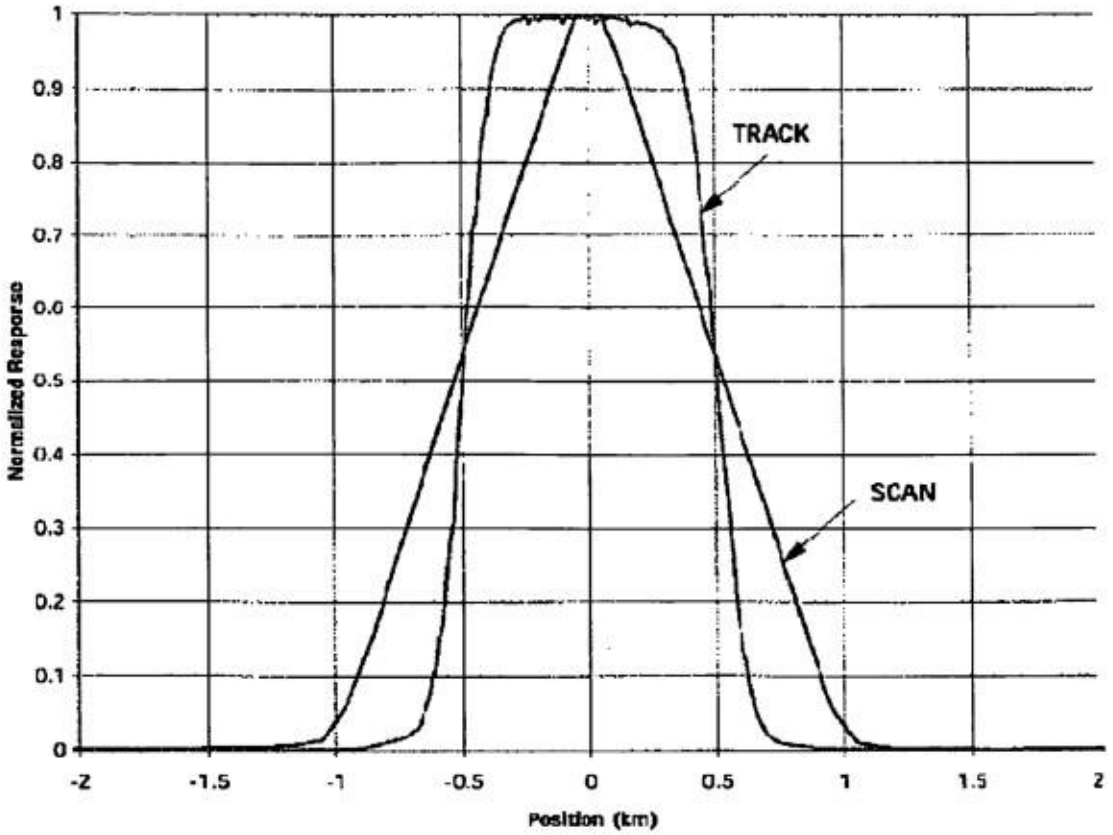

Figure 5.5: Line spread functions (along the track and scan directions) of band 10 of MODIS. The FWHMs of the functions measure approximately 1km, but the detector response extends beyond that. Figure after Barnes et al (1998).

5.4.2 Resampling algorithm

An algorithm was written in IDL to resample ASTER SO_2 retrievals to MODIS resolution. The input data are the 3D matrixes where each column of elements contains the information of one pixel (center position, temperature and SO_2 CA). The first step of the algorithm is to identify, for each pixel of the MODIS image, the pixel of ASTER that is the closest from its center and the surrounding cluster of 21x11 ASTER pixels corresponding to the extended sensitivity domain of the MODIS pixel. The second step is the generation of a synthetic MODIS pixel by applying the PSF to the CA value of each pixel of the cluster. This is done using an element per element matrix product between the PSF matrix and the cluster. MODIS pixels that contain subpixel clouds (detected by their brightness temperature on the ASTER image) are assigned an arbitrary SO_2 value of 99 and are excluded from the comparison process.

5.5 Results

5.5.1 Miyake-jima 1 april 2001

The first case study is the MODIS image of Miyake-jima that was acquired simultaneously to the ASTER image presented in chapter 3. This image can be considered as an ideal case for SO_2 retrievals in the TIR, with a large and concentrated SO_2 plume drifting in a rather dry and cold atmosphere over a homogeneous sea surface. The wider field of view of MODIS allows to visualize the SO_2 plume being transported over 200 km in a meandering pattern (figure 5.6). This can be due to change in the wind direction through time or to changes in plume altitude through time, plumes emitted at different altitudes being transported in different direction due to wind shear. Analysis of the radiosonde data from Hachiyo-jima Island, 200km south of the volcano do not allow for discriminating between the two hypotheses because they show both little change in plume direction through time and low vertical wind shear.

The original ASTER SO_2 map (displayed as figure 3.11 in chapter 3) was resampled and compared to the corresponding portion of the MODIS SO_2 map. The two SO_2 maps are shown in figure 5.6. Excellent agreement is observed between the two maps, and can be further confirmed in a quantitative way by examining the pixel per pixel comparison between the two datasets in figure 5.7. Each point of the graph has its abscissa being the SO_2 CA measured on a pixel of the MODIS SO_2 map, and its ordinate being the SO_2 CA of the corresponding pseudo pixel obtained by resampling the ASTER map. The regression line obtained from that dataset, $SO_2^{ASTER} = 0.142 + 1.011 * SO_2^{MODIS}$ with a R^2 of 0.92 is rather close to the ideal line $SO_2^{ASTER} = SO_2^{MODIS}$. The somewhat higher spread of the points that is observed at high column amounts is likely caused by the decrease of sensitivity (and hence lower S/N ratio) at high SO_2 burdens.

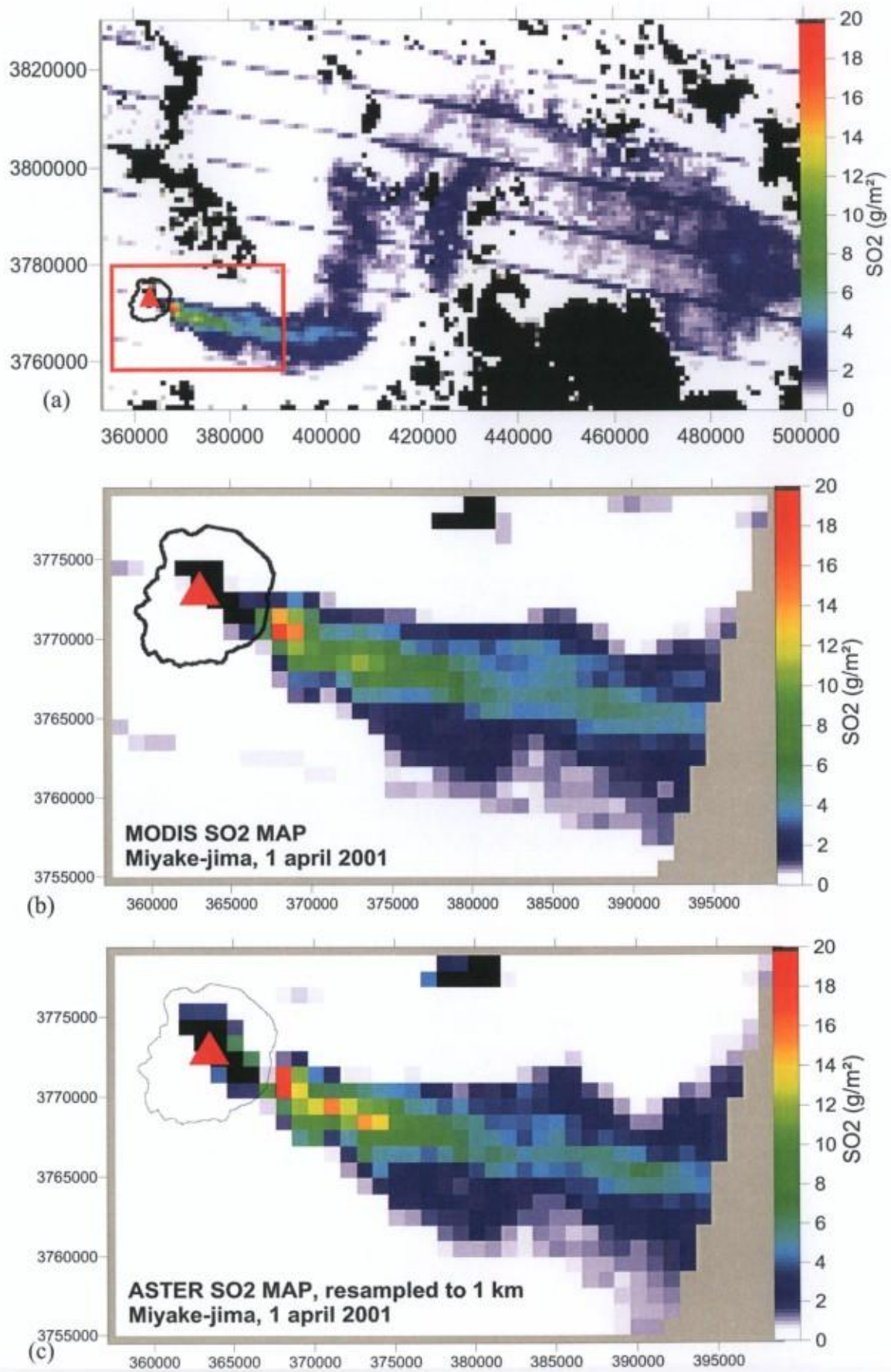

Figure 5.6: (a) MODIS wide view of the plume emitted by Miyake-jima on 1 April 2001. (b) Zoom on the red box of the map shown in (a). (c) ASTER SO_2 map resampled to the 1 km² MODIS pixels.

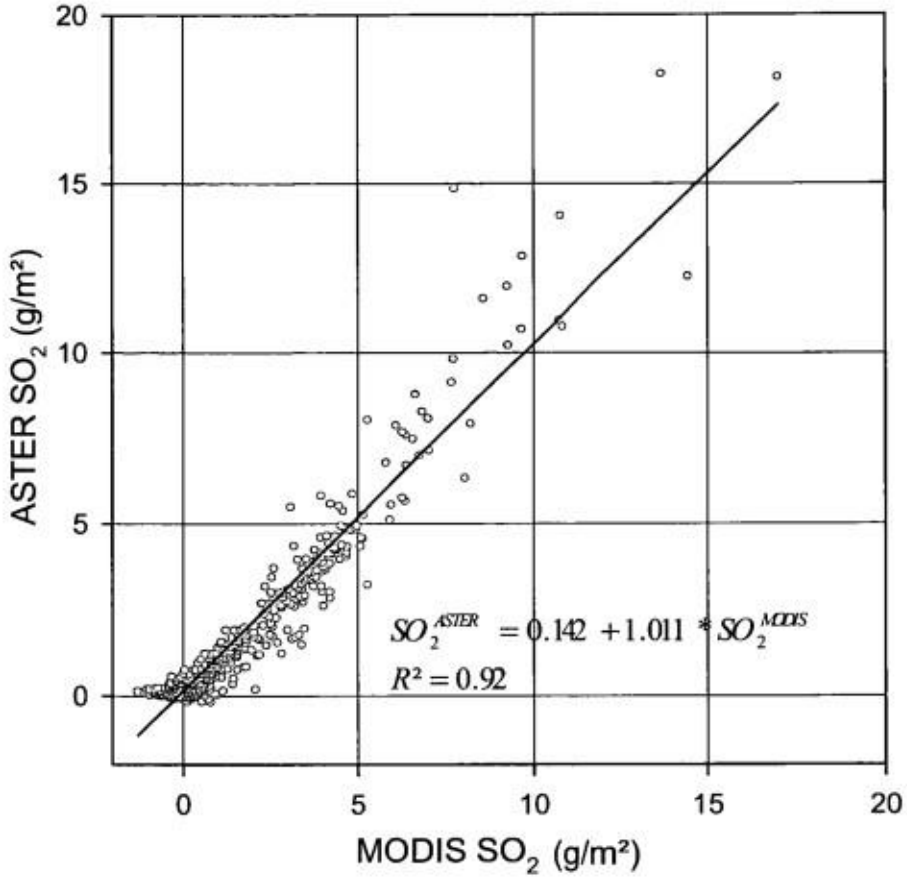

Figure 5.7: Scatter plot of SO_2 CAs of MODIS pseudopixels (i.e. obtained by resampling the ASTER SO_2 map with the PSF) versus the CAs actually retrieved using the MODIS image

5.5.2 Al-Mishraq, 14 July 2003

The Sulphur refinery of Al-Mishraq (central Iraq) underwent a one month long fire, believed to be of criminal origin, which released massive amounts of SO_2 in the regional low troposphere. This event represents the biggest anthropogenic SO_2 release to date. Carn et al. (2004) estimated the cumulated release of SO_2 to 464–655 kT, using the data of the UV sensor Earth Probe TOMS and an SO_2 reaction rate of 75% per day. This estimate agrees rather well with the ~400kt sulphur stock that was completely burned during the fire. Complete combustion of a 400kt stock of sulphur should theoretically have produced ~800 kT of SO_2, but part of the SO_2 might have resided too low and been missed by the TOMS satellite as its sensitivity for low altitude SO_2 is limited.

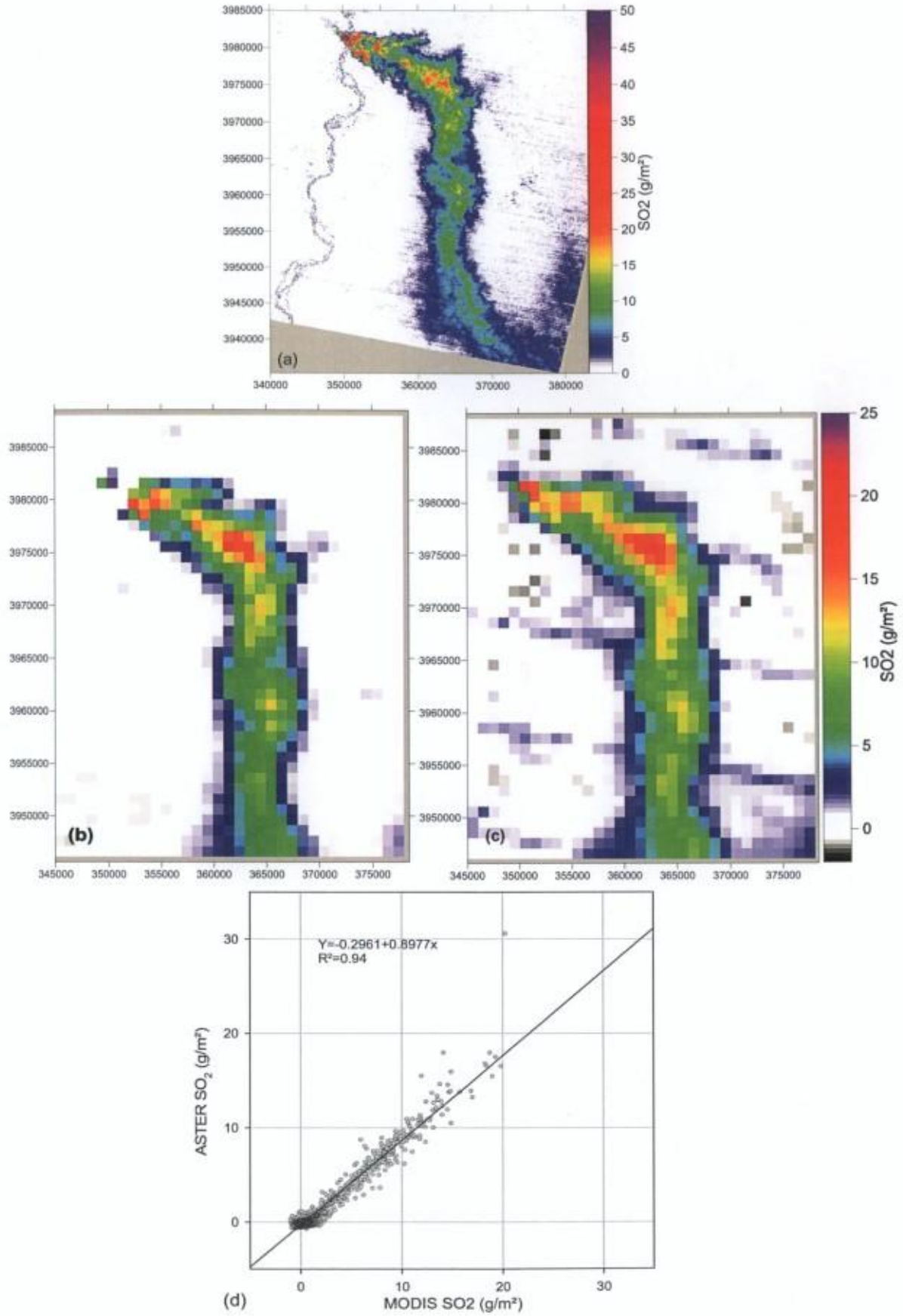

Figure 5.8: Comparison of ASTER and MODIS SO_2 retrievals in the plume from the sulphur fire of Al-Mishraq on 14 July 2003. (a) Original ASTER SO_2 map showing the hyper concentrated SO_2 plume. The Tigrus River, with its cold surface temperature, appear as a narrow ribbon of anomalous values. (b) Scatter plot of the pixel based comparison of the column amounts. (c) ASTER SO_2 map resampled to MODIS resolution. (d) Original MODIS SO_2 map.

Kearney et al. (2009) have compared SO_2 retrievals from two nearly contemporaneous images of TOMS and MODIS. They found similar masses of respectively 102 and 118 kt. Based on their map (see Kearney et al., fig. 3) MODIS seems to perform better at retrieving low altitude SO_2 than EP TOMS. Strong scatter affects the comparison of column amounts of individual EP TOMS pixels with the resampled MODIS retrievals (see Kearney et al., fig. 3 and 4).

ASTER acquired only one image of this exceptional sulphur dioxide release, on 14th July 2003. This image was analysed using the algorithm presented in chapter 3 to produce the SO_2 map of figure 5.8a. The extreme column amounts in that plume (up to 50g/m²) represent the highest values measured so far with ASTER, and possibly with any space borne sensor. When resampled to MODIS resolution, the ASTER SO_2 map looks again very similar to the "true" MODIS retrievals (figure 5.8b). The scatter plot, although, shows that MODIS seems to slightly overestimate ASTER (figure 5.8c). The regression line obtained on the two datasets for this case study is $SO_2^{ASTER} = -0.2961 + 0.8977\ SO_2^{MODIS}$, with a R^2 coefficient of 0.94.

5.5.3 Nyiragongo 19 June 2007

Nyiragongo volcano (Democratic Republic of Congo) has been hosting a permanent lava lake since 2002, and for several decades during the 20th century (Tazieff et al. 1977). The volcano has been one of the strongest permanent SO_2 emitter in the world since 2002 (Sawyer et al. 2008) and has caused regional acid rain due to fast reaction of the SO_2 in the moist tropical atmosphere. This tropical atmosphere complicates the retrievals of SO_2 because of meteorological clouds that often mask the volcanic plume and of spectral interference between water vapor and SO_2 around 8-9μm. The ASTER image of 19 June 2007, which contains very little meteorological clouds, was analysed together with the simultaneous MODIS image. The ASTER SO_2 map (figure 5.9a) has already been presented in chapter 4 where it was shown that the SO_2 flux retrieved with ASTER (52 kg/s) compares very well with that computed using OMI (45kg/s). The SO_2 map retrieved with the simultaneous MODIS image shows a distribution broadly similar to the resampled ASTER map, but with higher column amounts. This is confirmed in the scatter plot which shows that the MODIS column amounts are nearly 3 times higher than those of ASTER. The dispersion of the points is also significantly stronger than for the other case study. (Regression line of $SO_2^{ASTER} = 0.1364 + 0.342 * SO_2^{MODIS}$ with a R^2 of 0.37).

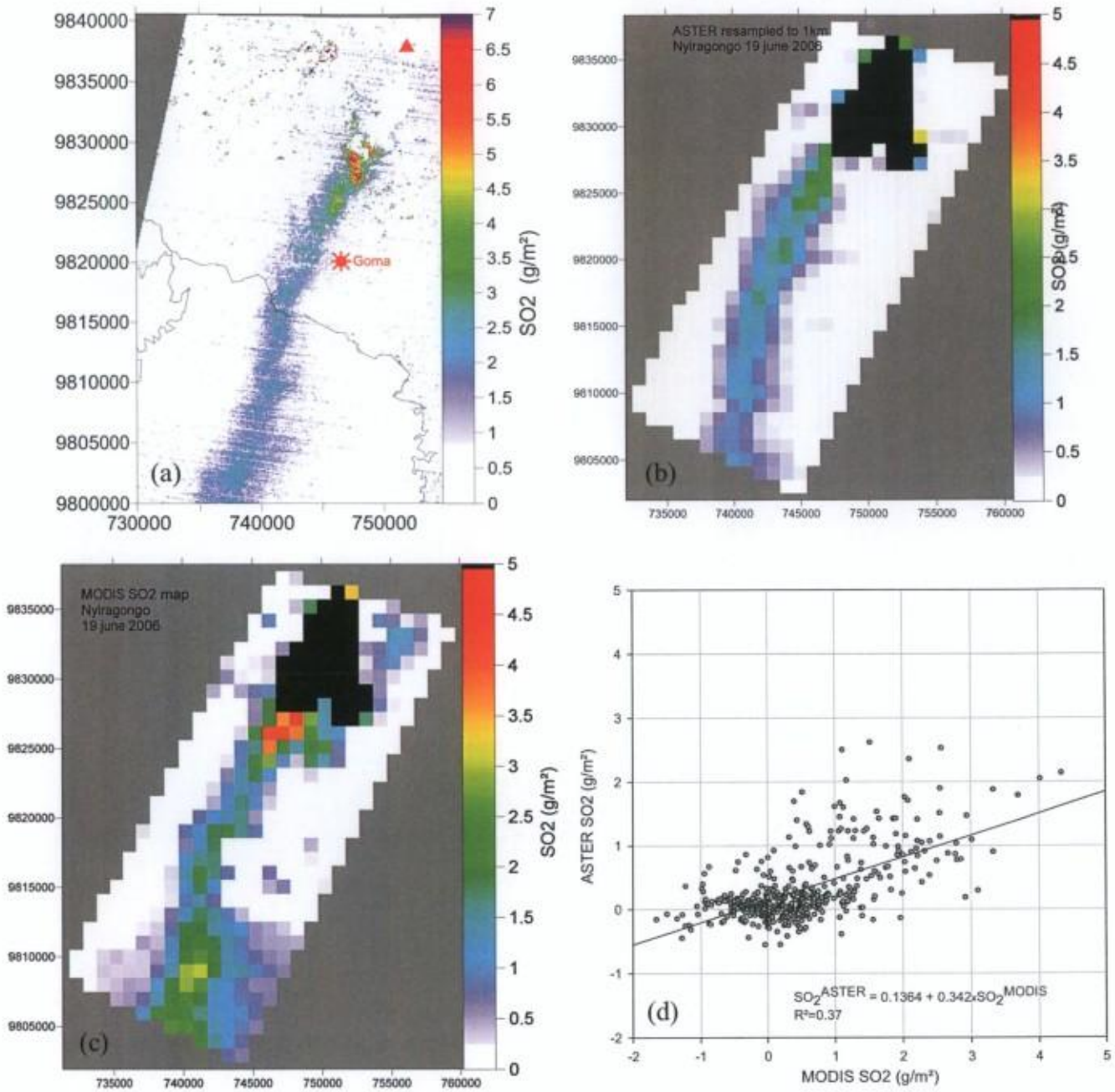

Figure 5.9: Comparison of ASTER and MODIS SO_2 retrievals in the plume of Mt Nyiragongo on 19 June 2007. (a) Original ASTER SO_2 map. (b) ASTER SO_2 map resampled to MODIS resolution. (c) Original MODIS SO_2 map. (d) Scatter plot of the pixel based comparison of the column amounts.

5.5.4 Etna, 3 August 2006

The ASTER image of Etna has also been presented in chapter 3, where the resulting column amount and fluxes were compared successfully to simultaneous scanning DOAS data. Here these results are compared with the simultaneous MODIS retrievals. In this case, the agreement between the two sensors is obviously poor. Looking at the SO_2 map in figure 5.10, one can see a marked contrast between the right and left portions of the image. The right portion, which corresponds to sea area, has MODIS CAs in agreement (or slightly overestimating) ASTER CAs. On the left portion however, corresponding to land surfaces, MODIS CAs are significantly underestimated compared to ASTER ones.

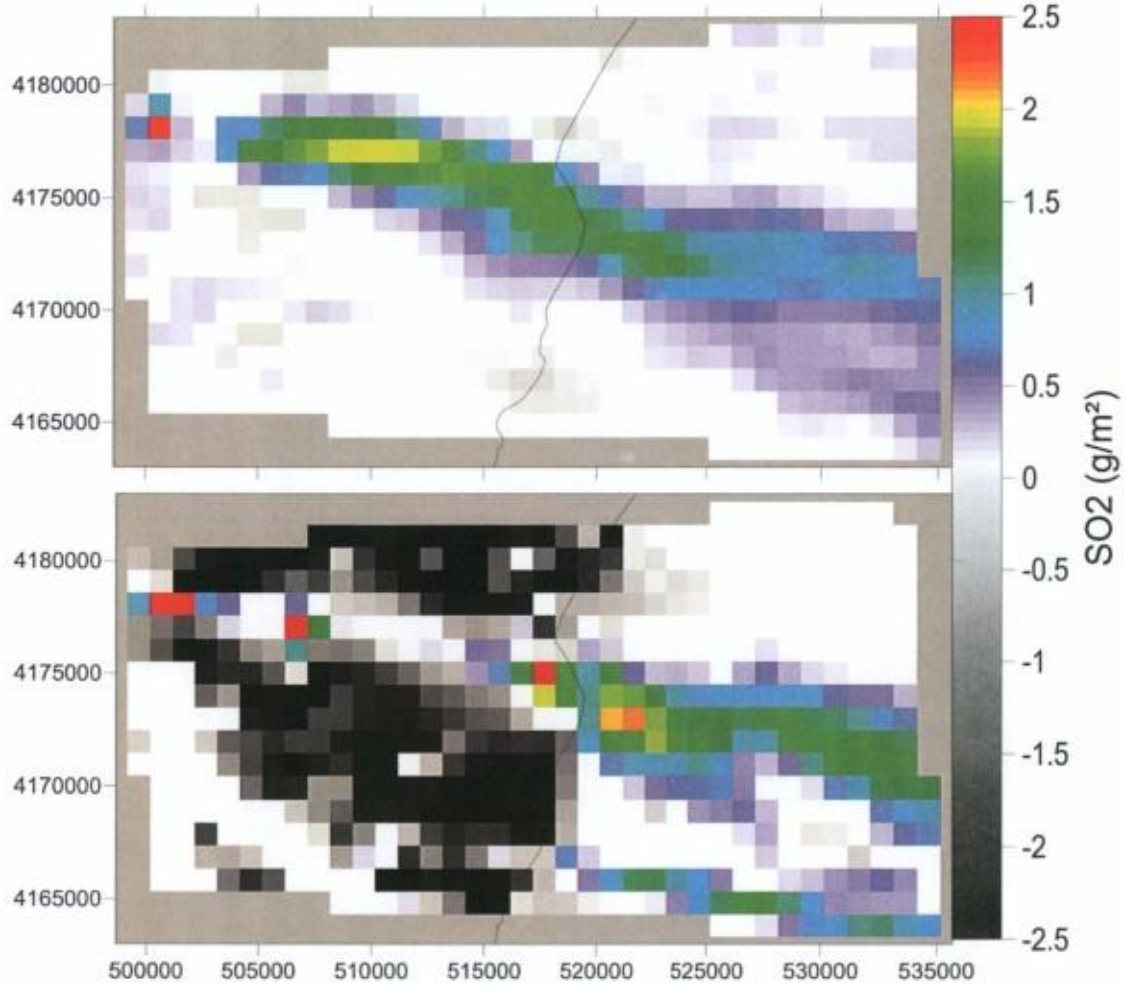

Figure 5.10: Comparison of ASTER and MODIS SO_2 retrievals in the plume of Mt Etna on 3 August 2006. (a) ASTER SO_2 map (see figure 3.14 for the original ASTER map) resampled to MODIS resolution. (b) Original MODIS SO_2 map. The black line represents the eastern coastline of Sicily.

The disparity as a function of surface type (and thus different emissivities) is further found on the scatter plot of figure 5.11, where three groups of pixels can be individualized. The "sea" group contains pixels with reasonable agreement between ASTER and MODIS, although the latter slightly overestimates the former. The "land" group contains pixel that are aligned on a broadly parallel slope although with a negative shift of about 2.5 g/m².

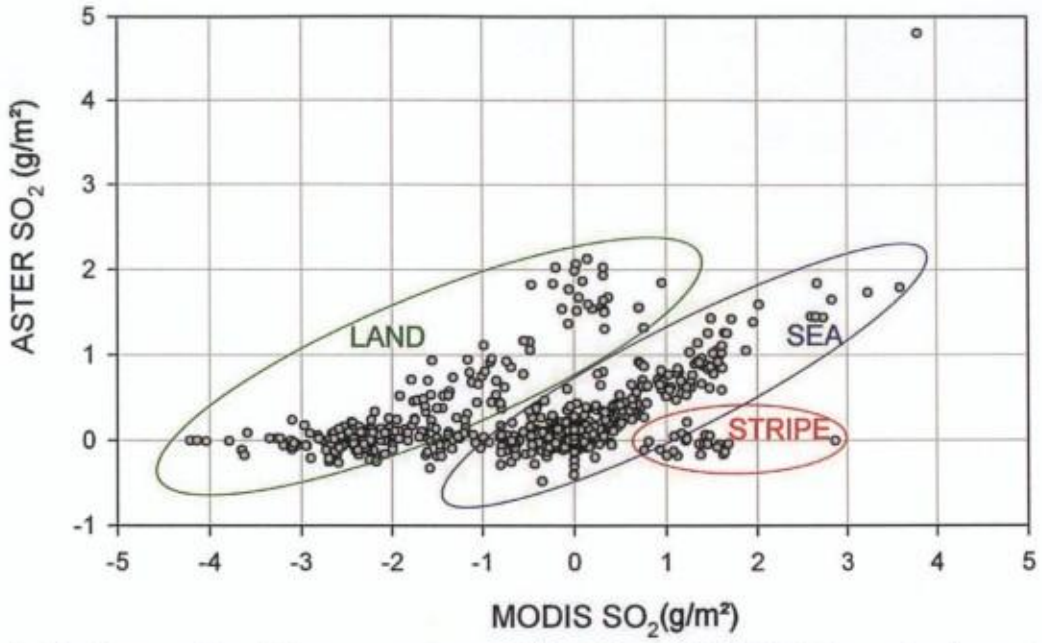

Figure 5.11: Scatter plot of the comparison of ASTER and MODIS SO_2 retrievals on 3 August 2006, showing the different populations of pixels, see text for explanations.

5.6 Discussion

5.6.1 Performance of the resampling algorithm

The good plume shape correspondence between the corresponding MODIS and ASTER-resampled SO_2 maps gives a reliable indication that the resampling algorithm performs well. The results of an earlier version of the algorithm, which did not take the PSF into account, are shown in figure 5.12. The comparison between figure 5.12 and its equivalent maps of figures 5.6 b and c shows that the actual MODIS SO_2 map has much less scatter than the ASTER map resampled without PSF. This is because, in the "real world", the PSF of the pixels produce more smoothing than the simplified 1km² resampling used to produce the map of figure 5.12. This illustrates the importance of applying the PSF when performing inter-sensor comparison. This was not done by Kearney et al. (2009, 2010) when they compared

retrievals of IR (MODIS) and UV (EP TOMS and OMI) sensors. This might explain part of the discrepancy in their comparisons. The problem is that characterising the PSF of a sensor is a complicated operation that has to be done in the laboratory pre-flight tests. The PSF of OMI for example has not been thoroughly characterised and is furthermore dependent of poorly characterised parameters such as polarisation (G. Pinardi, pers. comm., 2010).

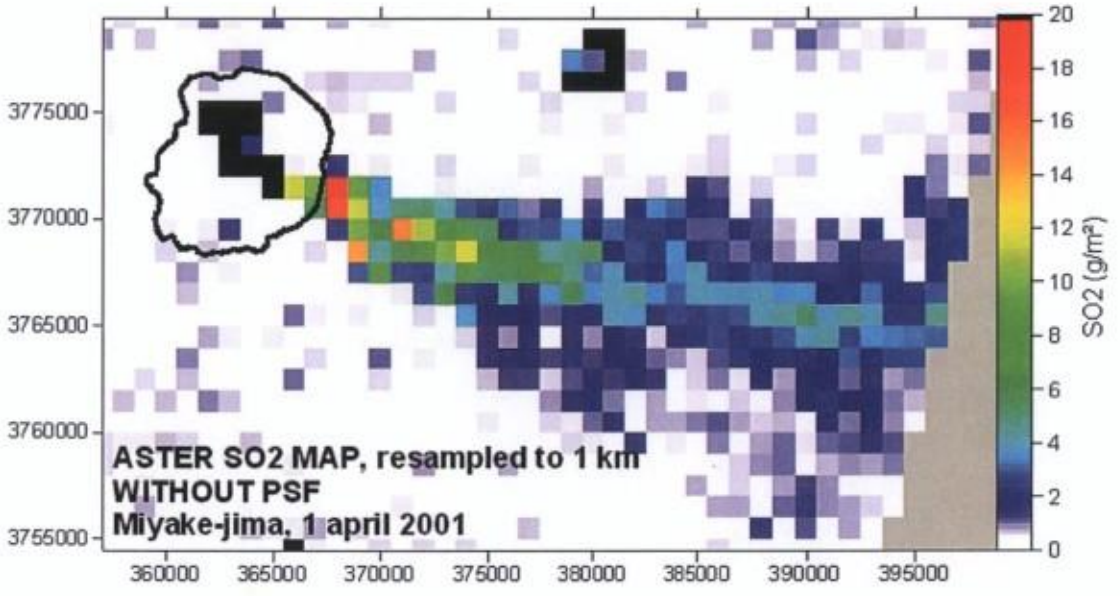

Figure 5.11: ASTER SO_2 map resampled to 1km without taking into account the PSF. The scatter in the map is significantly stronger then on the map of figure 5.5c, which does take the PSF into account.

5.6.2 An assessment of MODIS performances

ASTER retrievals, because of their good records in cross validation tests with DOAS and OMI data, and because of their demonstrated low sensitivity to water vapor, sulfate aerosols and surface emissivity, can be taken as a reference for assessing the quality of MODIS SO_2 retrievals. With ideal conditions (i.e. massive SO_2 plume, dry atmosphere and strong thermal contrast between the plume and the ground), a good agreement is obtained between ASTER and MODIS SO_2 retrievals, as shown by the case studies of Miyake-jima and, in a lesser extent, Al-Mishraq. However, MODIS performs poorly at retrieving SO_2 if the plume resides in a moist tropical atmosphere, or for small plumes, or when the underlying surface undergoes strong variation in emissivity (cf. the Etna case). Comparing MODIS SO_2 retrievals with ASTER retrievals helps to separate and quantify these three effects and

discriminate them between each other, and thus provides novel insights into retrievals of SO_2 by broadband IR sensors.

The SO_2 retrievals using MODIS in a tropical atmosphere, whose content in water vapor content is high and poorly known, suffer from both increased imprecision and inaccuracy. The former is related to the decreased signal to noise ratio induced by the higher optical thickness of the atmosphere and probably affects both sensors. The latter is caused by difference between the real and model content of atmospheric water vapor. According to Atmosphit simulations, an overestimation of this parameter would lead to an overestimation of the retrieved SO_2 and vice versa.

Another possible cause of overestimation in the MODIS retrievals in general comes from the presence of sulphuric acid aerosols in the plume. Volcanic plumes always contain significant amounts of liquid aerosol, dominated by H_2SO_4 liquid particles (e.g. Mather et al., 2004) that are hygroscopic and act as efficient condensation nuclei for atmospheric water vapor. Thermodynamic modelling by Martin et al. (2011) shows that the degree of relative humidity of the atmosphere plays a critical role on whether the aerosol particles are deliquescent (and therefore growing bigger) or not. When the plume is embedded in a moist tropical atmosphere, the particles of the aerosol will have a larger effective radius, which increases the plume optical thickness.

The effect of the sulfate aerosol should decrease the slope of the ASTER versus MODIS correlation (similarly to what is shown in figure 3.10b), because the concentration of the aerosol can be assumed to be somewhat proportional to SO_2 CA, and neglected outside of the plume. Conversely the effect of water vapor should affect all the pixels of the image and therefore shift the horizontal intercept of the regression line without significantly changing its slope coefficient. The shift can be positive or negative and is proportional to the amplitude of the difference between the real and model atmospheric humidity.

Surface emissivity can also introduce a significant bias in the retrievals, especially when strong contrasts are present over the image as shown in the Etna case study. The strong emissivity contrast between sea and bare land induce a bias of about 3 g/m² over all the land pixels (input emissivity in the model was set to 0.98, close to water emissivity). The resulting relative error is dramatic in that case, given that the plume is small and diluted (0-2 g/m²). Emissivity cannot be measured using classical methods under a volcanic plume (such as the Temperature Emissivity Separation algorithm (e.g. Gillepsie et al., 1998) because their spectral properties differ markedly from those of a "normal" atmosphere. A potential solution to this emissivity problem could be to define, manually and prior to any further processing,

domains of the image where appropriated emissivity spectra are input in the model. However this solution would require significantly more operations by the user and computation time than what is reasonably available for an operational algorithm.

5.7 Conclusion: MODIS, an outdated tool?

MODIS performances in measuring sulphur dioxide clearly suffer from the comparison with other current UV and IR sensors. Reduced sensitivity to SO_2 and coarse pixel size make retrievals of small plumes from passive degassing difficult. The biases induced by the potential interferers were quantified for the first time in this study, thanks to the comparison with simultaneous measurements with ASTER resampled to MODIS resolution. These biases are actually equal or superior in magnitude to the column amounts commonly encountered in the passive degassing plumes, making retrievals severely inaccurate. This is especially true for plumes located in a tropical atmosphere or over surfaces with strongly contrasted emissivity. Only for large emissions over homogenous surface and in a relatively dry atmosphere have the retrievals using MODIS an acceptable precision. This certainly restricts the interest of keeping on working with MODIS for retrieving SO_2. This statement is further supported by the fact that a number of space borne instruments provide SO_2 retrievals (using the IR or UV wavelength) with a better sensitivity, precision and accuracy, (if not ground resolution) than MODIS. Among these instruments, OMI (the Ozone monitoring Instrument, operating in the UV, Levelt et al., 2006, Carn et al., 2008) has become the paradigm of SO_2 measurements on orbit. Its retrievals over various volcanoes of the world show a good agreement with ASTER's retrievals, as shown in chapter 3 of this thesis. In the infrared, two high spectral resolution sensors, AIRS (Atmospheric Infrared Sounder, Carn et al, 2004, Prata and Bernardo, 2007) and IASI (Infrared Atmospheric Sounding Interferometer, Clarisse et al. 2008) also provide retrievals with excellent coverage and a ground resolution of about 15km per pixel. Finally one must emphasize that ground resolution, the only advantage of MODIS over the three aforementioned sensors, is not a critical issue for detecting plumes emitted by intense eruptions, because they are rapidly diluted and stretched over wide areas.

Chapter 6: Development of a UV camera for validation of satellite SO_2 measurements

6.1 Introduction

In the last years, UV-sensitive imaging systems were developed to map SO_2 distribution in volcanic plumes, under the independent efforts of two research teams in Japan (Mori and Burton, 2006) and in the United States (Bluth et al. 2007). This has led to a new generation of instruments that consist of a high sensitivity CCD camera coupled with one or two narrowband UV filters selecting the wavelength range of SO_2 absorption. These instruments allow 2D imaging measurements of volcanic SO_2 and flux measurements with a frequency of up to 1 Hz. Although presenting some issues (Kern et al., 2010b), exploitation of these instruments appears very promising in a wide range of research areas, such as modelling of plume rise and dispersion, comparison with simultaneous seismic and acoustic data and volcano monitoring. Such an instrument could also prove very useful for the validation of satellite measurements of SO_2, so we decided to develop one at ULB. When we start searching documentation and ordering components (late 2007), few SO_2 cameras existed in the world, as the technology was still emerging. Two years after, despite numerous unexpected vicissitudes, a complete package including an instrument and its data processing software has been developed and tested.

6.2 Theoretical background

The general principle of the SO_2 camera is similar to that of COSPEC (see chapter 1). The instrument measures the UV radiance transmitted by a volcanic plume in one or two discrete(s) wavelength domain(s). These radiance measurements are then converted into SO_2 column amounts by comparing them with measurements of calibration cells containing known amounts of SO_2. The wavelength domains of interest are selected with a band-pass filter mounted in front of the camera lens. The image recorded by a camera equipped with such a filter is a matrix where each pixel (i,j) measure a light intensity given by

$$I_{i,j} = \int_{\lambda} R_{i,j}(\lambda) F_{i,j}(\lambda) Q(\lambda) d\lambda \qquad (6.1)$$

$R_{i,j}(\lambda)$ is the radiance spectra diffused by the sky (see chapter 2.4), that generally varies across the image. $F_{i,j}(\lambda)$ is the spectral response function of the filter, which also varies across the image due to the dependence of the filter function on illumination angle (Kern et al., 2010b). $Q(\lambda)$ is the quantum efficiency of the camera (see section 6.3).

If the camera is looking at a volcanic plume containing SO_2 and aerosols, we can express I using the generalized expression of Beer-Lambert-Bouguer law introduced in chapter 2 (eq. 2.15). We thus obtain

$$I_{i,j} = \int_{\lambda} \mathrm{R0}_{i,j}(\lambda) \exp(-\chi(\lambda) - k(\lambda) C_S) F_{i,j}(\lambda) Q(\lambda) d\lambda \qquad (6.2)$$

Where R0 is the background sky radiance, $\chi$is the optical thickness of the aerosol, k is the absorption coefficient of SO_2 and C_S its slant column amount (SCA). The American team (Bluth et al. 2007, Dalton et al., 2009) developed an instrument using only one filter centered at 307 nm, where SO_2 absorption is quite strong. This technique (hereafter called "single filter technique") utilizes the integrated absorbance, expressed as (Kern et al, 2010b)

$$A_{i,j} = \ln\left(\frac{I0_{i,j}}{I_{i,j}}\right) = \ln\left(\frac{\int_{\lambda} \mathrm{R0}_{i,j}(\lambda) F_{i,j}(\lambda) Q(\lambda) d\lambda}{\int_{\lambda} \mathrm{R0}_{i,j}(\lambda) \exp(-\chi(\lambda) - k(\lambda) C_S) F_{i,j}(\lambda) Q(\lambda) d\lambda}\right) \qquad (6.3)$$

$I0_{ij}$, the background intensity, is not known for pixels containing SO_2. It must thus be reconstructed by extrapolating portion of images that do not contain SO_2. Slant column amount is then computed by comparing integrated absorbance of the image with the integrated absorbance of calibration cells. However, the major problem in this approach is that SO_2 is not the only source of light extinction. Aerosols inside the plume also contribute to the absorption of sky radiation by the plume (see chapter 2.5) and the single filter technique is unable to discriminate between the narrowband SO_2 and the broadband aerosol absorption. In some measurement configurations, the contribution of aerosol to the radiance measured by the camera can even be positive (enhanced backscattering of sun light). Field measurements by Kantzas et al. (2010) have demonstrated that the single filter method often leads to major over or underestimations of the SO_2 amount in the plume. To avoid, or at least reduce, the effect of aerosols, Mori and Burton (2006) developed the two filters technique. In this technique, images are alternatively taken with two filters: one centered at 310 nm, where SO_2 absorption is strong, and the other centered at 330nm where SO_2 absorption is negligible (see figure 2.7). As aerosol extinction is characterised by a broadband shape, it varies little over the 20nm interval between the two filters. Using the two filters approach, the contribution of aerosols can be removed by normalizing the radiance values of recorded at 310nm by the radiance recorded 330nm, and using the normalized absorbance $\alpha_{i,j}$, defined as

$$\alpha_{i,j} = \ln\left(\frac{\frac{I0_{i,j}^{310}}{I_{i,j}^{310}}}{\frac{I0_{i,j}^{330}}{I_{i,j}^{330}}}\right) = \ln\left(\frac{I0_{i,j}^{310}}{I_{i,j}^{310}}\right) - \ln\left(\frac{I0_{i,j}^{330}}{I_{i,j}^{330}}\right) \quad (6.4)$$

or, under its fully explicit analytical form:

$$\alpha_{i,j} = \ln\left(\frac{\int_{\lambda} R0_{i,j}(\lambda) F_{i,j}^{310}(\lambda) Q(\lambda) d\lambda}{\int_{\lambda} R0_{i,j}(\lambda) \exp(-\chi(\lambda) - k(\lambda) C_S) F_{i,j}^{310}(\lambda) Q(\lambda) d\lambda} \Bigg/ \frac{\int_{\lambda} R0_{i,j}(\lambda) F_{i,j}^{330}(\lambda) Q(\lambda) d\lambda}{\int_{\lambda} R0_{i,j}(\lambda) \exp(-\chi(\lambda)) F_{i,j}^{330}(\lambda) Q(\lambda) d\lambda}\right) \quad (6.5)$$

Approximating $\chi(\lambda)$as a constant over the 20nm wavelength interval between the 2 filters, it can be pulled out of the integral and simplified in the denominator. The normalized absorbance is thus simplified as

$$\alpha_{i,j} = \ln\left(\frac{\int_{\lambda} R0_{i,j}(\lambda) F_{i,j}^{310}(\lambda) Q(\lambda) d\lambda}{\int_{\lambda} R0_{i,j}(\lambda) \exp(-k(\lambda) C_S) F_{i,j}^{310}(\lambda) Q(\lambda) d\lambda}\right) \quad (6.6)$$

This new analytical expression of normalized absorbance is now independent on aerosol extinction. It is proportional to the SCA of SO_2 in an almost linear way, deviating from linearity only above ~4g/m² of SO_2 (figure6.6). Similarly to the single filter method, the SO_2 SCA is obtained by comparing the normalized absorbance of the plume to measurements of calibration cells. However, normalized absorbance, as we see in its fully explicit form, is a somewhat more complicated expression than what was suggested in the initial publications (Mori and Burton, 2006) and does not depend only on the SO_2 SCA. A thorough paper by Kern et al. (2010b) investigated several potential problems that arise from the spectral dependences of the background light and filter transmittance.

The radiance spectrum of the diffuse sky radiation, I0, is known to depend on the total slant column amount (SCA) of ozone and therefore on solar zenith angle (SZA), as shown in figure 6.1. High ozone SCA or high SZA reduce strongly the shortwave component of the diffuse sky radiance. The consequence of this is that the relation between apparent absorbance and SO_2 SCA will change through time, ambient light condition and latitude of the volcano. In order to take this effect into account, it is thus necessary to calibrate the instrument frequently (~every 15 min) by acquiring images of the calibration cells.

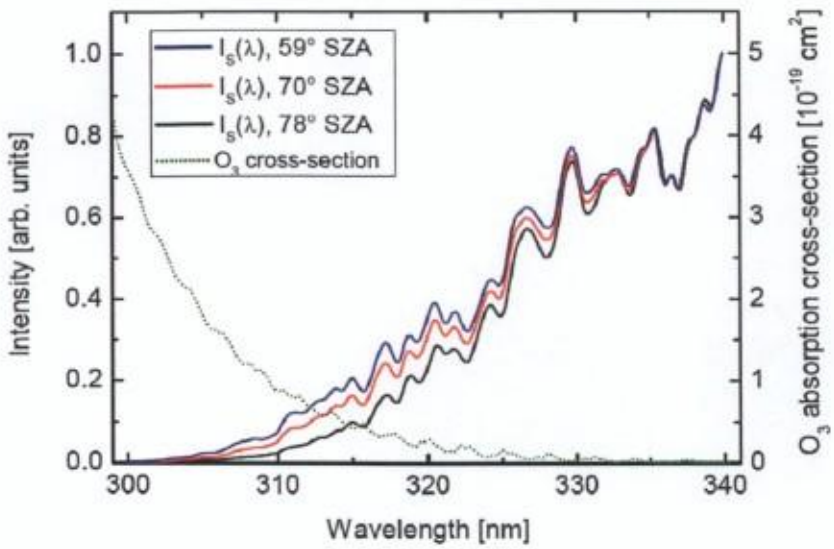

Figure 6.1: Variation of the spectral radiance of the diffused sky radiation with solar zenith angle (SZA). Shorter wavelengths are strongly attenuated at high SZA because the sun photons cross the ozone layer under a more oblique angle and hence have a longer path.

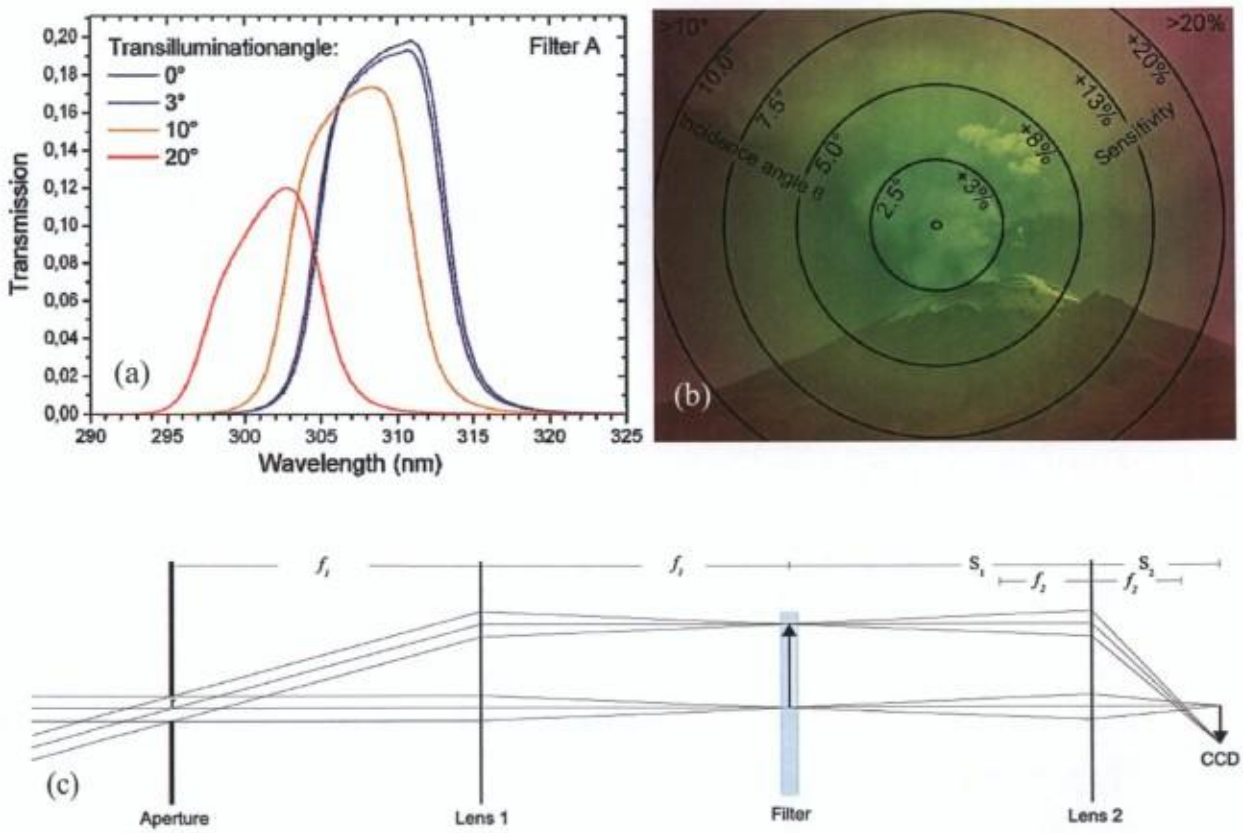

Figure 6.2:(a) Variation of the transmittance function for increasing illumination angles. The total transmittance decreases and the function shifts towards shorter wavelengths.
(b) Theoretical simulations of the variation of sensitivity to SO_2 due to this effect according to the simulation of Kern et al. (2010). (c) Optical setup designed by Kern et al (2010) to overcome the variable sensitivity issue. (Courtesy Leif Vogel)

Kern et al. (2010) have also shown that the transmittance function of the filters varies with illumination angle. The shift towards shorter wavelength and the decrease in total transmittance with increasing illumination angle are unavoidable properties of interference filters. The consequences of this are an increased sensitivity to SO_2 on the borders of the image together with a reduction of the light intensity known as vignetting (figure 6.2b). To overcome this potential problem, they built a camera with a very different optical scheme (figure 6.2c), with the filter being inserted between the two lenses, where the rays are subparallel to each other. Such a design is more complex to set up and is inferior in term of light throughput to the sensor (L. Vogel, pers. comm.). Kantzas et al. (2010) proposed a simple correction of the vignetting, which consists in dividing the measurement image by a previously acquired normalized image of a homogenous blue sky. After applying the correction method of (Kantzas et al. 2010), the spatial dependence of sensitivity was not observed anymore. Figure 6.3 shows that the normalized absorbance of the 1501 ppm.m calibration cell is homogenous instead of the 20% increase postulated by Kern et al. (2010).

Figure 6.3: Normalized absorbance of the1501 ppmm.m calibration cell. The image interior of the cell is homogeneous except for the right side, where some internal reflections on the cell's walls create some optical artefacts.

Finally, the most problematic aspect of the measurements using the SO_2 camera is the possible alteration of the relationship between the oblique column amount of SO_2 and its slant column amount. The oblique column amount is the quantity that is needed for calculating flux, while the slant column mount is the quantity that we actually measure with the camera. Two processes, discussed in chapter 2 and in (Kern et al., 2010a), can alter this relationship.

- Scattering of ambient photons into the field of view (light dilution) causes underestimation of the actual SO_2. As light dilution increases exponentially with the distance, one can limit its effect by reducing the distance between the camera and the plume.
- Multiple scattering inside the plume leads to an overestimation of the actual SO_2 column amount. However, simulation by (Kern el al, 2010) have shown that multiple scattering inside the plume has little impact over the air mass factor around 310nm, so the effect of multiple scattering on SO_2 camera measurements is thought to be limited. It can be further limited by acquiring measurements only on the optically thinner portions of the degassing plume.

6.3 Instrumental background

The core of UV cameras is the focal plane CCD (charge coupled device) sensors. A CCD sensor is constituted by a thin silicon layer connected to an array of semi-conductors elements. When the sensor is exposed to light, incoming photons hit the silicon layer, which emits electrons through the photo-electric effect. These electrons are captured by the semi-conductors (the physical pixels), which behave as electron wells, accumulating an electric charge proportional to the number of photon hitting the surface of the silicon layer above them. The wells are emptied from their electrons one after the other by applying a potential difference at the end of the sensor's rows and columns. The electronic current resulting from this flushing phase is then amplified and digitized, before being processed to reconstruct the image. An electronic offset, called bias current, is added to the "image current" during the digitization process, and will require a correction before the image can be processed. With this rough knowledge of how CCDs work, one can understand several important parameters for CCD imagery.

The quantum efficiency, $Q(\lambda)$ is the amount of electrons produced per photon through the photoelectric effect. It's a wavelength dependent quantity that is proper to each sensor model. The quantum efficiency has direct impact on the signal to noise ratio of the

instrument. For a given quantum efficiency, bigger pixel will produce a better signal to noise ratio because they collect more photons at their surface per unit of time. However this gain is achieved at the expense of image resolution.

The dark current is the current generated in the CCD arrays by other processes than the photoelectric effect. The dark current, which is also a property of the sensor model, is essentially produced by the thermo-electric effect. Therefore it is strongly dependent on temperature, and proportional to the exposure time. Quantitative photometry therefore requires cooling the sensor to a constant temperature, to maintain the dark current low and constant. Dark current can be substracted from a measurement image in post-processing, provided that some dark images (images with the shutter closed) have been acquired at the same temperature and exposure time as the measurement image.

Saturation of a pixel occurs when the amount of electrons produced during exposures exceeds the maximal capacity of its electron well. When the sensor is close to saturation, linearity between the amounts of photons and electrons is lost, and the electrons can bleed to neighbouring pixels. Thus, saturation has to be absolutely avoided for quantitative photometry. This can be achieved by reducing the exposure time or the focal aperture of the lens.

Image resolution, which is the corresponding size of image pixels, is given by the relation

$$X=X_{pix}D/D_f \qquad (6.7)$$

Where D is the distance between the plume and the instrument, D_f is the focal length of the lens and X_{pix} the physical size of the pixels in the CCD.

6.4 Choice of the components and building of the system

6.4.1 Optical parts

An Apogee Alta U260, costing 5500$, was chosen for the body of the camera. It has a very low dark current and can be cooled at 50K below ambient temperature thanks to four Peltier coolers equipped with fans, which regulate the sensor within a 0.5K range. The CCD sensor (KAF-0261E) has 512 x 512 pixelsof 20μm width. This pixel size yields a 2-5m resolution at usual viewing distance (2-5km), which is way sufficient for resolving details in volcanic plumes, while the pixels are large enough for insuring a high sensitivity and S/N ratio. The dark current of this camera is very low (~1 e-/s) as is the read-out noise (32 e-

RMS). Quantum efficiency at300-350 nm is not optimal though but instruments having better QE in that spectral area are significantly more expensive[1].

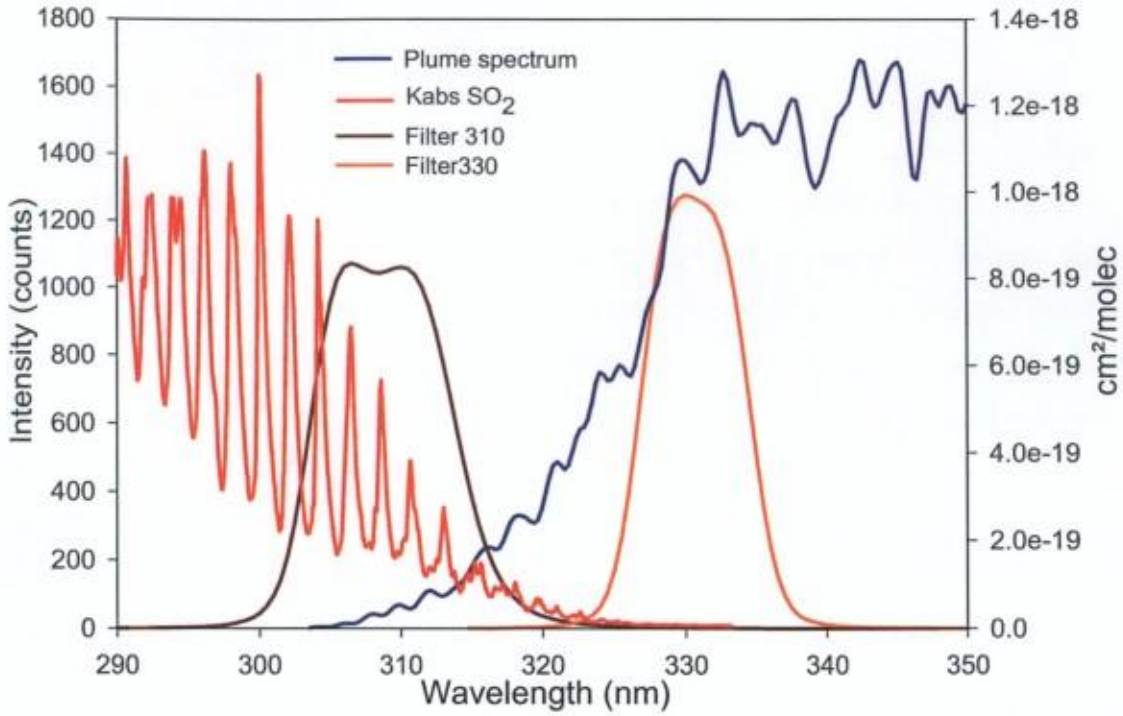

Figure 6.4 Transmittance function of the Asahi ZBPA310 and ZBPA330 filters. The absorption coefficient of SO_2 and the radiance spectrum of a SO_2 plume are shown for comparison.

Figure 6.5 The camera deployed in the field, showing its different components. (Sunshade was taken off for the photograph)

[1]Should we have had less funding constraints, we would probably have chosen an Alta U77, or an ANDOR iKon-M 934-BU2, which have a twice higher QE, but are also much more expensive.

RMS). Quantum efficiency at300-350 nm is not optimal though but instruments having better QE in that spectral area are significantly more expensive[1].

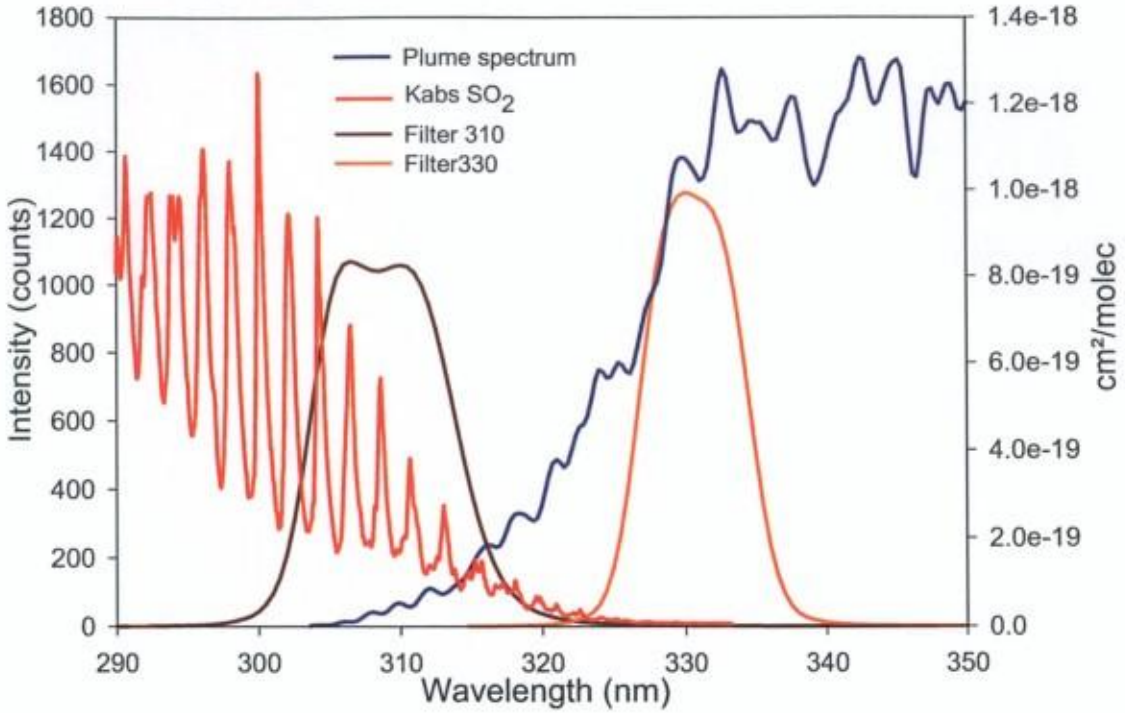

Figure 6.4 Transmittance function of the Asahi ZBPA310 and ZBPA330 filters. The absorption coefficient of SO_2 and the radiance spectrum of a SO_2 plume are shown for comparison.

Figure 6.5 The camera deployed in the field, showing its different components. (Sunshade was taken off for the photograph)

[1]Should we have had less funding constraints, we would probably have chosen an Alta U77, or an ANDOR iKon-M 934-BU2, which have a twice higher QE, but are also much more expensive.

The lens is a Pentax B2528-UV, made of UV grade silica. This lens has a fix focal length of 25mm, which corresponds to a viewing angle of about 23°, and a variable focal aperture from F2.8 to F16.

The two filters are Asahi ZBPA310 and ZBPA330, which have the centroid s of their transmittance functions at 310 and 330 nm respectively, FWHMs of 10 nm and peak transmittances of 0.65 and 0.45 respectively. The spectral transmittance of both filters is shown in figure 6.4. The filter models are the same as those used in (Mori and Burton, 2006).

6.4.2 Calibration cells

Commercial calibration cells of SO_2 are extremely expensive (1000$ per cell). Therefore, we chose to develop our own calibration cells, and after a few unsuccessful attempts, we succeeded in that work, thanks to the efficient help of Christian Hermans from the Belgian Institute for Space Aeronomy. Five quartz cells with sealable Pyrex filling tubes were purchased from NSG® at the price of 150$ each (NSG model 37UV5 with 0.5cm length). The cells were first vacuumed to ~10^{-4} hPa atmosphere, and then filled slowly with pure SO_2 up to the required pressure, measured with a precise and accurate manometer. The cells were sealed right after being filled with a small blowtorch. Negative pressure gradient between the interior of the cells and the atmosphere sealed the semi-molten Pyrex glass immediately, hampering SO_2 to leak or air to flow inside the cells. The concentration of SO_2 in the cells after sealing was precisely measured using an FTIR spectrometer (model BRUKER IFS120Mwith a resolution of 0.01 cm^{-1}) and the reference absorption cross-section of (Vandaele et al., 1994). The concentrations inside the cells are listed in table 6.1. We optimized the concentrations in our calibration cells in order to use the camera in plumes of strong SO_2 emitters, where column amounts commonly reach several grams per square meters. Absorbance varies linearly with respect of column amount until about 1500 ppm.m but increasing deviation from linearity was noted above this (see figure 6.6 and also Kazahaya, 2004, Dalton et al, 2009).

Pressure inside the cells (Torr)		SO_2 column amount		
Manometer	*FTUV calcul.*	*ppmm*	*molec/cm²*	*g/m²*
150.4	148.9	980	2.454E+18	2.609
229.9	228.1	1501	3.760E+18	3.997
309.7	323.1	2126	5.326E+18	5.662

Table 6.1: Partial pressure and column amount of SO_2 inside the three calibration cells.

6.4.3 Filter switcher

Once again, cost effectiveness was the first argument in the conception of a filter switcher. Commercial systems, controllable through a USB interface, are available, but are expensive and require an additional adaptator if used with a C-mount lens. A manual filter switcher was thus built from the moving part of a slide projector. Filters are mounted on the switcher by a clamping system (figure 6.5b). The whole system is simple and relatively robust, but requires a sunshade to hampers unfiltered light to be reflected on the inner side of the filters into the field of view of the lens. Manual switching of the filter takes about 1.5 second, so the typical time needed to acquire a pair of images is about 5 seconds. This delay may lead to some visible plume displacement between the 310 and 330 images that will cause some border effect on the processed SO_2 image. This effect was however not noticed on the Turrialba data because the plume displacement in term of pixel was small given the observation distance.

6.4.4 DOAS mount

An additional metal element was added to the camera to allow the collimating lens of a mini DOAS spectrometer to be mounted and aligned with the camera field of view. The spectrometer was an AVANTES Avaspec 2048 with a 0.27nm resolution.

6.5 Camera setting and data acquisition

The camera is powered by a car battery, via a DC/AC converter and connected to a laptop by a USB cable. The MaximDL software is used to control the camera. This software allows easy acquisition of long sequences of images with predefined exposure time and delay between two acquisitions. It also controls the thermal stabilization of the camera. The images are acquired with a F11 lens opening and exposure time varying between 0.2 and 0.7s, depending on the ambient luminosity.

Probably the most difficult part of operating an SO_2 camera in the field is choosing the right exposure time. We can see from figure 6.4 that the radiance at 330 nm is five to ten times higher than it is at 310nm. The ideal exposure time is thus a compromise between getting a sufficient S/N ratio with filter 310 and avoiding saturation on filter 330. This problem can be solved by using a different exposure time for each filter and a scaling factor in the post processing job. Due to changing of ambient light condition (caused mostly by variation of Solar Zenith angle and cloud cover) calibration must be performed regularly, by imaging the different calibration cells in a plume free zone. Typically this is done after each sequence of 100 pairs of images.

MaximDL acquires the images as FITS files (Flexible Image Transport System), a format used for astronomy. Each file weighs 520 Ko and contains a header with the acquisition date and time, the exposure time, the instrument temperature plus other instrumental parameters.

Simultaneously to the camera operation, UV spectra are acquired every 4 seconds with the mini DOAS spectrometer. The aim of this is to control the accuracy of the camera retrievals and if needed, applying a correction factor. The spectrometer is powered through a USB cable and controlled by laptop using the Mobile DOAS software developed by Caroline Fayt and Alexis Merlot at the Belgian Institute for Space Aeronomy. Each spectrum is the result of averaging 10 spectra acquired with a 4ms exposure time.

6.6 *Data Processing*

The creation of a software for processing and analysing the images of the SO_2 camera is probably the most innovative part of the camera work. The software, written in IDL, is interactive and easy to use, provided that all the input data have been acquired. The workflow of this algorithm is described in this section.

6.6.1 Precalibration

As a preliminary step, the images are precalibrated for removing the electronic offset and the dark current, and correcting the vignetting effect. These three operations are carried out using the pre-existing calibration routine of MaximDL. The vignetting correction needs a pair of pre-acquired images of a homogeneous blue sky (Kantzas et al. 2010). We use a series of ten pairs to decrease the noise induced by this operation. The intensity of the vignetting increases with the lens aperture (F-number) and is higher for images recorded with filter 310. Therefore, we pre-acquired two series (one per filter) of homogeneous images with each possible F-number. The appropriate pair of correcting images is chosen depending on the focal aperture used for acquiring measurement images.

6.6.2 DOAS measurements

The DOAS spectra are processed using the QDOAS software, developed by Caroline Fayt and Michel Van Roozendael (Fayt and Roozendael, 2001). The fitting window that is used in the DOAS processing spans315 to 330 nm, which, according to Kern et al. (2009), is better suited for high SO_2 burdens. Indeed, we found that fitting using this window produces the best measurements of our calibration cells and yields spectrally independent residuals in concentrated volcanic plumes such as those measured at Turrialba volcano. The reference spectrum used for the fitting is a blue sky spectra acquired in Brussels. Ozone, Ring effect, and NO_2 are fitted together with SO_2 using the reference spectra of Bogumil et al. (2003), Vandaele et al.(1994) respectively.

6.6.3 User input

Once the images are pre-calibrated, the user selects the series of images (FITS files) to be processed. The files are read and stored in a n-element data structure, where n is the number of image pairs composing the series. Each element of the structure is composed of two 512 x 512 arrays (for storing the pair of images), a string for the date and time and a real number for the exposure time. Another structure is created for storing the results produced by the program (SO_2 maps, SO_2 profiles, SO_2 flux, acquisition time, and wind speed).

The 310nm image of the first pair is displayed and the user defines two rectangular regions free of SO_2, one vertical and one horizontal, which will be used to reconstruct the background values of normalized absorbance. The user also defines two lines of pixels on the image: one parallel to the plume, which will be used to measure the wind speed, and the other perpendicular, which will be used to compute the SO_2 flux.

Then, normalized absorbance images of the calibration cells are constructed and displayed. The user can choose the portion of the calibration cells that will be used to retrieve the SO_2 in the plume. The aim of this operation is to exclude the borders of the cells from the analysis. A calibration array is built with the CAs of each cell and the average value of the normalized absorbance of each cell image. A typical calibration array is plotted in figure 6.6.

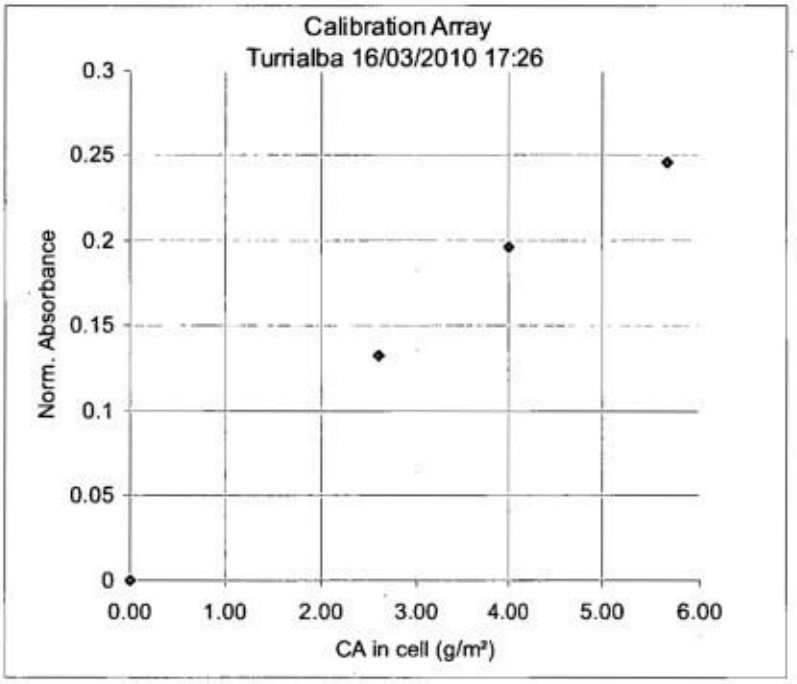

Figure 6.6 : Calibration array, obtained in Turrialba. The measured normalized absorbance of the cells is plotted as a function of the actual column of the cell. The relationship becomes slightly non linear for the most concentrated cell.

6.6.4 Computation of SO_2 maps

SO_2 maps can now be computed by the program. This is done by a routine that is called for each pair of images. The routine first calculates the vertical and horizontal variation coefficients (k_x and k_y) of the background radiance based on the two user defined SO_2-free regions (see figure 6.7a). The background radiance is then calculated over the whole images using a plane interpolation:

$$R_0(i,j)=R_0(c) + k_x i + k_y j \qquad (6.8)$$

Where i and j are the index of pixel row and column and $R_0(c)$ is the value of the background value at the intersection of the vertical and horizontal rectangles. Then, the normalized absorbance is calculated using equation 6.4 and the SO_2 column amounts are interpolated in the calibration array. The 512x512 array SO_2 map produced by this routine, as well as the header information are stored in the structure containing the results.

An optional routine was created to correct the SO_2 map using the DOAS measurements as a reference. First, the pinpoint DOAS measurements have to be collocated to the SO_2 map, because the DOAS telescope is not rigorously aligned with camera. For this, the map is divided into sub-arrays of 20x20 pixels (corresponding to the 1° opening of the telescope). The routine identifies the sub array whose temporal evolution of the SO_2 CA matches that measured with the DOAS. In practice, this is made by finding the sub-array (x,y) that yields the lowest least square sum $\sum_t \left(\frac{\partial \overline{C}_{x,y}(t)}{\partial t} - \frac{\partial \overline{C}_{DOAS}(t)}{\partial t} \right)^2$, where $\overline{C}_{x,y}(t)$ is the time series of SO_2 SCA averaged over the sub-array and $\overline{C}_{DOAS}(t)$ is the time series of SO_2 CA of the DOAS measurement.

A 3rd order polynomial is fitted to the $\overline{C}_{x,y}$ versus $\overline{C}_{DOAS}$ data series. Finally, the whole SO_2 map is corrected by applying the coefficients of the polynomial to the CAs of every elements of the 512x512 array.

6.6.5 Calculation of the wind speed and flux

For each SO_2 map, a vector of the CAs is created for the pixels of the parallel profile. Then, the derivative of the CAs vs. pixel number is computed numerically and stored in a vector. The same operation is applied to the next image. A least square minimization routine is used to find the number of pixel that produces the best match between the two derivative vectors. This number of pixels is converted into meters using equation 6.7 to obtain the displacement of the plume under the effect of the wind. The wind speed is obtained by dividing this displacement by the time interval between the two pairs of images.

The flux is calculated by summing the SO_2 CAs of all the pixels of the perpendicular profile and multiplying that sum by the pixel size and the wind speed.

6.6.6 Final output of the program

The final output produced by the program consists of an image file that contains a colour map of the SO_2 distribution in the plume and graphic representations of the SO_2 CA along the two user-defined profiles. The date and time, flux and wind speed are also displayed on the image. Such an image is displayed in figure 6.7c. A separate text file is also created by the program for storing the time series of these parameters. The results obtained with the camera during a field campaign in Turrialba volcano (Costa Rica) are discussed in the next chapter of this thesis.

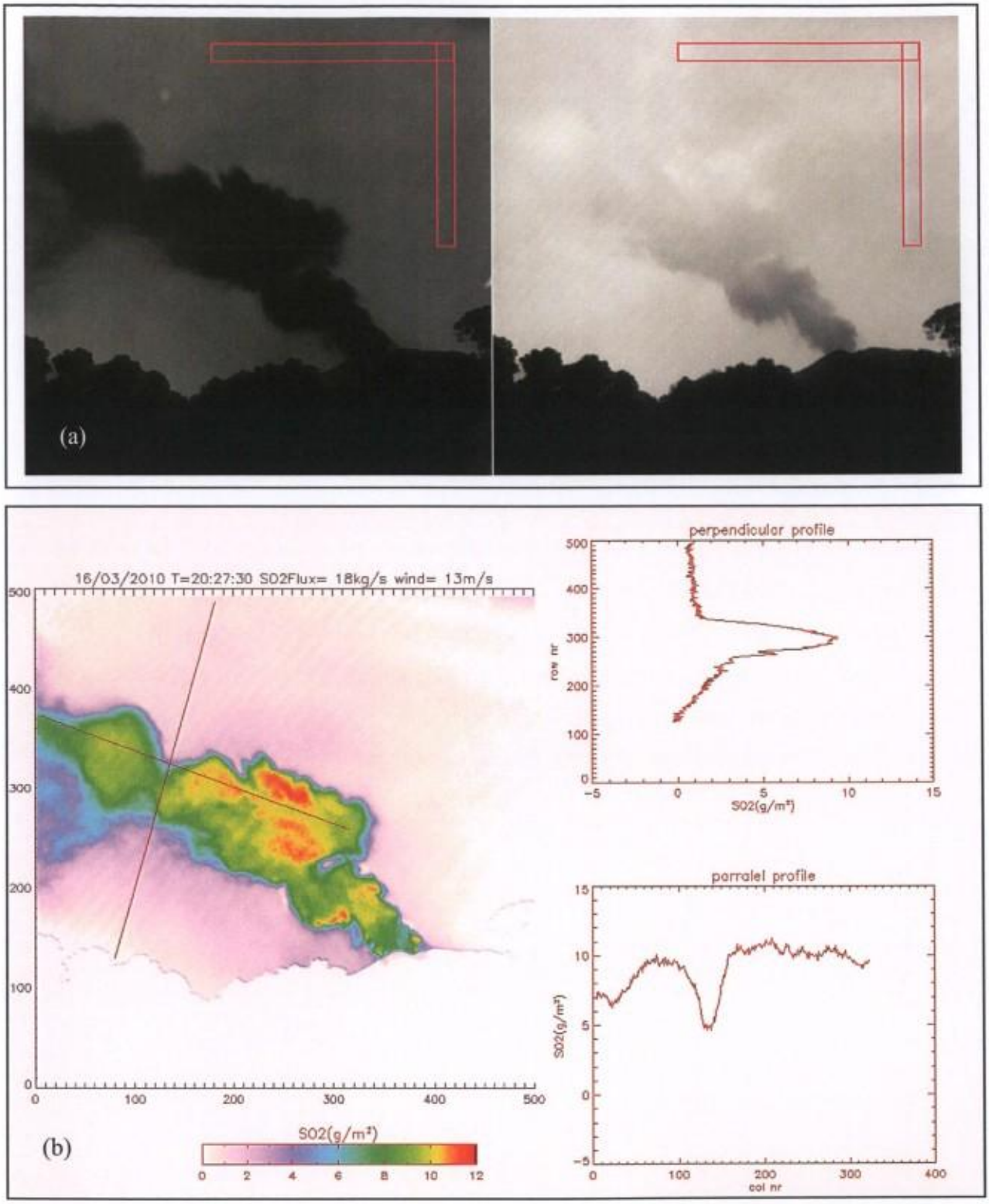

Figure 6.7: (a) Image of the plume of Turrialba volcano recorded with the 310nm bandpass filter (left) and with the 330 nm filter (right). Both images have already been corrected for bias, dark current and vignetting. The red rectangles are the user defined SO_2-free zone where the vertical and horizontal variation coefficients of the background intensity are evaluated. (b) Synthetic image produced by our data processing software. The SO_2 map is shown on the left part together, the two red lines being the user-defined profiles. The charts of SO_2 along the parallel and perpendicular profile are displayed respectively in the lower and upper right of the figure.

Chapter 7: Space and ground based measurements of SO_2 emissions from Turrialba Volcano (Costa Rica)

7.1 Abstract

This chapter is based on an article submitted for publication to the Bulletin of Volcanology. Systematic measurements of sulphur dioxide emitted by Volcán Turrialba (Costa Rica) are reported for the period 2009-2010. These measurements were obtained using images from ASTER (Advanced Spaceborne Thermal Emission and Reflexion radiometer), OMI (Ozone Monitoring Instrument) and the ground based UV camera described in chapter 6. These three very different instruments provide flux measurements in good agreement with each other, which demonstrate that they can be integrated for monitoring SO_2 fluxes. Fluxes from Turrialba increased fourfold in January 2010, following a phreatic explosion that formed a degassing vent in the Western crater of Turrialba. Since then, the flux are very high (30-50kg/s) but seems showing a slowly decreasing trend. We interpret this evolution as the start of open vent degassing from a recently intruded magma body. The opening of the degassing vent decreased the confining pressure of the magma body and allowed the gasses to bypass the hydrothermal system.

7.2 Introduction

Volcán Turrialba is an basaltic-andesitic stratovolcano in Costa Rica, located at the Easternmost end of the Cordillera Volcánica Central(CVC), a chain of active volcanoes that results from the subduction of the Cocos plate under the Caribbean plate (e.g. Carr et al., 2003). Turrialba summit culminates to 3340m a.s.l., and is only nine km distant from Volcán Irazú, another major volcano of the country. The rocks forming the edifice range from basalts to dacites. Three NE-aligned summit craters open inside a NE breached depression. Reagan et al (2006) did not find any debris avalanche associated with this structure so they suggested that it was formed by erosion during a hiatus in the activity of the volcano between 50000 and 8000 years BP). The last eruptive period, in 1864-1866 produced phreatomagmatic explosive activity and small pyroclastic flows (Reagan et al. 2006).

Starting in 1999, microseismicity under the volcano increased significantly (Barboza et al., 2003). Fumarolic activity has also been showing a noticable increase since 2002, with new fumarolic vents and fractures opening in and outside of the crater area. Acidic gases and aerosol emissions have been causing environmental acidification through wet and dry deposition. Severe chemical burns (chlorosis and necrosis) have affected both the native

mountain forest and the crops. Intense corrosion to the metallic parts of buildings and other infrastructure was also reported. (OVSICORI-UNA reports for Turrialba 2005-2010). Due to prevailing winds, these damages were concentrated on the upper western half of the volcanoes. However acidic deposition has recently been detected at localities as far as Santa Cruz de Turrialba, Pacayas, Llano Grande, the summits of Irazú and Barva volcanoes, and Guápiles, at a distance as far as 30-40 km from the top of Turrialba volcano (OVSICORI-UNA, 2010).

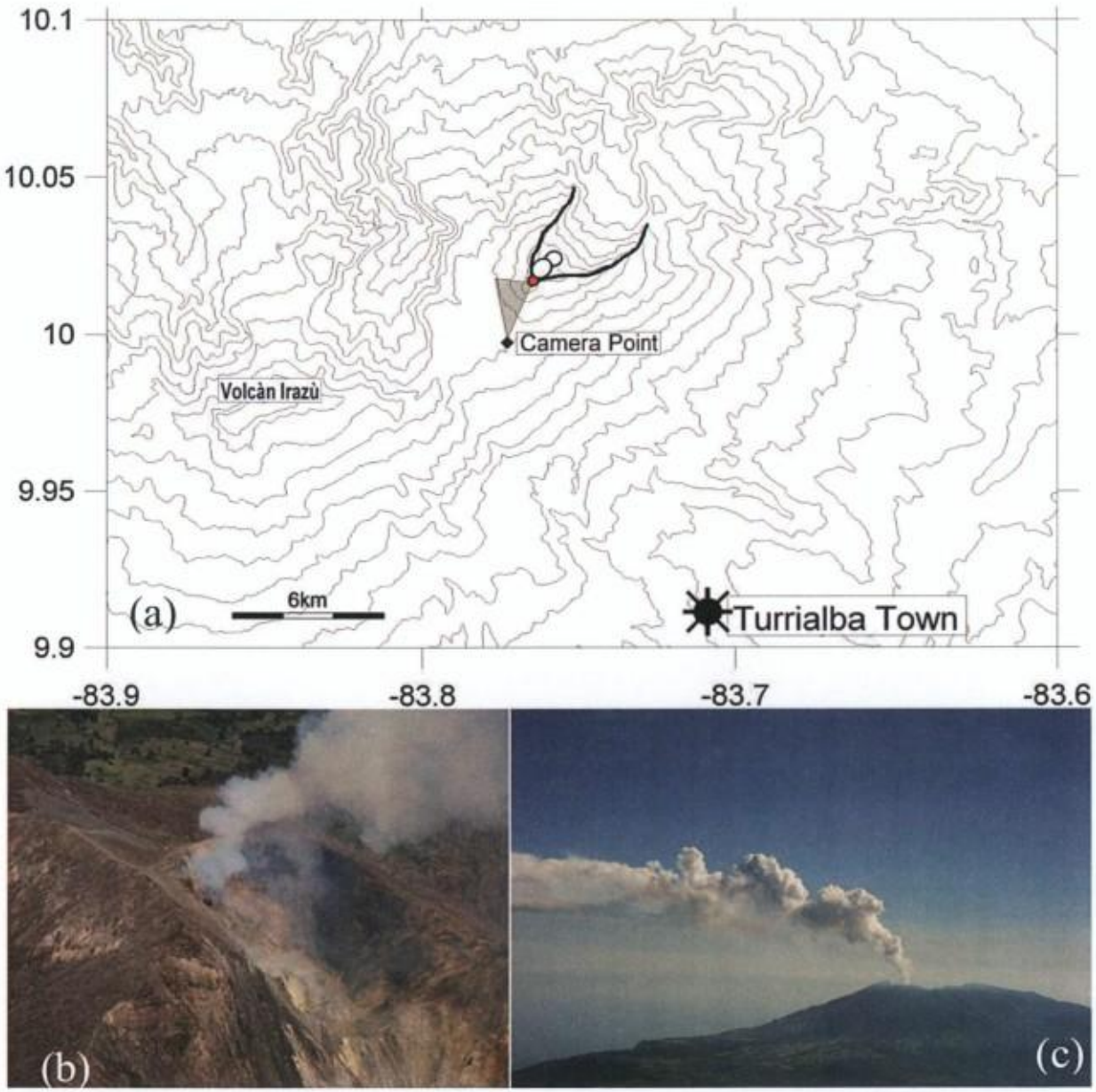

Figure 7.1: (a)Topographic map of the area of Volcán Turrialba showing the active western crater (red circle) and the position from where the UV camera measurements were done. (b) Degassing vent in the western crater on the 29 may 2010 (c) Degassing plume seen from the West on the 21July 2010 (photos courtesy of Federico Chavarría-Kopper).

Vaselli et al. (2010) have reported the result of regular gas analyses from the fumaroles in the central and western summit craters. Based on the increase of the SO_2/H_2S, $(HCl+HF)/CO_2$, S_{tot}/CO_2 ratios, they identified a three stage compositional transition of the fumaroles. Hydrothermal stage (since the eighties until fall 2001) was characterized by predominance of H_2O and low condensable species CO_2 and H_2S as well as by low temperature. In the hydrothermal/magmatic stage, temperature was still low (around 90°C, the boiling point of water at the altitude of the volcano), but increasing concentrations of acidic gases (SO_2, HCl and HF) were found in the fumaroles. This was indicating that the hydrothermal system was still controlling the temperature of the fumarolic discharge, but was not able anymore to scrub all the acidic gases emitted at depth by the magma chamber. Finally, since 2007 the composition and high temperature of the fumaroles indicate that the gases were directly supplied from the magma chamber with only limited interaction with the hydrothermal system. To explain these changes, Vaselli et al. (2010) proposed two different hypotheses:

(1) A cyclical process in the mass and heat balance between the magma chamber and the hydrothermal system, as has already been observed on other volcanoes.

(2) The intrusion of a magmatic body, which would supply increasing amounts of heat and acidic species until progressively drying out the overlying hydrothermal system and exceeding its scrubbing capacity.

The implications of these two hypotheses are profoundly different in terms of the future evolution of the volcano. While the first one implies only a localized risk of small scale phreatic explosion, the second can lead to much stronger and potentially hazardous magmatic eruption or eruptive period. Vaselli et al. (2010) therefore recommended implementing a closely monitoring program to discriminate between these two hypotheses and forecast an eventual magmatic activity.

This paper presents systematic SO_2 flux measurements obtained by processing images of OMI and ASTER satellites from September 2009 to August 2010 and with a UV camera in March 2010. We demonstrate that the SO_2 flux data obtained from these three sources are in a good agreement so that these methods are complementary. We also discuss the insights of these measurements into the ongoing magmatic-hydrothermal processes under Turrialba Volcano.

7.3 Instruments and methods

ASTER is an imaging multispectral radiometer that measures the thermal infrared radiation (TIR) emitted by the Earth surface in five spectral bands numbered B10 to B14 and respectively centered at 8.29, 8.63, 9.07, 10.66 and 11.32 μm. ASTER has a 90m resolution in the thermal infrared, which allows measuring SO_2 in small scale plumes, such as those typically produced by passive degassing. Its sensitivity is lower than OMI, because SO_2 absorption coefficient is not as strong in the TIR as in the UV. However the much finer ground resolution of ASTER compensates its lower sensitivity so that the detection limit in terms of lowest detectable flux is roughly equivalent between the two sensors (Campion et al., submitted). ASTER images are only 60km wide and are not acquired in continuous mode (Pieri and Abrams, 2004). Instead, image acquisitions can be programmed according to the needs. Therefore the rate of image acquisitions can be quite variable, between twice a week and a few per year. ASTER images are processed with the radiance ratio algorithm (Campion et al., 2010) to retrieve SO_2 column amounts (CA). The main advantage of this algorithm is its low dependence on surface emissivity, water vapor and sulfate aerosols. This is especially useful in tropical atmosphere, where atmospheric humidity is high and plumes usually contain a high load of condensed aerosol. The uncertainty on the retrieved CAs is usually about 20% for Turrialba plumes. Meteorological clouds located under the volcanic plume can increase this uncertainty significantly while clouds between the plume and the sensor completely mask the signal produced by SO_2 absorption. However, the band ratio algorithm contains a cloud detection routine excluding them from the analysis, as well as an error estimation routine. Plume temperature, a very important parameter for the accuracy of the retrievals, is estimated using opaque portions of the plume, often encountered close to the vent.

OMI is an imaging spectrometer that measures the ultra violet radiation backscattered (BUV) by the Earth surface and atmosphere over a 2700km swath (Levelt et al., 2006). OMI pixels are 13x24 km rectangles at Nadir and are gradually stretching at higher viewing angle off Nadir. This unprecedented ground resolution for a BUV satellite, together with its high sensitivity to SO_2 (5 DU in the lower troposphere) allows OMI to detect small scale plume produced by passive degassing (e.g., Carn et al., 2008). OMI SO_2 data are produced in near real time using two algorithms, the Band Residual Algorithm (Krotkov et al., 2006) for low abundance boundary layer SO_2, and the Linear Fit (Yang et al., 2006) for volcanogenic SO_2 that has usually a higher altitude and concentration.

In this study, we used the standard SO_2 product from OMI, which is publicly available athttp://mirador.gsfc.nasa.gov/cgi-bin/mirador/collectionlist.pl?keyword=omso2. Images are downloaded as HDF files containing four values of the SO_2 column amount, retrieved using four different a priori vertical profiles. These are called PBL_SO2, TRL_SO2, TRM_SO2 and STL_SO2 and correspond to SO_2 plumes centered at 0.7, 2.5 7.5 and 15 km respectively. For this study, the effective SO_2 column amount of each pixel is interpolated using these four values and an altitude of 3500m (for ECMWF wind speed of more than 10m/s at the volcano elevation) or 4000m (for slower ECMWF wind value), which are the values observed usually for Turrialba plumes. Fluxes are computed from the images using an IDL routine that defines transects as lines or columns of pixels across the plume, sums the CAs of every pixels of the profile and multiplies that sum by the wind speed times the cosine of the angle between the transect and the plume direction. The wind speed value comes from the ECMWF model at the time of overpass, coordinate of the volcano and plume altitude. The final flux value computed from an OMI image is obtained by averaging the fluxes from the six first profiles, excluding the one that is the closest to the volcano to avoid subpixel dilution. The accuracy of OMI measurement depends strongly on the accuracy of plume height estimation. For Turrialba, sensitivity tests show that a 500m overestimation of the plume altitude yields a ~20% underestimation in the retrieved CA. Further error arises from the non-linear absorption of UV radiations by high column amounts of SO_2, and from the sub-pixel distribution of the meteorological clouds and the SO_2 plume.

Ground based data were collected using an Alta U260 UV camera equipped with two narrowband pass filters centered at 310 and 330 nm mounted on a manual filter switcher (Mori and Burton, 2006). Images were acquired every 5 sec with a diaphragm opened at F11, and an exposure time varying between 0.5 and 0.8 s, but identical for both filters. All the images were corrected for vignetting using pre-acquired images of a cloud free sky, following the method proposed by Kantzas et al. (2010). For each pair of image, the normalized absorbance is calculated with

$$\alpha_{i,j} = \ln\left(\frac{I0_{i,j}^{310}}{I_{i,j}^{310}}\right) - \ln\left(\frac{I0_{i,j}^{330}}{I_{i,j}^{330}}\right) \qquad (1)$$

$I_{i,j}^{310}$ and $I_{i,j}^{330}$ are the vignette corrected light intensities measured with filter 310 and 330 respectively, and $I0_{i,j}^{310}$ and $I0_{i,j}^{330}$ are the synthetic background intensities, constructed with a planar extrapolation based on SO_2 free regions of the pair of images. The normalized absorbance image is then compared to calibration images of SO_2 free sky. These calibration images were acquired at the end of each series of 100 image pairs using quartz cells

containing 0, 980, 1501 and 2126 ppm.m of SO_2. Wind speed was calculated by measuring the displacement of SO_2 spikes and troughs measured over a profile parallel to wind direction. SO_2 flux is calculated by summing the SO_2 slant concentrations of each pixels of a profile perpendicular to the plume and multiplying by the equivalent length of the pixels and by the wind speed. All these operations are executed automatically using the program RobTraiteCamSO2, written in IDL. (See chapter 6 for more methodology details). Error on flux measurements come from radiative transfer effects (Kern et al., 2010a, 2010b) and uncertainty on the observation geometry

7.4 Results

During the reporting period, about 30 images of Turrialba volcano were acquired by ASTER. Many of them were too cloudy for providing useful information. These images were not analyzed. A screening was also done before analyzing OMI images, excluding the images for which the SO_2 plume was masked by high altitude clouds and those where no clear plume transport direction could be identified.

SO_2 maps produced with ASTER images are displayed in figure 7.2. ASTER's ground resolution is high enough for identifying the plume direction and structure, and for interpreting its transport mode following the terminology proposed by Kinoshita (1996). Coherent plume transport (linear dispersion) predominates, except perhaps on 21 April, where a fan structure in a weak wind field could be inferred. These observations suggest that, on the considered days, volcano topography had little influence over the wind field at the plume altitude. The ASTER SO_2 maps show homogeneous plumes, with no obvious puffs. Average fluxes measured by ASTER on each analysed images are reported as circles in figure 7.6. They ranged from 9 to 50 kg/s, showing a brutal increase in the beginning of 2010 and a progressive slow general decrease after that.

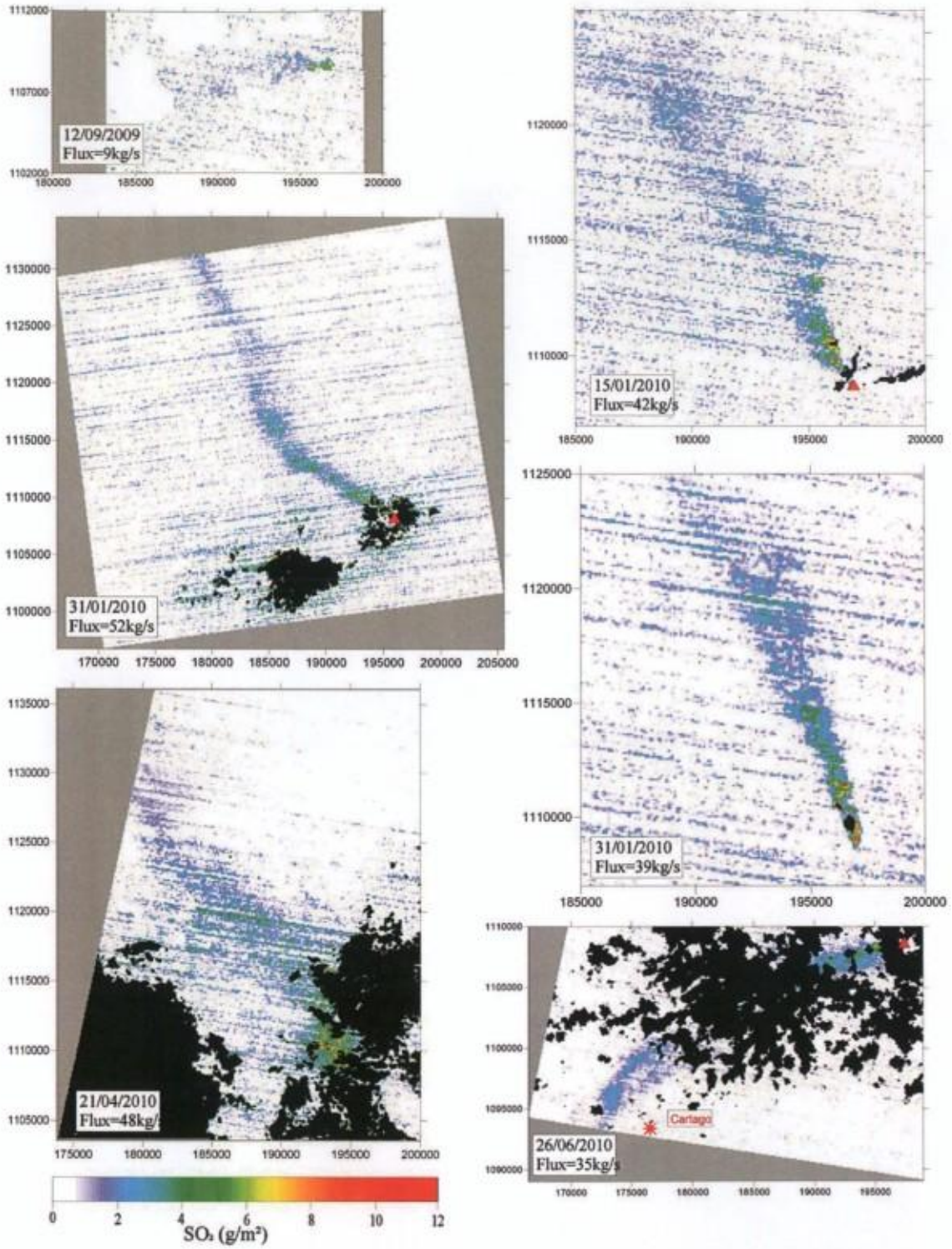

Figure 7.2: SO_2 maps of Turrialba plume generated with ASTER images. Colour scale of SO_2 column amounts is in g/m² and is the same for all the maps. Black spots are pixels where the thermal contrast between the plume and the underlying surface was too low to perform retrievals (clouds or night cooled highland ground).

Some of the OMI SO_2 maps analyzed in this work are displayed in figure 7.3. The distribution are not as spatially resolved as with ASTER due to the much coarser pixel size of OMI, but the noise in the retrieval is one orders of magnitude lower ($1g/m^2$ is equal to 35 Dobson Unit). On many days of 2009, no plume could be detected by visual inspection of the SO_2 images. The detection limit of OMI in terms of flux depends on the reflectivity, on the plume altitude and on the dispersion of the SO_2 by the local wind fields. In 2009, the SO_2 plume could be detected only in weak winds and low cloud conditions. In 2010 however, SO_2 is detected every day, and OMI SO_2 maps (showed in figure 7.3) show that emissions from Turrialba affect wide areas around the volcano. Although no strict comparison can be done due to the lack of simultaneous images, the fluxes computed with OMI show a trend similar to that of ASTER but possibly with slightly lower value and a stronger spread. This is thought to result from the coarser pixel size of OMI.

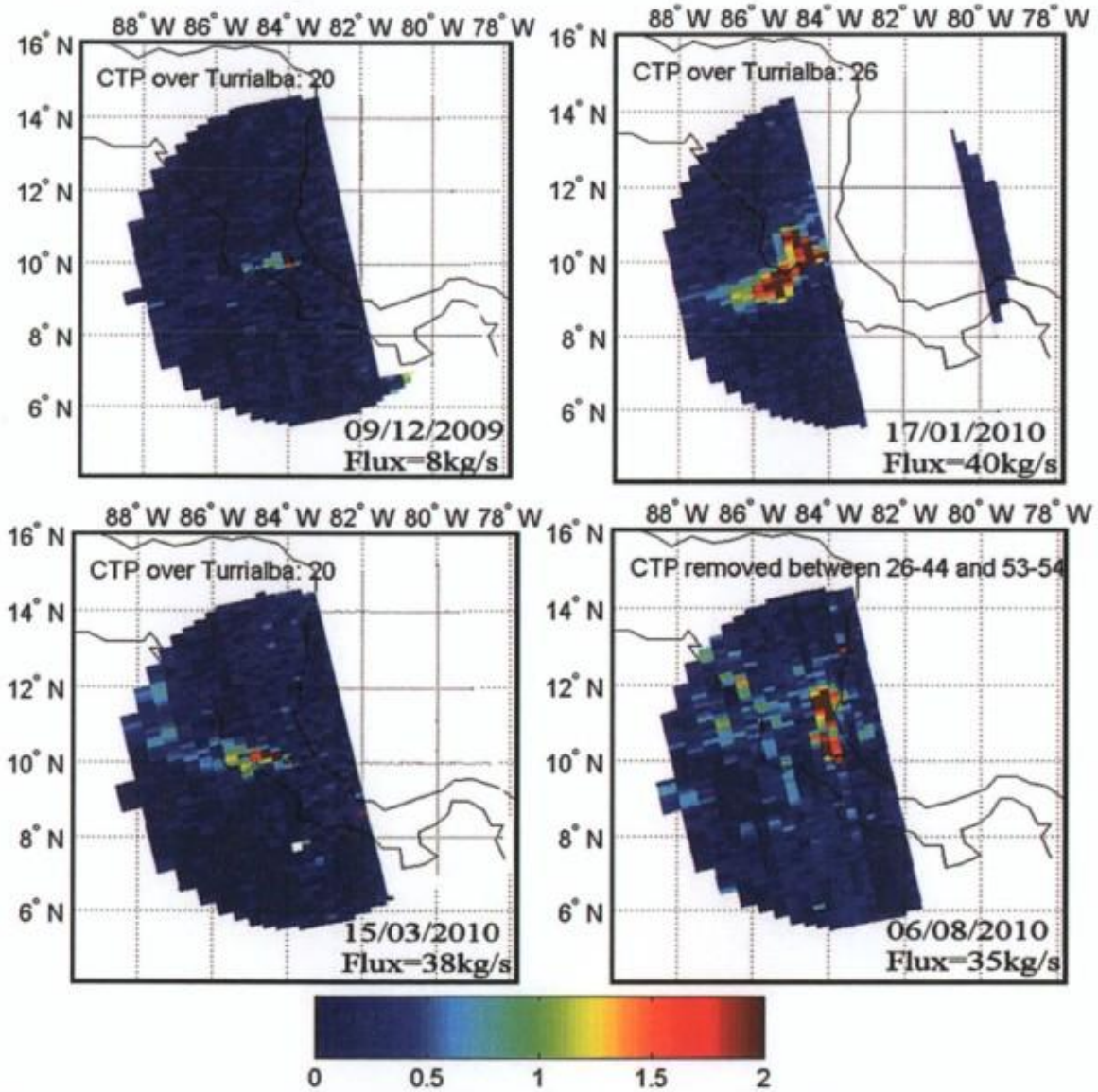

Figure 7.3: SO_2 maps of Turrialba plume generated using OMI data. Colour scale of SO_2 column amounts is in Dobson Units ($1DU=0.029g/m^2$) and is the same for all the maps.

Measurements with the UV camera were taken from a location 2.8 km South of the active crater (see map in figure 1), during a campaign on 15th and 16th March 2010. Examples of SO_2 images are shown in figure 4. More results are also available as GIF animations in the supplementary material available in the online version of the article. The presence of concentrated puffs is obvious in the images of figure 4. This is also reflected in the periodic flux variation in figure 7.5, each peak in the graph being associated with a puff crossing the measurement line. Interestingly, the puffing behaviour was not detected on the satellite images, presumably because the typical size of the puffs (100-200m according to the UV camera measurements) is too small to be resolved by ASTER and a fortiori by OMI. A comparison between the time series of flux and the RSAM (Real-time Seismic Amplitude Measurement) recorded on the rim of the crater shows no obvious correlation between the two data sets. Although the sequences of measurements are too short (10 min each) to draw definitive conclusions, this could suggest that the puffing is caused by unstable gas flow in the upper conduit or by at-vent atmospheric dispersion processes rather than by actual variation of the magma degassing.

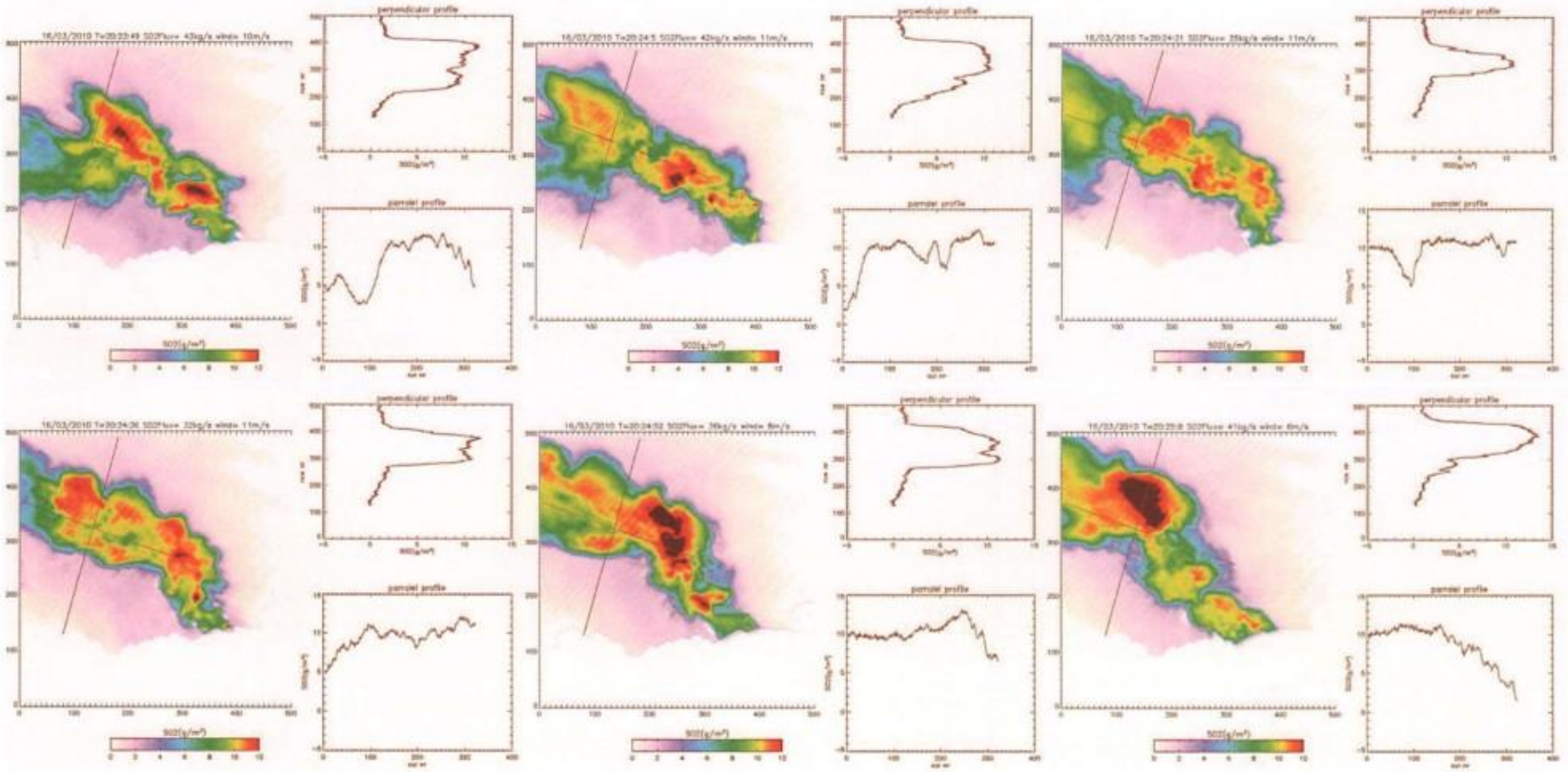

Figure7.4: SO_2 measurements obtained with the UV camera. The right frame of each image is a map of the column amounts of the plume, the two left frames are the column amount profiles measured over profiles perpendicular and parallel to the plume transport axis.

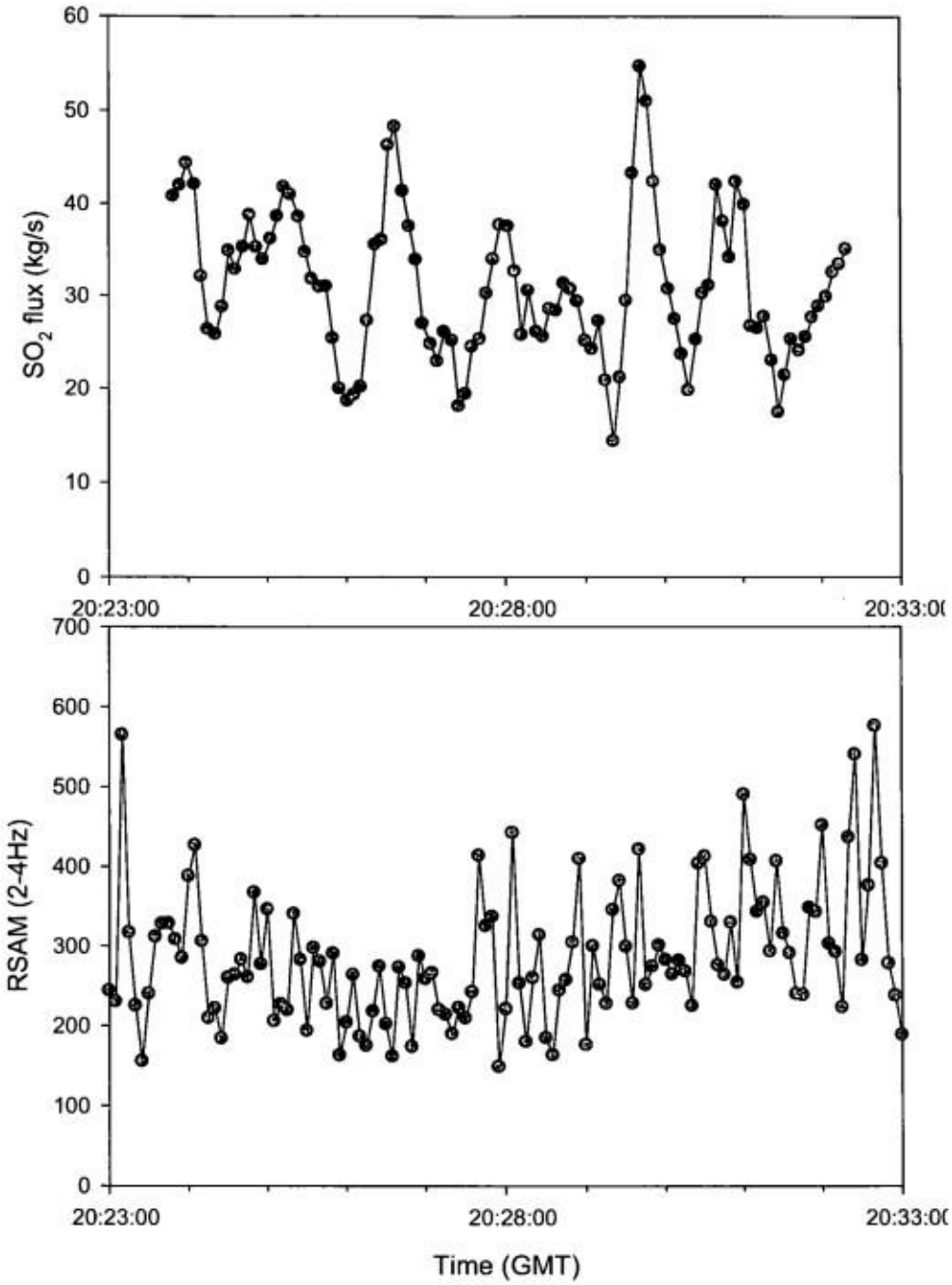

Figure7.5: Top panel: Evolution of SO_2 flux measured with the UV camera on 16th March 2010. Each peak in the flux was associated to the passage of a puff across the profile traced over the field of view of the camera. The' simultaneous record of RSAM (bottom panel) does not show any correlation.

7.5 Discussion

7.5.1 Comparison between the three methods

A remarkable aspect of this study is the good level of agreement between the fluxes inferred from the three observational methods (see figure 7.6). One should note, however, that we have here analyzed only images acquired under good conditions, i.e. not excessively cloudy sky and a well established wind field. In these conditions, all the three methods give accurate results and can be integrated for monitoring purposes. Each of these methods is indeed complementary. OMI provides regular images and can provide measurements even if there is a low cloud layer between the surface and the plume, but has limited precision due to its coarse pixel size. ASTER has better imaging capacity and precision, except for cloudy scenes, but its imaging frequency can represent an issue for regular monitoring. It's also worthwhile noting that both satellite methods yield flux values that depend on auxiliary data (plume height and wind speed) that can themselves be inaccurate. With the UV camera, on the contrary, these parameters can be determined accurately. However, accurately operating a UV camera requires a suitable observation point that has a cloud-free and sub-perpendicular view to the plume. It also requires the deployment of a team of 2 persons on the field, while satellite measurements can be made comfortably from an office. High temporal and spatial resolutions measurements with the UV camera allows insight into the short time scale variation in magma degassing that satellite cannot access. We believe that an ideal SO_2 monitoring program should include these three methods because they are extremely complementary between each other and with the classical DOAS measurements.

7.5.2 Temporal evolution and significance of the SO_2 fluxes

A significant increase of the fluxes is noted after early January (figure 7.6). From close to ASTER and OMI detection limit (5-10 kg/s for Turrialba), fluxes increase more than fourfold, reaching 30-50 kg/s. This increase coincides with a phreatic eruption on 5th January, which opened a new degassing vent in the west wall of the Western crater. This vent was (and is still, at the time of writing this article) emitting permanently high pressure and high temperature gases, causing jet like noise and incandescence of its walls. The flux values measured since early January 2010 place Turrialba among the five strongest permanent volcanic SO_2 emitters for the year 2010 (together with Ambrym, Etna, Nevado de Huila and Tungurahua).

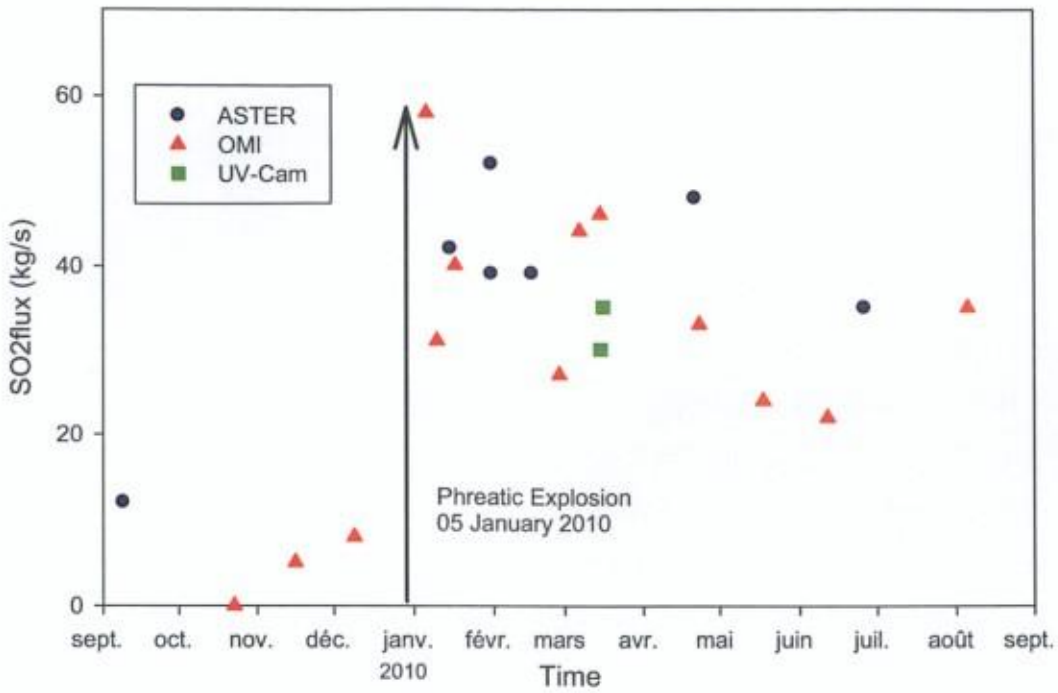

Figure 6 : Time evolution of the SO_2 fluxes emitted by Turrialba from September 2009 to September 2010, as measured using the ASTER and OMI satellite sensors and the ground based UV camera.

These high SO_2 flux values constitute a strong evidence that fresh, gas-rich magma has recently intruded or is intruding under Volcán Turrialba. An old magmatic body (dating for example from Turrialba last eruption) would likely be sulphur depleted and not be able to produce such a massive degassing. The opening of the 5 January vent probably promoted degassing of the intruding magma by locally decreasing its confining pressure, and allowed the gas to bypass the hydrothermal system. This agrees with the marked decrease in vigour and temperature of all the other fumarolic fields after the opening of the degassing vent (see figure 7.1b).

Fluxes have been remarkably high since early January although no magma has yet been emitted. We suggest that a mechanism of convective endogenous degassing (Kazahaya et al. 1994) is taking place under Turrialba to explain these observations. A calculated cumulative amount of about $1x10^6$ Tons of SO_2 has already been degassed from January to September 2010. Considering a magma with a density of 2.5 and an initial S content of 2500ppm (value measured in melt inclusions trapped in the olivines of the neighbouring Irazú volcano, Benjamin et al., 2007) this would imply the complete degassing of about $75x10^6$ m^3 of primitive magma. This is twice more than the tephra volume emitted during the last eruptive period of 1864-1866 ($<30x10^6$ m^3, Reagan et al., 2006). Convective endogenous degassing can lead to the complete gas exhaustion of relatively large magma bodies without leading to a significant eruption. The very slow fluxes decay that seems apparent since January could be the result of gradual volatile exhaustion. However, given that a direct pathway exists now between the magma and the surface, any sudden influx of new magma could trigger an eruption with little geophysical warning.

A last remarkable aspect of the degassing at Volcán Turrialba since January is that such huge gas fluxes are emitted through a rather narrow vent (~50x20m,OVSICORI-UNA reports for Turrialba 2005-2010). Experience with high temperature and high flux magmatic degassing through narrow vents shows that these vents are prone to sudden collapse and small scale explosions. Examples of this include Kilauea (USGS-HVO news releases, March 2008) in 2008, Etna in 1968 and 2010 (Le Guern et al., 1982; Corsaro, 2010) and Masaya (Duffel, 2003). As these events occur with little warning, the exclusion area around the summit craters should be maintained until the situation stabilizes.

7.6 Conclusion

SO_2 measurements obtained with these three different instruments agree well with each other and have allowed defining a clear trend in the SO_2 emissions of Turrialba. High SO_2 emissions since January are a strong evidence that the decade long unrest at the volcano has been caused by the intrusion of juvenile magma, and suggest that the volcano entered a new stage in the evolution described by (Vaselli et al, 2010). This stage is characterized by an open-vent magmatic degassing that bypass the scrubbing hydrothermal system. The apparent gradual decrease of the fluxes could indicate that the degassing magma body becomes slowly depleted in volatiles (About 1 Tg of SO_2 has been emitted over the study period). Even if the gradual degassing of the intruded magma body decreases the probability of an explosive eruption, this study also underlines two hazards associated to the current activity of Turrialba volcano. The first comes from the fact that a direct pathway exists now between the magma chamber and the surface, so any new magma input could trigger an eruption with little seismic precursory signs. The second results from the narrowness of the degassing vent, which could undergo sudden collapse and/or small scale explosion. Finally we think that integrated space and ground based imaging techniques probably represent the future of SO_2 measurements at active volcanoes thanks to their complementarity, reliability and ease of visualising the measured object at safe distance.

Chapter 8: Measuring SO_2 emissions of Eyjafjallajökull with the infrared images of ASTER.

8.1 Abstract

As this thesis was reaching its end, came what will probably remains as a landmark in the history of relations between volcano and the human civilization: the eruption of the Eyjafjallajökull. This eruption was a complex multistage event that had a profound effect on the life of hundreds of thousands of air travellers. Given the importance of the event, a last chapter was added to this thesis, to present the results of SO_2 retrievals obtained from ASTER images of this eruption. Thanks to the high latitude of the volcano, and to the urgent acquisition protocol of ASTER, numerous images of the eruptions were acquired from March to June 2010. These images were processed with the band ratio algorithm to obtain distribution maps of the SO_2 in the eruption plume. The effect of volcanic ash on the SO_2 retrievals using the band ratio algorithm is investigated in this chapter. Little effect is observed for large ash particles, while small ash particles cause a slight underestimation of the SO_2 retrievals (~2g/m² for the ash concentrations reported in the plume). However retrieval of SO_2 becomes inaccurate in the portions of the plumes that are nearly opaque due to extreme ash burden. Fluxes computed from the ASTER images show significant variations over time and provide insightful information about the eruptive dynamics. Three regimes of SO_2 emissions could be distinguished, which reflected the three main phases of the eruption. In March 2010, SO_2 was emitted at a moderate rate of ~35kg/sin a small plume that was bearing high concentrations of SO_2 but no volcanic ash. On 17th April, while the eruption was at its highest ash production phase, very little SO_2 was detected by ASTER in the quite large eruption plume. We propose that magma-meltwater interaction promoted SO_2 dissolution and its transformation into aqueous sulfate, so that only a small fraction of it was released into the atmosphere. Starting on 19th April copious amounts of SO_2 were again measured, indicating that the magma had was not in contact with water anymore. Radiated energy was also significantly higher, a further evidence that only limited magma-ice interaction was occurring. Flux in that last phase peaked at 250 kg/s. This value could still be slightly underestimated due to high ash content in the plume, which appeared nearly opaque in its proximal parts.

8.2 Introduction : eruption chronology

Before becoming famous in the whole world, Eyjafjallajökull was a relatively anonymous, but still well studied, stratovolcano of southern Iceland. Culminating at 1666m, most of the volcano is covered by a glacier (jökull means glacier in Icelandic). Its 1.5km wide summit crater is breached to the North and filled with a glacier that flowed northwards as a steep and crevassed glacier called Gigjökull. The bulk of the volcano is made of basalt from the transitional series, but trachyandesites and trachydacites are also found in the summit area. With only three low intensity eruptions in its

record (~AD 920, AD 1612 or 1613, and 1821-23, the last one being the only reliably describe done) it remained in the shadow of the neighbouring Katla volcano, one of biggest and most active central volcanoes in the country. Instead, the 2010 eruption was energetic and voluminous; and above all, it was a complex event. The wealth and variety of data collected from this eruption will certainly allow for a clear and detailed view of the processes involved, and more generally for an improvement in our general understanding on how volcanoes work. However, at the time of writing this thesis, much information about the eruption is still unpublished or only available under the form of preliminary reports and abstracts of conference presentations.

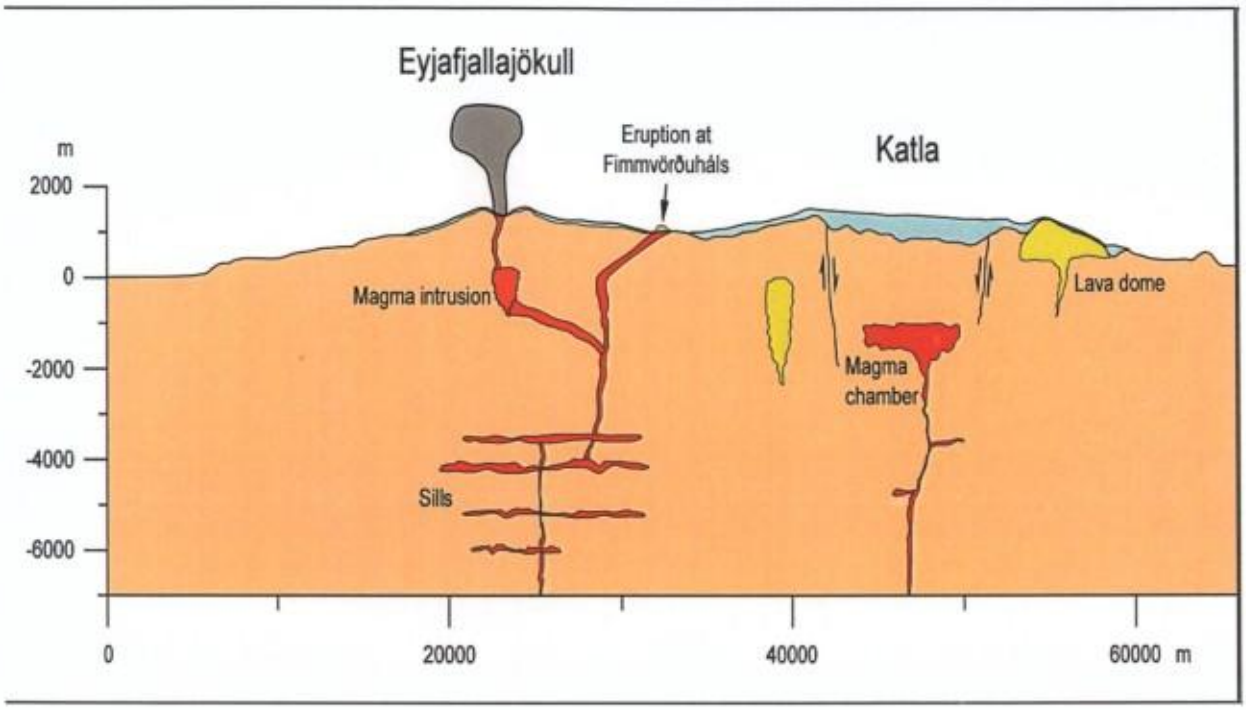

Figure 8.1: Interpretative E-W cross section beneath the Eyjafjallajökull and Katla central volcanoes. This illustration is based on localisation of pre-and-syneruptive earthquakes, petrologic analysis of the products and modelling of the deformation. (after Sigmundson et al., 2010)

8.2.1 Precursory signs

Several seismic crises affected the volcano during the two decades preceding the eruption. The most notable of them occurred in 1994, 1996, 1999-2000 and in mid 2009 (Hjaltadottir et al., 2009). Careful localization of the earthquake hypocenters allowed (Hjaltadottir et al., 2009) to interpret these seismic crises as successive intrusions of magma sills at different depth (20-25 km, 8-12 km and 1-4km bsl.), within the plumbing system of the volcano. GPS measurements and INSAR data revealed inflation associated with the shallowest of the seismic crises (Pedersen and Sigmundsson, 2004). In January 2010, seismicity and deformation picked up again, centered under the East flank of the

volcano, indicating renewal of magma inflow. As a result of this repeated seismic unrest and deformation, the occurrence of an eruption in the Eyjafjallajökull-Katla area did not came as a surprise for the Icelandic Volcanologists.

8.2.2 First phase: Flank eruption at Fimmvörduhàls

On March 20th 2010 at 23:00 GMT an eruptive fissure, approximately 500m long, opened at the Fimmvörduháls, an ice-free mountain pass between the Eyjafjallajökull and Myrdalsjökull glaciers. The popular recreation area of Thorsmork situated in the nearby Markarfljot valley, had been preventively evacuated a few hours before the eruption start as, a response to the risk of jökulhlaup, which are mudflows triggered by melting of the glacier at the contact of hot magma. Hawaiian style lava fountain (figure 8.2) rapidly built scoria cone around the most active vents of the fissure, while lava was emitted as aa type flows cascading in the steep gullies draining the area. This first phase of the eruption lasted for three weeks. The total volume of lava amounts to 25 10^6 m^3, which corresponds to an average effusion rate of 10-15 m^3/s. Compositionally, it is an olivine basalt from the transitional series containing 47% SiO_2 (Nordic Volcanological Institute website).

Figure 8.2: Lava fountains along the eruptive fissure at Fimmvörduhàls, on March 25, 2010. Photo Martin Rietze

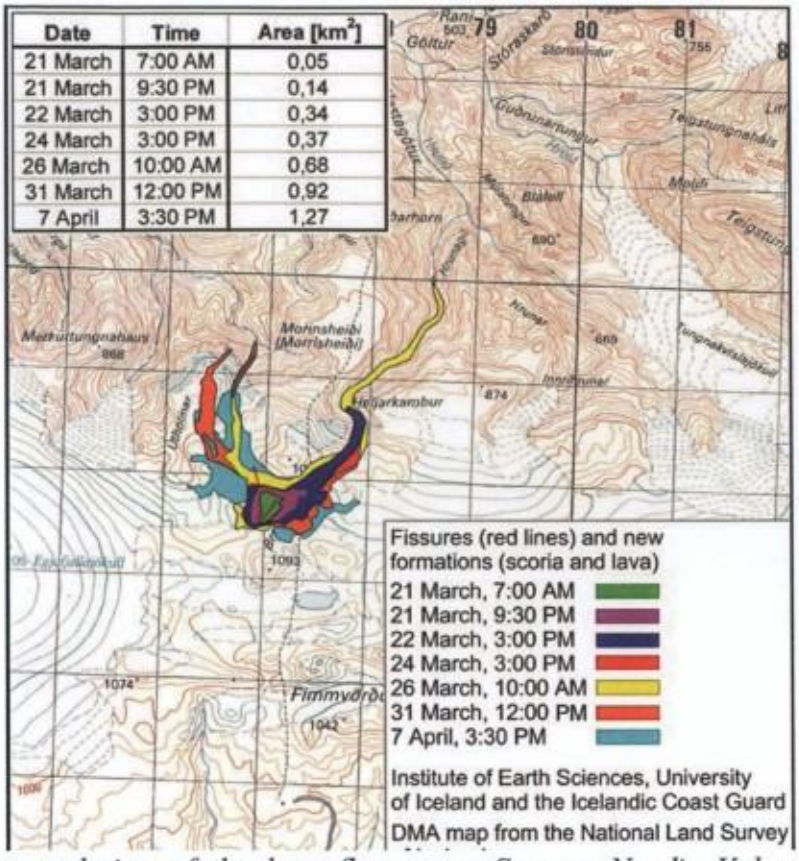

Figure 8.4: Map of the evolution of the lava flow area. Source: Nordic Volcanological Center, University of Iceland.

8.2.3 Second phase: Subglacial eruption at Eyjafjallajökull

On 12 April 2010 the eruption, which was on a declining phase already for several days, stopped completely; and seismic activity picked up again. The hypocenters migrated westwards of the initial fissure, indicating that the magma was migrating towards the conduit zone of Eyjafjallajökull central volcano. On 14 March 2010, new vents opened within the wide, ice filled central crater of Eyjafjallajökull central volcano. Massive melting of the crater glacier caused intense jökulhlaup that flowed northwards into the Markarfljot valley and then into the sea, causing minor damage to the local road network. The composition of the erupted products was markedly different from those of the first phase. The trachyandesite containing 55-58% SiO_2 results from the mixing between the rising basaltic magma and an older magma batch of trachydacitic composition, possibly a remnant of the 1881-83 eruption (Gudmunddson et al., 2011). Activity was violently explosive and produced an impressive ash plume that drifted southwards until Europe. The explosivity of the eruption was increased due to the interaction between the magma and the water of the melting glacier. This eruption pattern is commonly observed in eruptions from Icelandic volcanoes (e.g. Gudmundson et al., 2004) and is called hydromagmatic activity.

In detail, this type of activity involves a rapid and efficient conversion of the magma's thermal energy into kinetic energy, through a process named Fuel-Coolant Interaction (FCI), which has been studied experimentally (e.g.: Wohletz, 1986, Morrissey et al. 2000).

The first stage of FCI involves magma fragmentation under a thin film of superheated vapor insulating its surface from the water. Fragmentation is thought to be caused by a combination of processes, including magmatic gas expansion, thermal shock, instability at the fragmentation front and oscillating pressure of the vapor film.

In the second stage, as the fragmentation front progresses downwards in the magma, the fragments get intimately mixed with superheated liquid water and vapor. This is the stage involving most of the heat transfer from the magma to the water.

The last stage is characterized by rapid vaporization of the superheated water, which causes a vapor explosion that propels the fragmented magma upwards. Adiabatic expansion of the vapor continues during the expulsion and ascension of the vapor-ash mixture. Later during the ascent, the water vapor condensates due to the entrainment of cold air inside the vapor/ash jets. The ashes, which have a typically vitrous and angular texture and a black color are termed hyaloclastites

FCI is typically a cyclical process that repeats the succession of these three stages every few seconds, as long as magma and water are available. If the magma becomes insulated from the melt water, normal subaerial magmatic activity can start and build scoria cone and lava flow. In the case of the Eyjafjallajökull eruption, the hydromagmatic phase lasted only five days, because the glacier inside the crater was rather thin (about 150m) and because, drainage of the melt water through the steep slope under Gigjökull prevented the formation of intraglacial lake.

Figure 8.4: Hydromagmatic explosion and associated ash plume on 17th April 2010. Notice the black hyaloclastites jets and overlying water rich white volutes. Minor surges extend at the base of the eruption column. Photo T. Boeckel

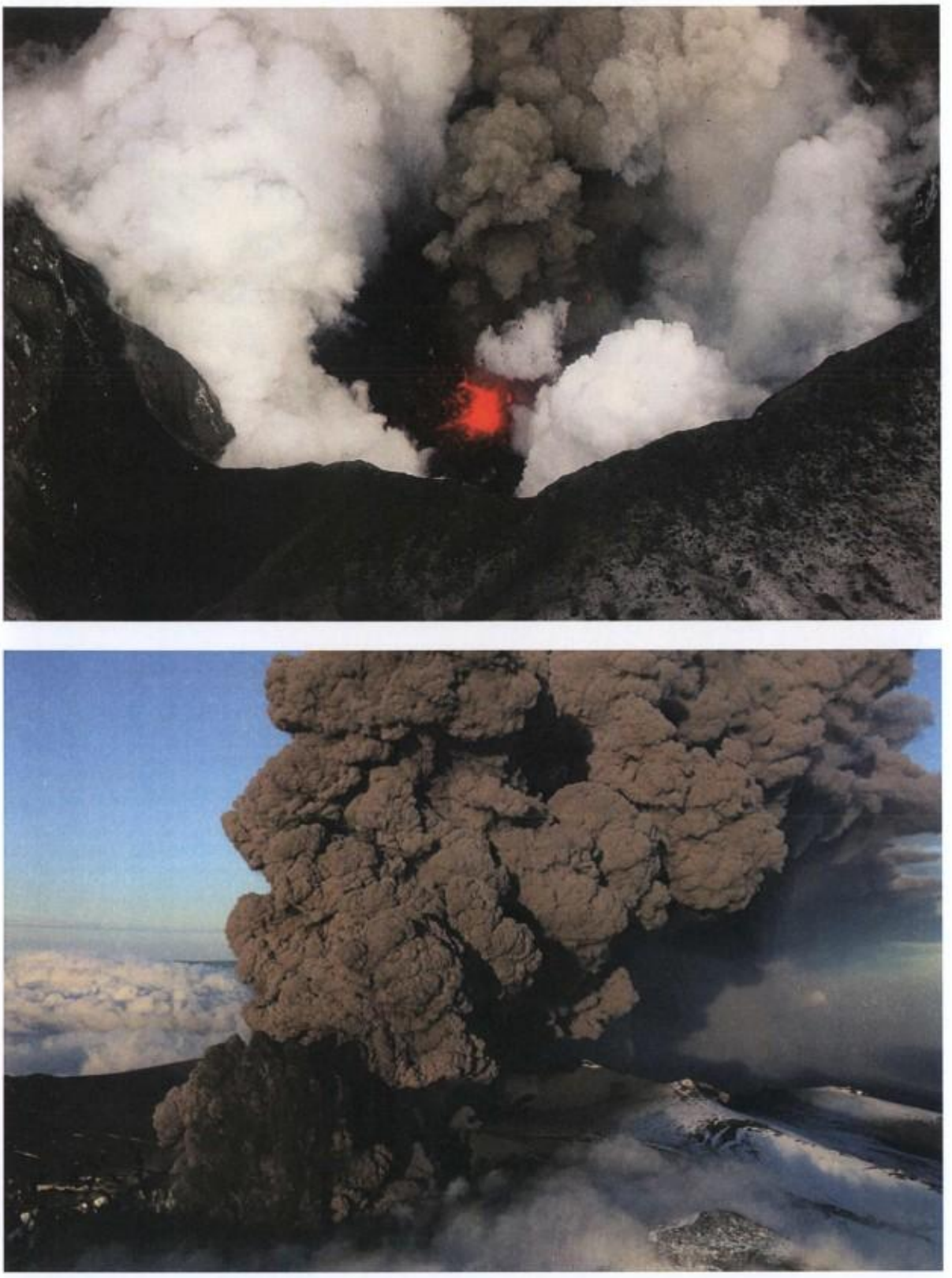

Figure 8.5: (a) Strombolian activity ejecting incandescent lava bombs on 19th April 2010. Notice the reduced ash production and the white smoke still coming from the edges of the collapsed glacier. Photo T. Boeckel. (b) Vulcanian phase producing a renewed ash plume on 12th May 2010. Photo R. Roscoe

8.2.4 Third phase: Magmatic activity at Eyjafjallajökull

Around 19th April 2010, the ash content of the plume started to decrease, while the proportion of coarser incandescent lava fragments launched by the eruptive vents increased significantly. Most of ice around the eruption vents had melted and the activity shifted towards purely magmatic type. However due to the differentiated nature of the magma (both more viscous and gas rich), the continuing eruption was significantly more explosive and violent than the basaltic eruption at Fimmvörduháls. Strombolian explosion (figure 8.5a) ejecting incandescent lava fragments with very loud detonations, alternated with more ash rich vulcanian explosions (figure 8.5b). Ash plumes produced by this activity had a homogenous gray color, and, contained few condensed water, indicating that magma fragmentation was mostly due to magmatic gases, and not anymore to steam explosions, although morphoscopic analyses of the ash particles, when published, are needed to confirm this. Lava flows were emitted towards the North, where it melted its way down Gigjökull. The eruption decreased in strength during the last days of April, then regained intensity in early May, and stopped around 23 of May. (Gudmundsson et al., 2011)

8.3 ASTER Images

Because ASTER flies on a polar sun-synchronous orbit, ASTER return time is considerably shorter over volcanoes located at high latitudes such as Eyjafjallajökull. Furthermore, as the eruption was a significant event with major impact over human activity, the sensor was programmed to acquire as many images of the eruption as possible. This result in a very complete coverage (17 images over 65 days) rarely achieved for other eruptions. Thanks to the expedited protocol of data acquisition and exchanged in application for space imagery of natural disasters, many of these images were available at no costs, instead of the ordinary tariff of 80$ per image. We restricted our analysis to these free expedited images, because they were found to cover all the phases of the eruption.

The ASTER images (L1BE format) were analysed for retrieving SO_2 using the methodology described in chapter 3. Plume height was estimating by comparing the temperature of opaque portions of the plume to the Keflavik radiosounding data, taken 150 km west of the volcano. SO_2 maps were generated for each image and SO_2 fluxes were computed from these maps by using the ECMWF value of wind speed at the altitude of the plume. Additionally, maps of the surface temperature, retrieved as a preliminary step of the SO_2 algorithm, were used to derive some information about the thermal energy radiated from the eruption. This is done by counting the thermally anomalous pixels, arbitrarily defined as having a temperature 10K higher than the surrounding background, as well as the saturated pixels.

8.3.1 1st April 2010

On 1st April 2010, the Hawaiian eruption with small lava fountain was ongoing at Fimmvörduhàls, when ASTER took that night image. Results are shown in figure 8.6. On the temperature map, the lava flow is clearly visible as a bilobate zone of hot pixels. It covers about 150 pixels in the TIR image, giving an approximate surface of 1.2 km². 35 pixels within this anomaly are saturated, (which implies an average temperature over 420K). The SO_2 map (figure 8.6b) reveals a small but concentrated SO_2 plume emanating from the eruptive vent and drifting southeastwards. A flux of 35kg/s is computed using the ECMWF wind speed at 2000m height (6m/s). This agrees well with the average flux of 30kg/s measured on that day with a mobile mini DOAS (Giuseppe Salerno, personal communication). This is a moderately high value for a gas flux, compatible with a mild eruption with rather low magma production rate at the eruptive fissure.

8.3.2 17th April 2010

This night time image was acquired one day after the eruption had started. Hydromagmatic explosive activity was at its strongest, with a copious ash production. The temperature map (figure 8.7b) shows a very cold plume with an apparent temperature as low as 240-250K, indicating that the plume was both high (this indicates an altitude of ~7km according to the radiosonde profile of Keflavik) and optically thick due to its high solid (ash and ice) aerosol content. The Brightness Temperature Difference method (Prata, 1989, Rose et al 1994) applied to the band 13 and 14 of the ASTER image fails to detect ash or ice unambiguously. However this method works rather bad for ASTER images, presumably because ASTER's B13 and B14 are closer to each other than to the bands of MODIS or AVHRR used for that method. The area of the thermal anomaly in the crater is about 0.8km² (98 pixels) but its highest temperature is only 300K. The SO_2 map shows only low amounts of SO_2 in the spectacular plume. This is very surprising at first glance, because the eruption was very intense at that time. The possible causes of this are discussed in section 8.4.

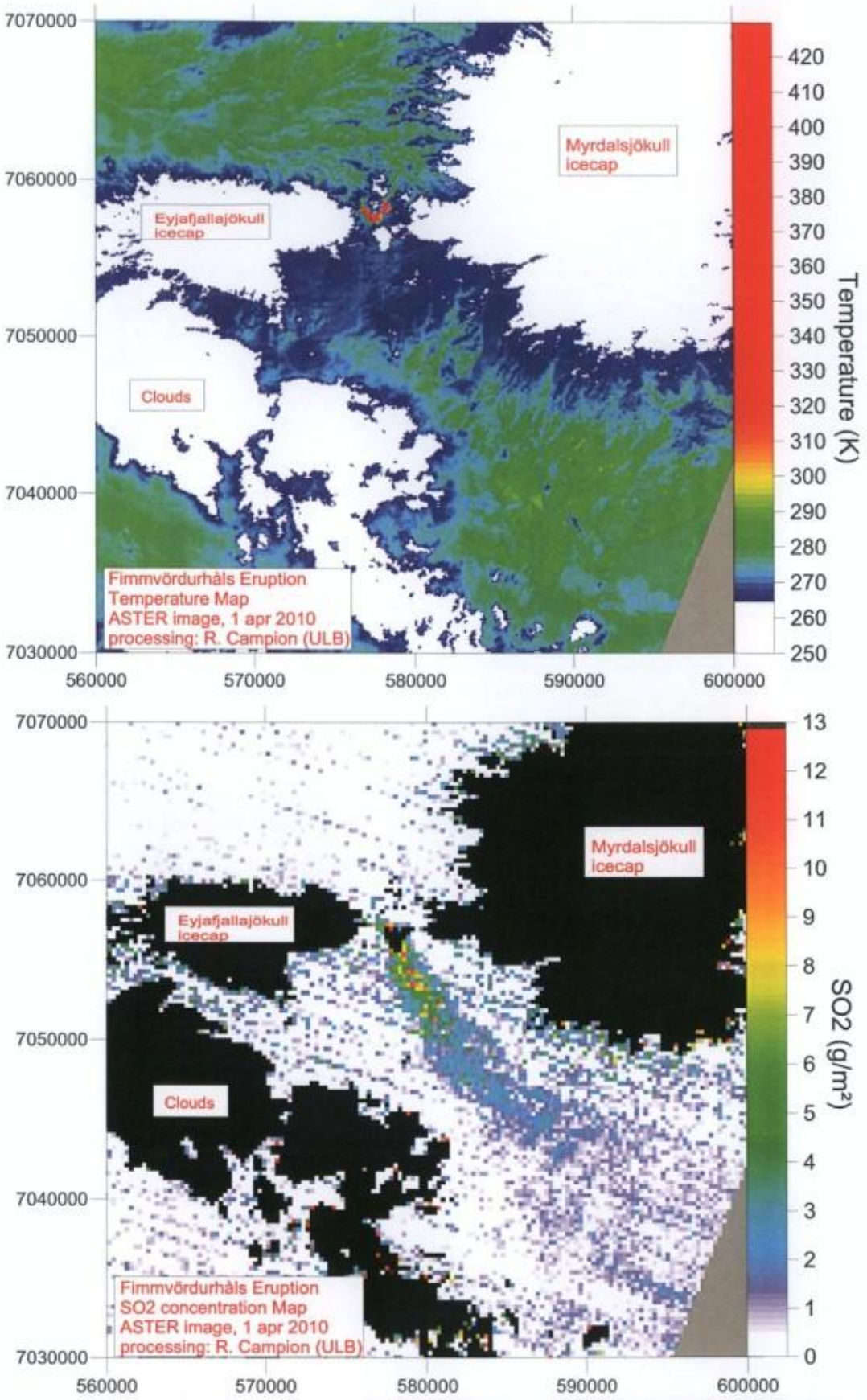

Figure 8.6: (a) Thermal map obtained from the TIR image of 1 April 2010. (b) SO_2 map showing the small but concentrated plume drifting south from the eruptive vents.

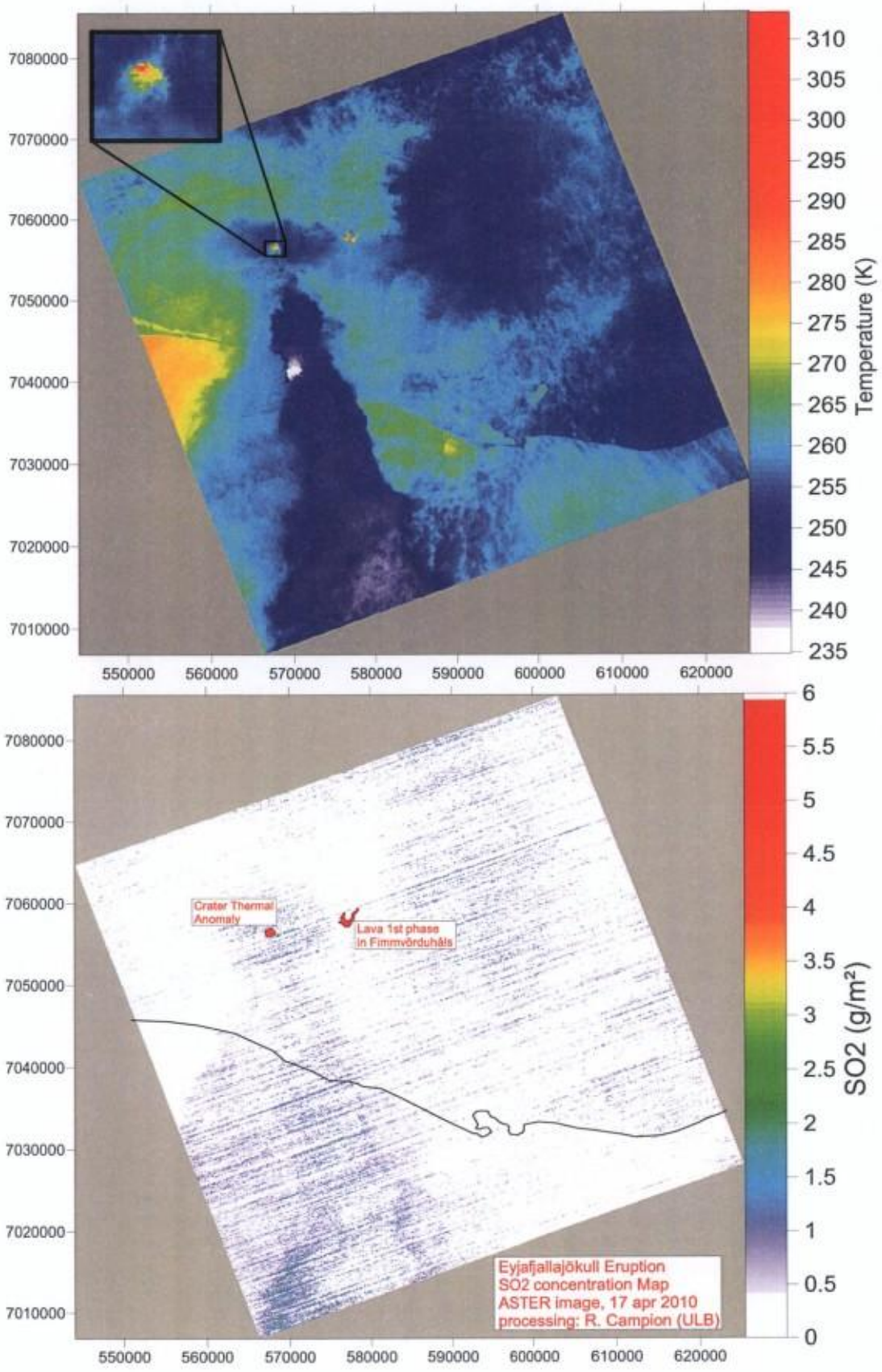

Figure 8.7: (a) Thermal map obtained from the TIR image of 17 April 2010. The plume (mostly ash and ice) is the cold area stretching south of the volcano (b) SO_2 map showing the very low column amounts of SO_2 in the plume.

8.3.3 19th April 2010

This daytime image was acquired soon after the transition of the eruption towards a purely magmatic strombolian activity. The thermal map (figure 8.8a) shows the return of a vigorous, thermal anomaly inside the crater. Its area is 0.4km² (48 pixels), which is less than on 17 April, but its temperature is much higher (between 350 and > 420K), and one saturated pixel. The SO_2 map shows a big and wide plume containing relatively high column amounts of SO_2 (2 to 5 g/m²). A second area of high SO_2 East of the main plume is probably an older plume detached from the volcano due to a rapid shift in wind directions on 19 April. This interpretation is supported by plume transport simulations by the NILU (Norwegian Institute of Aeronomy) using the Flexpart model (available on line http://www.youtube.com/watch?v=W8rCsr9b0u0). The SO_2 flux emitted by the volcano amounts to 130 kg/s, computed using a plume height of 4 km and a wind speed of 14m/s (ECMWF value at this altitude). This is a high value found only in intense eruptions (e.g. Nyamuragira, see chap. 4, or rarely in episodes of extreme passive degassing (e.g. Miyake-jima, see chap 3 or Anatahan, see chap 4). A robust magma flux is necessary to sustain such a high SO_2 flux.

8.3.4 12 May 2010

After a few days of nearly ash free strombolian activity accompanied with effusion of a viscous lava flow down Gigjokull, the eruption became again more explosive with increased ash production around May 6th. A notable decrease in the amplitude of the seismic tremor characterised this transition, whose cause is not yet known with certainty at the time of writing this manuscript. ASTER took a night time image on 12 may 2010. The thermal anomaly has increased in surface compare to 19thApril, amounting to 230 pixels, 25 of which are hot enough to saturate the TIR bands of ASTER. The ash plume, which is drifting to the Southeast, is conspicuous on the thermal map. The temperatures of the most opaque portions of the plume indicate a ~6km altitude. Obviously, the temperature measured in this plume (as well as for the previous images showing a plume containing some ash) is not the accurate ground temperature, nor the emissive temperature of the plume. Instead it is a mixing of these two end members, whose final value depends on the plume optical thickness. The SO_2 map is also showing significant amounts of SO_2 collocated with the ash plume.

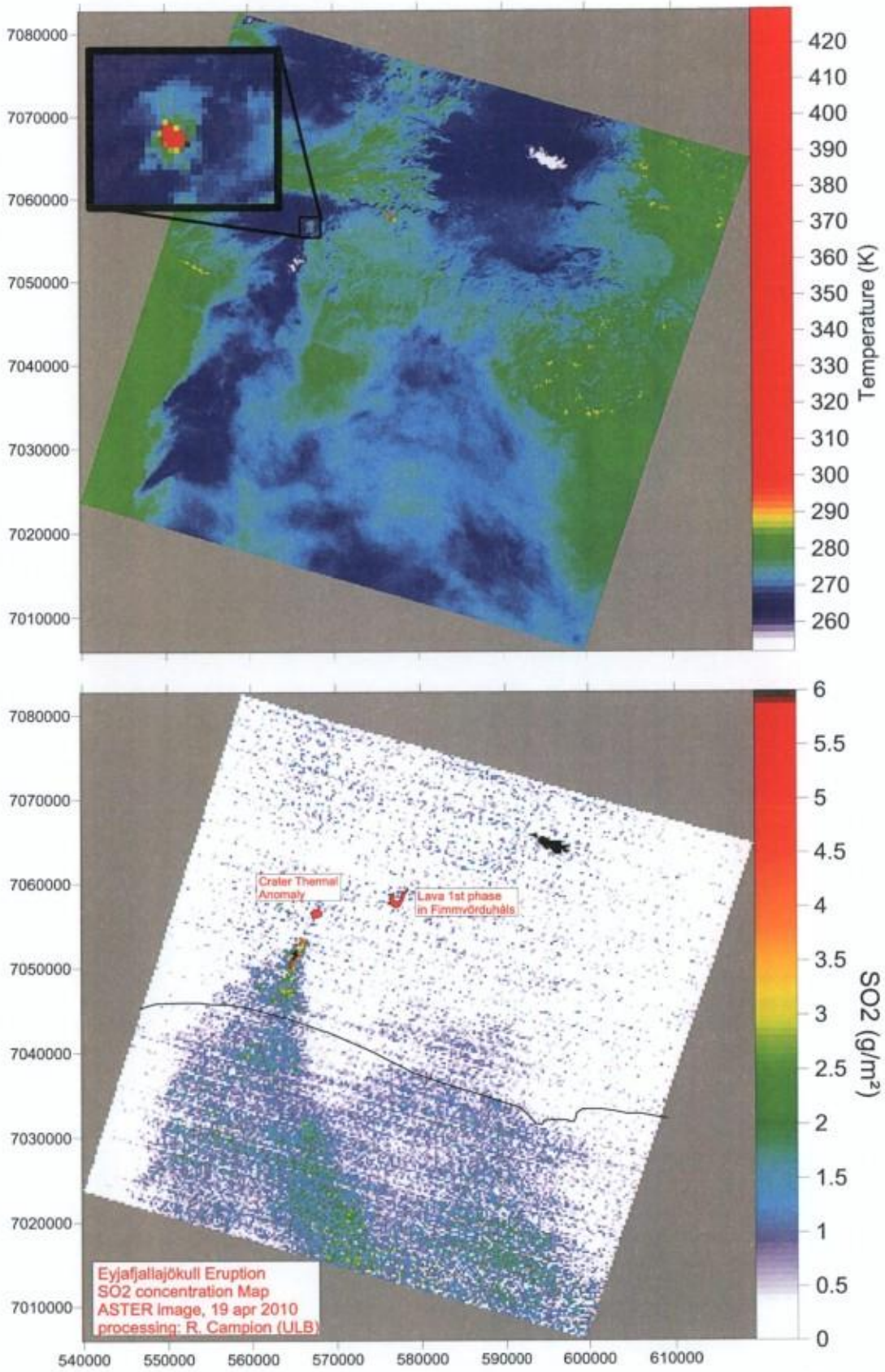

Figure 8.8: (a) Thermal map obtained from the TIR image of 19 April 2010. The plume (mostly ash and ice) has a complex shape due to an ongoing shift in wind direction. SO_2 map showing the significant column amounts in the plume.

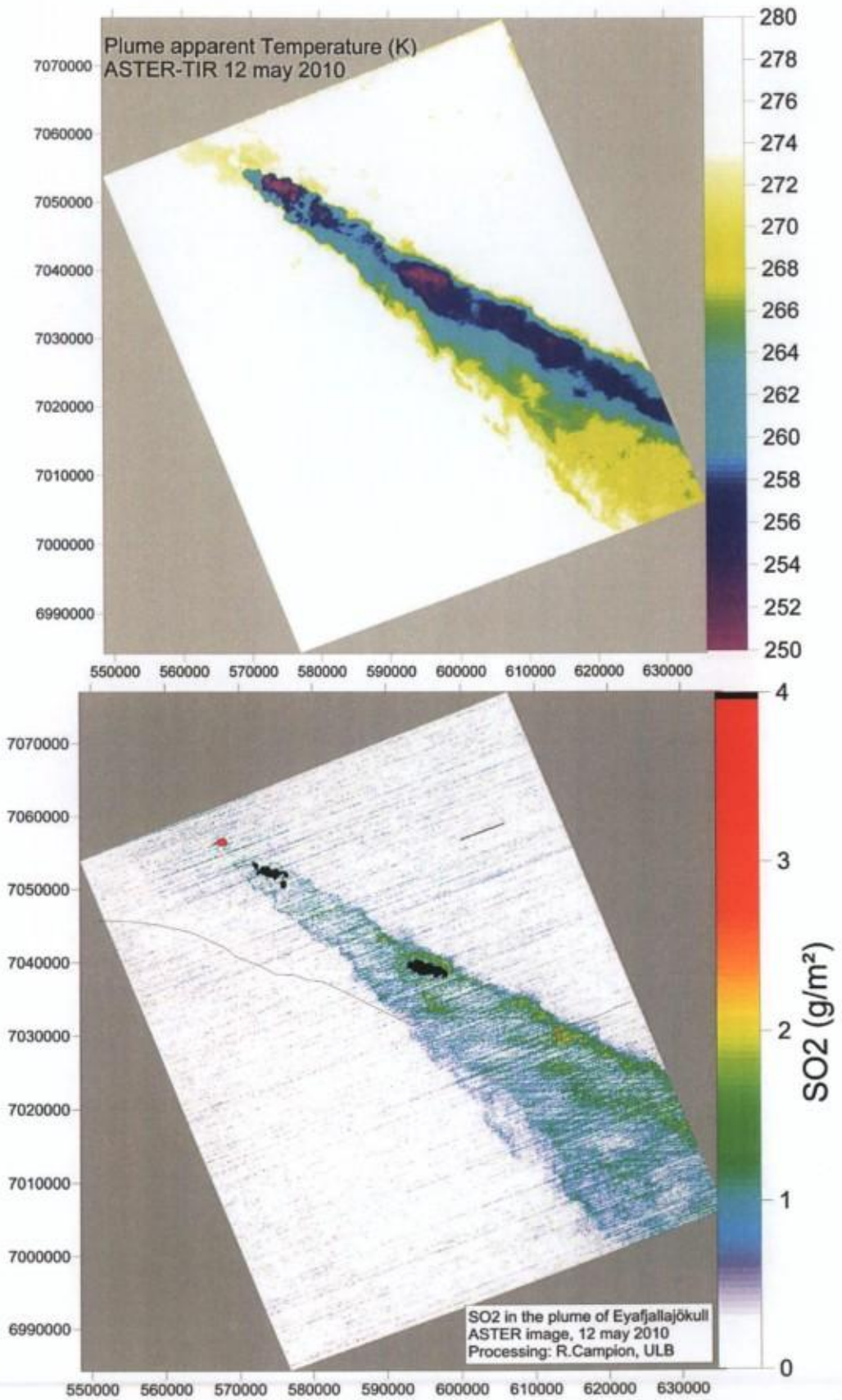

Figure 8.9: (a) Thermal map obtained from the TIR image of 12 May 2010 with a spectacular cold plume. The plume apparent temperature reflects changes in both the plume altitude and optical thickness. (b) SO_2 map of the plume, with the location of profile #200 indicated (cf. Figure 8.11).

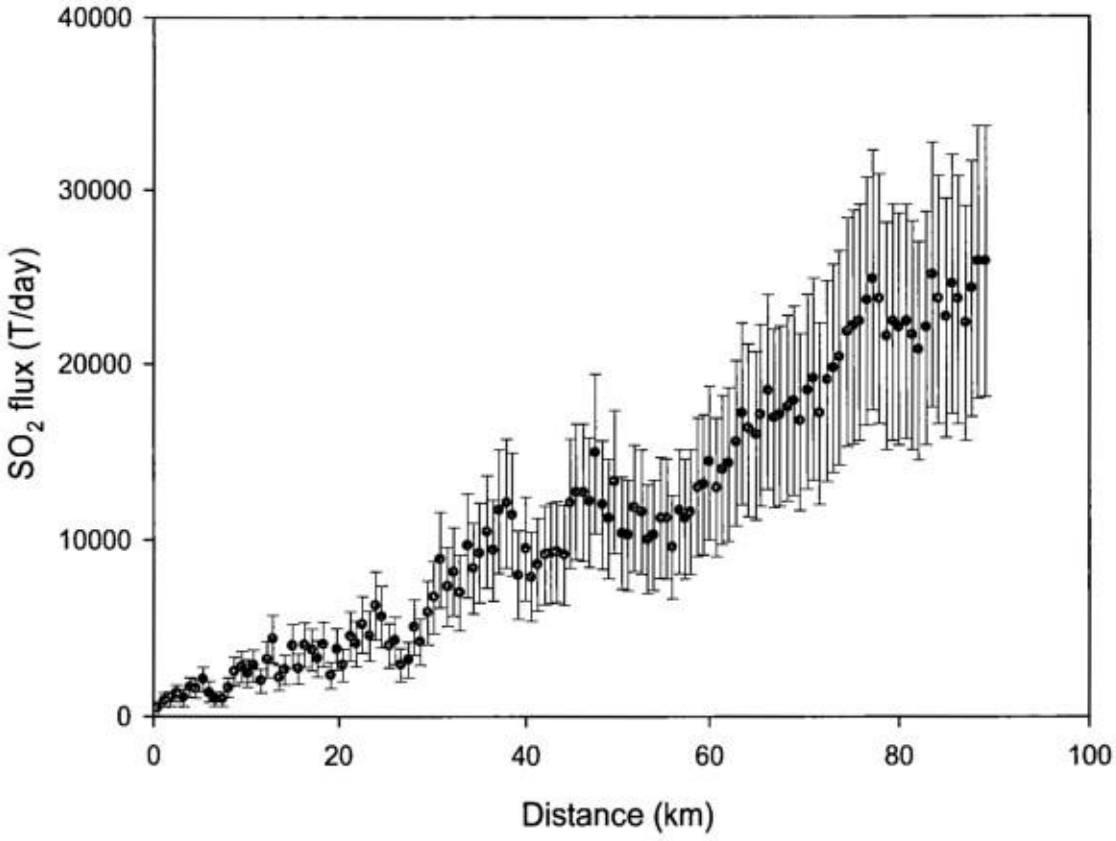

Figure 8.10: (a) SO_2 flux at increasing distance from the crater (the fluxes in the most proximal profiles were removed because of obvious underestimation).

However, the column amounts of SO_2 are apparently larger in the more distant part of the plume and the SO_2 flux seems to increase with distance to the crater, as shown in figure 8.10. In addition, as shown in figure 8.11, the retrieved SO_2 column amounts are sometimes larger in the edges of the plume than in its core. As this is observed only in the most proximal portion of the plume, it is probably an artefact created by the extreme ash loading of the plume. The optical thickness is so high that most of the radiation coming from the ground is blocked by the plume, which becomes the main source of radiation. Therefore only the upper part of the SO_2 plume is sensed by ASTER. As an optically thick plume seems to introduce a bias in the retrieved SO_2 column, the most realistic SO_2 fluxes are obtained at the greatest possible distance from the crater, where the ash content has already decreased. The effect of the ash on retrieval was further assessed using quantitative simulations of the radiative transfer, as detailed in the following section.

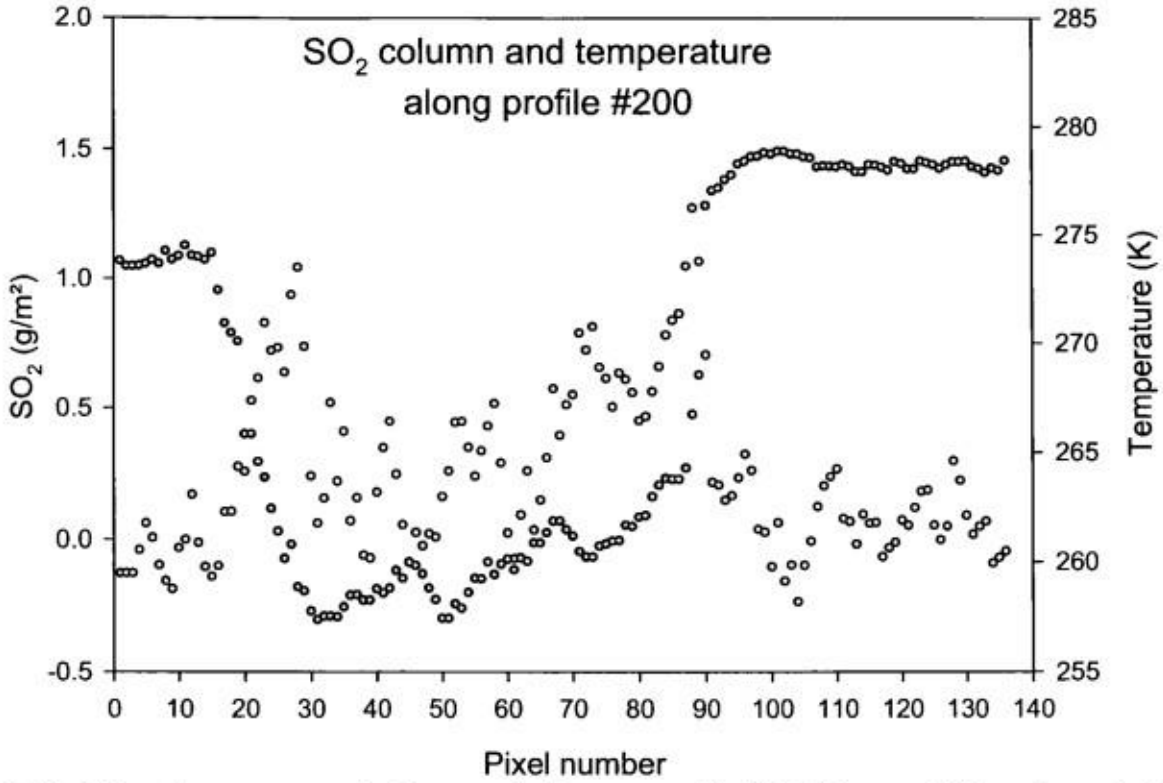

Figure 8.11: SO_2 column amount (red squares) along a profile (#200) located 18km downwind of the crater. An inverse correlation is evident with the apparent temperature of the plume (a proxy for its optical thickness) and the retrieved SO_2 column.

8.4 Effect of the Ash on the retrievals

Compared to the passive degassing plumes studied with ASTER in the previous chapters of this thesis, the eruptive plumes of Eyjafjallajökull contain significant amounts of ash, sometimes causing them to be optically thick in the 8-12 μm region. The band ratio algorithm, originally developed and validated for ash free plumes, has therefore to be tested for its ash sensitivity. A testing procedure was set as follow.

1. High resolution radiance spectra were simulated using Atmosphit, considering plumes with various SO_2 and ash contents. Mie scattering on ash particles inside the plume was modeled using Malut (Clarisse et al., 2010). We assumed spherical particles with the refractive indices of andesite measured by (Pollack et al., 1973), considering that the magma feeding the eruption was a trachyandesite containing 57-59% SiO_2. In order to assess the effect of particle size distribution, we ran three set of simulations with effective radii (R_{eff}) of respectively 2, 5 and 10 μm. The aerosol extinction efficiency calculated using Malut were then used was then used in Atmosphit to simulate the full (diffusion and absorption) radiative transfer in the plume and in the atmosphere.

2. The spectra were then integrated on the spectral response function of each ASTER bands to obtain simulated ASTER radiances for each value of SO_2 and ash. The radiances were arranged in 2D matrices $R_{i,j}$ where i and j represent the SO_2 and ash mass concentration (i= 0 to 10g/m², j= 0 to 15 g/m², with a step of 1g/m²).
3. We applied the band ratio algorithm to these matrices of "ashy" radiances and compared the retrievals to the model value of SO_2. An ideal algorithm would produce retrievals equal to the model value, and the difference between the retrieved and model SO_2 gives a theoretical estimation of the bias introduced by the presence of ash over the retrievals using the band ratio algorithm.

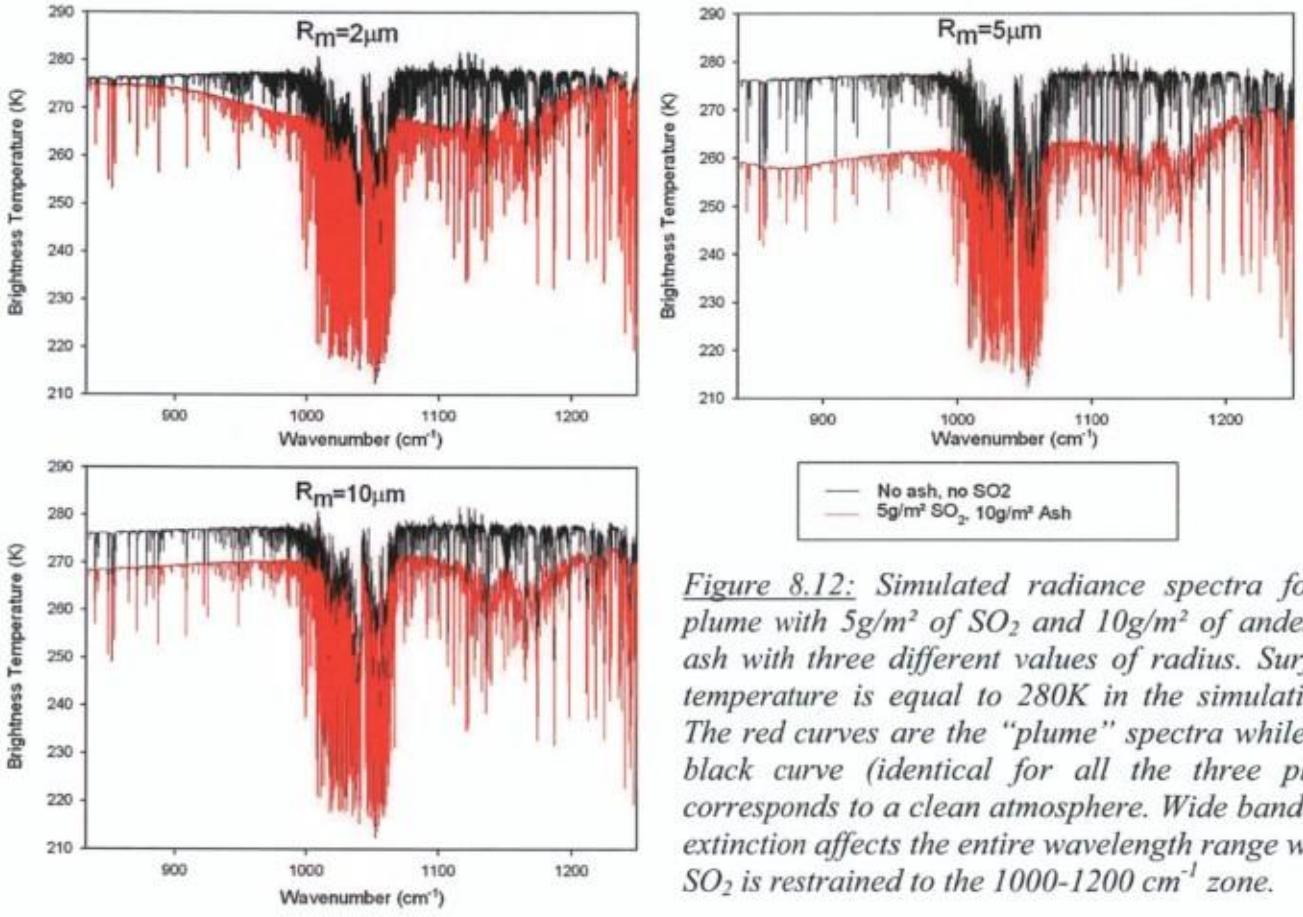

Figure 8.12: Simulated radiance spectra for a plume with 5g/m² of SO_2 and 10g/m² of andesitic ash with three different values of radius. Surface temperature is equal to 280K in the simulations. The red curves are the "plume" spectra while the black curve (identical for all the three plots) corresponds to a clean atmosphere. Wide band ash extinction affects the entire wavelength range while SO_2 is restrained to the 1000-1200 cm^{-1} zone.

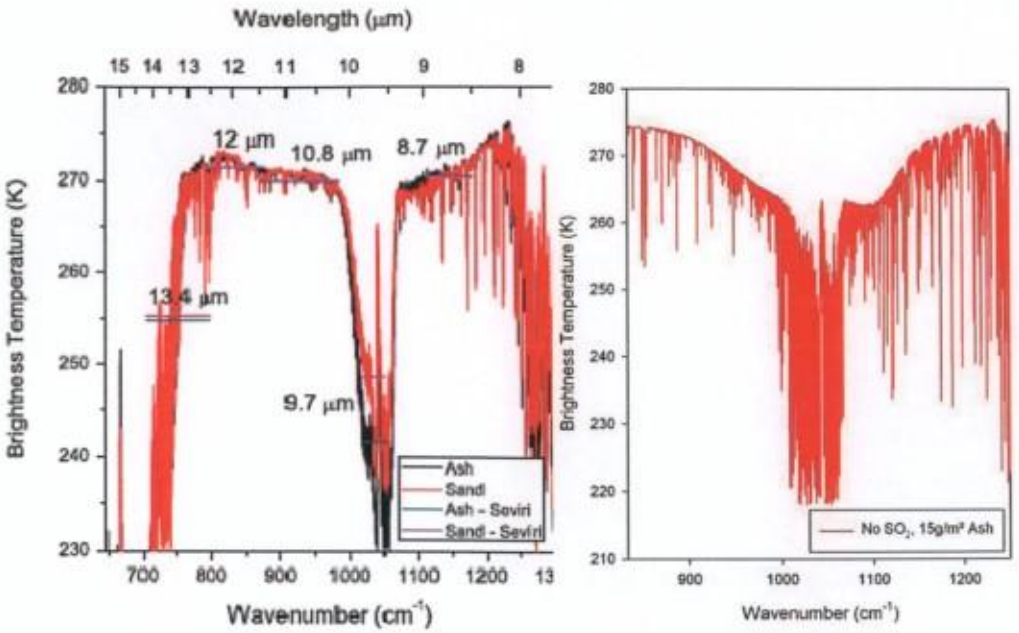

Figure 8.13: Brightness Temperature spectra of the ash plume of Eyjafjallajökull (a) measured by IASI (image from Clarisse et al., 2010) and (b) simulated using Atmosphit for15g/m² of ash with a 2μm effective radius.

Examples of simulated spectra of brightness temperature of a plume containing 5g/m² of SO_2 and 10g/m² of ash are presented in figure 8.12. The shape of the spectra is strongly dependent on R_{eff}, and so is the magnitude of the radiance attenuation. Big particles typically produce a flat spectrum while small particles produce a more concave spectrum. If we compare with an actual spectrum of proximal plumes registered by IASI (Infrared Atmospheric Sounding Interferometer), we see that the best match is obtained for particles with a 2 μm effective radius (figure 8.13).

The results of the tests of the band ratio algorithm on ash laden plumes are shown in figure 8.14 for the three considered ash sizes. In this figure, the SO_2 CA retrieved with the Band Ratio Algorithm is plotted against the CA input to the Atmosphit simulations. These plots show that the effect of ash on the SO_2 retrievals depends on their effective radius, as expected from the different spectral shapes observed on figure 8.12. Particles with a 2μm effective radius produce an overall underestimation of the SO_2 content, although of a small amplitude (-1.5 g/m² SO_2 for an ash loading of 10g/m²). The effect of ash on SO_2 retrieval seems maximal for particles with a 5μm radius. This is predicted by Mie theory, which states that the scattering efficiency of particles is maximal when the particle diameter approaches the wavelength of the incident light. This also agrees with the sensitivity study for ash retrievals by Stohl et al., (2011). For particles with this effective radius, the effect on the SO_2 retrievals depends on the SO_2 content itself. Low SO_2 contents appear underestimated while high SO_2 contents appear overestimated (by up to several g/m²). Particles with a 10μm and higher effective radius appear to have a negligible effect on SO_2 retrievals because their spectral extinction is relatively constant over the 8-10μm range. Of all the simulations made for this study, only those considering 2μm particles

produce results that can reproduce the observation from the "real world" that high ash loadings produce an underestimation of the SO_2 retrievals by the band ratio algorithm. It is important noting that, whatever the particle size, the effect of ash on the SO_2 retrievals increases with the ash load of the plume. Therefore the most reliable flux calculations are to be made in the more distal portions of the plume, where the ash loading has already decreased as a result of dispersion, aggregation and sedimentation. Under these conditions the SO_2 retrievals with ASTER should suffer only from a small underestimation (a few tens of percent) and reflect real source variations

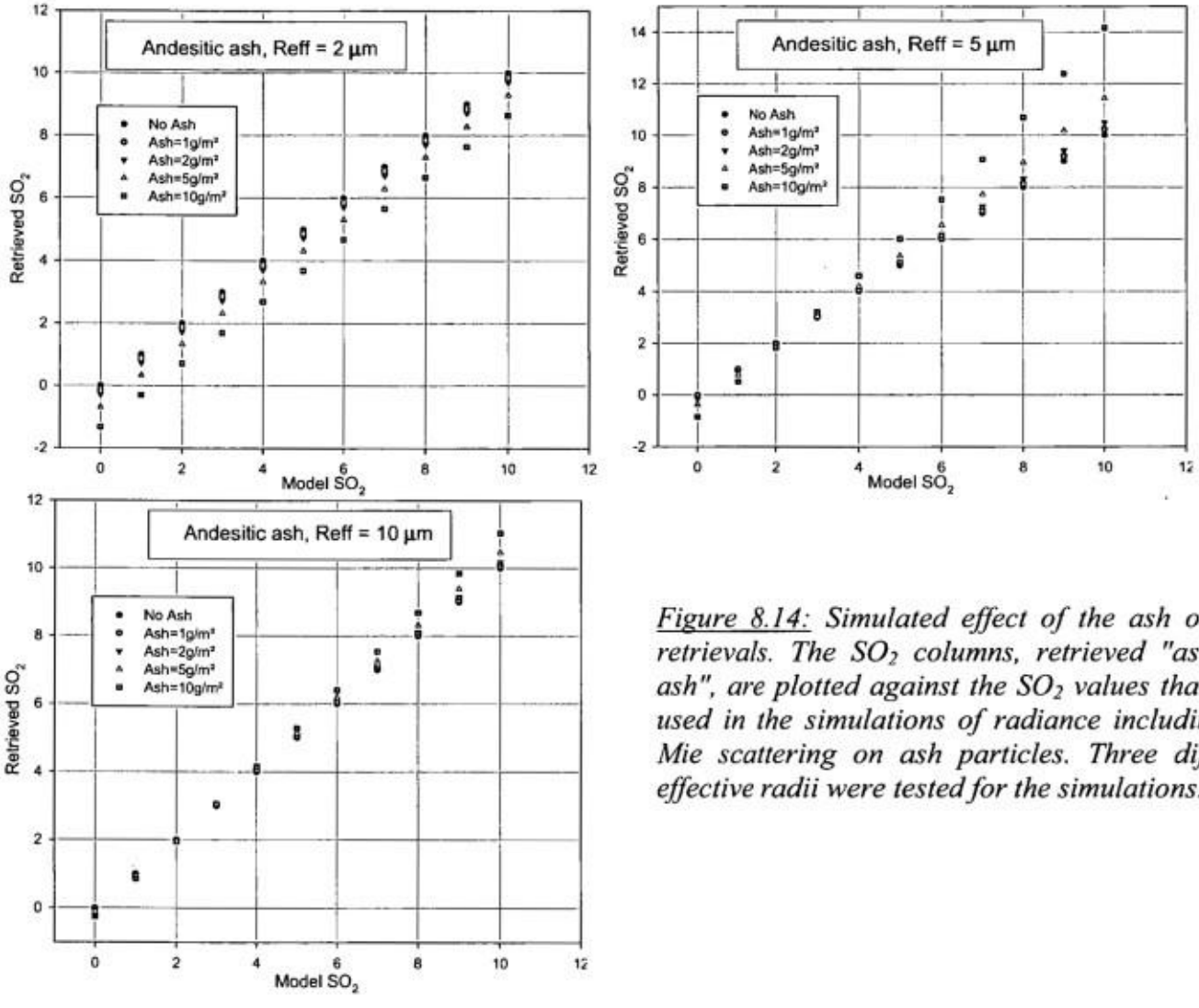

Figure 8.14: Simulated effect of the ash on SO_2 retrievals. The SO_2 columns, retrieved "as if no ash", are plotted against the SO_2 values that were used in the simulations of radiance including the Mie scattering on ash particles. Three different effective radii were tested for the simulations.

8.5 Discussion: significance of SO_2 flux variations.

SO_2 flux is usually a good proxy of the magma production rate during eruptions (e.g. Caltabiano et al., 1994, Sutton et al., 2003, review by Stix et al., 2008) The first phase of this eruption at Fimvörduhals provides an excellent illustration for this: a relatively low SO_2 flux (35kg/s) was produced during this mild eruption. This value is, for example, comparable to the typical fluxes measured at the East-Rift zone eruption of Kilauea (Sutton et al., 2003), an archetype of low intensity effusive eruption.

The most intense activity occurred during the five first days of the summit eruption, which produced the highest plumes and the largest part of the total eruptive volume (Guðmundsson et al., 2011.). One could expect the largest SO_2 release to occur simultaneously to this highly energetic phase, as was observed for the eruption of Hekla in 2000 (e.g. Rose et al., 2003). Amazingly however, SO_2 was below the detection limit on the image that ASTER took during this phase of activity. Other sensors documented the same pattern (Lieven Clarisse, pers. comm.). The most likely explanation for this is that the SO_2 emitted by the magma was rapidly dissolving into the melt water during the water-magma interactions. Indeed, according to the models of the Fuel-Coolant Interaction process, the thorough mixing between lava fragments and superheated water during the second phase of FCI should strongly favor dissolution of SO_2 (and other acidic volcanic gases as well) into the melt water. Even if not all the magmatic SO_2 has time to dissolve in the melt water during that mixing phase, more SO_2 can dissolve later into the white volutes of liquid aerosol that condenses when the vapor-tephra jets cool in contact with the atmosphere. An interesting approach to assess this dissolution hypothesis, and discriminate between early (mixing) and late (condensing) dissolution would be to establish a budget of the sulfate ions released by the jökulhlaups that accompanied the initial hydromagmatic phase of the eruptions. Once the glacier above the vent has been totally melted, the entire flux of SO_2 degassed by the magma could be transferred directly to the atmosphere. The simultaneity between the increase of the SO_2 flux on 19 April and the appearance of a strong thermal anomaly in the crater further supports the dissolution hypothesis. The high flux recorded on 12th may, towards the end of the eruption is intriguing as well, since most eruptions have their peak SO_2 emissions right after their beginning. The abundant ash that was present in the plume on that day must have been produced by volcanic gas expansion instead of magma-water interactions. High SO_2 flux and intense magma fragmentation both point towards a more gas-rich magma feeding the eruption during that period

If we extrapolate the average flux measurements of this study over the entire eruptive period, we obtain that a total of 0.7 GT SO_2wasinjected into the troposphere by the Fimmvorduhàls-Eyjafjallaökull eruption (70 kT during the flank basaltic phase and 530 kT during the summit andesitic phase). This value makes of this eruption a mid-size event in term of atmospheric injection of SO_2.

Summary and perspectives

This chapter summarizes the main results obtained in the framework of this thesis, and gives some outlook into the future of SO_2 measurements. This thesis was aimed at developing methods to quantify SO_2 emissions by volcanoes through passive degassing. The focus was put on passive degassing because it is the most relevant for volcano monitoring, whereas measurements of eruptive degassing is more relevant for studies about the climatic impact of eruptions or for airplane safety. However both measurements are obviously complementary, and the limit between strongly passive and weakly eruptive degassing is somewhat blurred. Passive degassing typically produces small-scale plumes that reside in the low to mid troposphere, at altitude below 5000m. This makes these plumes difficult to quantify and doing so requires satellites with high ground resolution and spectral bands located in atmospheric windows. This explains why IR atmospheric sounders such as AIRS or IASI, despite their high spectral resolution, cannot even detect these plumes.

9.1 ASTER and the band ratio algorithm

ASTER has been a unifying thread throughout of this thesis. The reason of this is that itshigh resolution fills the gap between highly localized ground based SO_2 measurements and the global coverage of the other satellites with coarser ground resolution. A relatively simple and straight forward method was developed to retrieve SO_2 column amounts and fluxes emitted by passive degassing volcanoes. This method, the band ratio algorithm is presented in chapter 3 and has been published in (Campion et al., 2010). Forward simulations of the radiative transfer have allowed to establish an error budget for that algorithm and have demonstrated its robustness. In particular, the retrievals with the band ratio algorithm were shown to depend very little on atmospheric humidity, H_2SO_4 aerosols, surface altitude and emissivity, four parameters that can bias retrievals of SO_2 with TIR sensors. On many volcanoes investigated in this thesis, ASTERs measurements of SO_2were in very good agreement with ground based data gathered by other groups of volcanologists, a further indication that the band ratio algorithm is accurate under many circumstances. In particular, the successful comparison between measurements by ASTER and a DOAS instrument on Mt Etna is one of the very few published cases of successful validation of Satellite measurements of SO_2 column amounts. The limits of application of the band ratio algorithm have also been well identified, which is important for operational monitoring. These limits are reached when in case of weak thermal contrast between the volcanic plume and the underlying surface.

9.2 Comparing ASTER with other sensors: OMI and MODIS

According to literature (Watson et al., 2004 and Carn et al., 2007), two other sensors have shown capabilities to quantify low tropospheric SO_2 emissions by passive volcanic degassing. These are OMI and MODIS.

In chapter 4, we compared the SO_2 flux measurements of ASTER and OMI (Ozone Monitoring Instrument). Flux is the only relevant quantity to compare because OMI and ASTER have a 2h delay between their overpass, and have very different pixel size (90x90 m versus 13x24 km). An innovative IDL routine was designed in order to compute fluxes from the standard OMI product and the wind data from the ECMWF. The two sensors are found to compare remarkably between each other in most circumstances. This is a very positive result for the future of space based monitoring of SO_2. It was further shown that the two sensors are very complementary in their best use conditions. ASTER is better for cloud-free scenes, while OMI is optimal when the plume is drifting above highly reflective cloud areas. Finally, this study allowed to establish an empirical detection limit for SO_2 flux measurements using current space based sensors: 5 kg/s.

In chapter five, we presented an algorithm to retrieve SO_2 with MODIS (MODerate resolution Imaging Spectroradiometer). Thanks to the simultaneity of ASTER and MODIS-Terra images, column amounts measured with the two sensors can be compared directly, provided that ASTER data are resampled to MODIS resolution. A sophisticated algorithm was designed to do this operation properly. Because of their good records in the comparison with other, spectrally independent methods such as OMI and ground based DOAS, ASTER measurements are used as a reference to evaluate the performance of MODIS. Comparing MODIS SO_2 retrievals to ASTER allows to demonstrate that several factors can bias MODIS retrievals, discriminate between the different bias source and quantify them. The final result of this study is that MODIS produces good results only in a restricted number of cases, which are:

- A large plume containing high SO_2 concentrations
- Plume drifting above a homogenous surface
- Strong thermal contrast between the plume and this surface (this condition is necessary for every retrieval method based on TIR)
- Low atmospheric water vapor content
- Low sulfate aerosol load

9.3 Development of a UV camera

The development of a UV camera to be used as a validation tool of satellite retrievals has been a somewhat different work from what was done in the rest of the thesis. At the time it was started, such instruments were still very few in the world, so nearly everything was developed from scratch, especially the software to process the data from the camera. If the operation of the camera on the field requires some experience, the data processing software is easy to use and intuitive. It handles the camera calibration using images of calibration cells and DOAS data, the creation of maps of the SO_2 CA in the plume, the automatic wind speed measurement, and the flux calculation. The results obtained in this work demonstrate all the potential of this emerging technology. During a field campaign that we set up with this instrument, we obtained imaging measurements of the intense SO_2 emissions from Volcán Turrialba in Costa Rica. The SO_2 fluxes computed from these images were in excellent agreement with the values measured by OMI and ASTER over that period, as shown in chapter 7.

9.4 Interest for Volcanology

Measurements are useful only if they can be interpreted and exploited; so the aim of our SO_2 measurements is to help understanding of volcano dynamics and ultimately to predict its future behavior. Chapter 7 and 8 fulfill this important objective of providing valuable information for Volcanology.

In chapter 7, we report SO_2 fluxes measured from space and ground at Volcán Turrialba. These measurements provide a strong evidence that an intrusion of juvenile magma was responsible for the decade-long unrest at that volcano, while other results such as ground deformations and fumaroles analysis have given unclear results. Furthermore the time evolution of the fluxes coupled with field observations by the Costa Rican volcanologists allow proposing a detailed interpretation of the activity of the volcano and even a prognosis of its future evolution.

In chapter 8, SO_2 measurements during the recent Eyjafjallajökull eruption have allowed to track SO_2 behavior during hydromagmatic interactions and to gain insight into the evolving dynamics of the eruption.

9.5 Perspectives: the future of SO_2 measurements.

SO_2 measurements on volcanoes underwent a revolution at the start of this decade, with the development of mini-DOAS spectrometers, and their deployment as permanent networks of automated scanning instruments. SO_2 fluxes from volcanoes equipped by such networks are now measured permanently during daylight at a frequency of one measurement every few minutes. This was a significant improvement compared to the few measurements per week that were available before the development of these networks.

A second revolution came with the advent of space-based sensors with high enough spectral and spatial resolutions for measuring SO_2 flux in small-scale plumes of passive volcanic degassing. In this thesis, measurements from these sensors have been intercompared for assessing their accuracy and limitations, and exploited for volcanological interpretation. The practical detection limit of 5kg/s established in this work will probably improve in a near future with the launch of new sensors, which are now in planning phase. In particular, the future BUV sensor TROPOMI, with a pixel size of 10x10km, should allow significant progress in term of detection limit. Similar improvement of detection limit in the TIR will be provided by the future HyspIRI sensor, which will have the same spectral characteristics as ASTER but a lower detector noise and an even smaller pixel size (60x60m). In addition, HyspIRI will have a much wider (400km) and continuous field of view, which will provide a global coverage in less than 5 days.

A third revolution is underway with the development of UV cameras capable of high frequency imaging SO_2 measurements. Potential applications of these instruments are numerous. Some take advantage from their imaging abilities, such as mapping SO_2 emissions of fumarolic zones, improving the accuracy of SO_2 flux by a better characterization of the wind field. Others gain from the high frequency of flux measurements such as comparison with seismic or infrasonic measurements. All these applications will likely lead to breakthroughs in our understanding of how volcanoes work, because gases are the driving forces of volcanic eruptions.

References

Afe O. T., Richter A., Sierk B., Wittrock F. and Burrows J. P. (2004) BrO Emission from Volcanoes-a Survey using GOME and SCIAMACHY Measurements, Geophys. Res. Lett., 31, L24113, doi:10.1029/2004GL020994

Aiuppa A., Moretti R., Federico C., Giudice G., Gurrieri S., Liuzzo M., Papale P., Shinohara H. and Valenza M. (2007)Forecasting Etna eruptions by real-time observation of volcanic gas composition, Geology; v. 35; no. 12, p. 1115-1118

Allard P.(1983) The origin of water, carbon, sulphur, nitrogen andrare gases in volcanic exhalations: evidence from isotope geochemistry, *in*: H. Tazieff and J.C. Sabroux (Eds.),*Forecasting Volcanic Events*, Elrevier. Amsterdam, p.337-386.

Allard P. (1997) Endogenous Magma degassing and storage at Mount Etna. Geophys. Res. Lett. 24, p. 2219-2222.

Allard P., Burton M., Murè F. (2005) Spectroscopic evidence for a lava fountain driven by previously accumulated magmatic gas,Nature 433, p. 407-410.

Allard P. (2010) A CO2-rich gas trigger of explosive paroxysms at Stromboli basaltic volcano, Italy, J. Volcanol. Geoth. Res. 189, p. 363–374

Andres R. and Kasgnoc A. D.(1997) A time-averaged inventory of subaerial volcanic sulfur emissions, J. Geophys. Res. 103(D19), p. 25251-25261

Arai K. and Tonooka H.(2005) Radiometric performance evaluation of ASTER VNIR, SWIR and TIR, IEEE Transactions on Geoscience and Remote Sensing, Vol. 43, No. 12, p. 2725-2732.

Barboza V., Fernàndez E., Martinez M., Duarte E., Van der Laat R., Marino T., Hernàndez E., Valdés J., Sàenz R., Malavassi E. (2003) Changes in the activity of Turrialba volcano: seisimicity, geochemistry and deformation, Seismol. Res. Lett., p. 74-215

Barnes W.L., Pagano T.S., Salomonson V.V. (1998)Prelaunch Characteristics of the Moderate Resolution Imaging Spectroradiometer (MODIS) on EOS-AM1, IEEE Trans. Geoscience & Remote Sensing, Vol. 36, No. 4, p. 1088-1100

Benjamin E.R., Plank T., Wade J.A., Kelley K.A., Hauri E.H., Alvarado G.E. (2007) High water contents in basaltic magmas from Irazù Volcano, Costa Rica., J. Volcanol. Geother. Res., Vol. 168, (1-4), p. 68-92

Bhartia P. (2002) OMI Algorithm Theoretical Basis Document (Vol. II), NASA Goddard Space Fligt Center http://eospso.gsfc.nasa.gov/eos_homepage/for_scientists/atbd/docs/OMI/ATBD-OMI-02.pdf

Beer R., *Remote Sensing by Fourier Transform Spectrometry*, Wiley-Interscience, New York, 1992

Bishop F. C., Smith J. V., Dawson J. B.(1975) Pentlandite-magnetite intergrowth in De Beers spinel lherzolite: review of sulfide in nodules, Physics and Chemistry of The Earth, Vol. 9,p. 323-337

Bluth G.J.S and Rose W.I. (2004) Observations of eruptive activity at Santiaguito volcano, Guatemala, J. Volcanol. Geotherm. Res. 136, p. 297–302

Bluth G. J. S., Shannon J. M., Watson I. M., Prata A. J., and Realmuto V. J. (2007) Development of an ultra-violet digital camera for volcanic SO_2 imaging, J. Volcanol. Geotherm. Res., 161, p. 47–56.

Bobrowski N., Hönninger G., Galle B., and Platt U. (2003) Detection of bromine monoxide in a volcanic plume, Nature, 423, p. 273-276

Bobrowski N, Hönninger G., Lohberger F., Platt U. (2006)IDOAS: A new monitoring technique to study the 2D distribution of volcanic gas emissions, J. Volcanol. Geotherm. Res 150, p. 329-338

Bogumil K., Orphal J., Homann T., Voigt S., Spietz P., Fleischmann O.C., Vogel A., Hartmann M., Bovensmann H., Frerick J., and Burrows J.P. (2003) Measurements of molecular absorption spectra with the SCIAMACHY pre-flight model: Instrument characterization and reference data for atmospheric remote sensing in the 230-2380 nm region, J. Photochem. Photobiol. A.: Chem. 157, p. 167-184

Branan Y., Harris A., Watson I.M., Phillips J.C., Horton K., Williams-Jones G.W.& Garbeil, H. (2008) Investigation of at-vent dynamics and dilution using thermal infraredradiometers at Masaya volcano, Nicaragua,J. Volcanol. Geotherm. *Res.*, 169, p. 34-47

Brasseur G. P. and Granier C. (1992) Mount Pinatubo aerosols, chlorofluorocarbons, and ozone depletion. Science, p. 257-1239

Burnham, C.W. (1975) Water and magmas: a mixing model. Geochim. Cosmochim. Acta39, pp. 1077–1084

Burton, M., P. Allard, F. Murè, and C. Oppenheimer (2003) FTIR remote sensing of fractional magma degassing at Mt. Etna, Sicily, *in* Volcanic Degassing, edited by C. Oppenheimer, D. M. Pyle, and J. Barclay, Spec. Publ. Geol. Soc., 213, p. 281-293

Burton M., P. Allard, F. Murè and A. La Spina(2007) Magmatic gas composition reveals the source depth of slug-driven Strombolian explosive activity, Science 317, p. 227–230.

Caltabiano, T., Romano, R., and Budetta, G. (1994) SO_2 flux measurements at Mount Etna (Sicily), *J. Geophys. Res.*, 99, 12, p. 809– 12

Campion R., Salerno G.G., Coheur P., Hurtmans D., Clarisse L., Kazahaya K., Burton M., Caltabiano T., Clerbaux C., Bernard A. (2010) Measuring volcanic degassing of SO_2 in the lower troposphere with ASTER band ratios, J. Volcanol. Geotherm. Res., 194(1-3), p. 42-54

Carn S.A., and Bluth G.J.S. (2003) Prodigious sulfur dioxide emissions from Nyamuragira volcano, D.R. Congo. Geophys. Res. Lett. 30(23), 2211

Carn S. A., Krueger A. J., Krotkov N. A.., Gray M. A (2004) Fire at Iraqi sulfur plant emits SO_2 clouds detected by EarthProbe TOMS, Geophys. Res. Let., vol. 31, L19105, doi:10.1029/2004GL020719

Carn S.A. Krueger A.J., Arellano S., Krotkov N.A., Yang K (2008) Daily Monitoring of Ecuadorian volcanic degassing from space, J. Volcanol. Geotherm. Res., 176, p. 141–150

Caroll M.R. and Webster J. D. (1994) Solubilities of sulfur, noble gases, nitrogen, chlorine, and fluorine in magmas,*in*M R. Carroll and J. R. Hollaway (eds),*Volatiles in Magmas*, Reviews in Mineralogy and Geochemistry, vol. 30, 1, p. 231-279

Carr M. J., Feigenson M. D.,Patino L. C., Walker J. A. (2003) Volcanism and geochemistry in Central America: Progress and problems, AGU Geophysical Monograph, vol. 138, p. 153-174

Churikova T., Wörner G., Mironov N., Kronz A. (2007) Volatile (S, Cl and F) and fluid mobile trace element compositions in melt inclusions: implications for variable fluid sources across the Kamchatka arc, Contrib. Mineral. Petrol. 154, p. 217–239

Clarisse L., Hurtmans D., Prata A.J., Karagulian F., Clerbaux C., De Mazière M.s and Coheur P-F.(2010) Retrieving radius, concentration, optical depth, and mass of different types of aerosols from high-resolution infrared nadir spectra. Appl. Opt. 49, p. 3713-3722

Clarisse, L., Coheur, P. F., Prata, A. J., Hurtmans, D., Razavi, A., Phulpin, T., Hadji-Lazaro, J., Clerbaux, C. (2008) Tracking and quantifying volcanic SO_2 with IASI, the September 2007 eruption at Jebel at Tair, Atmos. Chem. Phys., 8, p. 7723–7734

Clarisse L., D. Hurtmans, A.J. Prata, F. Karagulian, C. Clerbaux, and P.-F. Coheur. (2010)Retrieving aerosol properties from nadir observed high resolution spectra. Applied Optics, 49, 19, p. 3713-3722.

Clough, S. A., M. W. Shephard, E. J. Mlawer, J. S. Delamere, M. J. Iacono, K. Cady-Pereira, S. Boukabara, and P. D. Brown(2005) Atmospheric radiative transfer modeling: a summary of the AER codes, Short Communication, J. Quant. Spectrosc. Radiat. Transfer, 91, 233-244.

Coheur, P.-F., Barret, B., Turquety, S., Hurtmans, D., Hadji-Lazaro, J., Clerbaux C., 2005, Retrieval and characterization of ozone vertical profiles from a thermal infrared nadir sounder, J. Geophys. Res., 110, D24303.

Corradini S., Merucci L. and Prata A.J. (2009) Retrieval of SO_2 from thermal infrared satellite measurements: correction procedures for the effects of volcanic ash, Atmos. Meas. Tech., 2, 177–191

Corradini, S., Pugnaghi, S., Teggi, S., Buongiorno, M.F., Bogliolo, M.P., 2003. Will ASTER see the Etna SO_2 plume?, Int. J. Remote Sens. 24 (6), 1207- 1218.

Corradini, S., Spinetti C., Carboni E., Tirelli C., Buongiorno M.F., Pugnaghi S., Gangale G., Mt. Etna tropospheric ash retrieval and sensitivityanalysis using Moderate Resolution ImagingSpectroradiometer measurements, Journ. Appl. Rem. Sens., Vol. 2, 023550 (2008)

Corsaro R.A. (2010)INGV weekly volcanological report on Etna activity, 5-11 March 2010,http://www.ct.ingv.it/index.php?option=com_docman&task=doc_download&gid=1662&Itemid=330

Daag A., Tubianosa B., Newhall C., Tungol N., Javier D., Dolan M., Perla J., Reyes D., Arboleda R., Martinez A., Regnalado T (1996)Monitoring Sulfur Dioxide Emission at Mount Pinatubo. *In:* Newhall C. and Punongbayan R. (eds.), *Fire and Mud: Eruptions and Lahars of Mount Pinatubo, Philippines.* PHILVOLCS and USGS.

Dalton M. P., Watson I. M., Nadeau P. A., Werner C., Morrow W., and Shannon J. M. (2009) Assessment of the UV camera sulfur dioxide retrieval for point source plumes, J. Volcanol. Geoth. Res., 188, 358–366

Delgado Granados H., Cárdenas González L., Piedad Sánchez N. (2001) Sulfur dioxide emissions from Popocatépetl volcano (Mexico): case study of a high-emission rate passively degassing erupting volcano, Journal of Volcanology and Geothermal Research, v. 108, p. 107–120.

Delgado Granados H. (2008) Large Volcanic-SO_2 fluxes: COSPEC measurements at PopocatépetlVolcano (Mexico), *In:* Williams-Jones, G., Stix, J. & Hickson, C. (eds.) *The COSPEC Cookbook: Making SO_2 Measurements at Active Volcanoes*. IAVCEI, Methods in Volcanology, 1, p.191-217

Delmelle P., Stix J., Bourque C. P.-A., Baxter P. J., Garcia-Alvarez J., and Barquero J, 2001: Dry deposition and heavy acid loading in the vicinity of Masaya volcano, a major sulfur and chlorine source in Nicaragua, Environ. Sci. Technol. 35, 1289–1293.

Delmelle P. (2003) Environmental impacts of tropospheric volcanic gas plumes. *in* Oppenheimer C., Pyle D. M., and Barclay J. (Eds), *Volcanic Degassing*, Spec. Publ. Geol. Soc., 213, 381-399

Duffell,H.J., Oppenheimer C., Pyle D.M., Galle, B., McGonigle A.J.S., Burton M.R.(2003) Changes in gas composition prior to a minor explosive eruption at Masaya volcano, Nicaragua. J. Volcanol. Geotherm. Res. 126, p. 327–339

Eatough D. J., Caka F. M., and Farber R. J. (1994) The conversion of SO_2 to sulfate in the atmosphere, Isr. J. Chem., 34, p. 301–304.

Edmonds M., Oppenheimer C., Pyle D.M. (2001) A model for degassing at the Soufrière Hills Volcano, Montserrat, West Indies, based on geochemical data, Earth. Plan. Sc. Lett., 186, 2, p.159-173.

Edmonds M, Herd RA, Galle B, Oppenheimer C (2003a) Automated, high time-resolution measurements of SO_2 flux at Soufrière Hills Volcano, Montserrat., Bull. Volc. 65, p.578-586

Edmonds M., Oppenheimer C., Pyle D.M., Herd R.A. and Thompson G. (2003b) SO_2 emissions from Soufrière Hills Volcano and their relationship to conduit permeability, hydrothermal interaction and degassing regime, J. Volcanol. Geotherm. Res., 124, p.23-43

Edner H., Ragnarson P., Svanberg S., Wallinder E., Ferrara R., Cioni R., Raco B., and Taddeucci G. (1994) Total fluxes of sulfur dioxide from the Italian volcanoes Etna, Stromboli, and Vulcano measured by differential absorption lidar and passive differential optical absorption spectroscopy, J. Geophys. Res., 99(D9), 18,827–18,838,

Elias T., Sutton A.J., Oppenheimer C., Horton K.A., Garbeil H., Tsanev V., McGonigle A.J.S., and Williams-Jones G. (2006) Intercomparison of COSPEC and two miniature ultraviolet spectrometer systems for SO_2 measurements using scattered sunlight. Bull. Volc., v. 68, p. 313-322.

Fayt C. and Van Roozendael M. (2001) WinDOAS 2.1 Software User Manual, http://uv-vis.aeronomie.be/software/WinDOAS/WinDOAS-SUM-210b.pdf

Fischer T.P. and Marty B. (2005) Volatile abundances in the sub-arc mantle: insights from volcanicand hydrothermal gas discharges, J. Volcanol. Geotherm. Res. 140, p. 205– 216

Fischer T.P., Morrissey M.M., Calvache M.L., Gómez D., Torres R., Stix J., Williams S.N.(1994) Correlations between SO_2 flux and long-period seismicity at Galeras volcano.
Nature 368, p. 135–137.

Francis P.W., Oppenheimer C., Stevenson D.(1993) Endogenous growth of persistently active volcanoes, *Nature* 366, p. 554-557

Francis P., Burton M.R., Oppenheimer C.(1998)Remote measurements of volcanic gas compositions by solar occultation spectroscopy. Nature 396, 567–570.

Galle B., Oppenheimer C., Geyer A., McGonigle A.J.S., Edmonds M., Horrocks L. (2002) A miniaturized ultraviolet spectrometer for remote sensing of SO_2 fluxes: A new tool for volcano surveillance. J. Volcanol. Geoth. Res. 119:241-254

Galle B., Johansson M., Rivera C., Zhang Y., Kihlman M., Kern C., Lehmann T., Platt U, Arellano S, Hidalgo S(2010) NOVAC - A global network for volcano gas monitoring: network layout and instrument description. J. Geophys. Res. Atmospheres, 115, D05304.

Graf, H.-F., Feichter, J., Langmann, B. (1997) Volcanic sulfur emissions: estimates of source strength and its contribution to the global sulfate distribution. J. Geophys. Res. 102., 10727-10738.

Gerlach T.M. (1982) Interpretation of volcanic gas data from tholeiitic and Alkaline Mafic Lavas, Bull. Volc. Vol. 45, 3, p. 235-244

Gerlach T. M. (2003) Elevation effects in volcano applications of the COSPEC, in Oppenheimer, C., Pyle, D. M., and Barclay, J., eds., Volcanic Degassing: Geological Society of London Special Publication 213, p. 169-175.

Giggenbach W.F. (1975) A simple method for the collection and analysis of volcanic gases. Bull. Volcanol. 39, p. 132-145.

Giggenbach W.F. (1980) Geothermal gas equilibria. Geochim. Cosmochim. Acta 44, p.2021-2032.

Gillespie A., Rokugawa S., Matsunaga T., J CothernS., Hook S., Kahle A. B.(1998)A Temperature and Emissivity Separation Algorithm for Advanced Spaceborne Thermal Emisssion and Reflection Radiometer (ASTER) Images. IEEE Transactions on Geoscience and Remote Sensing, 38, 4, 1113 – 1126.

Grattan J.P., Durand M. & Taylor S. (2003) Illness and elevated human mortality coincident with volcanic eruptions. *In* Oppenheimer, C., Pyle, D.M., and Barclay, J. (eds) *Volcanic Degassing*, Geological Society, London, Special Publication 213, p. 401-414.

Gudmundsson M.T., Sigmundsson F., Björnsson H. and Högnadóttir Th. (2004) The 1996 eruption at Gjálp, Vatnajökull ice cap, Iceland: efficiency of heat transfer, ice deformation and subglacial water pressure, Bull. Volc. 66, p. 46–65.

Gudmundsson M.T., Hoskuldsson A., Larsen G., Thordarson T., Oddsson B., Hognadottir T., Jonsdottir I.,Björnsson H., Petersen N.G., and Magnusson E. (2011) Eyjafjallajökull April-June 2010: An explosive-mixed eruption of unusually long duration, Geophysical Research Abstracts, Vol. 13, EGU2011-12542, EGU General Assembly 2011

Hilton D. R., Fischer T. P., McGonigle A. J. S., and de Moor J. M. (2007) Variable SO_2 emission rates for Anatahan volcano, the Commonwealth of the Northern Mariana Islands: Implications for deriving arc-wide volatile fluxes from erupting volcanoes, Geophys. Res. Lett., 34, L14315

Hjaltadottir S., Vogfjord K. S. and Slunga R. (2009) Seismic signs of magma pathways through the crust at Eyjafjallajokull volcano, South Iceland: Icelandic Meteorological Office report, VI 2009-013 http://www.vedur.is/media/vedurstofan/utgafa/skyrslur/2009/VI_2009_013.pdf

Horrocks L., Oppenheimer C., Burton M. and Duffell H. (2003) Compositional variation in tropospheric volcanic gas plumes: evidence from ground-based remote sensing, in *Volcanic degassing*, Geological Society Special Publications, 213, p.349-369.

Huang, C. Townshend, J.R.G., Liang, S. Kalluri, S.N.V. and Defries, R.D. (2002) Impact of sensor's point spread function on land cover characterization, assessment and deconvolution. Rem. Sens. Envir., 80, p.203-212.

Iguchi M., Yakiwara H., Tameguri T., Hendrasto M., Hirabayashi J. (2008) Mechanism of explosive eruption revealed by geophysical observations at the Sakurajima, Suwanosejima and Semeru volcanoes.J. Volcanol. Geotherm. Res., 178, 1, p.1-9

JaupartC. and Vergniolle S. (1988) Laboratory models of Hawaiian and Strombolian eruptions. Nature 331, p.58-60

Johansson M, Galle B, Rivera C, Zhang Y (2009a) Tomographic Reconstruction of Gas Plumes Using Scanning DOAS. Bull. Volc. 71, p. 747-751.

Johansson M, Galle B, Zhang Y, Rivera C, Chen D, Wyser K (2009b) The Dual-Beam mini-DOAS technique, measurements of volcanic gas emission, plume height and plume speed with a single instrument. Bull. Volc. 71, p. 1169-1178.

JPL HysPIRI group (2009) NASA 2008 HyspIRI Whitepaper and Workshop Report, *JPL Publication 09-19*, accessed in March 2011, downloadable at http://hyspiri.jpl.nasa.gov/downloads/public/2008%20HyspIRI%20Whitepaper%20and%20Science%20Workshop%20Report-r2.pdf

Kantzas E.P., McGonigle A.J.S., Tamburello G., Aiuppa A., Bryant R.G. (2010) Protocols for UV camera volcanic SO_2 measurements, J. Volcanol. Geotherm. Rese. 194, 55–60

Kazahaya K, Shinohara H, Saito G (1994) Excessive degassing of Izu-Oshima volcano: magma convection in a conduit. Bull. Volc. 56, p.207-216

Kazahaya K., Shinohara H., Uto K., Odai M., Nakahori Y., Mori H., Iino H., Miyashita M., Hirabayashi J.(2004) Gigantic SO_2 emission from Miyake-jima volcano, Japan, caused by caldera collapse. Geology, v.32, 5, p.425-428.

Kearney C.S., Dean K., Realmuto V.J., Watson I.M., Dehn J., Prata F. (2008) Observations of SO_2 production and transport from Bezymianny volcano, Kamchatka using the MODerate resolution Infrared Spectroradiometer(MODIS). Int. J. Remote Sens 29(22):6647–6665

Kearney C., Watson I.M., Bluth G.J.S., Carn S.A., and Realmuto V. (2009) A Comparison of Thermal Infrared and Ultraviolet Retrievals of SO_2 in the Cloud Produced by the 2003 Al-Mishraq State Sulfur Plant Fire.Geophys. Res. Lett., 36, L10807, doi:10.1029/2009GL038215.

Kern C., Sihler H., Vogel L., Rivera C., Herrera M., Platt U. (2008) Halogen oxide measurements at Masaya Volcano, Nicaragua using active long path differential optical absorption spectroscopy. Bull. Volc. 71, p. 659-670

Kern C. (2009) *Spectroscopic measurements of volcanic gas emissions in the ultra-violet wavelength region*, Unpublished PhD thesis, University of Heidelberg.

Kern C., Deutschmann T., Vogel L., Wöhrbach M., Wagner T., and Platt U. (2010a) Radiative transfer corrections for accurate spectroscopic measurements of volcanic gas emissions, Bull. Volcanol.,72, 233–247

Kern C., Kick F., Lüubcke P., Vogel L., Wöhrbach M., and Platt U. (2010b) Theoretical description of functionality, applications, and limitations of SO_2 cameras for the remote sensing of volcanic plumes. Atmos. Meas. Tech., 3, 733–749

Kinoshita K. (1996) Observation of flow and dispersion of volcanic clouds from Mt. Sakurajima, Atmospheric Environment, 30, 16, p. 2831-2837

Krotkov N. A., Carn S. A, Krueger A. J., Bhartia P. K., Yang K. (2006) Band Residual Difference Algorithm for Retrieval of SO_2 from the Aura Ozone Monitoring Instrument (OMI) IEEE Trans. Geosc. Rem. Sens., 44, 5, p. 1259-1266.

Krueger A.J. (1983) Sighting of El Chichon sulfur dioxide clouds with the Nimbus 7 total ozone mapping spectrometer. Science 220, p. 1377–1379

Krueger A.J., Walter L.S., Bhartia P.K., Schnetzler C.C., Krotkov N.A., Sprod I., and Bluth G.J.S., (1995) Volcanic sulfur dioxide measurements from the Total Ozone Mapping Spectrometer (TOMS) Instruments. J. Geophys. Res., 100, p. 14,057 - 14,076.

Krueger A.J., Schaefer S.J., Krotkov N.A., Bluth G. and Barker S. (2000) Ultraviolet Remote Sensing of Volcanic Emissions. *In:* P.J. Mouginis-Mark, J.A. Crisp and J.H. Fink, Editors, *Remote Sensing of Active Volcanism, AGU Geophysical Monograph* vol. 116, p. 25–43.

Kusakabe M., Komoda Y., Takano B. and Abiko T. (2000) Sulfur isotopic effects in the disproportionation reaction of sulfur dioxide in hydrothermal fluids: implications for the $\delta^{34}S$ variations of dissolved bisulfate and elemental sulfur from active crater lakes, J. Volcanol. Geotherm. Res., 97, p. 287-307

Lacasse C., Karlsdottir S., Larsen G., Soosalu H., RoseW. I., and Ernst G. G. J. (2004) Weather radar observations of the Hekla 2000 eruption cloud, Iceland, Bull. Volc., 66, p.457–473.

Le Guern F., Nohl A., Bicocchi P. (1979) Field measurements of volcanic gases: Vulcano Island (Italy), Kilauea (Hawaii, U.S.A.), Merapi (Java, Indonesia), Bull. Volc., 45, 3, p.229-233

Le Guern F., Tazieff H., Vavasseur C., Zettwoog P. (1982) Resonance in the gas discharge of the Bocca Nuova, Etna (Italy), 1968-1969. J. Volc. Geoth. Res., 12, 161-166.

Le Guern, F. and Bernard, A. (1982) Etude des mécanismes de condensation des gaz magmatiques. Exemple de l'Etna (Italie). Bull. Volc. 45: 161-166.

Le Guern F. (1982) Les débits de CO_2 et SO_2 volcaniques dans l'atmosphère. Bull. Volc. 45, 197-202

Lee C., Kim Y. J., Tanimoto H., Bobrowski N., Platt U., Mori T., Yamamoto K., and Hong C. S. (2005) High ClO and ozone depletion observed in the plume of Sakurajima volcano, Japan. Geophys. Res. Lett., 32 , 21809

Levelt P. F., van den Oord G. H. J., Dobber M. R., Mälkki A., Visser H., de Vries J., Stammes P., Lundell J., and Saari H. (2006) The Ozone Monitoring Instrument, IEEE Trans. Geosci. Remote Sens., 44(5), p.1093–1101

Liou K.N. (2002) *An Introduction to Atmospheric Radiation. 2nd edition*, Academic Press, San Diego, 583 p. (International Geophysics Series, Volume 84). Book Reviews

Love S.P., Goff F., Counce D., Siebe C., Delgado H. (1998) Passive infrared spectroscopy of the eruption plume at Popocatépetl volcano, Mexico. Nature, 396, p. 563–567

Martin R.S., Ilyinskaya E., Sawyer G.M., Tsanev V.I., Oppenheimer C. (2011) A re-assessment of aerosols from Masaya volcano, Nicaragua, Atmospheric Environment, 45, p. 547-560

Mather T. A., Allen G., Oppenheimer C., Pyle D.M. and McGonigle A. J. S. (2003) Size-Resolved Characterisation of Soluble Ions in the Particles in the Tropospheric Plume of Masaya Volcano, Nicaragua: Origins and Plume Processing. J. of Atmospheric Chemistry 46, p. 207-2037.

Mather T. A., Tsanev V. I., Pyle D. M., McGonigle A. J. S., Oppenheimer C., and Allen A. G. (2004) Characterization and evolution of tropospheric plumes from Lascar and Villarrica volcanoes, Chile, J. Geophys. Res., 109, D21303

Matiella-Novak M.A., Watson I.M., Delgado-Granados H., Rose W.I., Cardenas-Gonzalez L. and Realmuto V.J. (2007) Volcanic emissions of Popocatepetl volcano, Mexico, quantified using Moderate Resolution Imaging Spectroradiometer (MODIS) infrared data: a case study of the December 2000-January 2001 emissions, J. Volcanol. Geoth. Res., 170, p. 75-85

McGonigle A. J. S., Thomson C. L., Tsanev V. I. and Oppenheimer C. (2003) A simple technique for measuring power station SO_2 and NO_2 emissions, Atmosph. Envir., V. 38, 1, p.21-25

McGonigle A. J. S., Delmelle P., Oppenheimer C., Tsanev V. I., Delfosse T., Williams-Jones G., Horton K., Mather T. A.(2004) SO_2 depletion in tropospheric volcanic plumes. Geophys. Res. Lett., 31, L13201, doi:10.1029/2004GL019990.

Metrich N. and Clochiatti R. (1996) Sulfur abundance and its speciation in oxidized alkaline melts, Geochim. Cosmochim. Act., Vol. 60, p. 4151-4160

Metrich N. And Wallace P.J. (2008) Volatile Abundances in Basaltic Magmas and Their Degassing Paths Tracked by Melt Inclusions, Reviews in Mineralogy and Geochemistry; January 2008; v. 69;1; p. 363-402

Millán M.M.(2008)Absorption Correlation Spectrometry. *In*: Williams-Jones, G., Stix, J. & Hickson, C. (eds.) *The COSPEC Cookbook: Making SO_2 Measurements at Active Volcanoes*. IAVCEI, Methods in Volcanology, 1, 121-167.

Moffat A.J. and Millán M.M. (1971) The application of optical correlation techniques to the remote sensing of SO_2 plumes using skylight. Atmospheric Environment, v. 5, p. 677-690

Mori T. and Notsu K. (1997) Remote CO, COS, CO_2, SO_2, HCl detection and temperature estimation of volcanic gas. Geophys. Res. Lett. 24, 2047–2050.

Mori T. and Burton M.(2006) The SO_2 camera: A simple, fast and cheap method for ground-based imaging of SO_2 in volcanic plumes, Geophys. Res. Lett., 33, L24804

Mori T., Mori T., Kazahaya K., Ohwada M., Hirabayashi J., Yoshikawa S. (2006) Effect of UV scattering on SO_2emission rate measurements, Geophys. Res. Lett. 33:L17315

Moretti R., Papale P., Ottonello P. (2003) A model for the saturation of C-O-H-S fluids in silicate melts, *in* C. Oppenheimer, D. M. Pyle, and J. Barclay (Eds), *Volcanic Degassing*, Geol. Soc. Spec. Publ., 213, p. 81-101

Morrissey M.M., Zimanowski B., Wohletz K. (2000) Phreatomagmatic Fragmentation. *In:* Sigurdsson (Ed) *Encyclopedia of Volcanoes*, Academic Press, San Diego, CA, p. 431-445.

Nadeau P.A., Williams-Jones G. (2009) Apparent downwind depletion of volcanic SO_2 flux - lessons fromMasaya Volcano, Nicaragua. Bull. Volc., 71, p.389-400

Newcomb G. and Millán M.M. (1970) Theory, applications and results of the long-line correlation spectrometer. IEEE Trans. on Geoscience Electronics 8, p. 149-157.

Notsu K. and Mori T. (2010)Chemical monitoring of volcanic gas using remote FT-IR spectroscopy at several active volcanoes in Japan, Appl. Geoch., 25, p. 505-512

Ölafsdottir R, Höskuldsson A, Grönvold K, (2002) The evolution of the lava flow from Hekla eruption 2000. Abstract in: Proc 25th Nordic Geological Winter Meeting, Reykjavik,

Oppenheimer C., Francis P., Stix J. (1998) Depletion rates of sulphur dioxide in tropospheric volcanic plumes. Geophys. Res. Lett., 25(14), p.2671-2674.

Oppenheimer C., Tsanev V.I., Braban C.F., Cox R.A., Adams J.W., Aiuppa A., Bobrowski N., Delmelle P., Barclay J. and McGonigle A.J.S. (2006) BrO formation in volcanic plumes. Geochim. Cosmochim. Act. 70, p.2935-2941

OVSICORI-UNA (collective), Observatorio Vulcanológico y Sismológico de Costa Rica reports for Turrialba Volcano (2005-2010) http://www.ovsicori.una.ac.cr/vulcanologia/Volcan_Turrialba.htm# (accessed March 2010, in Spanish)

Palmer K.F. and Williams D. (1974) Optical constants of sulfuric acid; application to the clouds of Venus?, Appl. Optics, Vol. 14, No 1, p.208-219.

Pedersen R. and Sigmundsson F. (2004) InSAR based sill model links spatially offset areas of deformation and seismicity for the 1994 unrest episode at Eyjafjallajökull volcano, Iceland. *Geophys. Res. Lett.* **31**: L14610, doi:10.1029/2004GL020368.

Pieri D. and Abrams M. (2004) ASTER watches the world's volcanoes: a new paradigm for volcanological observations from orbit. J. Volcanol. Geotherm. Res. 135, 13-28.

Platt U. and Stutz J. (2008) *Differential Optical Absorption Spectroscopy - Principles and Applications.* Springer, Berlin Heidelberg New York, p. 1-597

Pollack J., Toon O., and Khare B. (1973) Optical properties of some terrestrial rocks and glasses, Icarus 19, p.372–389

Prata, A. J. (1989) Observation of volcanic ash clouds using AVHRR-2 radiances, Int. J. Rem. Sens., 10, 4–5, p.751–761

Prata A. J., Rose W. I., Self S. and O'Brien D. M. (2003) global, long term sulphur dioxide measurements from TOVS data: a new tool, for studying explosive volcanism and climate, *In* Oppenheimer C. And Robock A. (eds), *Volcanism and the Earth Atmosphere*, Geophysical Monograph 139, p.75–92

Prata A. J. and Bernardo C. (2007) Retrieval of volcanic SO_2 column abundance from Atmospheric Infrared Sounder data, J. Geophys. Res., 112, D20204.

Prata A. J. and Kerkmann J. (2007) Simultaneous retrieval of volcanic ash and SO_2 using MSG-SEVIRI measurements, Geophys. Res. Lett., 34, L05813

Pugnaghi S., Gangale. G., Corradini S., Buongiorno M.F. (2006) Mt. Etna sulfur dioxide flux monitoring using ASTER-TIR data and atmospheric observations. J. Volcanol. Geotherm. Res., 152, p. 74-90

Randel W., Wu F., Russell J., Waters J., and Froidevaux L. (1995) Ozone and temperature changes in 5 the stratosphere following the eruption of Mount Pinatubo, J. Geophys. Res., 100, p. 16753–16764.

Reagan M., Duarte E., Soto G J., Fernandez E. (2006) The eruptive history of Turrialba volcano, Costa Rica, and potential hazards from future eruptions. *In:* Rose W I, Bluth G J S, Carr M J, Ewert J W, Patino L C, and Vallance J W (eds), *Volcanic hazards in Central America*, Geol. Soc. Amer. Spec. Pap., 412, p. 235-257

Realmuto V.J., Abrams M., Buongiorno M.F., Pieri D.(1994) The use of thermal infrared image data to estimate the sulfur dioxide flux from volcanoes: A case study from Mount Etna, Sicily, July 29, 1986, J. Geophys. Res. 99(B1), p. 481-488.

Realmuto V.J., Sutton A.J., Elias T. (1997) Multispectral thermal infrared mapping of sulfur dioxide plumes: A case study from the East Rift Zone of Kilauea Volcano, Hawaii, J. Geophys. Res., 102(B7), 15057-15072.

Robock A. (2000) Volcanic eruptions and climate. Reviews of Geophysics 38(2): 191-219.

Rodriguez L. A., Watson I. M., Edmonds M., Ryan G., Hards V. L., Oppenheimer C. and Bluth G. J. S. (2008) SO_2 loss rates in the plume emitted by Soufrière Hills volcano, Montserrat. Journ. Volcanol. Geotherm. Res., 173 (1-2). p. 135-147.

Rose W.I., Gu Y., Watson I.M., Yu T., Bluth G.J.S., Prata A.J., Krueger A.J., Krotkov N., Carn S., Fromm M.D., Hunton D.E., Ernst G.G.J., Viggiano A.A., Miller T.M., Ballenthin J.O., Reeves J.M., Wilson J.C., Anderson B.E., Flittner D.E. (2003) The February–March 2000 eruption of Hekla, Iceland from a satellite perspective. *In*: Robock A. and Oppenheimer C. (Eds.), *Volcanism and Earth's Atmosphere,* AGU Geophysical Monograph 139,p. 107– 132.

Rose W. I., Millard G.A., Mather T.A., Hunton D.E., Andserson B., Oppenheimer C., Thornton B.F., Gerlach T.M., Viggiano A.A., Kondo Y., Miller T.M., Ballenthin J.O. (2006) Atmospheric chemistry of a 33-34 hour old volcanic cloud from Hekla Volcano (Iceland): insights from direct sampling and application of chemical box modelling, J. Geophys. Res. 111:D20206

Rothman L.S., I.E. Gordon, A. Barbe, D.C. Benner, P.F. Bernath, M. Birk, V. Boudon, L.R. Brown, A. Campargue, J.-P. Champion, K. Chance, L.H. Coudert, V. Dana, V.M. Devi, S. Fally, J.-M. Flaud, R.R. Gamache, A. Goldman, D. Jacquemart, I. Kleiner, N. Lacome, W.J. Lafferty, J.-Y. Mandin, S.T. Massie, S.N. Mikhailenko, C.E. Miller, N. Moazzen-Ahmadi, O. Naumenko, A.V. Nikitin, J. Orphal, V.I. Perevalov, A. Perrin, A. Predoi-Cross, C.P. Rinsland, M. Rotger, M. Simecková, M.A.H. Smith, K. Sung, S.A. Tashkun, J. Tennyson, R.A. Toth, Vandaele, A.C., and J. Vander Auwera (2008) The HITRAN 2008 molecular spectroscopic database, J. Quant. Spectrosc. Radiat. Transfer 82, p. 5-44.

Rowe G. L., Brantley S. L., Fernandez J.F. and Borgia A. (1995) The chemical and hydrologic structure of Poas Volcano, Costa Rica, J. Volcanol. Geotherm. Res., 64, p. 233-267

Salerno, G.G., M.R. Burton, C. Oppenheimer, T. Caltabiano, V.I. Tsanev, N. Bruno (2009a) Novel retrieval of volcanic SO_2 abundance from ultraviolet spectra, J. Volcanol. Geotherm. Res. 181, p.141–153

Salerno G.G., Burton M.R., Oppenheimer C., Caltabiano T., Randazzo D., Bruno N., Longo V. (2009b)Three-years of SO_2 flux measurements of Mt. Etna using an automated UV scanner array: Comparison with conventional traverses and uncertainties in flux retrieval. J. Volcanol. Geotherm. Res., 183, p. 76-83

Sawyer G.M., Carn S.A., Tsanev V.I., Oppenheimer C. and Burton M. (2008) Investigation into magma degassing at Nyiragongo volcano, Democratic Republic of Congo. Geochemistry, Geophysics and Geosystems. Vol. 9, doi: 10.1029/2007GC001829.

Scaillet B. and Pichavant M. (2003) Experimental constraints on volatile abundance in arc magmas and their implications for degassing processes, *in* Oppenheimer C., Pyle D. M., and Barclay J. (Eds) *Volcanic Degassing*, Geol.Soc. Spec. Publ., 213, p.23–52

Shinohara H., Ilyama J.T., Matsuo S.(1989) Partition of chlorine compounds between silicate melt and hydrothermal solutions: I. Partition of NaCl-KCl. Geochim. Cosmochim. Acta 53, p.2617-2630.

Sigmundsson F., Hreinsdóttir S., Hooper A., Árnadóttir T., Pedersen R., Roberts M.J., Óskarsson N., Auriac A., Decriem J., Einarsson P., Geirsson H., Hensch M., G. Ófeigsson B., Sturkell E., Sveinbjörnsson H., Feigl K.L. (2010) Intrusion triggering of the 2010 Eyjafjallajökull explosive eruption, Nature, 2010, vol. 468, n°7322, p. 426-430

Slezin Y. B. (2003)The mechanism of volcanic eruptions (a steady state approach), J. Volcanol. Geotherm. Rese. 122 (1–2), p. 7–50

Solomon S. (1999) Stratospheric ozone depletion: a review of concepts and history, Reviews of Geophysics, 37, 3, p. 275–316

Sparks, R.S.J.S (2003) Dynamics of magma degassing, *in* Oppenheimer C., Pyle D. M., and Barclay J. (Eds), *Volcanic Degassing*, Geol.Soc. Spec. Publ., Geol.Soc. Spec. Publ., 213, p. 5-22

Spilliaert N., Metrich N., Allard P. (2006) S–Cl–F degassing pattern of water-rich alkali basalt: Modelling and relationship with eruption styles on Mount Etna volcano. Earth. Plan. Sc. Let. 248, p.772-786

Stix J., Williams-Jones G. and Hickson C. (2008) Applying the COSPEC at Active Volcanoes. *In:* Williams-Jones G., Stix J. & Hickson C. (eds.) *The COSPEC Cookbook: Making SO_2 Measurements at Active Volcanoes*. IAVCEI, Methods in Volcanology, 1, p. 121-167.

Stohl A., Prata A. J., Eckhardt S., Clarisse L., Durant A., Henne S., Kristiansen N. I., Minikin A., Schumann U., Seibert P., Stebel K., Thomas H. E., Thorsteinsson T., Tørseth K., and Weinzierl B. (2011) Determination of time- and height-resolved volcanic ash emissions for quantitative ash dispersion modeling: the 2010 Eyjafjallajökull eruption, Atmos. Chem. Phys. Discuss., 11, 5541-5588

Stoiber R.E., Maliconico L.L., Williams S.N. (1983) Use of the Correlation Spectrometer at Volcanoes. *In*: H. Tazieff and J.C. Sabroux (eds.), *Forecasting volcanic events*, Elsevier, p. 425-444.

Stoiber R.E., Williams S. N., Huebert B. (1987) Annual contribution of sulfur dioxide to the atmosphere by volcanoes. J. Volcanol. Geotherm. Res. 33: 1-8.

Sutton J.A., Elias T., and Kauahikaua J. (2003) Lava-Effusion Rates for the Pu'u 'Ö'ö-Küpaianaha Eruption Derived from SO_2 Emissions and Very Low Frequency (VLF) Measurements, USGS professional paper 1676, accessed on April 2010 at http://pubs.usgs.gov/pp/pp1676/pp1676_08.pdf

Symonds R.B., Rose W. I., Bluth G. J. S. and Gerlach T. M. (1994) Volcanic gas studies: methods, results and applications, *in* M R. Carroll and J. R. Hollaway (eds), *Volatiles in Magmas*, Mineralogical Society of America Reviews in Mineralogy 30, p. 1-66.

Symonds R.B., Gerlach T.M., and Reed M.H.(2001) Magmatic gas scrubbing: implications for volcano monitoring. J. Volcanol. Geotherm. Res. 108, p. 303–341.

Tazieff H. (1970) New investigations on eruptive gases. Bull. Volc., v. 34, p. 1-18

Tazieff H.(1977) An exceptional Eruption: Mt Niragongo, Jan. 10th 1977. Bull. Volc., v. 40, p. 189-200

Tazieff H. and Sabroux J.C. (eds, 1983) *Forecasting volcanic events.* Elsevier, Amsterdam, 635 p.

Theys N., Van Roozendael M., Dils B., Hendrick F., Hao N., De Mazière M. (2009) First satellite detection of volcanic bromine monoxide emission after the Kasatochi eruption, Geophys. Res. Lett. 36, L03809

Thomas H.E., Watson I.M., Kearney C.K., Carn S.A., Murray S.J. (2010) A multi-sensor comparison of sulphur dioxide emissions from the 2005 eruption of Sierra Negra volcano, Galápagos Islands, Rem. Sens. Environ, doi:10.1016/j.rse.2009.02.019

Tilling, R.I. and Lipman R.W. (1993) Lessons in reducing volcanic risk, Nature 364, p. 277-280.

Trunk L. and Bernard A. (2008) Investigating crater lakes warming using ASTER thermal imagery: Case studies at Ruapehu, Poás, Kawah Ijen, and Copahué Volcanoes, Journ. Volcanol. Geotherm. Res., 178, p. 259-270

Urai M. (2004) Sulfur dioxide flux estimation from volcanoes using Advanced Spaceborne Thermal Emission and Reflection Radiometer: A case study of Miyake-jima volcano, Japan, J. Volcanol. Geotherm. Res., 134, p. 1-13

Vandaele A.C., Simon P.C., Guilmot J.M., Carleer M., and ColinR. (1994) SO_2 Absorption Cross Section measurement in the UV using a Fourier Transform Spectrometer, J. Geophys. Res., 99, p. 25599-25605

Vaselli O., Tassi F., Duarte E., Fernández E., Poreda R. Huertas J. (2010). Evolution of fluid geochemistry at the Turrialba volcano (Costa Rica) from 1998 to 2008. Bull. Volc., 72(4), p.397-410.

Wallace P. and Carmichael I.S.E. (1992) Sulfur in basaltic magmas, Geochim. Cosmochim. Acta, 56, p. 1863–1874

Wallace, P. J. (2001) Volcanic SO_2 emissions and the abundance and distribution of exsolved gas in magma bodies. J. Volcanol. Geotherm. Res., 108, p. 85-106.

Watson I.M. and Oppenheimer C. (2001) Photometric observations of Mt. Etna's different aerosol plumes, Atmosph. Environm. 35, p.3561-3572

Watson I.M., Realmuto V.J., Rose W.I., Prata A.J., Bluth G.J., Gu Y., Bader C.E. Yu, T. (2004) Thermal infrared remote sensing of volcanic emissions using the moderate resolution imaging spectroradiometer, J. Volcanol. Geotherm. Res., p. 135-75-89.

Wen S. and Rose W. I. (1994) Retrieval of sizes and total masses of particles in volcanic clouds using AVHRR bands 4 and 5, J. Geophys. Res., 99(D3), p. 5421–5431

Williams-Jones G, Rymer H, Rothery DA (2003) Gravity changes and passive SO_2 degassing at the Masaya caldera complex, Nicaragua, J. Volcanol. Geotherm. Res. 123 (1–2), p. 137–160

Williams-Jones, G., Stix, J. & Hickson, C. (2008)*The COSPEC Cookbook: Making SO_2Measurements at Active Volcanoes*. IAVCEI, Methods in Volcanology, 1

Wohletz K.H. (1986) Explosive magma-water interactions: Thermodynamics, explosion mechanisms, and field studies, Bull. Volc. 48, p. 245-264.

Wright R., Carn S.A., Flynn L.P. (2005) A satellite chronology of the May-June 2003 eruption of Anatahan volcano, J. Volcanol. Geotherm. Res. 146, p. 102–116

Yang K., KrotkovN. A., Krueger A. J., CarnS. A., Bhartia P. K., and Levelt P. F. (2007) Retrieval of large volcanic SO_2 columns from the Aura Ozone Monitoring Instrument: Comparison and limitations, J. Geophys. Res., 112, D24S43

Yang K., Krotkov N. A., Krueger A. J., Carn S. A., Bhartia P. K., and Levelt P. F. (2009) Improving retrieval of volcanic sulfur dioxide from backscattered UV satellite observations, Geophys. Res. Lett., 36, L03102

Yang K., Liu X., Bhartia P. K., Krotkov N. A., Carn S. A., Hughes E. J., Krueger A. J., Spurr R. J. D., and Trahan S. G. (2010) Direct retrieval of sulfur dioxide amount and altitude from spaceborne hyperspectral UV measurements: Theory and application, J. Geophys. Res., 115, D00L09, doi:10.1029/2010JD013982.

Young S. R., Voight B. and Duffell H. J. (2003) Magma extrusion dynamics revealed by high-frequency gas monitoring at Soufrière Hills volcano, Montserrat, *in* C. Oppenheimer, D. M. Pyle, and J. Barclay (Eds.), *Volcanic Degassing*, Geol. Soc. Spec. Publ., 213, p. 219–230